Wegener Center
SCIENTIFIC REPORT
106 | 2024

Precise orbit determination and excess phase processing for radio occultation: Integrated uncertainty estimation for climate applications

Josef Innerkofler

December 2024

financially supported by

Climate Change Graz
Field of Excellence
University of Graz

FWF Österreichischer Wissenschaftsfonds

FFG Forschung wirkt.

Wegener Center

UNI GRAZ

EUMETSAT

esa

The Wegener Center for Climate and Global Change is an interdisciplinary, internationally recognized research and graduate education institute of the University of Graz that is pooling the University's expertise in Climate, Environmental and Global Change. It brings together research teams and scientists from fields such as geophysics and climate physics, meteorology, economics, geography, and social sciences. At the same time, close links are maintained and further developed with many national and international cooperation partners. The research interests range from monitoring, analysis, and modeling of climate and environmental change to the investigation of climate change impacts and the analysis of the human dimensions of these changes related to mitigation, adaptation, and loss & damage. More information at **wegcenter.uni-graz.at**.



Alfred Wegener (1880 – 1930), after whom the Wegener Center is named, was founding holder of the University of Graz Geophysics Chair (1924 – 1930). In his work in the fields of geophysics, meteorology, and climatology he was a brilliant scientist and scholar, thinking and acting in an interdisciplinary way, far ahead of his time with this style. The way of his ground-breaking research on continental drift is a shining role model. His sketch on the relations of continents based on traces of an ice age about 300 million years ago (left) as basis for the Wegener Center Logo is thus a continuous encouragement to explore equally innovative ways: paths emerge in that we walk them (motto of the Wegener Center).

The present report is the result of a PhD thesis work completed in July 2024. The work was supported by Austrian federal funds through the Aeronautics and Space Agency of the Austrian Research Promotion Agency (FFG-ALR) and the Austrian Science Fund (FWF) as well as by European funds through the European Space Agency (ESA) and the European Organization for the Exploitation of Meteorological Satellites (EUMETSAT); for details on funded projects see the Acknowledgements in the scientific papers contained in the work.

SR 106 | 2024 Precise orbit determination and excess phase processing for radio occultation: Integrated uncertainty estimation for climate applications

ISBN 978-3-9508053-5-1 December 2024

Suggested citation:
Innerkofler, J. (2024), Precise orbit determination and excess phase processing for radio occultation: Integrated uncertainty estimation for climate applications, Wegener Center Scientific Report 106-2024, Wegener Center Verlag, University of Graz, Austria, December 2024. ISBN 978-3-9505053-5-1

(c) 2024 Wegener Center Verlag, University of Graz, Austria
The usage of images, tables, or texts of this Scientific Report is permitted for non-commercial purposes if appropriate credit is given.
For any other purposes, please contact: wegcenter@uni-graz.at

Publishing institution:
Wegener Center for Climate and Global Change, University of Graz
Brandhofgasse 5, 8010 Graz, wegcenter.uni-graz.at

Contact: Josef Innerkofler
josef.innerkofler@uni-graz.at

Josef INNERKOFLER

Precise orbit determination and excess phase processing for radio occultation: Integrated uncertainty estimation for climate applications

Doctoral thesis

submitted in fulfillment of the requirements for the

Doctor of Natural Sciences

in Doctoral Program in Natural Sciences

at the University of Graz

Faculty of Environmental, and Regional Sciences and Education

Supervisor: Prof. Dr. Gottfried KIRCHENGAST

Wegener Center for Climate and Global Change & Institute of Physics,
University of Graz, Austria

2024

Supervisor

Univ.-Prof. Dr.rer.nat. Gottfried Kirchengast
University of Graz, Austria

Co-Adviser

Dr.rer.nat. Marc Schwärz
University of Graz, Austria

Abstract

The Intergovernmental Panel on Climate Change (IPCC) states that global warming is an ongoing threat and its worldwide environmental and socioeconomic implications call for a reliable global observational foundation of climate change processes for adequate actions of adaption and mitigation. By observing Essential climate variables (ECVs), such as atmospheric temperature and humidity, from space, the Global Navigation Satellite System (GNSS) radio occultation (RO) measurement technique is highly valuable to support these challenges with the provision of climate benchmark data. Since uncertainties in RO measurements play a significant role in the application for climate monitoring and modeling, this thesis emphasized their better quantification and established a climate-quality processing approach for low-level RO data within the new Reference Occultation Processing System (rOPS) of the Wegener Center for Climate and Global Change.

This approach comprised the implementation of a precise orbit processing subsystem, providing GNSS transmitter and RO receiver orbit and clock data, including estimates of uncertainty and careful quality control. In a subsequent step, based on the orbit and clock data, a new implementation of RO excess phase processing, which was not yet part of rOPS, was realized. Thus, the raw measurement data and their estimated uncertainties can be processed to atmospheric ECVs while ensuring SI-traceability. The integrity of this novel implementation is ensured by extensive evaluation of the uncertainty estimates and by cross-comparison of the atmospheric profiles with data from other international RO processing centers. It also has been used for the evaluation of new RO mission data.

As an important benefit of this work, rOPS, now independent of externally pre-processed input data, represents a highly valuable software utility for the cross-evaluation of existing RO processing systems, the identification of structural uncertainties in RO data, and the evaluation of future RO missions. Rigorous uncertainty propagation along the RO retrieval chain, based on the estimated profile uncertainties at excess phase level, also provides substantial benefit for RO climate research and monitoring, as well as for climate trend detection and weather prediction applications.

Zusammenfassung

Der Weltklimarat IPCC bezeichnet die globale Erderwärmung und ihre weltweiten umweltbezogenen und sozioökonomischen Auswirkungen als eine anhaltende Bedrohung und fordert daher eine zuverlässige globale Beobachtungsgrundlage für Maßnahmen zur Klimawandel-Anpassung und zum Klimaschutz. Die Methode der Radio-Okkultation (RO) auf Basis von Navigationssignalen des Global Navigation Satellite System (GNSS) ist für diese Aufgabe besonders geeignet, da sie es ermöglicht Klimareferenzdaten durch die satellitengestützte Beobachtung von Schlüsselvariablen des Klimas wie Temperatur und Feuchtigkeit in der Atmosphäre bereitzustellen. Dabei spielen die Unsicherheiten der RO-Messungen eine erhebliche Rolle bei ihrer Anwendung für Klimamonitoring und -modellierung. In dieser Arbeit wurde daher ein neuer Prozessierungsansatz für qualitativ hochwertige RO-Klimadaten innerhalb des neuen Reference Occultation Processing System (rOPS) des Wegener Centers für Klima und Globalen Wandel erarbeitet.

Dieser Ansatz umfasste die Implementierung eines Prozessierungssystems für die präzise Bahnbestimmung von GNSS-Sender- und RO-Empfänger-Satelliten, einschließlich einer Unsicherheitsschätzung und sorgfältiger Qualitätskontrolle. Auf Grundlage der präzis berechneten Satellitenbahnen wurde in weiterer Folge eine neue Implementierung der sogenannten Exzessphasen-Prozessierung realisiert, welche die Verknüpfung von den RO-Rohmessdaten und ihren geschätzten Unsicherheiten zu den atmosphärischen Klimavariablen in der Prozessierung sicherstellt. Die Integrität dieser neuartigen Implementierung wurde durch sorgfältige Evaluation der Unsicherheitsschätzungen und mittels Vergleichen der Ergebnisse mit Daten anderer internationaler RO-Prozessierungszentren sichergestellt. Weiters wurde rOPS auch zur Evaluierung neuer RO-Missionsdaten verwendet.

Als maßgebliches Resultat dieser Arbeit stellt rOPS, nun unabhängig von extern vorverarbeiteten RO-Eingangsdaten, ein äußerst wertvolles Softwaretool für die Evaluierung bestehender RO-Prozessierungssysteme, die Identifizierung struktureller Unsicherheiten in RO-Daten und die Evaluierung zukünftiger RO-Missionen dar. Eine verlässliche Unsicherheitsberechnung entlang der RO-Prozessierungskette, basierend auf den geschätzten Unsicherheiten der Exzessphasen-Daten, bietet auch erhebliche Vorteile für die Datennutzung in Klimamonitoring und Klimaforschung sowie für die Erkennung von Klimatrends und Anwendungen in der Wettervorhersage.

Acknowledgments

The two most powerful warriors are patience and time

— Leo Tolstoy

In retrospect, it took a great deal of patience and time to bring this dissertation over the finishing line, but as the saying goes: "the journey is the reward". This journey would not have been what it was if it was not for all the fellow "warriors" who accompanied me and became friends along the way. I therefore would like to express my heartfelt gratitude to all those of you who encouraged and supported me on this challenging yet rewarding endeavor.

First and foremost, I would like to express my sincerest gratitude to my supervisor Prof. Gottfried Kirchengast. His shared expertise and professional guidance, his motivational support, the facilitation of research stays, and securing financial resources during this time were more than highly appreciated. I am deeply thankful to my co-advisor Marc Schwärz for his readiness to assist in drilling into programming issues whenever needed and being an overall highly important support. I am particularly grateful also to Prof. Jens Wickert for his willingness to act as second thesis referee and examiner.

I am profoundly thankful to Christian Marquardt, Yago Andres and colleagues for the extremely helpful introduction to precise orbit determination and their overall encouragement during and besides my visits at EUMETSAT (Darmstadt, Germany). At my research stay at UCAR (Boulder, CO, USA) I was able to deepen my insights into RO low-level data processing through many fruitful discussions. Many thanks to Doug Hunt, Bill Schreiner and the entire COSMIC team, in particular also to Therese Rieckh, for the warm welcome. Special thanks are expressed to Adrian Jäggi and colleagues of AIUB (Bern, Switzerland) for the hands-on support with the Bernese GNSS software. The assistance of Congliang Liu and colleagues from NSSC/CAS and NSMC/CMA (Beijing, China) on FengYun satellite data processing is greatly appreciated. Many thanks are extended also to all my co-authors for their support and sharing of their expertise. Furthermore, I gratefully acknowledge all the data providers for having shared their valuable

data and tools as an essential basis for this research (see the detailed data sources credits in the research articles).

I am highly appreciative to all the persons who have been associated with the Doctoral Programme Climate Change (DKCC), for having facilitated an excellent environment to practice interdisciplinarity and broaden the view beyond the dissertation topic. In this context I want to express particular gratitude to all the fellow students, especially those of you who became members of the extended "Innerkofler Family"; it has truly been a delight.

My special thanks are extended to all members of the ARSCliSys research group, and the rOPS development team in particular, and beyond this really to all the people of Wegener Center for the countless intermissions, which promoted scientific discourse, triggered the thirst for knowledge, and brought fun and joy into a hard-working scientist's life. I am extremely thankful also to the people in the administration office, for providing an island of serenity between chasing deadlines and for their endless patience with my entangled travel expenses requests.

My warmest gratitude goes out to all my friends and loved ones, to those of you who shared all the victories and defeats in ice-hockey, with whom I conquered the mountains, shared musical delights, explored remote places, and cherished many special moments. You all provided a welcoming distraction from the stresses and day-to-day challenges of a doctoral student.

Last but not least, I want to express my warmest gratitude with all of my heart to my family, to my siblings and to my parents, for always being encouraging and a stable backing in the ups and downs of life, supporting me in all my interests, whether inside or besides academia.

Contents

Abstract v

Zusammenfassung vii

Acknowledgments ix

Contents xi

Preface 1

I. Synopsis 3

1. Introduction 5

2. Atmospheric remote sensing for climate monitoring 9
2.1. Satellite based climate monitoring 9
2.2. Essential climate variables (ECVs) 11
2.3. GNSS radio occultation (RO) for climate 11
2.3.1. Properties of benchmark observations from RO 12
2.3.2. Traceability of RO measurements 15
2.3.3. Time as a fundamental standard 16
2.4. Estimation of measurement uncertainties 19
2.4.1. Concepts of measurement uncertainty 19
2.4.2. Uncertainty in RO measurements 20
2.4.3. Quality assessment and stability of the measurements . . . 21
2.5. Research challenges 22

3. Methodology and data 23
3.1. RO measurement technique 23
3.2. Reference Occultation Processing System 27
3.2.1. Precise orbit determination 28
3.2.2. RO excess phase processing 29
3.2.3. From excess phase to ECVs 30

3.3. Data 30
3.3.1. GNSS RO tracking data 30
3.3.2. GNSS transmitter orbit and clock data 32
3.3.3. Atmospheric field data 33
3.3.4. Auxiliary data 34

II. Research articles **35**

4. Paper 1: Precise orbit determination for climate applications of GNSS radio occultation including uncertainty estimation **37**
1. Introduction 40
2. Missions and spacecraft payload 41
3. Processing setup and description 43
3.1. Data and tools 43
3.2. Precise orbit determination 44
3.3. Orbit solutions 45
3.4. Satellite laser ranging 46
3.5. Uncertainty modeling 47
4. Results and discussion 49
4.1. Orbit comparison 49
4.2. Satellite laser ranging validation 51
4.3. Uncertainty estimation 53
5. Conclusions 54

5. Paper 2: GNSS radio occultation excess phase processing for climate applications including uncertainty estimation **63**
1. Introduction 65
2. Processing setup and system modeling 67
2.1. Input data preparation 68
2.2. Daily and event-based system modeling 69
3. Excess phase processing and algorithmic description 72
3.1. Excess phase processing 72
3.2. Quality control and uncertainty estimation 77
4. Results and discussion 81
4.1. Statistical analysis 84
4.2. Uncertainty analysis 85
5. Summary & conclusions 86

6. Paper 3: Evaluation of excess phase and bending angle data from FengYun-3 radio occultation based on two independent processing chains **97**
1. Introduction 99
2. Data and methods 101
2.1. FengYun-3 mission and data 101
2.2. Validation setup 102
3. Results 104
3.1. Precise orbit determination cross-evaluation 104
3.2. Excess phase and bending angle profile statistics 105
3.3. Excess phase cross-evaluation 106
3.4. Bending angle validation 108
4. Conclusions 110

III. Summary and conlusions **115**

7. Summary and conclusions **117**
7.1. Main results of research articles 118
7.1.1. Summary and conclusions for Paper 1 118
7.1.2. Summary and conclusions for Paper 2 119
7.1.3. Summary and conclusions for Paper 3 119
7.2. Synthesis conclusions and prospects 120

List of Acronyms **123**

List of Figures **131**

List of Tables **135**

Bibliography **137**

Preface

This thesis is based on the following peer-reviewed publications (Papers 1 and 2) and preprint-article publication (Paper 3):

Paper 1:

Innerkofler, J., Kirchengast, G., Schwärz, M., Pock, C., Jäggi, A., Andres, Y., and Marquardt, C. (2020). "Precise Orbit Determination for Climate Applications of GNSS Radio Occultation including Uncertainty Estimation". *Remote Sens.* 12(7), 1180. DOI: 10.3390/rs12071180

Author contributions: The conceptualization and methodology were provided by GK, CP, JI, and MS. The precise orbit determination software and the embedment into the Reference Occultation Processing System (rOPS) framework was prepared and implemented by JI, MS, CP, and AJ. The validation was extensively supported by JI, MS, AJ, YA, CM, and GK. JI performed the formal analysis and the investigations, created visualizations, and wrote the original draft of the paper. GK, MS, AJ, CP, YA and CM supported the writing by reviewing and editing the manuscript. JI, MS, and GK took care of the data curation and project administration. GK provided supervision throughout the process on all aspects of the study and managed the resources and funding acquisitions. All authors have read and agreed to the published version of the manuscript.

Paper 2:

Innerkofler, J., Kirchengast, G., Schwärz, M., Marquardt, C., and Andres, Y. (2023). "GNSS radio occultation excess-phase processing for climate applications including uncertainty estimation". *Atmos. Meas. Tech.* 16, 5217–5247. DOI: 10.5194/amt-16-5217-2023

Author contributions: The conceptualization and methodology were provided by JI and GK, embedded into the rOPS framework conceived by GK. JI elaborated the detailed algorithms, performed the computational implementation and the analysis, prepared the figures, and wrote the first draft of the paper. GK supported this work with the provision of detailed design input and advice on all aspects of the

study and significant contributions to the writing of the paper. The computational implementation was extensively supported by MS. MS, CM, and YA advised on a range of technical and scientific aspects and contributed through writing (review and editing). All authors participated in the consolidation of the paper for submission and towards publication.

Paper 3:

Innerkofler, J., Liu, C., Kirchengast, G., Schwärz, M., Meng, X., Bai, W., Hu, P., Sun, Y., Liao, M., Hu, X. (2024). "Evaluation of excess phase and bending angle data from FengYun-3 radio occultation based on two independent processing chains". *Res. Square*, Research Article Preprint. DOI: 10.21203/rs.3.rs-4400072/v1

Author contributions: Conceptualization was provided by JI and GK, with support also by YS, WB, and XH. Methodology was provided by JI, GK, CL, and XM. JI elaborated the detailed algorithms and evaluation setup. CL and ML conducted the FengYun GNOS data preparation and the format conversion. JI, XM, PH, and CL performed the computational implementation and the analysis. JI prepared the figures and wrote the draft of the paper. GK supported this work with the provision of detailed design input and advice on all aspects of the study and significant contributions to writing of the paper. The computational implementation and analysis was extensively supported by MS. CL and ML advised on a range of technical and scientific aspects of the FengYun satellite data and were responsible for the data provision from NSSC and NSMC. YS and XH provided the supervision to FengYun satellite data processing and analysis work from NSSC and NSMC. All authors participated in the consolidation of the paper for submission and towards publication.

The thesis starts with a synopsis in Part I in which the research questions are introduced and motivated. The scientific context and background are given and an overview on used methods and data sets is provided. Part II presents the main scientific results in the form of three published papers and Part III the overall summary and conclusions. Finally, lists of acronyms, figures, and tables as well as a bibliography can be found at the end of this thesis.

Part I.

Synopsis

1. Introduction

It is unequivocal that human influence has warmed the atmosphere, ocean and land since pre-industrial times.

— IPCC 2021

The Intergovernmental Panel on Climate Change (IPCC) states that up to now the Earth's atmosphere and oceans have warmed, the amounts of snow and ice decreased, and sea levels have risen. The increase in uptake of energy in the climate system is due to additional radiative forcing mainly caused by an increase in the concentration of atmospheric greenhouse gases, particularly Carbon Dioxide (CO_2) emitted by anthropogenic combustion processes (IPCC 2021). With global warming ongoing and its worldwide environmental and socioeconomic implications, improvement in the observational foundation of Earth's climate system has become more important than ever (IPCC 2021).

The Global Climate Observing System (GCOS), an international non-governmental organization co-sponsored by the World Meteorological Organization (WMO), aims to provide climate system information on physical, chemical and biological properties, in the atmospheric, oceanic, terrestrial, hydrologic, and cryospheric domains (GCOS 2015). Following the guidelines of GCOS the establishment and preservation of climate benchmark data records for the detection, projection, and attribution of changes in the climate system are considered essential (GCOS 2021).

In order to qualify as climate benchmark data, the data need to be globally (satellite-based), long-term stable, of high accuracy, and referenced (traceable) to a known standard, such as Systeme International (SI) units, measuring Essential Climate Variables (ECVs) (Bojinski et al. 2014). In the atmosphere, these are, among others, temperature and water vapor. However, in many cases ECVs are not measured directly but inferred indirectly employing a retrieval from other measurements (GCOS 2010a). From such an underlying dataset, a so-called Fundamental Climate Data Record (FCDR), ECVs processed with multiple steps, can serve as climate benchmark data.

The Global Navigation Satellite System (GNSS) Radio Occultation (RO) (Kursinski et al. 1997; Hajj et al. 2002) is one such highly valuable measurement technique which qualifies for providing climate benchmark data established on an FCDR based on the principle measurement of time (SI-unit). First the method was applied in stellar (J. L. Elliot 1996) and planetary occultation (Eshleman 1973; Fjeldbo and Eshleman 1965) and later, with the rise of GNSS, also adopted for probing the Earth's atmosphere (T. P. Yunck et al. 1988), this measurement technique has now been providing measurements for decades. The long term calibrated measurements (Steiner et al. 2020) of an FCDR make it an eligible choice for climate applications and validation of other observing systems.

RO data processing requires a sophisticated retrieval in order to infer ECVs from the raw measurement data. One realization, implemented at Wegener Center for Climate and Global Change (WEGC), is the Reference Occultation Processing System (rOPS) software (Kirchengast et al. 2016; Kirchengast et al. 2018) providing a continuous processing chain starting from the raw satellite measurements. This incorporated the recent implementation, as part of rOPS, of the Precise Orbit Determination (POD) of the receiver satellites and the excess phase (denoting the signal path extension induced by the atmosphere) processing as a fundamental part of the work of this thesis.

For climate applications it is inevitable to accompany the measurements with estimation of uncertainties attributed to the measurements, which is also required and emphasized by the GCOS. rOPS features the calculation of systematic and random uncertainties, implemented following JCGM 2008a, at each step of the retrieval. In particular, this work focuses on estimation of uncertainties for the calculated orbits and the excess phase calculations.

The thesis is structured in three parts, first the synopsis (Part I) provides a broad introduction to the topic, secondly the peer-reviewed research articles forming the core part of the research (Part II), and lastly a concluding summary (Part III). The synopsis in Part I puts the work in context of the global climate monitoring problem and the research challenges specific to this work in Chapter 2. Chapter 3 introduces the RO measurement technique and the rOPS processing system, as well as the corresponding data and sources required for the processing.

Part II of this thesis comprises three research articles following the native sequence of processing RO data (Chapters 4 to 6). Chapter 4 describes the precise orbit determination setup employed at WEGC in Paper 1: *Precise orbit determination for climate applications of GNSS radio occultation including uncertainty estimation*, followed by Chapter 5 that describes the excess phase processing in Paper 2: *GNSS radio occultation excess phase processing for climate applications including*

uncertainty estimation, and Chapter 6 describing the validation of new mission data in Paper 3: *Evaluation of excess phase and bending angle data from FengYun-3 radio occultation based on two independent processing chains.* Chapter 7 in Part III finally provides a consolidated summary of the work conducted and an overall collection and synthesis of the conclusions.

2. Atmospheric remote sensing for climate monitoring

I enjoyed the rich color spectrum of the earth. It is surrounded by a light blue aureole that gradually darkens, becoming turquoise, dark blue, violet, and finally coal black.

— Yuri Gagarin

For measuring the state of the climate system globally, remote sensing data from near-Earth orbiting satellites are indispensable. Different measurement techniques exploit different interactions of electro-magnetic waves with the Earth's atmosphere. Fundamental to all measurement techniques and the application for climate monitoring is the proper calibration and validation of the data and safeguarding their reliability in terms of a sophisticated quality control of the measurements. Another important aspect to adequately fit the purpose of climate research is that the underlying processing of the data must be fully traceable, and therefore repeatable, and uncertainties attributed to the measurements need to be quantified. In the following I discuss the requirements and feasibility of atmospheric remote sensing in general and then with focus on RO.

2.1. Satellite based climate monitoring

In the past, meteorological observations primarily served the purpose for weather forecasting and therefore are limited in the use for long-term monitoring of a changing climate, which can significantly influence trend analysis (Thorne et al. 2005). Also, space-based observations of the free atmosphere, above the planetary boundary layer, suffered from the short life-span, inter-calibration issues, and unbalanced spatial distribution of the measurements. Limitation in the temporal and vertical resolution of the measurements pose further problems to climate trend detection and quantification (Bodeker et al. 2016; GCOS 2007).

These limitations pushed the establishment of GCOS in 1992, with the aim to ensure that the observations and information needed to address climate related issues are obtained and made available to all potential users (GCOS 2010b). Following this endeavor GCOS formulated principles for climate monitoring (GCOS 2015, Appendix 6) with the background idea to incorporate a long-term, user driven operational system for providing the observations needed for monitoring the climate system, detecting and attributing climate change, assessing anthropogenic impacts, and supporting adaptation to climate variability and change (GCOS 2015).

The need for an international reference observing network was challenged with the establishment of the GCOS Reference Upper Air Network (GRUAN) (Seidel et al. 2009). Designed to provide accurate atmospheric climate data records GRUAN is envisaged as a network of 30 to 40 high-quality, long-term, upper-air observing sites that are built on, but not confined to, the larger GCOS upper-air network. Up to date there exist 14 certified stations[1] (with more to be certified) providing balloon-borne atmosphere soundings and ground-based measurements. However, obviously it still has the limitation of an unequally distributed station network around the globe with challenges in the unbiased calculation of averages, due to different qualities of radiosonde data (Ladstädter et al. 2015). It became evident that a reference observing system has to be satellite based.

For improved global coverage and high resolution measurements from space, observation systems of the Earth's atmosphere on board of satellites in Low Earth Orbit (LEO) are a fitting choice. Various measurement systems are realized in this segment (e.g., Elachi and Zyl 2006), but only few are in question for adoption and fulfilling the requirements following the climate monitoring principles of the GCOS (GCOS 2015, Appendix 6). With respect to upper air temperature measurements from Advanced Microwave Sounding Unit (AMSU)/Advanced Technology Microwave Sounder (ATMS) style instruments provide the longest record of data (since 1979) of global coverage, however those measurements also suffer from substantial uncertainties due to inter-satellite offsets and diurnal drift biases (Wang and Zou 2014; Ladstädter et al. 2011). From the beginning of this century also hyperspectral measurements (e.g., Atmospheric Infrared Sounder (AIRS), Infrared Atmospheric Sounding Interferometer (IASI), Cross-track Infrared Sounder (CrIS) instruments) have been shown to be suitable for inferring temperature profiles (GCOS 2021). However, despite immense efforts to calibrate and homogenize these upper-air data, the long-term climate trends in the troposphere and stratosphere are still subject to controversy (Ladstädter et al. 2015).

[1] https://www.gruan.org/network/sites

In contrast to classical space-based measurement techniques based on the physics of radiative transfer RO measurements can be considered a refractometric procedure based on the atmosphere's refractive index, as one of its fundamental properties (cf. Section 3.1). The measurements are space-time based with high vertical resolution tying the measurements to the fundamental standard of time (SI-traceability). Therefore, RO has the potential to fulfill the requirements of a reference dataset for selected ECVs in the upper-air atmosphere domain and has been adopted in GCOS in 2011 (GCOS 2011).

2.2. Essential climate variables (ECVs)

The concept of ECVs was introduced by GCOS in 2003 in order to enhance the systematic observation of a limited set of critical variables for climate monitoring (GCOS 2003; Bojinski et al. 2014). Per definition, an ECV is a physical, chemical, or biological variable or group of linked variables that critically contributes to the characterization of Earth's climate (Bojinski et al. 2014). In a broader concept ECVs are identified using the following criteria.

- Relevance: The variable is critical for characterizing the climate system and its changes.
- Feasibility: Observing or deriving the variable on a global scale is technically feasible using proven, scientifically understood methods.
- Cost effectiveness: Generating and archiving data on the variable is affordable, mainly relying on coordinated observing systems using proven technology, taking advantage where possible of historical datasets.

Currently there are 55 ECVs[2] defined by GCOS grouped in an atmosphere, land, and ocean domain (see Table 2.1), widely adopted in science and politics. RO contributes to measuring air temperature, water vapor, and pressure in this context.

2.3. GNSS radio occultation (RO) for climate

Following the GCOS climate monitoring principles (GCOS 2015, Appendix 6), RO data records have the potential to serve as climate benchmark observations. According to GCOS, satellite systems for climate monitoring are required to provide global coverage, with an overlap between missions for elimination of inter-satellite biases and homogeneity and consistency between time-series observations.

[2] https://gcos.wmo.int/en/essential-climate-variables/about

Table 2.1.: Overview on Essential Climate Variables. Variables inferred from RO in bold. (Adapted from Bojinski et al. 2014)

Atmosphere	
Surface:	Air temperature, wind speed and direction, water vapor, pressure, precipitation, surface radiation budget
Upper air:	**Temperature**, wind speed and direction, **water vapor**, cloud properties, Earth radiation budget (including solar irradiance)
Composition:	Carbon dioxide, methane, other long-lived greenhouse gases, ozone and aerosol supported by their precursors
Ocean	
Surface:	Sea surface temperature, sea surface salinity, sea level, sea state, sea ice, surface current, ocean color, carbon dioxide partial pressure, ocean acidity, phytoplankton
Subsurface:	Temperature, salinity, current, nutrients, carbon dioxide partial pressure, ocean acidity, oxygen, tracers
Terrestrial	
	River discharge, water use, groundwater, lakes, snow cover, glaciers and ice caps, ice sheets, permafrost, albedo, land cover (including vegetation type), fraction of absorbed photosynthetically active radiation, leaf area index, above-ground biomass, soil carbon, fire disturbance, soil moisture

Furthermore, high accuracy measurements of ECVs with adequate temporal and spatial resolution need to be provided including the identification of random errors and time dependent biases. In the following the specific key characteristics of RO measurements which address these requirements are established.

2.3.1. Properties of benchmark observations from RO

- **Global coverage**: With the abundance of signal sources from different GNSS transmitter systems, comprising Global Positioning System (GPS), Global'naya Navigatsionnaya Sputnikovaya Sistema/Global Navigation Satellite System (GLONASS), Galileo Navigation Satellite System (Galileo), and BeiDou Navigation Satellite System (BDS), the number of potential measurements obtained by RO missions in LEO increased over time. Previously only designed to record GPS signals, more recent RO receivers in space now enable measurements from multiple GNSS. Also often considered as globally pseudo-randomly distributed measurements of opportunity, RO measurements in

fact are primarily governed by the orbit altitude and inclination of the receiving satellite in LEO, and to a lesser extent by the GNSS satellites in low inclination. Most RO missions orbit the Earth in a high inclination (polar) orbit (e.g., Challenging Mini-Satellite Payload (CHAMP), Meteorological Operational (Metop), FengYun-3 (FY-3), Constellation Observing System for Meteorology, Ionosphere, and Climate-1 (COSMIC-1)). Complemented by RO receivers in low-inclination orbits (e.g., COSMIC-2) this ensures coverage of all latitudes. Additionally, the number of globally available RO measurements increased with the launch of small satellite RO constellations from commercial satellite data providers (e.g., Spire Global, Inc. (Spire), GeoOptics, PlanetiQ) which contribute to improved global coverage.

- **Spatial resolution**: With respect to GCOS the requirement for air temperature ECV demands a vertical resolution of 1 to 2 km in the troposphere and the stratosphere. The limb-sounding geometry of RO typically features a high vertical resolution of about 100-200 m in the troposphere and about 500 m in the lower stratosphere (Kursinski et al. 1997; Gorbunov et al. 2004). The effective resolutions in general decrease moving from low to high latitudes. Especially at high latitudes the effective resolution shows a notable dependence with altitude varying from 0.2 km at 10-15 km to 1.4 km at 22-27 km (Zeng et al. 2019). The horizontal resolution accounts to 200 km to 300 km, which is relatively low compared to radiosondes or nadir-looking satellite instrumentation, but still considered sufficient for the calculation of climatologies with spatially averaged data (Foelsche et al. 2008).

- **Temporal resolution**: After the RO proof-of-concept mission Global Positioning System/Meteorology (GPS/MET) in 1995 (Rocken et al. 1997; Hajj and Romans 1998), the launch of the CHAMP mission in 2001 denotes the beginning of continuous RO measurements extending up to today and into the future with a varying number of occultation events per day, depending on the RO missions in space over time (cf. Section 3.3.1). This incessant data record provides foundation for the analysis of seasonal and long-term interannual changes. On a daily basis the GNSS signal frequency domain in the microwave L-band (e.g., GPS: $\lambda_{L1} = 0.19\,\text{m}$, $\lambda_{L2} = 0.24\,\text{m}$) allows penetration of clouds (virtually all-weather capability) and the independence of sunlight ensures 24 hours of measurements resolving the diurnal cycle. An occultation event lasts approximately 1-2 minutes depending on the exact measurement geometry which is an important feature for the long-term stability and inter-calibration of RO measurements.

- **Self-calibration and long-term stability**: The "self-calibrating" nature of the RO measurement technique is particularly important for the resulting data records to be used for climate monitoring purposes, since data of different satellites can be combined without the need of inter-calibration (Foelsche et al. 2008). This is ensured by the RO intrinsic relative phase shift measurements to the unaffected signal propagation at high altitudes in absence of the influence of the atmosphere, which implies long-term stable measurements without inter-calibration issues between different RO missions. The assumption behind this principle is that the atmosphere is virtually stable within the short measurement time of few minutes and assures reproducibility and homogeneity as demanded for Climate Data Records (CDRs) by the GCOS.

- **Accuracy**: The accuracy of RO measurements is affected by diverse error sources; some of them more or less pronounced depending on the atmospheric altitude domain. In the stratosphere the accuracy is predominantly impaired by thermal noise (instrumentation quality), local multipath, and ionospheric residual phase noise. Below, in the troposphere, other effects prevail; such as atmospheric multipath, horizontal drift of the vertical RO profiles, and the uncertainty in water vapor abundance (most pronounced in the tropics) (Kursinski et al. 1997; Schreiner et al. 2007). Additionally, residual ionospheric and atmospheric disturbances, accuracy of satellite orbit and clock solutions (discussed in Paper 1), and inversion procedures (e.g., high altitude initialization of the Abelian integral) have to be taken into account. We elaborate on those influences in more detail with respect to the inferred excess phase data in Paper 2, Section 3.2 therein.

- **Atmospheric key variables**: RO is capable to derive upper-air atmospheric variables, such as temperature, water vapor, and pressure, from the initially measured phase delays induced by the signal's refraction in the Earth's atmosphere. The measurement of such ECVs is central to the climate monitoring principles by the GCOS. With a dedicated retrieval necessary to obtain the final atmospheric parameters the GCOS also demands the data processing algorithms to be rigorously documented in a traceable setup starting from the raw measurements, including identification of attributed uncertainties of the measurements.

The estimation of the uncertainties in the low-level RO data processing can be articulated as one of the key goals of this thesis (see Section 2.5). For a more detailed overview on the number of RO measurements over time and their geographical distribution (global coverage) the reader is referred to Section 3.3.1.

2.3.2. Traceability of RO measurements

Like most remote sensing techniques, GNSS RO does not measure ECVs directly but they are inferred by indirect measurements of other variables. In the case of RO the atmospheric ECVs (temperature, pressure, and water vapor) are deduced from the measured phase delay employing a dedicated retrieval. One of the limitations of RO is the fact that the returned vertical atmospheric profiles have high vertical resolutions but require a priori information to disentangle temperature and humidity components in the troposphere as well as the fact that uncertainties in the lower troposphere increase (GCOS 2021).

In fact, the use of external data that facilitate the RO retrieval algorithms also affects the measurement and retrieval errors of the final ECVs (Wee and Kuo 2015). These auxiliary data entering the retrieval hence partially degrade the fundamental traceability (SI-second) with increasing influence in each step of the retrieval. In contrast, evaluation of the basic low-level RO data entering the retrieval, is less dependent on external data and therefore features more stable processing with narrow uncertainties of the measurements.

In a first step of the RO retrieval this regards the calculation of the excess phase path (also simply referred to as excess phase) induced by interaction (refraction and prolongation) of the GNSS signals within the atmosphere on their way from the transmitter to the receiver satellite compared to the signal path in the absence of the atmosphere (in vacuum above the atmosphere, depicted in Figure 2.3). This excess phase data record is then potentially useful for climate studies, since uncertainties and the influence of auxiliary data are limited. This was already demonstrated in a dedicated simulation study by Yuan et al. 1993, where the authors indicated that trends in excess phase data time series can be used for detection and monitoring of global and regional climate change.

For this reason the RO processing at WEGC underwent a substantial revision with the decisive change to comprise processing starting from raw measurement data in its rOPS (Kirchengast et al. 2018; Innerkofler et al. 2023). This also included the independent calculation of the LEO receiver satellite orbits with a sophisticated quality control, presented in Paper 1 (Chapter 4). Prior to those changes, the processing at WEGC used excess phase profiles along with primed

Table 2.2.: The seven SI base units (left) and their corresponding defining constants (right). (Adapted from Bureau International des Poids et Mesures 2019)

Base quantity	Base unit	Defining constant	Numerical value
time	second (s)	Cs133 transition	9 192 631 770 (Hz)
length	meter (m)	speed of light	299 792 458 (m/s)
mass	kilogram (kg)	Planck constant	6.626 070 15 10^{-34} (Js)
electric current	ampere (a)	elementary charge	1.602 176 634 10^{-19} (C)
therm. temperature	kelvin (K)	Boltzmann constant	1.380 649 10^{-23} (J/K)
amount of substance	mole (mol)	Avogadro constant	6.022 140 76 10^{-23} (mol-1)
luminous intensity	candela (cd)	luminous efficacy	683 (lm/W)

(interpolated to the measurement times) orbit and clock data available at the Data Analysis and Archive Center (CDAAC) (Angerer et al. 2017). The implementation of these two initial fundamental steps towards a closed chain in the derivation of ECVs comprises the core work of this thesis. Besides the extension of the base retrieval, the decided focus was given to the quality control and estimation of uncertainties in the POD processing and excess phase calculation. This now allows inspection of the over 30 year old hypothesis to use RO low-level data (excess phases) for climate change detection (Yuan et al. 1993), planned as follow-on work of this thesis.

In that sense an excess phase record from RO can be considered an FCDR; a long-term data record of calibrated and quality-controlled data designed to allow the generation of homogeneous products that are accurate and stable enough for climate monitoring (GCOS 2021). A further requirement is the traceability to fundamental standards which is in the case of RO secured by atomic clocks aboard the GNSS satellites, which I will discuss in more detail in the following section.

2.3.3. Time as a fundamental standard

As one of the seven SI units defined by the Bureau International des Poids et Mesures (BIPM), listed in Table 2.2, time is fundamental. Specified in 1967 “The second is the duration of 9 192 631 770 periods of the radiation corresponding to the transition between the two hyperfine levels of the ground state of the caesium 133 atom” (Comité International des Poids et Mesures (CIPM) 1967).

As one realization the time keeping within various GNSS systems (Hollberg 2020), is also based on atomic rubidium or cesium clocks as well as hydrogen masers, depicted in Figure 2.1. Usually GNSS satellites are equipped with several atomic

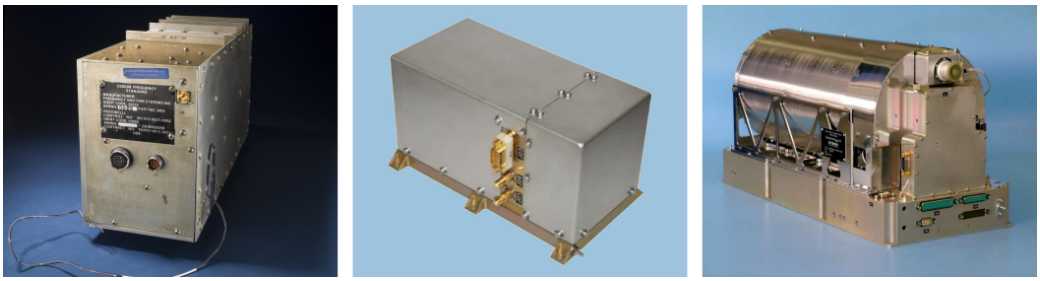


Figure 2.1.: Space-qualified GNSS atomic clocks: Cesium atomic clock built for the first GPS satellites in the late 1970 (left; https://timeandnavigation.si.edu/multimedia-asset/cesium-frequency-standard); Galileo rubidium atomic clock (middle; https://insidegnss.com/atomic-clocks-selected-for-galileos-second-generation/); Passive hydrogen maser clock for the use in Galileo GNSS (right; https://www.researchgate.net/figure/Passive-Hydrogen-Maser_fig2_259574715).

clocks (usually three to four), which are kept in synchronization with the ground network. The accuracy of the GNSS satellite's atomic clocks is essential for precise positioning and remote sensing applications. Only these highly resolved clocks allow the RO method an accuracy of adequate quality within the requirements for climate monitoring by the GCOS.

Current atomic clocks feature an accuracy of a 1 second Allan deviation of between 10^{-11} and 10^{-12}; more recent clocks even higher accuracy (Boldbaatar et al. 2023; Jaduszliwer and Camparo 2021). Figure 2.2 shows the representative Allan deviation in dependency of the averaging time for different clock types and GNSS systems. With future prospects of novel optical frequency standards, which might initiate a redefinition of the definition of the SI second (Bize 2019), generations of atomic clocks for GNSS satellites to come will continue to increase the accuracy standards for timing.

In addition to the GNSS clocks, the less stable LEO receiver clocks play a crucial role in RO data processing. Responsible for measuring the phase of the incoming GNSS signals, their accuracy co-determines the quality of the derived variables. Prone to timing inaccuracies and clock drifts the estimation of these receiver clock errors (biases) within the POD, as discussed in Paper 1 (Chapter 4), is indispensable. The receiver clock information enters the RO retrieval and is required for the correction of the raw measurement time stamps and the correct calculation of the signal transmission time through elimination of the receiver clock biases in the excess phase calculation (see Paper 2, Figure 6 therein). Depending on the accuracy of the receiver clock of various RO missions, different strategies for the removal of the clock biases are applied.

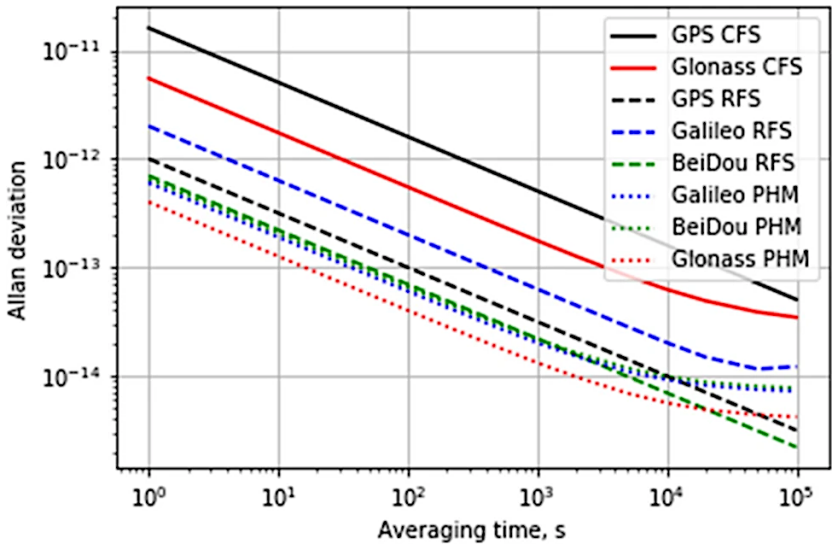


Figure 2.2.: Representative Allan deviation versus averaging time for a variety of GNSS flight clocks: cesium frequency standard (CFS), rubidium frequency standard (RFS), passive hydrogen maser (PHM). (Source: Jaduszliwer and Camparo 2021)

For satellites with sufficiently stable receiver clocks (e.g., Metop, Gravity Recovery and Climate Experiment (GRACE)) the clock biases estimated along with the orbit position and velocity calculation in the POD can be applied directly in the processing, so no differencing needs to be applied, commonly referred to as zero-differencing (e.g., as demonstrated for Metop in Paper 2). For less stable receiver clocks (e.g., CHAMP, COSMIC-1), so-called single-differencing method needs to be applied, where the receiver clock is eliminated with the aid of an additional inter-satellite link from the receiver to a non-occulting GNSS satellite (Schreiner et al. 2010), as depicted in Figure 2.3. If zero-differencing can be applied it is the preferred method, because the use of an additional inter-satellite link in the case of single-differencing introduces additional noise in the processing (Schreiner et al. 2011; Bai et al. 2018).

In the early times of GPS, when Selective Availability (S/A) intentionally reduced the accuracy of GPS for commercial users by degradation of the broadcast orbits and satellite clock dithering (Rocken and Meertens 1991), double-differencing was applied to reduce clock errors for RO processing. This was achieved by the elimination of clock biases with additional use of GPS ground station data. With the termination of S/A on May 2, 2000 the variation of the GPS transmitter clocks was reduced (Wickert et al. 2002), so the continuous RO record starting in 2001 with the launch of the CHAMP satellite is not subject to double-differencing anymore.

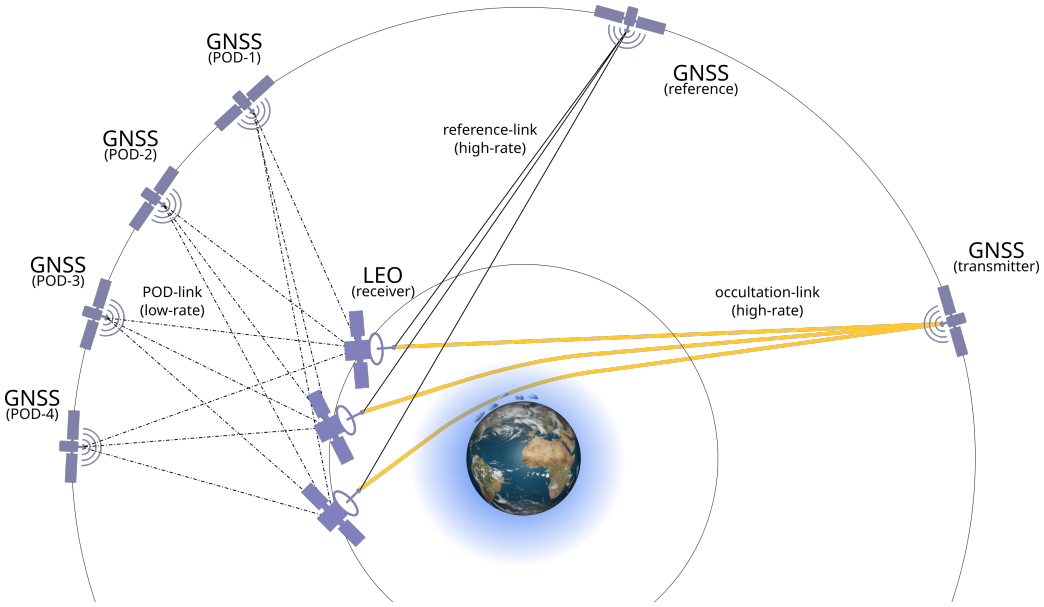


Figure 2.3.: Schematic of RO measurement principle. Radio signals from the occulting GNSS satellite pass through the atmosphere (and are refracted) on their way to the faster moving LEO receiver satellite. Depending on the differencing method applied, additional measurements of a GNSS reference satellite are employed. The precise orbit of the LEO satellite is derived by measurements obtained from the LEO zenith antenna used for POD.

2.4. Estimation of measurement uncertainties

2.4.1. Concepts of measurement uncertainty

Following the requirements by GCOS the random error and time dependent biases of an observational data set serving as climate benchmark data need to be identified. The Guide to the Expression of Uncertainty in Measurement (GUM) from the Joint Committee for Guides in Metrology (JCGM) provides an international standard for the evaluation and expression of uncertainty in measurements. Introduced in 1993 by the Comité International des Poids et Mesures (CIPM) and the BIPM it serves the community with guidelines on how to compute and communicate measurement uncertainty, promoting full information on how uncertainty statements are arrived and how to propagate them (see JCGM 2023, Annex A for a concise overview on the various parts of the GUM documentation).

With respect to RO remote sensing observations the uncertainties need to be determined, classified, and their magnitudes estimated, starting from the raw measurement data and along their propagation through the retrieval to ECVs. One decisive goal of the revision of WEGC's RO processing system was the integrated uncertainty estimation and propagation for each individual measurement and at

each step of the retrieval (Kirchengast et al. 2016), building upon the concepts of GUM (JCGM 2008b). Here I revisit the most important characteristics from the adaption for rOPS based on the GUM, which have been elaborated in more detail with respect to RO in (Schwarz 2018, Chapter 2).

2.4.2. Uncertainty in RO measurements

In the studies comprised in this thesis, and in a broader sense with respect to WEGC RO data processing, we generally categorize uncertainty in estimated random and estimated systematic uncertainties. Although it is advised in JCGM 2008b to avoid this separation, because uncertainties from systematic effects are not considered any different in nature to those from random effects, it was justified for RO data processing in Schwarz 2018, Chapter 2.3.2 therein. However, central to the GUM is the avoidance of the term error (which is not known), but using uncertainty instead: "A parameter, associated with the result of a measurement, that characterizes the dispersion of the values that could reasonably be attributed to the measurand" (JCGM 2008b).

In this categorization contributions to the uncertainty budget from unpredictable or stochastic temporal and spatial variability in repeated observations are considered estimated random uncertainties. Following essentially the characteristics of stationary processes these effects can be estimated per individual RO event, given the high noise-resolving sampling rate along the vertical profiles.

One recommendation by the GUM is to identify systematic effects (biases) and correct them if known, while residual biases are assumed to reside within certain bounds. These (conservative) bounds are then referred to as estimated systematic uncertainty. Within RO data processing we distinguish between estimated *basic* systematic uncertainties on the one hand, and estimated *apparent* systematic uncertainties on the other hand.

The estimated apparent systematic uncertainties will essentially behave as random uncertainties in ensemble averaging over a sufficient number of many RO events. The estimated basic systematic uncertainties, in contrast, are indifferent and will remain systematic when calculating averages over individual RO events. This differentiation is important with respect to the calculation of ensemble averages (such as climatologies), since the estimated basic systematic uncertainties will not average out and thus fundamentally limit the accuracy of these products.

The work conducted within this thesis represents a major contribution to the implementation of a traceable RO processing setup including the provision of estimated random and estimated systematic uncertainties. Not only was the base

retrieval extended for POD and low-level RO data processing to atmospheric excess phase profiles, but also algorithms for the attributed uncertainties at each of these processing steps were implemented from scratch. In this way this work complements the uncertainty propagation already implemented in previous work starting from simulated excess phase uncertainty estimates downwards along the RO retrieval chain to ECVs (Schwarz et al. 2017; Schwarz et al. 2018; Schwarz 2018). The estimation of uncertainties of calculated orbits and at excess phase level was established in the peer-reviewed research articles in Paper 1 (Chapter 4) and Paper 2 (Chapter 5) as an essential part of this thesis.

2.4.3. Quality assessment and stability of the measurements

As stated earlier in Section 2.3.1, RO in principle does not require inter-calibration between different missions. However, different receiver types, orbital modes, orbit stability (attitude), clock stability, and processing strategies might influence the overall outcome for climate applications (Steiner et al. 2020). It is therefore important to assess the quality of the measurements as well as of the implementation of the underlying processing algorithms before the measurements are assimilated in subsequent analysis.

For this reason, the implementation of the POD and excess phase processing within this work incorporates a well founded quality control in order to dismiss or flag profiles which are considered un-physical or of degraded quality. The quality control of the data starts by monitoring the quality of the orbit and clock solutions and the attributed uncertainties from the POD processing (Paper 1, Chapter 4) and is continued in the excess phase processing with multiple quality checks on the inferred excess phase profiles (Paper 2, Chapter 5). This allows detection of profiles of minor quality, an important feature for climate applications.

The assessment of the processing system also plays an important role for the quality of the resulting climate data, in particular for newly launched RO missions in space (e.g., Masters et al. 2020). This is demonstrated in (Paper 3, Chapter 6) in which we analyzed and assessed the quality of RO measurements from the FY-3 meteorological satellite series. The study revealed deficiencies between different data versions processed and certain periods of degraded data quality (in particular in the early years of the FengYun-3C (FY-3C) mission) by comparing results from two independent processing chains. Not being aware of those deficiencies and including them in further evaluations can degrade the results and lead to complications in the use and interpretation of the analysis.

2.5. Research challenges

So far I discussed various aspects of remote sensing for climate application with dedicated focus on RO low-level data processing. The considerations also raised scientific challenges which I want to formulate and address in the following.

From an overarching perspective this thesis challenges the climate monitoring problem by establishing a new FCDR based on RO excess phase data. This has been proposed and simulated in the beginning of the 1990s already, yet un-proven (Yuan et al. 1993). In preparation for challenging the hypothesis that RO excess phase data are a valuable dataset for climate change detection and monitoring, this work comprises the implementation of low-level data in WEGC's processing system and provides detailed algorithmic description. Within this task the following three research challenges have been identified.

1. *Which uncertainty components in the POD processing are essential contributors to the RO uncertainty budget and how can they be incorporated in WEGC's rOPS processing system? What is a sufficiently capable and also efficient orbit processing design that enables a quality monitoring for long-term RO climate data processing without the use of external orbit solutions?*

2. *Based on the POD climate-quality processing setup, how to enable SI-traceable climate data processing by the implementation of RO excess phase processing starting from raw observation data? Which uncertainty components in the excess phase processing can be derived from the POD and the raw measurements and how can they serve the quality monitoring of excess phase data?*

3. *Exploring specifically also a newer RO mission that is not yet part of international climate re-processings, to which extent is the RO dataset from the Chinese meteorological FengYun-3 (FY-3) satellite series applicable for climate analysis?*

The first research challenge is addressed in Paper 1 (Chapter 4) of this thesis. In a follow-up Paper 2 (Chapter 5) we addressed research challenge 2, presenting a novel setup of RO excess phase data processing including the estimation of random and systematic uncertainties. Paper 3 (Chapter 6), concerned with research question 3 discussed the climate utility of the FY-3 excess phase and bending angle data by comparing two independent processing chains by WEGC and the National Space Science Center (NSSC)/National Satellite Meteorological Center (NSMC).

3. Methodology and data

There's a way to do it better – find it

— Thomas A. Edison

In this chapter I revisit the foundation and development of the RO method and present the measurement principle in more depth in Section 3.1. The employed occultation processing software, WEGC's rOPS, and its enhancements compared to predecessor versions are discussed in Section 3.2. In Section 3.3, the data characteristics and sources utilized in the processing are introduced, with dedicated focus on the parts relevant to this study.

3.1. RO measurement technique

The occultation method was first applied decades ago for remote sensing of planetary atmospheres (Baum and Code 1953). With a star (the Sun) as natural radiation source, its transmitted rays are refracted and attenuated in the atmosphere of a planet on their way to Earth (J. L. Elliot 1996). Up to today stellar occultations and transits are used to infer key parameters of planetary atmospheres, as well as the presence of atmospheric gravity waves and zonal winds (Sicardy 2022).

With the launch of interplanetary spacecrafts first artificial radio sources were used in the 1960s to study planetary atmospheres. Mariner 3 and 4 were the first missions to apply RO for the sensing of the atmosphere of Mars (Yunck 2002; Fjeldbo and Eshleman 1968). Later Mariner missions, as well as Pioneer and Voyager missions, used the method to study the atmospheres of the other planets in the solar system (e.g., Eshleman 1973; Fjeldbo et al. 1976; Tyler 1987).

Although RO was applied to probe planets (and moons) throughout the solar system it was not found feasible for Earth until the late 1980s when a group at Jet Propulsion Laboratory (JPL) proposed observing GPS signals from space to make use of the RO method for sounding Earth's atmosphere (Yunck et al. 2000; Yunck 2002). So only the advent of GPS challenged the problem of having a suitable

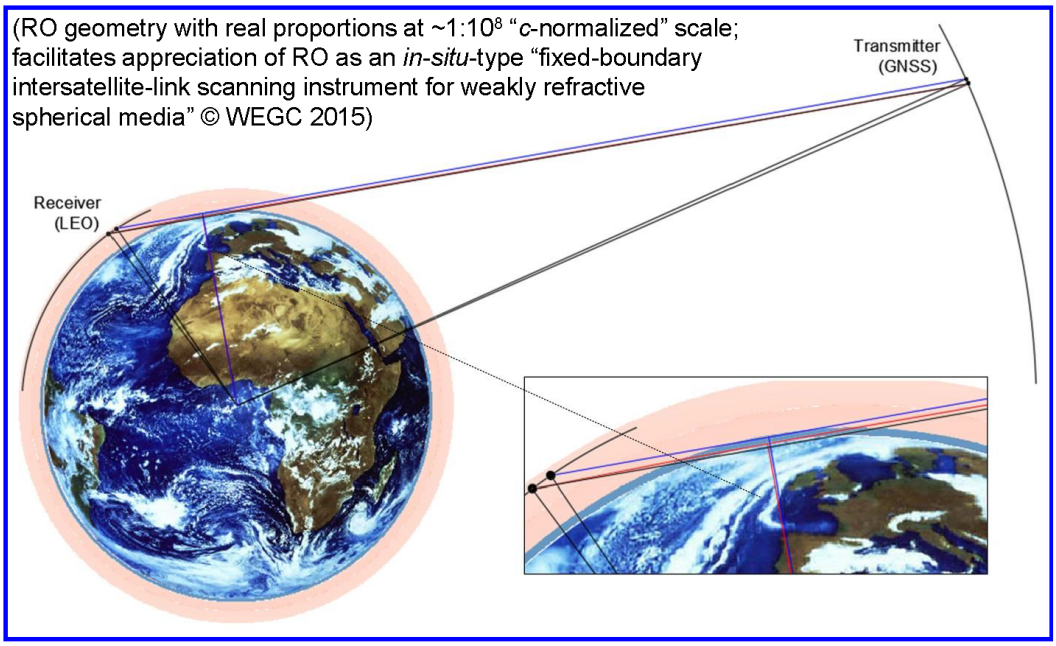


Figure 3.1.: Schematic view of the RO observing geometry with real proportions at $1 : 10^8$ scale as a "planetary system instrument" and zoom-in depicted in the insert. The insert shows the signal propagation path on top of the atmosphere (blue; no refraction) and the difference between the straight-line connection (black) and refracted propagation path (red) in the lower atmosphere. (Source: Kirchengast et al. 2018)

radio source in space outside of Earth's atmosphere. This set the stage for the low cost GPS/MET demonstration experiment led by the University Corporation for Atmospheric Research (UCAR) which was ultimately launched in 1995 (Rocken et al. 1997; Steiner et al. 1999). Although RO is also capable of sounding the ionosphere (Hajj and Romans 1998; Schreiner et al. 1999; Luntama 2009), the focus of this study lies in remote sensing of Earth's neutral atmosphere.

Already schematically introduced in Figure 2.3 of the previous chapter, the RO measurement geometry with real proportions of a random occultation event is shown in Figure 3.1. This realistic representation of the inter-satellite link between the GNSS satellite and RO receiver satellite illustrates the weak refraction of the radio signal(s) in the atmosphere and the high GNSS orbit altitudes compared to the relatively low orbiting receiver satellite in LEO.

Since the orbital velocity of a satellite in the gravity field of Earth is indirectly proportional to the distance from the center of mass, it becomes evident that the RO receiver satellite in LEO (typically orbiting the Earth at orbit altitudes between 400 km to 800 km) is moving fast (at about 7-8 $\mathrm{km\,s^{-1}}$) compared to the slower

moving GNSS transmitter satellites orbiting the Earth at an altitude between 20,000 km to 23,000 km and with a velocity of approximately $4\,\mathrm{km\,s^{-1}}$.

This relative velocity difference between the two satellites taking part in an occultation measurement rules two major categories of RO measurement geometries: (1) rising occultations and (2) setting occultations, where the LEO satellite rises/sets behind the horizon from the viewpoint of the slower moving GNSS transmitter satellite, respectively. Furthermore, each of those measurement geometries can be subdivided depending on the direction the GNSS satellite is moving. One such setting event, where the transmitter satellite is rising, is illustrated in Figure 3 of Paper 2 (Chapter 5) defining locations and angular variables of an occultation event.

So given the relative motion of the transmitter and receiver satellites GNSS signals actively scan the atmosphere in limb sounding geometry from top to bottom (setting event) or vice versa (rising event). The transmitted signals arrive with a time delay at the receiving RO satellite in LEO, induced by the signal's refraction in the Earth's atmosphere, compared to a straight-line propagation on top of the atmosphere. The bending of the signal is ruled by the refractivity gradient, which increases exponentially with decreasing distance to the Earth's surface. With typical RO receiver sampling rates of 50 to 100 Hz, changes in the phase delay are measured on a dense time grid during an occultation event lasting about 1-2 minutes, resulting in near vertical phase profiles.

The relation between the signal's optical path length L and the refractive index n can be established through Fermat's principle of least times (Born and Wolf 1999)

$$L_i = \int_{\mathrm{GNSS}}^{\mathrm{LEO}} n(f_i, s)\mathrm{d}s = \min, \tag{3.1}$$

stating that the ray path s between the GNSS and LEO satellite seeks the path of least times. The refractive index n is dependent on f_i, which denotes the different GNSS signal frequencies.

With the additional application of the fundamental Snell's law of refraction and Bouguer's formula (Pirscher 2010; Born and Wolf 1999), and under assumption of spherical symmetry using the correction of the Earth's oblateness (Syndergaard 1998) the relation between the bending angle and the refractive index can be established. By doing so, Fjeldbo et al. 1971 derived the total ray path as the integral of incremental bending along the entire ray path

$$\alpha(a) = 2a \int_{r=r_t}^{r=\infty} \frac{1}{\sqrt{(nr)^2 - a^2}} \frac{\mathrm{d}n}{n\,\mathrm{d}r}\mathrm{d}r, \tag{3.2}$$

where α is the bending angle and a the impact parameter (see Figure 3 in Paper 2 for geometrical illustration). Inversion of the Abel integral in Equation 3.2 allows to derive the refractive index n from known bending angle α and impact parameter a (Steiner et al. 1999).

The refractive index is governed by the thermodynamic state of the atmosphere and therefore also affects the optical path length L. This relation is exploited to infer atmospheric parameters (ECVs) from the measured phase delays (Smith and Weintraub 1953; Kursinski et al. 1997)

$$N = c_1 \frac{p}{T} + c_2 \frac{e}{T^2} + c_3 \frac{n_\mathrm{e}}{f_i^2} + c_4 W, \tag{3.3}$$

where p is the atmospheric pressure in hPa, T the atmospheric temperature in K, e the partial water vapor pressure in hPa, n_e the electron density in m^{-3}, f_i the transmitter frequency in Hz, and W the mass of condensed water in the atmosphere in $\mathrm{g\,m}^{-3}$. The constants completing the formula are $c_1 = 77.60$ $\mathrm{K\,hPa}^{-1}$, $c_2 = 3.73 \cdot 10^5$ $\mathrm{K}^2\,\mathrm{hPa}^{-1}$, $c_3 = 4.03 \cdot 10^7$ $\mathrm{m}^3\,\mathrm{s}^{-2}$, and $c_4 = 1.4$ $\mathrm{m}^3\,\mathrm{g}^{-1}$. Since the refractive index variations in the atmosphere are rather small it is common to use the relation to refractivity $N = 10^6 \cdot (n - 1)$.

The dispersive nature of the ionosphere in the frequency domain of GNSS signals allows to eliminate the electron density term of Equation 3.3 with small residual errors (e.g., Sokolovskiy et al. 2009b; Angling et al. 2018; Danzer et al. 2021). Also, the impact of condensed water in form of liquid water or ice crystals is very small compared to the other terms (Kursinski et al. 1997). The effect of water vapor can be disregarded in regions above 8 km at polar latitudes and 14 km at tropical latitudes (Foelsche et al. 2008; Scherllin-Pirscher et al. 2011a).

Neglecting those contributions in Equation 3.3 in first order allows to calculate dry temperature and dry pressure profiles using the hydrostatic equation and the equation of state (Pirscher 2010), also referred to as dry-air retrieval (cf. Figure 3.2, ODP). The physical atmospheric parameters and water vapor profiles are derived in the moist-air retrieval using auxiliary temperature data provided by operational analysis centers (e.g., European Centre for Medium-Range Weather Forecasts (ECMWF)).

Concluding the thermodynamic state of the dry atmosphere, the ionosphere, the moist atmosphere, and atmospheric scattering from water dictates the atmospheric refractivity. The refractivity (or refractive index) in turn affects the phase path from the GNSS to the LEO satellite. RO data processing requires an inversion algorithm to invert these relations in order to infer ECVs from the measured

phase delays and calibrated excess phase profiles. The dedicated retrieval and its realization within rOPS is addressed in the next chapter.

3.2. Reference Occultation Processing System

The development of rOPS is based on the predecessor versions and experiences gained with the development of the End-to-End Generic Occultation Performance Simulation and Processing System (EGOPS) (Fritzer et al. 2009; Kirchengast et al. 2012) and the Occultation Processing System (OPS), with OPSv5.6 being the latest version (Angerer et al. 2017; WEGC EOPAC team 2021). The aim of the scientific software project is to provide benchmark-quality RO data as a reference for calibration and validation purposes of other remote sensing satellite data, but foremost for climate monitoring, research, and services, complementary to near real-time applications.

Figure 3.2 shows the main components of rOPS, including the Daily System Modeling (DSM), Event System Modeling (ESM), and Occultation Data Processing (ODP), and their common interactions. The main RO retrieval algorithm is implemented in the ODP, while the DSM observation geometry and atmospheric background modeling as well as the ESM geometry and environment, atmospheric model profiles, and residual bias profiles parts serve as auxiliary subsystems for the ODP. The cornerstone of this new RO processing system design at WEGC is the inclusion of the Level 1a excess phase processing which is in turn dependent on the DSM observation geometry modeling providing precise orbit and clock data of the GNSS and LEO satellites. A more detailed discussion of the rOPS subsystems can be found in Paper 2, Section 2 therein.

With the extension of WEGC's processing system with the POD subsystem and the excess phase processing (realized in rOPS), the conjunction to the raw SI-traceable occultation measurement data is established. Previously, in OPSv5.6, the processing started from excess phase profiles provided by CDAAC. Closing the gap between the raw measurement data and the Level 1b bending angle retrieval (Figure 3.2; ODP), is one major contribution to rOPS realized within this work. Furthermore, this forms the basis for a refined implementation of the uncertainty estimation and propagation within rOPS, also part of this work.

In particular the newly integrated POD processing and excess phase processing, introduced in Paper 1 (Chapter 4) and Paper 2 (Chapter 5), respectively, represent the main part of the study. In the following their structure is elaborated and relevant details are discussed.

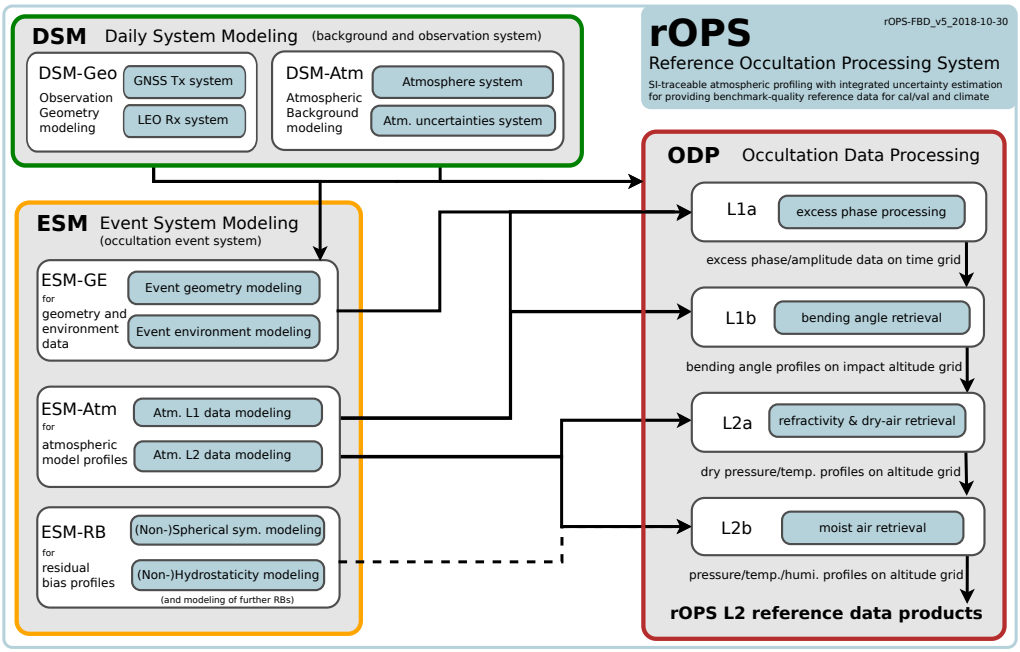


Figure 3.2.: Overview of the rOPS in form of a functional block diagram, illustrating the design and logic of the system modeling and data analysis approach, indicating its main systems and subsystems as well as its core, the occultation data processing system with the processors. (Source: Kirchengast et al. 2018)

3.2.1. Precise orbit determination

Knowledge of precise position and velocity as well as determination of clock biases of the satellites taking part in an occultation is essential for the concept of RO. While for GNSS orbits the RO community usually relies on products from the International GNSS Service (IGS) or other international analysis centers, the receiver orbits are deduced based on non-occulting GNSS satellite orbits and their transmitted signals tracked by the navigation antenna of the LEO receiver satellite (see Figure 2.3). The estimated clock errors are particularly important since they are on the one hand used for the correction of the RO measurement time stamps and on the other hand for the calculation of the atmospheric excess phases, depending on the differencing method applied (see Section 2.3.3).

Nominally the GNSS orbit products are provided at sampling intervals of 300 s and/or 900 s and the clock error estimates at 30 s and/or 5 s. The LEO orbits and clocks, calculated within rOPS, are sampled at 30 s based on GNSS signals recorded with a frequency of typically 1 or 10 Hz, depending on the receiver flown on board of different RO missions. For georeferencing the RO measurements, these orbit data are interpolated to the high frequency occultation data, typically sampled at

rates of 50 or 100 Hz, an important step for the ingestion of the orbit data into the Level 1a excess phase processing (Hunt et al. 2018).

In order to ensure a closed chain of estimated uncertainties within rOPS a concept was established and realized, using GNSS orbit input data from different analysis centers and employing two different software packages (Bernese: Dach et al. 2015; Navigation Package for Earth Orbiting Satellites (NAPEOS): Springer 2009). Additional assessment of the quality of the POD data provides valuable information for the retrieved RO profiles and also for the long-term evolution of orbit data possibly affected by orbital drifts, hardware degradation, and software modifications which might influence final climate data products. The estimated uncertainties within the POD are then used to derive uncertainties of the excess phase measurements, and further for the uncertainty propagation in the core RO retrieval (ODP).

For a detailed discussion of the POD processing realized within rOPS including the estimation of random and systematic uncertainties and the quality control towards climate-quality RO processing the reader is referred to Paper 1 (Chapter 4): *Precise orbit determination for climate applications of GNSS radio occultation including uncertainty estimation.*

3.2.2. RO excess phase processing

Given the orbits and clock biases of the transmitter and receiver satellites the phase measurements obtained by the LEO receiver satellite's occultation antenna can be georeferenced in space and time. The precise satellite positions are used to calculate the geometrical distance (straight-line connection) between the GNSS and the LEO satellite which enables to separate the atmospheric influences from the total phase path measured, yielding vertical atmospheric excess phase profiles as a function of time. This complex task comprises several steps including the interpolation of the satellite positions, velocities, and clock errors, relativistic corrections, antenna and attitude correction, navigation data demodulation, and measurement time-stamp correction, towards the final excess phase calculation (see Paper 2, Figure 6 therein).

Based on the calculated excess phases, the next step is to estimate the random and systematic uncertainties of the data with a detailed assessment of the quality of each profile (Paper 2, Section 3.2). These data can then serve as FCDR featuring narrow uncertainties and limited influence of external data (Section 2.3.2). In the subsequent RO retrieval the calculated excess phase data serve as input for the

Level 1b bending angle retrieval including uncertainty estimates for the following uncertainty propagation along the RO retrieval chain to the ECVs.

For a detailed discussion of the excess phases processing (including the estimation of random and systematic uncertainties and the quality control towards climate-quality RO processing), the event system modeling, and the forward modeling of excess phases realized within rOPS, the reader is referred to Paper 2 (Chapter 5) : *GNSS radio occultation excess phase processing for climate applications including uncertainty estimation.*

3.2.3. From excess phase to ECVs

Earlier publications elaborated on the retrieval of bending angles (Schwarz et al. 2018) and subsequently of refractivity and atmospheric profiles (Schwarz et al. 2017; Li et al. 2019) including insights on the uncertainty propagation starting from estimated random and estimated systematic uncertainties of the excess phase profiles. A detailed step-by-step description of the rOPS inversion algorithms from the quality controlled excess phase profiles to physical pressure, temperature, and humidity profiles is provided by Schwarz 2018, Appendices A to C.

3.3. Data

The data at the core of this thesis are GNSS signals collected by the GNSS receiver onboard of the RO satellites in LEO. This comprises the navigation tracking data observed by the zenith antenna and the occultation tracking data obtained from the limb-viewing occultation antenna(e). During processing of the occultation data several auxiliary data sources are exploited for the calibration of the measurements. Furthermore, we employ ECMWF global reanalysis and forecast data for quality checks within the processing, the estimation of uncertainties, the background initialization, and the evaluation of the processed data. More details on the data in use follow.

3.3.1. GNSS RO tracking data

As described in Section 3.1 the basic measurement entity of RO are phase and range observed by the GNSS receiver onboard of the RO satellites. Those observations are based on the radio wave propagation through the atmosphere and time-tagged with the receiver clock time stamps. Based on the receiver and transmitter satellite's relative location to each other, resulting measurements of opportunity are pseudo-randomly distributed. Figure 3.3 shows a representative overview of RO retrieved

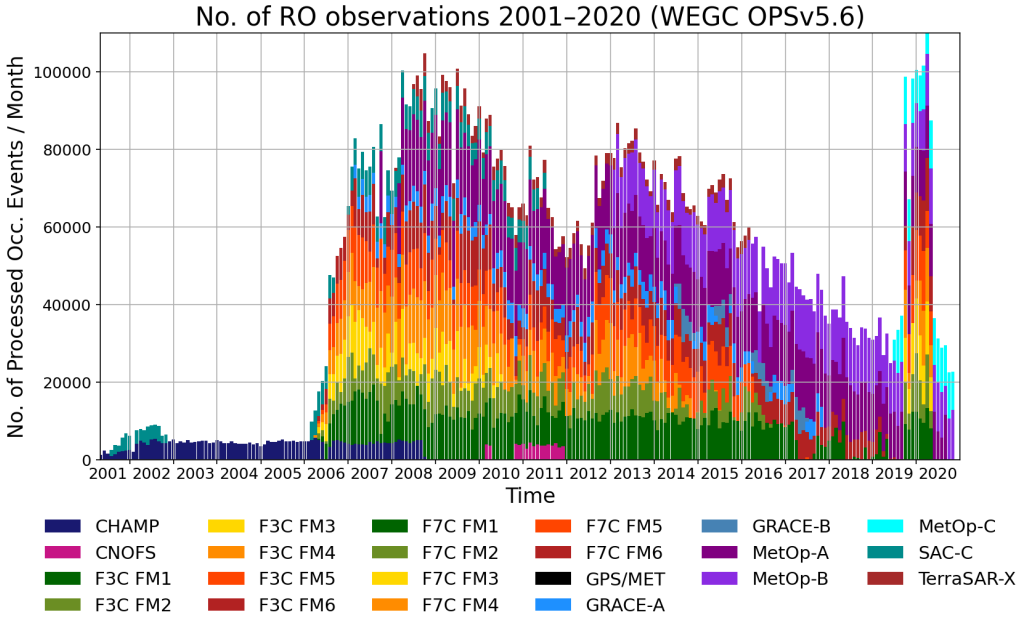


Figure 3.3.: Number of RO observations provided by major missions from beginning 2001 to end of 2020 based on input data by CDAAC and processed by WEGC-OPSv5.6. The number of occultations decrease significantly mid-2020, due to a change in the orbit data sampling rate of COSMIC, which has not been adopted for this data version.

temperature profiles available from various RO missions covering almost two decades from 2001-2020 (WEGC EOPAC team 2021, doi:10.25364/WEGC/OPS5.6:2021.1).

In the last years the space market changed. The rise of cheap launch opportunities (SpaceX; Jones 2018) and the reduction in size and mass of the satellites is linked to lower satellite production costs and fast implementation cycles. This allowed commercial companies, such as Spire (data quality assessment study: Innerkofler et al. 2020a; Marquardt et al. 2020), PlanetiQ, or GeoOptics to enter the market in the field of RO. Despite their actual and planned contribution to the total number of RO measurements per day the commercial aspects are still controversially discussed by the community (Cirac-Claveras 2019).

In particular, commercial data are subject of discussion due to uncertainties in terms of availability, open data access, full traceability, global and local time coverage, and long-term reliability. On the other hand, the increase in number of occultations per day has potentially positive impact for climate research and for Numerical Weather Prediction (NWP). The ongoing Radio Occultation Modeling Experiment (ROMEX)[1] project found a total number of approximately 35,000 RO

[1] https://irowg.org/ro-modeling-experiment-romex

profiles per day from major RO missions for a three-month period (September to November 2022) (Anthes et al. 2024). However, the authors predict a significant gap in RO observations in less than ten years and strongly advice planning for follow-on missions and acquisitions.

For long-term RO data analysis not only a stable number of occultation measurements per day and a regular geographical distribution is desired but also the local time coverage of the measurements needs to be considered. Strongly dependent on the LEO satellite orbits, the predominance of similar (polar) orbits among RO missions leads to observations aggregating at related local times. Figure 3.4 illustrates this for the COSMIC-1 mission with different local times covered between northern and southern hemispheres and further reveals seasonal dependencies. This unbalanced distribution in space and time induces sampling errors in RO climatologies (Shen et al. 2021). The imbalance in local time distribution is also evident when investigating combined RO observations from multiple missions (Anthes et al. 2024).

Another aspect, in particular for RO climate applications, is the provision, accessibility, and long-term availability of RO low-level data. In order to ensure traceability (see Section 2.3.2) between different (re-)processings and data versions the raw measurement data must be delivered prior to any data selection by the providers and long-term storage must be guaranteed. This applies occultation observations as well as to the navigation tracking data.

3.3.2. GNSS transmitter orbit and clock data

While the LEO receiver orbit positions, velocities, and clock biases are calculated within rOPS's processing chain, as part of the DSM observation geometry modeling (see Fig. 3.2), GNSS orbit and clock products are retrieved from the IGS and Center for Orbit Determination (CODE) (IGS 2024) analysis centers. The data are used as input for the LEO POD processing in order to reconstruct the precise orbits and clock bias estimates of the LEO receiver satellite and for the correct orbit arc extraction in the ODP excess phase processing.

As a fundamental aspect of climate quality data processing the two different sources for GNSS orbit data are exploited. While CODE orbit products are used as primary solution for the RO processing, IGS orbit products are used to ensure the quality of the transmitter orbit and clock data and detect possible derogation in the GNSS input data. Furthermore, measures of uncertainties are derived from these independently processed orbits. The actual setup and according details can be found in Paper 1 (Chapter 4).

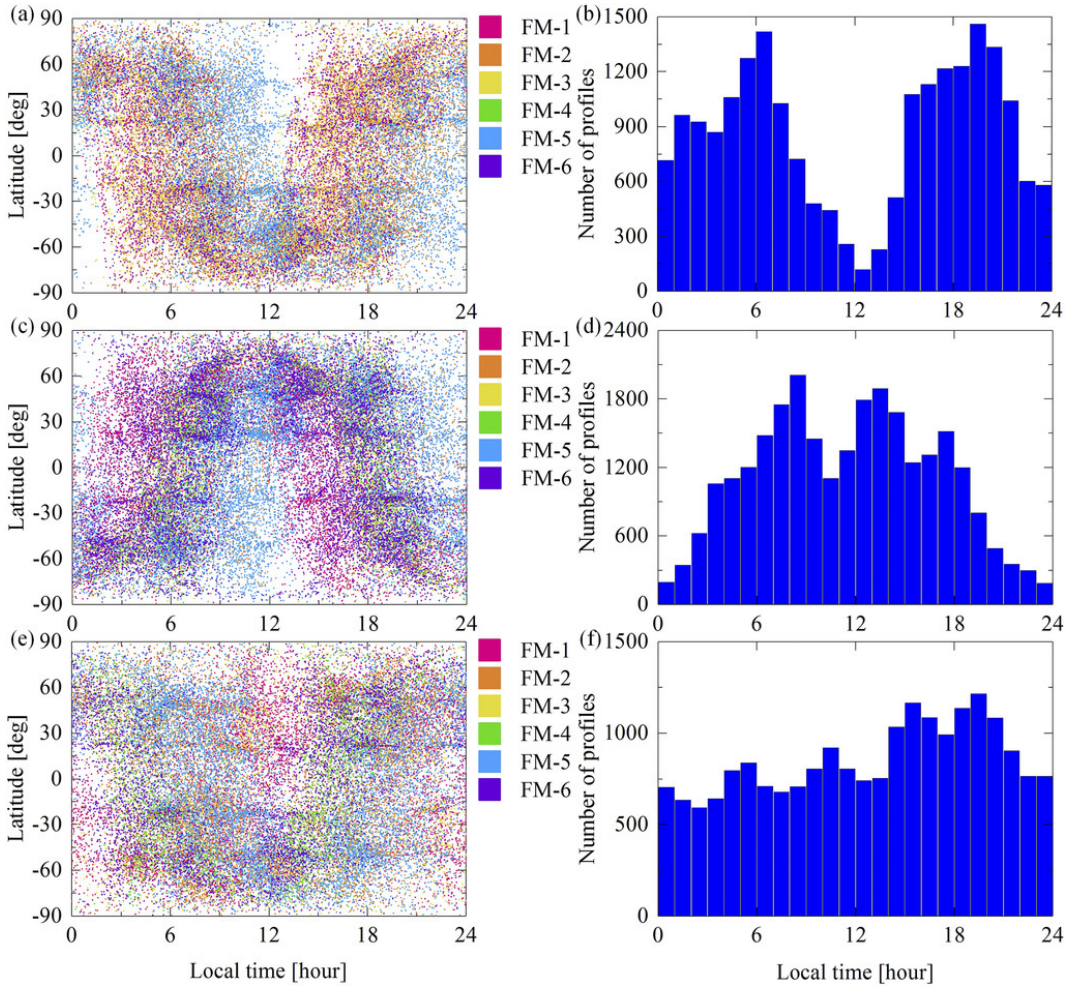


Figure 3.4.: Distribution of COSMIC-1 RO profiles in the first period of (a) January 2007, (c) March 2007, and (e) January 2008 based on latitude and local time. Panels (b), (d), and (f) show the number of COSMIC-1 RO profiles in the northern hemisphere as a function of local time in the corresponding period. (Source: Shen et al. 2021)

3.3.3. Atmospheric field data

There are multiple atmospheric reanalysis datasets using different forecast models available (see Fujiwara et al. 2022, Table 2.1 therein). In this work, and in support of the rOPS processing system in general, ECMWF field data were chosen due to their proven quality (Bauer et al. 2015). The ECMWF Re-Analysis Version 5 (ERA5) short-range forecast data from the Integrated Forecasting System (IFS) (Hersbach et al. 2020) are employed for background initialization, quality control, and in support of the uncertainty estimation in rOPS.

The short-range forecast data is essentially a pure model state with no direct information from assimilated data, an important aspect since RO data are assimilated into ECMWF analysis as of late 2006 (Healy 2007; Hersbach et al. 2020). This way the rOPS retrieval prevents possible correlations when using ECMWF analysis data for the evaluation of the final ECVs calculated by rOPS. For the evaluation at excess phase level the ECMWF refractivity field data were used to extract forward modeled excess profiles interpolated to the individual event locations. These model profiles play an important role in the assessment of the quality of the calculated excess phase profiles and for derivation of estimated random and estimated systematic uncertainties. A detailed description of the forward modeling algorithm to excess phase level is provided in Paper 2 (Chapter 5), Section 2.2 therein. The usage of the forward-modeled excess phases for the quality control of the calculated excess phases is discussed in Section 3.2 of the same paper.

3.3.4. Auxiliary data

In addition to the primary data discussed so far, various supplementary datasets are exploited in WEGC's rOPS data processing. Section 3.1 in Paper 1 (Chapter 4) and Section 2.1 in Paper 2 (Chapter 5) provide a comprehensive overview on the data sources exploited by the POD and excess phase subsystems of rOPS, respectively.

Part II.

Research articles

4. Paper 1: Precise orbit determination for climate applications of GNSS radio occultation including uncertainty estimation

Innerkofler, J., Kirchengast, G., Schwärz, M., Pock, C., Jäggi, A., Andres, Y., and Marquardt, C. (2020). "Precise Orbit Determination for Climate Applications of GNSS Radio Occultation including Uncertainty Estimation". *Remote Sens.* 12(7), 1180. DOI: 10.3390/rs12071180

remote sensing

MDPI

Article

Precise Orbit Determination for Climate Applications of GNSS Radio Occultation including Uncertainty Estimation

Josef Innerkofler [1,2,3,*], Gottfried Kirchengast [1,2,3], Marc Schwärz [1,2], Christian Pock [1,†], Adrian Jäggi [4], Yago Andres [5] and Christian Marquardt [5]

1 Wegener Center for Climate and Global Change (WEGC), University of Graz, Brandhofgasse 5, 8010 Graz, Austria; gottfried.kirchengast@uni-graz.at (G.K.); marc.schwaerz@uni-graz.at (M.S.); christian.pock@knapp.com (C.P.)
2 Institute for Geophysics, Astrophysics and Meteorology/Institute of Physics, University of Graz, Universitätsplatz 5, 8010 Graz, Austria
3 FWF-DK Climate Change, University of Graz, Liebiggasse 9, 8010 Graz, Austria
4 Astronomical Institute University of Bern (AIUB), University of Bern, Sidlerstrasse 5, 3012 Bern; adrian.jaeggi@aiub.unibe.ch
5 European Organisation for the Exploitation of Meteorological Satellites (EUMETSAT), Eumetsat Allee 1, 64295 Darmstadt, Germany; yago.andres@eumetsat.int (Y.A.); christian.marquardt@eumetsat.int (C.M.)
* Correspondence: josef.innerkofler@uni-graz.at; Tel.: +43-316-380-8460
† Current address: KNAPP AG - Logistics, Günter Knapp-Straße 5-7, 8075 Hart bei Graz, Austria.

Received: 29 February 2020; Accepted: 31 March 2020; Published: 7 April 2020



Abstract: Global Navigation Satellite System (GNSS) Radio Occultation (RO) is a highly valuable remote sensing technique for probing the Earth's atmosphere, due to its global coverage, high accuracy, long-term stability, and essentially all-weather capability. In order to ensure the highest quality of essential climate variables (ECVs), derived from GNSS signal tracking by RO satellites in low Earth orbit (LEO), the orbit positions and velocities of the GNSS transmitter and LEO receiver satellites need to be determined with high and proven accuracy and reliability. Wegener Center's new Reference Occultation Processing System (rOPS) hence aims to integrate uncertainty estimation at all stages of the processing. Here we present a novel setup for precise orbit determination (POD) within the rOPS, which routinely and in parallel performs the LEO POD with the two independent software packages Bernese GNSS software (v5.2) and NAPEOS (v3.3.1), employing two different GNSS orbit data products. This POD setup enables mutual consistency checks of the calculated orbit solutions and is used for position and velocity uncertainty estimation, including estimated systematic and random uncertainties. For LEOs enabling laser tracking we involve position uncertainty estimates from satellite laser ranging. Furthermore, we intercompare the LEO orbit solutions with solutions from other leading orbit processing centers for cross-validation. We carefully analyze multi-month, multi-satellite POD result statistics and find a strong overall consistency of estimates within LEO orbit uncertainty target specifications of 5 cm in position and 0.05 mm/s in velocity for the CHAMP, GRACE-A, and Metop-A/B missions. In 92% of the days investigated over two representative 3-month periods (July to September in 2008 and 2013) these POD uncertainty targets, which enable highly accurate climate-quality RO processing, are satisfied. The moderately higher uncertainty estimates found for the remaining 8% of days (∼5–15 cm) result in increased uncertainties of RO-retrieved ECVs. This allows identification of RO profiles of somewhat reduced quality, a potential benefit for adequate further use in climate monitoring and research.

Keywords: LEO satellites; precise orbit determination; radio occultation; satellite laser ranging; CHAMP; GRACE; Metop; uncertainty estimation; validation; climate applications

1. Introduction

Precise orbit determination (POD) has become indispensable for many space-borne applications that monitor the Earth's climate system, one of which is Global Navigation Satellite System (GNSS) [1,2] radio occultation (RO) [3–5]. The RO remote sensing technique is considered highly valuable for atmosphere and climate sciences since it provides high-vertical-resolution measurements over the troposphere and stratosphere with global coverage, high accuracy, long-term stability, and virtually all-weather capability [6,7]. During an occultation measurement GNSS signals scan the atmosphere in limb sounding geometry and arrive with a time delay at the receiving RO satellite in low Earth orbit (LEO), which is due to the signal's refraction in the Earth's atmosphere. A vertically rising or setting occultation event is observed depending on whether the GNSS transmitter satellite rises or sets behind the Earth's horizon from the viewpoint of the rapidly moving LEO receiver satellite.

The atmospheric excess phase path, which denotes the difference between the geometric straight-line distance between transmitter and receiver satellite and the signal's bended propagation path, can be derived from the measured time delays and reliable POD results. This traceability to fundamental time standards ensures long-term stability and no need for calibration [8–10]. The short-term stability of an individual RO event of about 1 to 2 min duration is satisfied by highly stable clock oscillators. Finally, essential climate variables (ECVs) [11], such as temperature, pressure, and tropospheric water vapor, can be derived from the raw measurements utilizing a dedicated RO *retrieval*. Resulting, the GNSS RO space-geodetic observing system delivers an abundance of geographically distributed vertical profiles of ECVs all over the globe, which can be averaged and used for climate studies.

Due to the unique properties of occultation soundings introduced above and global availability since 2001, records of basic RO measurements (i.e., atmospheric excess phase or derived Doppler shift) have the potential to serve as *Fundamental Climate Data Record* (FCDR): A well-characterized, global, and long-term stable data record for the derivation of accurate and stable ECVs, globally and covering timespans from days to decades [12,13]. However, in order to fully exploit this potential and provide climate benchmark data for meteorology, climate research, climate monitoring as well as for calibration and validation, the accuracy of RO data needs to be assessed. That includes quantification of remaining uncertainties throughout the entire retrieval, starting from raw measurement data with the modeling of the observation geometry, to derivation of atmospheric excess phase data, to the final thermodynamic ECVs (Figure 1).

While the quality and high accuracy of RO in the upper-troposphere and lower-stratosphere regions is well-acknowledged (e.g., [14–16]) and high consistency has been assessed between different RO retrievals of leading international processing centers [10,17,18], a rigorous uncertainty estimation and propagation throughout the entire RO retrieval remains an important but incomplete task. In addition, the former occultation processing system at WEGC [16] lacks this utility since the retrieval starts from external excess phase data and thus does not tie to the raw measurements and the physical unit of time. The new Reference Occultation Processing System (rOPS) [19,20] developed at WEGC, on the contrary, aims to establish such a fully traceable processing comprising all retrieval steps [19,21,22]. For this reason, the rOPS features the integration of RO low-level data processing starting from the raw satellite observation data. This low-level processing comprises the RO observation geometry modeling within the daily system modeling (DSM) and the level 1a (L1a) excess phase processing [23] as part of the occultation data processing (ODP) chain (cf. Figure 1). The DSM provides an advanced setup for POD of the RO receiver satellites in LEO, including the capability to routinely assess the uncertainties of the computed orbit data for climate-quality processing, which is presented in this paper.

In order to ensure highly consistent and accurate RO-derived ECVs tied to the raw measurements, precise orbit positions, velocities, and clock estimates of the GNSS transmitter satellites and LEO RO receiver satellites need to be determined and their attributed uncertainty assessed. In this study we focus on the assessment of orbit position and velocity, whereas the satellites clock characteristics and stability will be discussed in a separate publication focusing on RO excess phase processing.

Numerous past studies have evaluated the relationship between LEO orbit accuracy and atmospheric parameters derived from RO [3,24–29]. Based on the orbit accuracy specifications deduced from these studies, the POD processing presented in this study aims for a daily LEO orbit accuracy within 5 cm in position and 0.05 mm/s in velocity respectively, enabling highest quality RO retrieval results. In order to test these orbit requirements we routinely calculate different orbit solutions for mutual consistency check employing two independent POD software packages Bernese GNSS software v5.2 [30] (in short "Bernese" hereafter) and NAPEOS v3.3.1 [31], and use GNSS orbit and clock data from different orbit data archives, the Center for Orbit Determination in Europe (CODE) [32] and the International GNSS Service (IGS) [33].

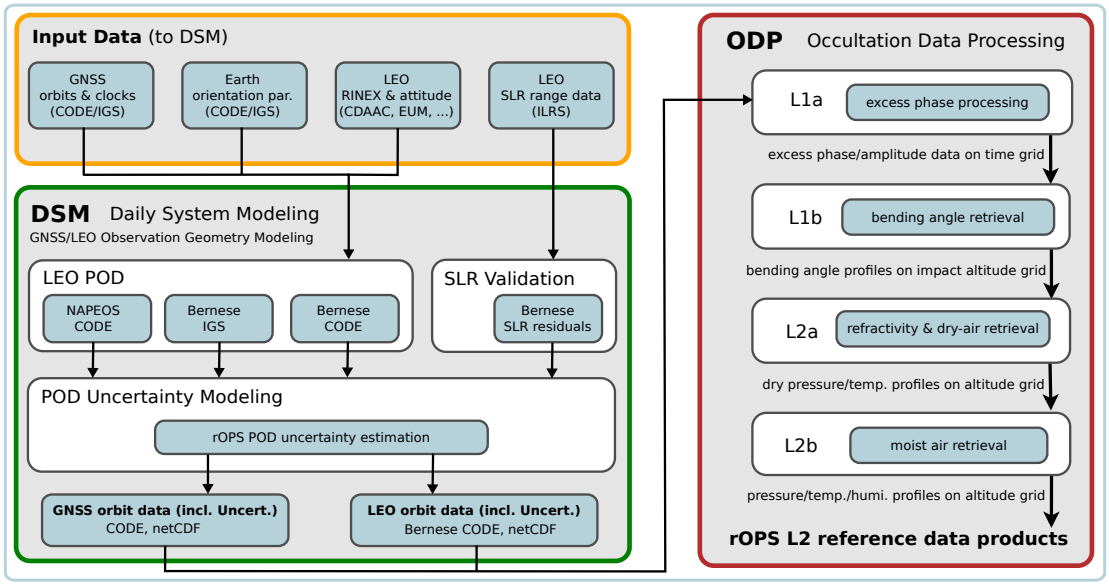


Figure 1. Schematic overview of parts of Wegener Center for Climate and Global Change (WEGC)'s Reference Occultation Processing System (rOPS) relevant to this study, comprising the input data for the precise orbit determination (Input Data; orange box), the daily system modeling (DSM; green box), and the occultation data processing (ODP; red box). For spelling of institution acronyms (in Input Data and DSM boxes) and further description see Section 3. The ODP box outlines the main level 1 and level 2 retrieval steps (L1a to L2b) from excess phase to essential climate variables (ECVs).

The computation of estimated random and systematic orbit uncertainties is based on orbit inter-comparison between the different solutions, the analysis of satellite laser ranging (SLR) residuals, and random error propagation within Bernese. Finally, days exceeding the orbit accuracy target specifications are associated with increased uncertainty estimates and flagged for the subsequent occultation data processing. Building (also) on these POD uncertainty estimates, the uncertainty propagation along the RO level 1 and level 2 data processing chain (ODP in Figure 1) ultimately delivers thermodynamic ECVs jointly with uncertainty estimates. This processing leads to reference data products enabling added-value for climate monitoring and applications from the co-estimated uncertainties.

Following this introduction, Section 2 starts with an overview of the processed missions. Section 3 introduces the data and software used followed by the description of POD and SLR technique, and the uncertainty estimation approach. Results are presented and discussed in Section 4. In Section 5 a summary and conclusion is provided.

2. Missions and Spacecraft Payload

The life-time of the RO satellite missions selected for the present study of POD for climate applications span the entire RO era, starting with first continuous long-term RO measurements

obtained by CHAllenging Minisatellite Payload (CHAMP) in February 2001. The Gravity And Climate Experiment (GRACE) mission provided RO measurements since 2006, although it has been in space since 2002 and previously activated the RO receiver for testing [34]. Meteorological operational satellite A (Metop-A), the first of a series of three meteorological satellites developed in cooperation by the European Organization for the Exploitation of Meteorological Satellites (EUMETSAT) and the European Space Agency (ESA), switched on its RO instrument 8 days after its launch on 19 October, 2006, followed by Metop-B on 17 December, 2012, before the series was completed with the launch of Metop-C from Guiana Space Centre, Kourou on 7 November, 2018 [35].

The CHAMP satellite was launched on July 15, 2000 into a near-polar but non sun-synchronous orbit of 87.3° inclination and a mean initial orbit altitude of 454 km which decreased over time despite intermediate orbit raise maneuvers, to 325 km approaching the decay. The German Research Centre for Geosciences (GFZ) managed mission provided measurements for atmospheric, magnetic and gravity field research before its end-of-lifetime after over 10 years in space [36]. The onboard *BlackJack* Global Positioning System (GPS) receiver [37], manufactured by the National Aeronautics and Space Administration's (NASA) Jet Propulsion Laboratory (JPL), is connected to a multi-antenna system including a zenith-looking choke ring antenna for navigation tracking of inter-satellite links at a rate of 0.1 Hz, an anti-velocity facing antenna array for occultation tracking at 50 Hz, and a nadir looking antenna for altimetry measurements.

The receiver front-end and electronics support dual-frequency tracking in 16 × 3 channels for C/A, P1, and P2 code respectively. Out of all channels, 12 are allocated for POD (effectively only a maximum of 10 GPS satellites were tracked simultaneously [37,38]) and the remaining 4 channels are reserved for operation in occultation mode for atmospheric sounding [27,39] or alternatively for altimetry measurements. The satellite's orientation relative to the inertial reference frame is recorded in quaternions (1 Hz) by two dual-headed Advanced Star Camera (ASC) assemblies developed by the Technical University of Denmark (DTU) [40,41]. Also onboard, a Laser Retroreflector (LRR), consisting of four cube corner prisms designed by GFZ [42,43], is mounted on the platform. The LRR passively reflects short laser pulses from an emitting ground station on Earth, thus allowing for the calculation of satellite laser ranges [44].

The GRACE twin satellite mission was a joint mission between NASA and the German Aerospace Center (DLR) and launched into similar near-circular orbits of 89.5° inclination and about 500 km altitude on 17 March, 2002. The two identical satellites were separated approximately 220 km in nominal orbit for the primary mission goal of measuring climate-relevant variations of the Earth's gravity field [45,46]. As a follow-on mission to CHAMP, GRACE features a similar design and payload, with an identical ASC and LRR mounted on the platform. Supplementary, the K-Band ranging system enables measuring the separation changes between the two satellites to micrometer precision in order to map the Earth's gravity field [47]. Equipped with a similar BlackJack GPS receiver as CHAMP [48], signals received with the zenith antenna are used for POD and the aft-looking antenna provides RO measurements for sensing physical properties of the atmosphere [34,49].

As secondary mission goal RO instrumentation was tested on both GRACE satellites for shorter periods before continuous activation of RO measurements on 22 May, 2006 on GRACE-A [27]. The majority of measurements were obtained by GRACE-A intermitted by shorter periods of occultations by GRACE-B (Jul-Dec 2014, Jun-Oct 2015, Apr-Sep 2016) when swapping maneuvers took place, making GRACE-B the trailing satellite [16]. Therefore, we limit the evaluations in this paper to the quality assessment of GRACE-A, seen as representative for both flight models. After decommissioning and atmospheric reentry of GRACE on 24 December, 2017 (GRACE-B) and 10 March, 2018 (GRACE-A) the success of the mission was continued with the launch of GRACE follow-on in May 2018 [50,51]. However, as of early 2020, RO data from this follow-on mission are not yet available to the community.

As part of the EUMETSAT Polar System the Meteorological Operational (Metop) satellite series consists of three flight models Metop-A/B/C, which were placed sequentially in time (see above) in

a sun-synchronous polar orbit of about 98.7° inclination and an altitude between 796 and 884 km [52]. The centerpiece for GPS inter-satellite tracking is the onboard GNSS Receiver for Atmospheric Sounding (GRAS) developed by Saab Ericsson Space [53,54]. The GRAS unit provides dual-frequency navigation and occultation tracking at 12 × 3 channels for L1 C/A and L1/L2 P(Y). A zenith-looking antenna observes GPS satellite signals at 8 channels with a sampling rate of 1 Hz for POD [28,29]. Furthermore, 4 channels are shared by two high-gain beam forming antennas looking in flight velocity and anti-velocity direction for rising and setting occultations respectively, supporting closed loop (50 Hz) and open loop (1 kHz) measurements [55].

For orientation of the satellite a nominal alignment is applied for the POD. In contrast to CHAMP and GRACE, the Metop satellites are not equipped with an LRR for orbit verification from the terrestrial laser tracking network. Up to this day, the Metop satellite series serves with an almost constant number of occultations per day and thereby underscores its importance as a reliable long-term backbone mission for numerical weather prediction and climate research [56].

3. Processing Setup and Description

3.1. Data and Tools

The processing setup presented in this study depends on various data sources (see also Figure 1): The GNSS transmitter satellite orbits are acquired from analysis centers (ACs) of the well-established International GNSS Service IGS, whereas data for the GPS-based POD of the receiver satellites in LEO are provided by the respective mission operators and scientific RO groups. SLR data are obtained from the International Laser Ranging Service (ILRS, https://ilrs.cddis.eosdis.nasa.gov/data_and_products/data_centers) [57,58], as a service of the International Association of Geodesy.

The GNSS orbit, clock, and Earth orientation parameter (EOP) are taken from the CODE reprocessing product series 2015 (repro2015, https://dx.doi.org/10.7892/boris.75876.3) [59] and for mutual cross-check of the derived LEO orbits from the IGS second reprocessing (repro2, http://acc.igs.org/reprocess2.html) [60]. The IGS multi-AC product combines weighted solutions from 9 contributing ACs, one of which is CODE. Although the combined IGS solutions comply with an orbit accuracy of 2.5 cm in satellite position and 75 ps in satellite clock (http://www.igs.org/products) [61,62], their implementation for RO-oriented POD is limited through the lack of provision of clock products at 30 s sampling within repro2 [63].

The CODE reprocessing series repro2015, on the contrary, offers clock estimates with a sampling of 5 s starting January 1, 2003, in addition to 30 s clocks [64]. Another substantial difference to previous versions of the CODE reprocessing is the first use of the extended Empirical CODE Orbit Model (ECOM2) within repro2015 [65]. The present 5 min clock sampling of the combined IGS solution induces a deterioration of the clock interpolation to high rate occultation data at 50 Hz sampling rate and thus also in the subsequent RO processing. Therefore the JPL solution (another highly weighted orbit product within IGS repro2 besides CODE) is currently selected, for cross-check, as a second GNSS orbit input dataset. This will be revised with the availability of the upcoming third reprocessing of the IGS (http://acc.igs.org/repro3/repro3.html).

Both data centers provide long-term stable data products until February 2015 with consistent alignment to ITRF2008. With regard to the impending POD reprocessing effort of the continuous RO era at WEGC starting from 2001 up to recently, both data sets are prolonged with final products from CODE and IGS, which are aligned to ITRF2014.

GPS receivers onboard of RO satellites record navigation tracking data from the zenith antenna for orbit processing and occultation tracking data from the limb-looking atmospheric sounding antenna(s) (Section 2). For POD with Bernese and NAPEOS the binary data from the receiver are either already provided in, or need to be converted to Receiver Independent Exchange Format (RINEX) [66]. Additionally, information in form of either measured or simulated Euler angles or quaternions provides knowledge on the satellite's attitude. The GPS observation data from the LEO receiver are acquired

from COSMIC Data Analysis and Archive Center CDAAC (https://cdaac-www.cosmic.ucar.edu/cdaac) for CHAMP and GRACE, JPL (https://podaac.jpl.nasa.gov) for GRACE, and EUMETSAT (https://eoportal.eumetsat.int) for Metop. The attitude data are acquired from CDAAC (CHAMP: as measured and provided by GFZ; Metop: nominal type) and JPL (GRACE).

The conversion from binary to RINEX format might include a pre-processing and screening of the data, as it is the case for GRACE. In the current setup two different sources for GRACE observation data are exploited: (1) CDAAC: L1A raw data which show inferred clock biases reaching up to 0.5 µs before reset (native to the GRACE clock oscillator [34,49]); (2) JPL: L1B screened data, where the clock trend is eliminated in the screening process but at the same time the phase observations are altered [67]. Primarily, the latter data are used among highly precise geodetic applications. For the application of RO, however, it is important to note that the native clock offset is required for the correction of the occultation time stamps and range calculation (for removal of GPS receiver oscillator drift in zero differencing). Optimally handled, both data (L1A and L1B) should achieve closely similar results in POD. However, the processing of the large clock trends poses challenges to the POD software packages that might not be optimally handled in the software versions used for this study and somewhat decreases the quality of the resulting orbits.

The internal quality assessment and uncertainty estimation is based on two independent software packages: Bernese GNSS software v5.2 [30], a widely used multi-GNSS data processing software capable of LEO-POD developed at AIUB, and NAPEOS v3.3.1 [31], another state-of-the-art GNSS data processing software developed and maintained by the European Space Operations Centre (ESOC) of ESA. Both software packages are capable of multi-GNSS and support the SLR tracking system for orbit validation. The SLR results presented in this paper are calculated with the Bernese software.

A similar overall processing strategy for LEO POD is inherent to the individual software packages but they vary in detail (Appendix A illustrates the setups used). Furthermore, Bernese was used to propagate random error estimates based on software extensions by AIUB [68,69]. The different models and processing setups of the Bernese and NAPEOS packages as used in this study are summarized in Table 1. The subsequent uncertainty calculations are carried out by separate routines of the rOPS.

3.2. Precise Orbit Determination

Overall, there are three different approaches to the orbit determination of satellites in LEO: (1) kinematic; (2) dynamic; and (3) reduced-dynamic. For *kinematic* POD [70] no force models are applied to the LEO, and the satellite positions are solely derived geometrically from the GNSS observations. The independence from dynamical models makes the kinematic approach attractive for many applications, e.g., gravity field determination [71]. However, kinematic orbit determination is sensitive to data problems in GNSS measurements, bad GNSS constellation (limited visibility), and data gaps [72]. Employing *dynamic* modeling [73] can overcome the strong dependence on the quality of the GNSS observation. Gravitational and non-gravitational force models are introduced to constrain the estimate of the orbit and ensure a continuous orbit in periods of low visibility and data gaps. The quality of the resulting orbit solution is limited to the quality of the force modeling.

The strong dependence on the force models may be reduced by a so-called *reduced-dynamic* approach [74–76]. By applying additional empirical parameters [68] the satellite trajectory is adjusted to the observations and the residuals are minimized, which results in orbit solutions of highest quality. For the application of RO, reduced-dynamic approaches are favored over a kinematic approach because of the need of RO for the orbit to be consistent, continuous, and of high precision. These requirements ensure the most accurate interpolation of the position, velocity, and clock estimates to the occultation measurements of an average duration of 2 min with a 50 Hz sampling rate. The usage of empirical orbit parameters differs between POD software packages. NAPEOS follows a more dynamical approach with fewer empirical parameters applied compared to the setup of Bernese as used for this study [77].

Introducing CODE and JPL GNSS orbits (15 min) and clocks (30 s sampling, see Section 3.1) the LEO orbit determination is performed using Bernese and NAPEOS. In general the processing

setup is similar to both software packages. Bernese employs a discrete kinematic approach for the initial code observations-based orbit and uses orbit integration to obtain a continuous a-priori orbit. In NAPEOS, however, initial values from the implemented Bancroft algorithm [78] serve as a basis for a dynamic orbit fit through the observations. Subsequently, iterative data screening (cycle slip and outlier detection) takes place before the final orbit integration. In Bernese the final orbit is established by means of empirical accelerations to the estimation process [79]. Models and parameters applied in the orbit processing are summarized in Table 1.

For processing raw observation data with large inherent clock estimates, such as for GRACE (cf. Section 3.1), the aforementioned processing scheme of Bernese was extended introducing an additional a-priori orbit calculation and modified data screening options.

Table 1. Summary of orbit processing models, parameters, and data. For more detailed descriptions see the references cited herein and the sofware documentations [30,31].

	Bernese GNSS Software v5.2	**NAPEOS v3.3.1**
Reference system		
Polar motion and UT1	IERS C04 08	IERS finals2000A.data
Polar model	IERS 2010 Conventions [80]	IERS 2003 Conventions [81]
Precision/Nutation	IERS 2010 Conventions	IERS 2003 Conventions
Reference frame	ITRF 2008 [82]	ITRF 2008
GPS measurement characteristics		
Observations	undifferenced ionosphere corrected code and phase	undifferenced ionosphere corrected code and phase
Sampling	30 s	30 s
Elevation angle cut-off	5 degrees	5 degrees
GPS antenna PCO/PCV	igs08.atx [83]	igs08.atx
Antenna phase wind-up	applied [61]	applied
Relativity	applied	applied
GPS parameters		
GPS orbits	CODE repro2015 (15 min) / IGS repro2 (15 min)	CODE repro2 (15 min)
GPS clocks	CODE repro2015 (5 s/30 s) / IGS repro2 (30 s)	CODE repro2 (5 s/30 s)
Gravitational forces		
Gravity field model (static)	EGM2008 (120 × 120) [84]	EIGEN-6S2 (120 × 120) [85]
Solid Earth tides	applied (IERS2010)	applied (IERS2003)
Ocean tide model	FES2004 (50 × 50) [86]	FES2004 (50 × 50)
Planetary ephemeris	DE-405 [87]	DE-405
Earth pole tide	IERS2010	IERS2003
Ocean pole tide	IERS2010	IERS2003
Non-gravitational forces		
Atmospheric density model	n/a	MSISE-90 [88]
Atmospheric drag	n/a	constant area (10/24 h)
Radiation pressure model	n/a	constant area
Earth Radiation	n/a	NAPEOS model for Albedo and IR
1/rev empiricals	n/a	1/12 h (along- and cross-track)
Other empiricals	piece-wise constant accelerations in RTN (every 6 min); constraints: 0.5 nm/s^2	n/a
Arc cut		
Arc lengths	24 h	24 h
Maneuvers	n/a	n/a
Handle of data gaps	yes	yes
Estimation		
Estimation	batch least squares	batch least squares

3.3. Orbit Solutions

In order to enable internal quality assessment and uncertainty estimation for the LEO RO receiver orbit, independent from orbit products of external providers, three POD runs are conducted routinely and in parallel at WEGC (see also Figure 1):

- WEGC-BC: The orbit solution selected for the following RO data processing. The calculation is based on Bernese and the GNSS orbit and clock data from the CODE reprocessing in 2015; referred to as *primary* solution hereafter.
- WEGC-BI: Same Bernese setup as for WEGC-BC above but employing GNSS orbit and clocks from JPL (as part of IGS repro2).
- WEGC-NC: This solution is calculated using NAPEOS, introducing the GNSS orbit and clock products from CODE as for WEGC-BC.

Among these three orbit solutions the latter two only serve for the quality assessment of the primary solution and the uncertainty estimation through inter-comparison and are not used in the further RO processing.

Additionally, for this study external orbit data from other leading processing centers are used for the validation of the internal primary solution. This comprises orbits from UCAR ([89,90]), EUMETSAT [28,91], and AIUB [92,93]. First inter-agency comparison at WEGC was carried out within a prototype study of several test days [94]. The extensive UCAR/CDAAC RO data archive holds standard re-processed orbits from their reprocessing campaign 2016 for CHAMP and Metop and post-processed orbits for GRACE. EUMETSAT provided orbit products used for comparison for Metop-A/B and CHAMP. AIUB, as a leading institute for orbit determination provides reliable orbit solutions for the CHAMP and GRACE missions. Table 2 summarizes the different orbit solutions used in this study.

Table 2. Orbit solutions and metadata used in this study.

Solution Identifier	Analysis Center	Software	GNSS Data	Remark
Internal Solutions				
WEGC-BC	WEGC	Bernese 5.2	CODE	primary solution
WEGC-BI	WEGC	Bernese 5.2	IGS-JPL	control run
WEGC-NC	WEGC	NAPEOS 3.3.1	CODE	control run
External Solutions				
UCAR	UCAR	Bernese		https://cdaac-www.cosmic.ucar.edu
EUM	EUMETSAT	NAPEOS		https://eoportal.eumetsat.int
AIUB	AIUB	Bernese		http://ftp.aiub.unibe.ch

3.4. Satellite Laser Ranging

Laser ranging to LEO satellites is a highly valuable complementary technique for validation of GNSS-derived orbits, since it uses completely independent measurements from the global geodetic ground station network of the ILRS [44,95]. SLR observations are obtained by measuring the two-way signal travel time from an SLR ground station to a satellite equipped with a Laser Retroreflector (LRR), which passively reflects the short laser pulses emitted. For most ILRS stations a one-way range precision typically ranging from 0.3–1.8 cm is achieved [58,96]. The signal travel time, corrected for propagation effects and translated into a range R, is then compared to the range from the orbit determination:

$$\Delta R_{\mathrm{SLR}} = R_{\mathrm{SLR}} - R_{\mathrm{POD}}. \quad (1)$$

Due to the measurement geometry the SLR residuals ΔR_{SLR} for high-orbiting GNSS satellites are most sensitive to the radial component of the orbit solution. For satellites in LEO, which are in general tracked at lower elevation angles, however, SLR range is sensitive to all orbital components. In an idealized concept of zero mean error and even distribution of the standard deviation in all directions the 3D position standard error can be approximated by $\sigma_{\mathrm{pos}} = \sqrt{3\sigma_{\mathrm{SLR}}}$ [44]. This idealization disregards that LEO passes are more sensitive in north-south direction to the along-track component and in east-west direction to cross-track component [97].

The SLR residuals then serve in our context as a measure for orbit accuracy, supporting the detection and estimation of potential systematic errors. Station coordinates for the observation

modeling were taken from the Satellite Laser Ranging Frame 2008 (SLRF2008, https://ilrs.cddis.eosdis.nasa.gov/science/awg/SLRF2008.html) in alignment with the GNSS orbit products used in the POD (Table 1).

3.5. Uncertainty Modeling

The estimation of uncertainties attributed to POD poses a challenging task since the accuracy of an orbit in an absolute sense is difficult to determine, but measures for orbit uncertainty can be derived through validation. Hence, as part of the RO processing at WEGC the novel POD setup of the rOPS provides a capability to compute estimated *systematic* and *random* position and velocity uncertainties for LEO and GNSS satellites from orbit inter-comparison (internal solutions, Table 2), satellite laser ranging residuals, and propagated random errors in LEO results.

In a conservative approach all systematic uncertainty estimates of an orbit found to be below an a-priori defined *conservative bound* uncertainty (u_{CB}) are set to this low-bounding value. Otherwise, if exceeding this bound, they are kept at the derived value (as described below). In addition, the overall smaller estimated random uncertainties contribute in a root-mean-squares (RMS) sense to the total combined uncertainty budget for receiver (Rx) and transmitter (Tx) satellites respectively, as follows:

$$u_c^{\mathrm{Sat}} = \sqrt{\left(u_s^{\mathrm{Sat}}\right)^2 + \left(u_r^{\mathrm{Sat}}\right)^2} \qquad \text{for} \quad \mathrm{Sat} = \mathrm{Rx}, \mathrm{Tx}, \tag{2}$$

where u_r denotes the estimated random uncertainty and u_s the total estimated systematic uncertainty. u_s is per definition always $\geq u_{\mathrm{CB}}$ as described for the LEO satellites next.

3.5.1. LEO Systematic Uncertainty Estimates

LEO satellite orbits with derived systematic uncertainties within a 3D root-mean-squared (RMS) $u_{\mathrm{CB}}^{\mathrm{Rx}}$ of 5 cm (position) and 0.05 mm/s (velocity) threshold promote negligible errors into the final atmospheric variables derived from RO. Furthermore, this threshold is regarded as conservative, since it fulfils the RO quality requirement of an error not higher than about 0.05 mm/s in along-occultation-path velocity [3,29], which is the most critical POD variable for RO retrieval quality.

In our approach several sources are exploited for the estimation of the LEO orbit uncertainties. First, the inter-comparison of different orbit products routinely calculated (Section 3.3) allows for an assessment of the generic consistency between the individual orbit solutions. Since the employed POD software packages, processing setup, parametrization, models, and GNSS data used are regarded as sufficiently independent, possible systematic errors are considered plausibly estimated. In addition, independent SLR tracking can also reveal systematic deficiencies in the orbit determination and help identify the most accurate solution. The following three measures are derived on a daily basis for checking the WEGC-BC primary solution:

(a) WEGC-BC vs. WEGC-NC difference (*LEO POD cross-check*):
Based on GNSS orbit input from CODE the orbit differences are driven by computational setup and model considerations of the different LEO POD software packages employed.

(b) WEGC-BC vs. WEGC-BI difference (*GNSS input sanity-check*):
The orbit computations are carried out by Bernese with different GNSS orbit, clock, and EOP data and might reveal deficiencies in the transmitter orbit modeling.

(c) WEGC-BC vs. SLR difference (*SLR validation cross-check*):
Analysis of SLR residuals for missions equipped with an LRR. This validation represents snapshots because of the limited number of available SLR measurement sequences per day.

The overall 3D-RMS estimate is calculated from epoch-wise differences in radial, along-track, and cross-track components as well as the RMS from the 1D SLR residuals, resulting in one daily scalar estimate per measure. From these three scalar uncertainty measures for (a), (b), and (c), termed

$u_{(a)}, u_{(b)}, u_{(c)}$ hereafter, the final systematic uncertainty estimate u_s^{Rx} for the primary orbit solution is derived as follows:

$$u_s^{Rx} = \max\left(u_{CB}^{Rx},\ \sqrt{u_{(a)}^2 + u_{(b)}^2 + u_{(c)}^2}\right);\ \text{if } u_{(x)} < u_{CB}^{Rx} \text{ then } u_{(x)} = 0,\ \ x \in \{a,b,c\}. \quad (3)$$

Such a variance combination of the uncertainty measures ensures a reasonable RMS estimate even if the individual components are not fully independent (according to the Guide to the Expression of Uncertainty in Measurement by the Joint Committee for Guides in Metrology (JCGM) [98]; see also [99] (pp. 29–44 therein)). Note that laser ranging residuals only contribute their measure $u_{(c)}$ to the calculation if available. The position uncertainties (in units cm) are empirically found (cf. Figure 2) to map with a factor around 1/1000 to the velocity uncertainties (in units mm/s); hence we adopted a conversion factor of 1/1000 for this mapping.

3.5.2. LEO Random Uncertainty Estimates

For the estimation of random uncertainty we consider the error propagation in Bernese based on formal errors of position and velocity as introduced in [68,69]. However, the estimation from the variance-covariance information of the parameter estimation of the POD depends mainly on the observation constellation and hence is considered an optimistic estimate. We therefore conservatively apply a coverage factor of 2 for an increased confidence interval for the estimate. In line with advice in JCGM [98], suggesting coverage factors typically in the range 2 to 3, the role of such a factor is to ensure that non-quantified components of the overall uncertainty are accounted for within the expanded uncertainty range. In our case the factor of 2 serves this purpose. The radial, along-track, and cross-track uncertainty components of position and velocity (Figure 2) are also combined in a 3D-RMS sense.

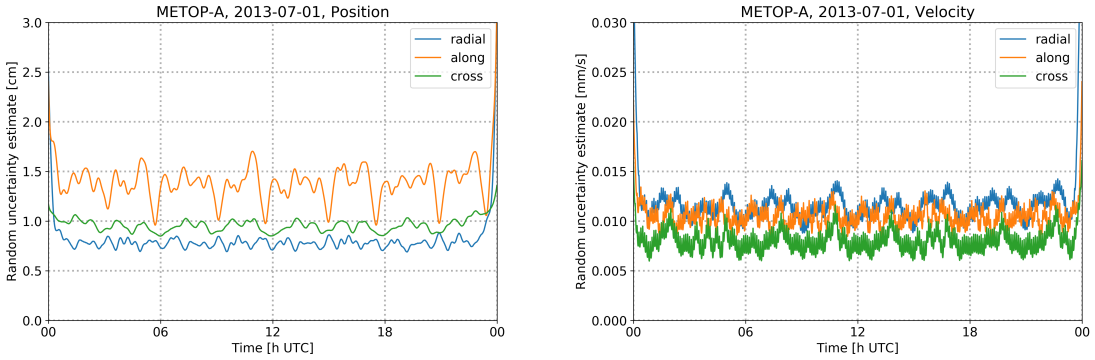


Figure 2. Propagated random uncertainty estimates (based on propagating standard errors) from Bernese for Metop-A on an example day (1 July, 2013), for position (**left**) and velocity (**right**), for the radial, along-track, and cross-track components. Coverage factor of 2 applied.

3.5.3. GNSS Uncertainty Estimates

The quantification of systematic and random uncertainty estimates for the GNSS satellites is based on the exploitation of existing analyses from the GNSS expert community. For the random uncertainty we introduce a fixed conservative bound estimate of 1 cm, adapted from the analysis of formal errors of GPS [100]. The systematic uncertainty is specified with a 3 cm conservative bound estimate, denoted u_{CB}^{Tx} hereafter, established from SLR investigations [101,102] and long-arc analysis [62,63]. Although only two GPS spacecraft were equipped with an LRR, their position quality is expected to be of similar level as they are less influenced by gravitational forces through their higher orbit. In addition to the conservative threshold values the accuracy codes (AccCode) given in the header of the SP3 orbit files (ftp://igs.org/pub/data/format/sp3c.txt) serve as a daily indicator of formal

accuracy and may increase the systematic uncertainty estimate for the individual GNSS satellites as follows:

$$u_s^{\mathrm{Tx}} = \max\left(u_{\mathrm{CB}}^{\mathrm{Tx}},\ 2^{\mathrm{AccCode}}\right), \tag{4}$$

where the accuracy codes map as an integer base-2 logarithm: $\mathrm{AccCode} = \log_2(\sigma)$ [60].

Analogous to the combined uncertainty of the LEO, the systematic and random uncertainty estimates for the GNSS are combined in a RMS sense (Equation (2)). The GPS satellite orbit uncertainty estimates depicted in Figure 3 suggest a factor around 1/5000 from position to velocity for the random errors. In order to provide also some room for unmodeled systematic effects, the corresponding uncertainty estimates for velocity are conservatively computed with a conversion factor of 1/3000 from GNSS position uncertainty estimates (in units cm) to velocity uncertainty estimates (in units mm/s).

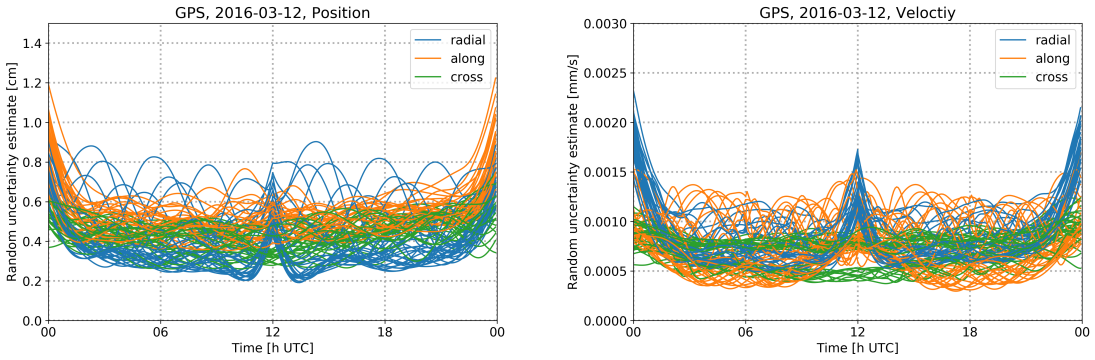


Figure 3. Propagated random uncertainty estimates (based on propagating standard errors) from Bernese for the constellation of GPS satellites on an example day (12 March, 2016), for position (**left**) and velocity (**right**), for the radial, along-track, and cross-track components. Coverage factor of 2 applied.

4. Results and Discussion

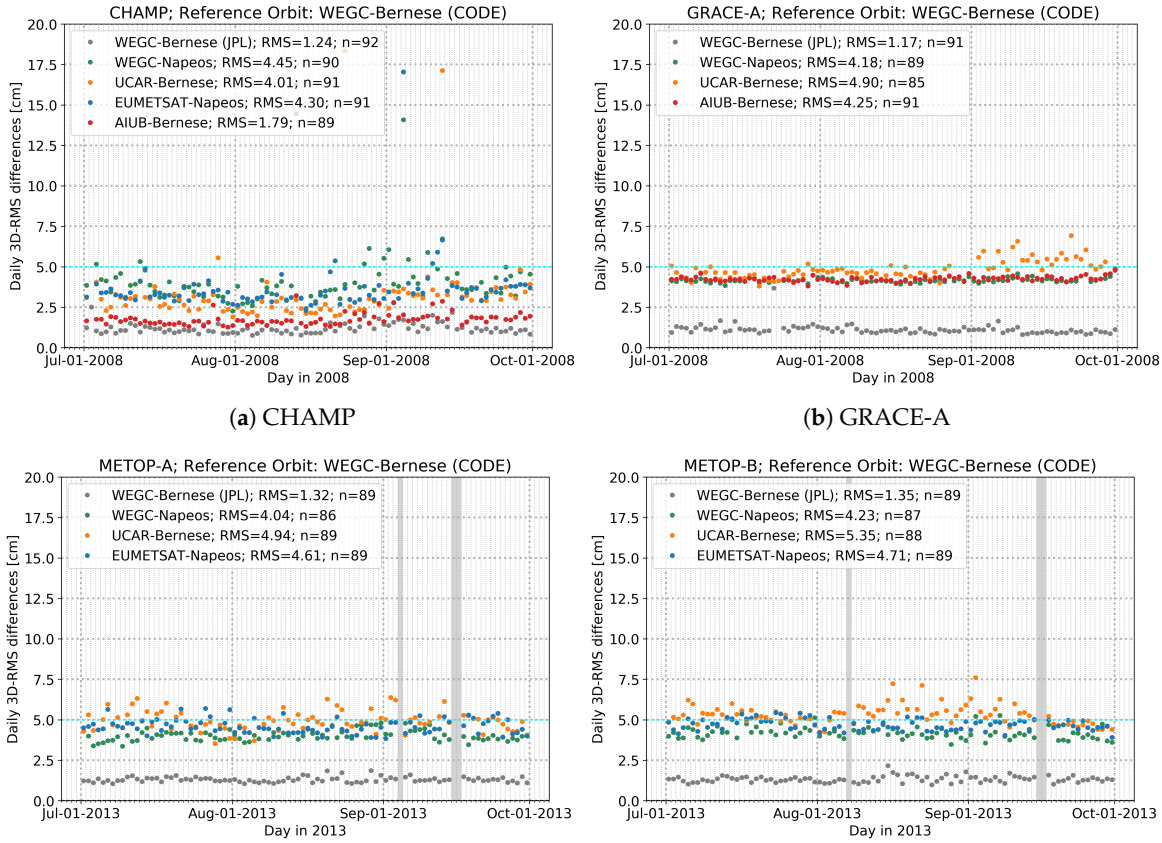
Three different orbit solutions are calculated routinely within WEGC's POD processing (listed in Table 2). In order to assess the quality of the orbit solution designated for further RO processing (WEGC-BC), different analyses are performed. The WEGC-BC primary solution is compared to internal control runs (WEGC-BI, WEGC-NC) and orbit solutions from external processing centers (Section 4.1). Satellite laser ranging residuals are analyzed (Section 4.2), and measures for the orbit uncertainties are derived (Section 4.3). The results cover the analysis for CHAMP and GRACE-A in July to September 2008 and the same time period in 2013 for Metop-A/B.

4.1. Orbit Comparison

As outlined in Section 3.5, the inter-comparison of the different precise orbit products allows for a realistic assessment of the accuracy and might reveal possible systematic errors. Figure 4 shows daily 3D-RMS differences in position between the WEGC-BC solution and externally provided orbits. The corresponding position and velocity differences in radial, along-track, and cross-track directions are summarized in Table 3. When comparing the different orbit solutions overall best agreement is found for the comparison of WEGC-BC and WEGC-BI. This can be expected from the fact that in this case the differences are simply governed by the impact of different GNSS orbit, clock, and associated EOP data while using the same POD software with consistent processing settings. For all missions the RMS of the daily 3D-RMS series does not exceed 1.4 cm. However, a single day for GRACE-A of about 4 cm difference can be found. The WEGC-NC solution generally compares at a similar level to WEGC-BC as the external solutions, with the exception of decreased differences found between WEGC-BC and AIUB for CHAMP.

CHAMP. For the CHAMP mission best agreement is found with AIUB with an RMS of about 1.8 cm (note: 3 days from AIUB are missing in the provided data). Solutions from WEGC-NC, EUMETSAT, and UCAR compare at a similar level, where the comparison to UCAR features a slightly better comparison with an RMS of about 4.0 cm. Individual days still exhibit differences above the 5 cm threshold.

GRACE. Differences from orbit comparison for GRACE-A presented are higher than results from space-geodetic applications, such as gravity field recovery [46]. However, results from those applications are based on screened observation files (available from JPL) where the clock error was detrended and altered substantially, compared to the raw observation files available at CDAAC. As already outlined in Section 3.1, dealing with such large clock trends poses challenges in handling the data by the POD software packages. This leads to comparison results indicating a slightly degraded quality but still within the conservative bounds for RO. Note that while the WEGC-NC and AIUB solutions are based on these screened L1B products, all other solutions are based on the raw L1A observation data.



(**a**) CHAMP (**b**) GRACE-A

(**c**) Metop-A (**d**) Metop-B

Figure 4. Daily 3D-root-mean-squared (RMS) orbit differences between the WEGC-Bernese (CODE) primary solution and WEGC-Bernese (JPL), WEGC-Napeos, UCAR, EUMETSAT, and AIUB orbit solutions for: (**a**) CHAMP and (**b**) GRACE-A from July to September 2008, and (**c**) Metop-A and (**d**) Metop-B for July to September 2013. Gray shading in the Metop-A/B panels indicates three excluded days where an orbit maneuver took place (Metop-A: 2013-09-04; Metop-B: 2013-08-07) or satellite attitude from CDAAC is missing (2013-09-15, 2013-09-16). Rare outliers exceeding 20 cm in 3D-RMS difference (10 days total for all four satellites) have been disregarded for the calculation of the overall RMS noted as part of the legend (in units cm). The number of total days included in the calculation for each orbit solution is denoted by "n".

Table 3. Orbit comparison for position and velocity in radial, along-track, cross-track, and corresponding 3D-RMS for different orbit solutions compared to WEGC-Bernese primary precise orbit determination solution listed for CHAMP and GRACE-A (Jun/Jul/Aug 2008) and Metop-A/B (Jun/Jul/Aug 2013). Days exceeding 20 cm in 3D-RMS (10 days) have been disregarded in the statistics.

ID	Position (cm)				Velocity (mm/s)			
	Radial	Along	Cross	3D	Radial	Along	Cross	3D
CHAMP: vs. WEGC-BC								
WEGC-BI	0.40 ± 0.09	0.82 ± 0.23	0.74 ± 0.31	1.20 ± 0.31	0.005 ± 0.001	0.005 ± 0.001	0.006 ± 0.002	0.010 ± 0.002
WEGC-NC	2.11 ± 0.51	3.16 ± 1.77	1.35 ± 0.39	4.10 ± 1.75	0.023 ± 0.012	0.023 ± 0.007	0.028 ± 0.015	0.044 ± 0.019
UCAR	1.67 ± 0.75	2.47 ± 2.20	1.24 ± 0.48	3.31 ± 2.26	0.015 ± 0.011	0.015 ± 0.011	0.018 ± 0.016	0.028 ± 0.022
EUM	1.96 ± 0.55	2.81 ± 2.04	1.45 ± 0.40	3.78 ± 2.05	0.025 ± 0.014	0.024 ± 0.005	0.029 ± 0.014	0.046 ± 0.020
AIUB	0.89 ± 0.10	1.19 ± 0.36	0.90 ± 0.26	1.76 ± 0.37	0.018 ± 0.001	0.017 ± 0.001	0.024 ± 0.001	0.034 ± 0.002
GRACE-A: vs. WEGC-BC								
WEGC-BI	0.39 ± 0.07	0.78 ± 0.32	0.68 ± 0.22	1.13 ± 0.33	0.005 ± 0.001	0.005 ± 0.002	0.006 ± 0.002	0.009 ± 0.003
WEGC-NC	0.76 ± 0.12	4.01 ± 0.12	0.85 ± 0.25	4.17 ± 0.15	0.025 ± 0.001	0.026 ± 0.001	0.035 ± 0.002	0.050 ± 0.002
UCAR	3.04 ± 0.36	3.29 ± 0.52	1.84 ± 0.35	4.86 ± 0.58	0.038 ± 0.002	0.038 ± 0.002	0.045 ± 0.002	0.070 ± 0.003
AIUB	0.60 ± 0.08	4.03 ± 0.13	1.16 ± 0.33	4.25 ± 0.16	0.021 ± 0.001	0.022 ± 0.001	0.033 ± 0.001	0.045 ± 0.001
Metop-A: vs. WEGC-BC								
WEGC-BI	0.48 ± 0.07	0.97 ± 0.13	0.71 ± 0.18	1.31 ± 0.16	0.006 ± 0.001	0.006 ± 0.001	0.007 ± 0.001	0.011 ± 0.001
WEGC-NC	3.04 ± 0.22	2.09 ± 0.33	1.56 ± 0.31	4.02 ± 0.32	0.028 ± 0.005	0.026 ± 0.005	0.025 ± 0.007	0.046 ± 0.009
UCAR	2.76 ± 0.45	2.99 ± 0.57	2.66 ± 0.45	4.90 ± 0.61	0.029 ± 0.003	0.029 ± 0.003	0.032 ± 0.003	0.052 ± 0.004
EUM	2.88 ± 0.16	2.58 ± 0.24	2.41 ± 0.65	4.59 ± 0.44	0.023 ± 0.003	0.025 ± 0.003	0.029 ± 0.005	0.045 ± 0.006
Metop-B: vs. WEGC-BC								
WEGC-BI	0.49 ± 0.08	0.99 ± 0.15	0.72 ± 0.20	1.33 ± 0.20	0.006 ± 0.001	0.006 ± 0.001	0.007 ± 0.001	0.011 ± 0.001
WEGC-NC	3.14 ± 0.28	2.38 ± 0.36	1.43 ± 0.32	4.21 ± 0.39	0.028 ± 0.005	0.026 ± 0.004	0.029 ± 0.007	0.048 ± 0.008
UCAR	3.08 ± 0.47	3.02 ± 0.53	3.04 ± 0.48	5.31 ± 0.61	0.032 ± 0.004	0.030 ± 0.004	0.035 ± 0.004	0.056 ± 0.005
EUM	3.08 ± 0.17	2.95 ± 0.33	1.92 ± 0.44	4.70 ± 0.34	0.024 ± 0.003	0.026 ± 0.003	0.032 ± 0.005	0.048 ± 0.006

In Figure 4b increased values of comparison in September 2008 and missing days end of August for UCAR can be seen for GRACE-A, which is in accordance with periods when the satellite clock error is peaking before it is reset. Also, increased along-track differences (Table 3) compared to solutions based on pre-screened RINEX suggest a shift in time. In particular for the comparison of the primary solution, and the one by AIUB, the use of different low-level input data leads to increased differences for GRACE-A (4.3 cm) compared to the same comparison conducted for CHAMP (1.8 cm). With respect to the AIUB solution as reference, which can be considered a particularly reliable reference due to its K-band validation [69], WEGC orbits compare better than UCAR (WEGC-NC 1.5 cm, WEGC-BC 4.3 cm, WEGC-BI 4.7 cm; UCAR 6.5 cm).

Metop. In principle, a similar characteristics of the comparison results is found for both Metop satellites. Apart from the WEGC-BI solution, best agreement is found against WEGC-NC with an RMS of about 4.0 cm and 4.2 cm for Metop-A and Metop-B, respectively. Individual days of the comparison are slightly exceeding the 5 cm threshold, and furthermore days with increased differences against UCAR can be observed in August and September leading to an overall RMS close to and slightly exceeding 5 cm for Metop-A and Metop-B, respectively. These findings are consistent with earlier results from orbit inter-comparison for Metop [28]. Note that both Metop satellites undergo a maneuver in the considered period. Additionally, two days with missing attitude from CDAAC remain currently unprocessed.

Finally we note that in general all orbit solutions for the presented missions (including those from UCAR, EUMETSAT, and AIUB) satisfy the introduced RO-application-oriented target specification of 5 cm in position and 0.05 mm/s in velocity.

4.2. Satellite Laser Ranging Validation

Limited to the CHAMP and GRACE-A missions, which are equipped with an LRR, Table 4 summarizes the laser ranging residuals statistics for the two missions using normal point data available from (1) all stations and (2) a high-quality subset of 12 stations. The station selection was applied in

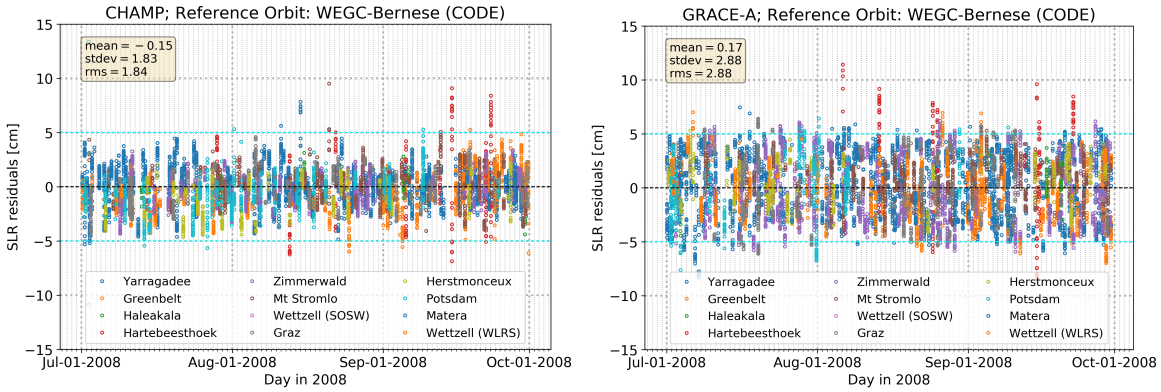
order to discriminate between different performance levels among the stations of the ILRS network [44]. The results comprise the internal and external POD solutions derived from GPS measurements. Figure 5 illustrates SLR residuals that were calculated based on observations from the selected high-quality stations only and the WEGC-BC primary orbit.

In general, the mean and standard deviation for the validated orbit solutions (Table 4) decreases with the limitation to high-quality (HQ) stations. For GRACE-A, however, the WEGC-BC, WEGC-BI, and UCAR solutions, which are all solutions based on unscreened L1A GPS navigation tracking data, show a larger mean for the HQ station selection than for all stations. Furthermore, regardless of the station selection, those solutions exhibit standard deviations more than two times larger than the WEGC-NC and AIUB solutions, which are based on the screened L1B GPS navigation tracking data (see Section 3.1).

Table 4. Mean and standard deviation (in cm) of SLR residuals for the full set of SLR stations and selected high-quality (HQ) stations for CHAMP and GRACE-A in Jun/Jul/Aug 2008.

Solution	CHAMP		GRACE-A	
	All Stations	HQ Stations	All Stations	HQ Stations
WEGC-BC	-0.49 ± 2.35	-0.15 ± 1.83	-0.02 ± 3.08	0.17 ± 2.88
WEGC-BI	-0.49 ± 2.49	-0.13 ± 1.98	0.01 ± 3.19	0.21 ± 2.95
WEGC-NC	-1.04 ± 2.61	-0.75 ± 2.10	-0.70 ± 1.92	-0.44 ± 1.39
UCAR	-0.19 ± 2.43	0.15 ± 2.01	0.03 ± 4.26	0.44 ± 4.30
EUMETSAT	-0.40 ± 2.48	-0.12 ± 2.08	n/a	n/a
AIUB	-0.84 ± 2.32	-0.56 ± 1.77	-0.43 ± 1.77	-0.15 ± 1.12

The SLR residuals in Figure 5 are based on high-quality station subset after applying a 20 cm outlier rejection and an elevation mask of 10 degrees. The high quality stations contribute from 70% (GRACE-A) to 71% (CHAMP) to all normal tracking points, a number generally high since the GRACE and CHAMP missions were top-ranked according to the ILRS mission priority list (https://ilrs.cddis.eosdis.nasa.gov/missions/mission_operations/priorities/priorities_20080926.html).



(**a**) CHAMP (**b**) GRACE-A

Figure 5. SLR residuals of (**a**) CHAMP and (**b**) GRACE-A orbits for July to September 2008, calculated with Bernese using GNSS input from CODE for a set of 12 high-quality SLR stations (legends at bottom). Average mean, standard deviation, and 3D-root-mean-square (RMS) estimates over the period are noted in the upper-left legend (units cm). For outlier rejection a 20 cm threshold and a station's elevation mask of 10 degrees was applied.

Overall, the SLR intercomparison results do not exhibit notable systematic variations within the time periods considered. With a similar number of observations (CHAMP: 8271, GRACE-A: 8533) both data series show a small mean. However, the larger scattering which is observed for GRACE-A (Figure 5b) manifests in an increased standard deviation of about 1 cm compared to CHAMP. Furthermore, it was found that using screened L1B RINEX data for the GRACE-A POD

reduces the standard deviation (comparable to CHAMP), although this is not applicable in the case of RO (Section 3.1).

4.3. Uncertainty Estimation

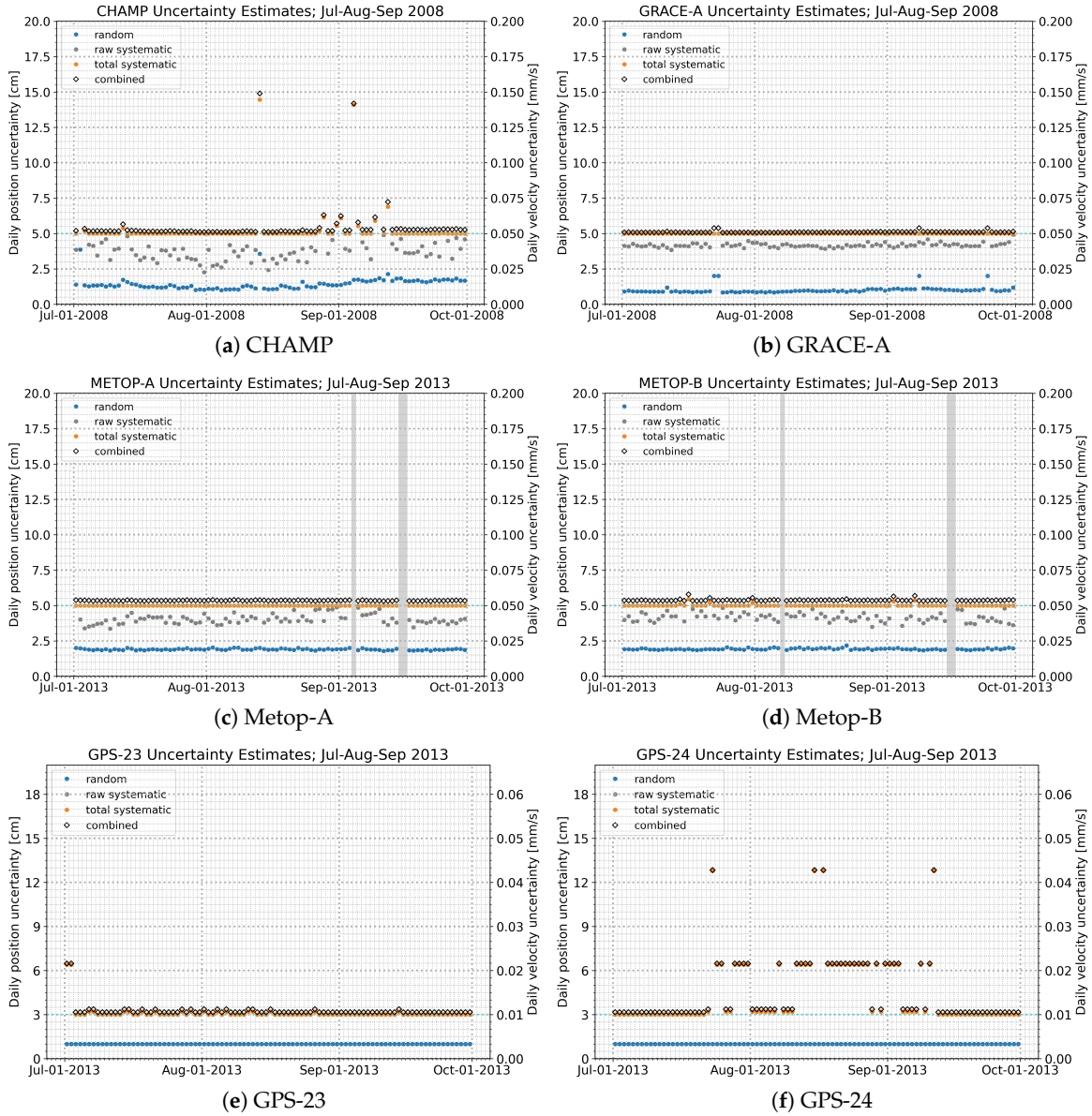
The results of the uncertainty estimation as introduced in Section 3.5 are illustrated in Figure 6, and summarized in Table 5 (3-month mean and standard deviation range), for the RO LEO satellites under investigation and two representative GPS transmitter satellites possibly involved in an occultation event (one GPS delivering good estimates and one slightly degraded). The component estimates in Table 5 use plausible fractional weighting of the 3D variance (u^2_{3D}) [69,89]. In case of a typical day, when the geometry modeling system (Figure 1) delivers results within highest-quality demands for RO processing, the 3D-RMS uncertainties are generally obtained near the conservative bound of 5 cm in position and 0.05 mm/s in velocity for the LEO satellite.

LEO satellites. The estimated random uncertainties for all missions (Figure 6, panels (a) to (d)) show consistent behavior over time, with lowest values found for GRACE. On days where the uncertainty calculation failed due to missing input (i.e., the POD of one of the control orbit runs was not successful) the estimated random uncertainty is set to a conservative estimate of 2 cm, which leads to a slightly increased combined uncertainty estimation on those days for GRACE. For the majority of days, the raw-estimated systematic uncertainty component stays within the conservative bound. In particular this applies to most days for GRACE and the Metop satellites. For CHAMP some more days are found that moderately exceed the conservative-bound threshold.

GPS satellites. With regard to the GPS transmitter satellites (Figure 6, panels (e) and (f)), the estimated random uncertainties are fixed to the predefined conservative value of 1 cm (cf. Figure 3). The estimated systematic uncertainty, as derived from the accuracy codes, reveals some days of decreased orbit accuracy. Since the estimated uncertainties are empirically mapped with a conversion factor of 1/3000 from position to velocity (Section 4.3), it is well visible that the contribution of GPS velocity uncertainties is quite minor compared to the velocity uncertainties derived for the LEO satellites.

Table 5. Random and systematic position uncertainty estimates (3D) and decomposed with 3D-variance weighting factors w into radial ($w_r = 0.25$), along-track ($w_a = 0.35$), and cross-track ($w_c = 0.4$) components.

Satellite	Random (cm)				Systematic (cm)			
	3D	Radial	Along	Cross	3D	Radial	Along	Cross
CHAMP	1.44 ± 0.42	0.72 ± 0.21	0.85 ± 0.25	0.91 ± 0.27	5.28 ± 1.39	2.64 ± 0.69	3.13 ± 0.82	3.34 ± 0.88
GRACE-A	1.00 ± 0.23	0.50 ± 0.11	0.59 ± 0.13	0.64 ± 0.14	5.00 ± 0.00	2.50 ± 0.00	2.96 ± 0.00	3.16 ± 0.00
Metop-A	1.90 ± 0.05	0.95 ± 0.03	1.13 ± 0.03	1.20 ± 0.03	5.00 ± 0.00	2.50 ± 0.00	2.96 ± 0.00	3.16 ± 0.00
Metop-B	1.93 ± 0.06	0.96 ± 0.03	1.14 ± 0.03	1.22 ± 0.04	5.02 ± 0.07	2.51 ± 0.04	2.97 ± 0.04	3.17 ± 0.05
GPS-23	1.00 ± 0.00	0.50 ± 0.00	0.59 ± 0.00	0.63 ± 0.00	3.11 ± 0.50	1.55 ± 0.25	1.84 ± 0.29	1.97 ± 0.31
GPS-24	1.00 ± 0.00	0.50 ± 0.00	0.59 ± 0.00	0.63 ± 0.00	4.75 ± 3.19	2.37 ± 1.60	2.81 ± 1.89	3.00 ± 2.02



(**a**) CHAMP (**b**) GRACE-A

(**c**) Metop-A (**d**) Metop-B

(**e**) GPS-23 (**f**) GPS-24

Figure 6. Daily position and velocity uncertainty estimates for the WEGC-Bernese (CODE) primary solution for (**a**) CHAMP and (**b**) GRACE-A from July to September 2008, and for (**c**) Metop-A, (**d**) Metop-B, (**e**) GPS-23, and (**f**) GPS-24 for July to September 2013. The "raw systematic" values denote the estimated systematic uncertainties before applying the conservative bound value (u_{CB}) while the "total systematic" values show the estimates including this low-bounding value.

5. Conclusions

Climate benchmark data derived from GNSS RO require accurate and robust POD of the GNSS transmitter and LEO receiver satellites taking part in an occultation measurement. In this paper we presented a novel setup for routine quality assessment and uncertainty estimation of the daily LEO receiver satellite orbits independent from external validation sources. The GNSS orbit uncertainty estimates were complemented by building on existing error estimates from the GNSS community. As part of WEGC's rOPS we provide estimates of systematic and random uncertainties associated with the orbit determination, deduced from different LEO POD runs, SLR measurements, and formal uncertainty analysis. We focused on the validation of the WEGC primary orbit solution, which is chosen to deliver the receiver orbit positions, velocities, and clock estimates for subsequent RO processing and the derivation of atmospheric profiles of ECVs.

For the performance assessment of the extended POD setup we investigated 3 representative months of data from July to September in 2008 (CHAMP and GRACE-A) and 2013 (Metop-A/B). The comparison of the WEGC primary solution with orbit solutions from internal control runs showed reliable agreement within 5 cm in position and 0.05 mm/s in velocity, which is the target threshold specification set for high-quality orbit products for RO climate applications. This threshold is also satisfied for most days in an inter-comparison with orbits from the external providers UCAR, EUMETSAT, and AIUB. SLR residuals using selected high-quality ground stations, available and used for CHAMP and GRACE-A, exhibited a mean and standard deviation of -0.15 ± 1.83 cm and 0.17 ± 2.88 cm, respectively, well within the target ranges. Interchange of the GNSS orbit data used with one POD software, without altering the processing setup, shows relatively small differences in the orbit inter-comparison. This suggests that different POD software implementations and configuration settings are more relevant to the uncertainty estimation than potential quality differences in the GNSS orbit data products.

Overall, the uncertainty estimates are found to be within the specified target thresholds for 92% of the days considered. The remaining 8% of days exhibit higher uncertainties of order 5 to 15 cm. This is still adequate for RO processing and at the same time results in somewhat increased uncertainty estimates of the derived ECVs, after propagation through the rOPS retrieval chain. These results suggest a high processing standard and robustness, shared among all processing centers, and indicate rOPS POD system readiness for long-term climate reprocessing of RO data records from CHAMP, GRACE, and the Metop satellite series.

Further modifications of the observation geometry system of rOPS may be applied in future with the inclusion of other RO missions and enhancements of the basic uncertainty estimation. As another important RO mission, we currently integrate POD processing of FORMOSAT-3/COSMIC (Formosa Satellite mission-3/Constellation Observing System for Meteorology, Ionosphere, and Climate) [103]. This will show the retrieval performance implications of the rOPS POD setup for the case of overall degraded POD quality (about 15–25 cm position uncertainties [90]), due to less favorable attitude behavior of the rather small COSMIC spacecraft and restrictions in processing observations from two POD antennas.

For the time being, the further RO processing of FORMOSAT-3/COSMIC data, as well as of the RO data from the more recent FengYun-3 operational satellite series [104] and the commercial CubeSat constellation of Spire [105], is prepared with using the LEO orbits from these data providers together with fixed adopted values of position and velocity uncertainty estimates based on their orbit quality assessments. As part of the future multi-satellites portfolio, we will also process the very recent FORMOSAT-7/COSMIC-2 RO data [106]. Another aspect is that the processing of orbit arcs is currently limited to 24 h arcs, restricting calculation of orbit overlap statistics or long-arc analysis, which in future might serve as an additional measure in the uncertainty estimation process.

As a next step, the upcoming RO reprocessing at WEGC will provide a thorough long-term performance check of the current implementation of this new POD subsystem and may motivate additional modifications and improvements. Based on the encouraging results of this study we expect to obtain high-quality ECV data records for climate monitoring and research.

Author Contributions: Conceptualization and methodology, G.K., C.P., J.I. and M.S.; software, J.I., M.S., C.P. and A.J.; validation, J.I., M.S., A.J., Y.A., C.M. and G.K.; formal analysis, investigation, visualization and writing-original draft preparation, J.I.; writing-review and editing, G.K., M.S., A.J., C.P., Y.A. and C.M.; data curation and project administration, J.I., M.S. and G.K.; supervision, resources and funding acquisition, G.K. All authors have read and agreed to the published version of the manuscript.

Funding: The research at WEGC was supported by the Aeronautics and Space Agency of the Austrian Research Promotion Agency (FFG-ALR) under the Austrian Space Applications Programme (ASAP) projects OPSCLIMPROP (proj. no. 840070), OPSCLIMTRACE (proj. no. 844395), and EOPCLIMTRACK (proj. no. 859773) funded by the Ministry for Transport, Innovation, and Technology (BMVIT). Funding was also provided by the Austrian Science Fund (FWF) under research grant W1256-G15 (Doctoral Programme Climate Change – Uncertainties, Thresholds and Coping Strategies).

Acknowledgments: The authors are grateful to the Center for Orbit Determination in Europe (CODE Bern), the International GNSS Service (IGS), and the Jet Propulsion Laboratory (JPL Pasadena) for their reprocessing effort and the publicly provided access to GNSS orbit, clock, and earth orientation parameter data. We are equally thankful to the International Laser Ranging Service (ILRS) for their effort to collect and publicly provide satellite laser ranging observations. We also appreciate and acknowledge the availability of GPS observations of low Earth orbit satellites shared by UCAR/CDAAC Boulder, JPL Pasadena, and GFZ Potsdam. We thank D. Arnold for the discussion and support in processing with the Bernese GNSS software and H. Peter and T. Springer for discussion and support with the NAPEOS software. We furthermore thank colleagues from WEGC's RO & Climate team, in particular A. Leuprecht, for support on the rOPS framework setup and computations. We also thank F. Ladstädter from WEGC for his help and discussions.

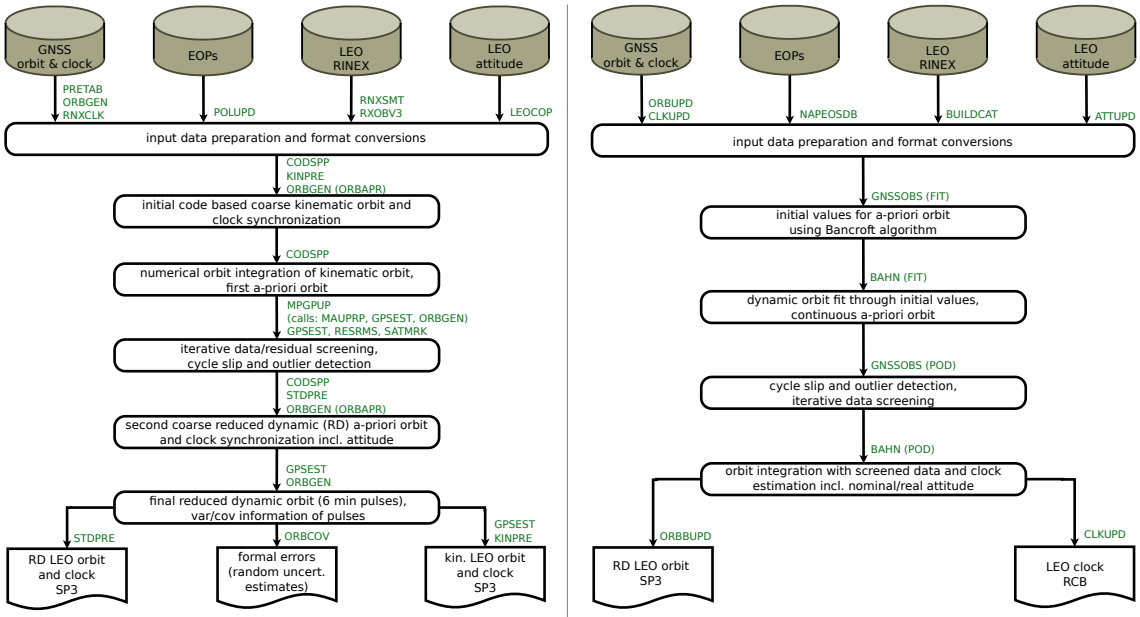
Conflicts of Interest: The authors declare no conflict of interest.

Abbreviations

The following abbreviations are used in this manuscript:

AC	Analysis Center
ASC	Advanced Star Camera
CB	Conservative Bound
CDAAC	COSMIC Data Analysis and Archive Center
CHAMP	CHAllenging Minisatellite Payload
CODE	Center for Orbit Determination in Europe
DSM	Daily System Modeling
DLR	German Aerospace Center
DTU	Technical University of Denmark
ECOM	Empirical CODE Orbit Model
ECV	Essential Climate Variable
EOP	Earth Orientation Parameter
ESA	European Space Agency
ESOC	European Space Operations Centre
EUMETSAT	European Organization for the Exploitation of Meteorological Satellites
FCDR	Fundamental Climate Data Record
GNSS	Global Navigation Satellite System
GFZ	German Research Centre for Geosciences
GPS	Global Positioning System
GRACE	Gravity And Climate Experiment
GRAS	GNSS Receiver for Atmospheric Sounding
IERS	International Earth Rotation and Reference Systems Service
ILRS	International Laser Ranging Service
IGS	International GNSS Service
IR	Infrared
ITRF	International Terrestrial Reference Frame
JCGM	Joint Committee for Guides in Metrology
JPL	Jet Propulsion Laboratory
LEO	Low Earth Orbit
LRR	Laser Retroreflector
Metop	Meteorological Operational
NASA	National Aeronautics and Space Administration
ODP	Occultation Data Processing
PCO	Phase Center Offset
PCV	Phase Center Variation
POD	Precise Orbit Determination
RCB	Receiver Clock Bias file format
RINEX	Receiver Independent Exchange Format
RO	Radio Occultation
rOPS	Reference Occultation Processing System
RTN	Radial-Transverse-Normal
SLR	Satellite Laser Ranging
SP3	Standard Product 3 orbit file format
UCAR	University Corporation for Atmospheric Research

Appendix A



(**a**) Bernese GNSS Software (**b**) NAPEOS Software

Figure A1. Schematic illustration of the orbit processing setup of the Bernese and NAPEOS software packages used in this study for the LEO POD. The main processing steps from input data (top) to POD results (bottom) are shown and software-internal routines used for specific steps are indicated by their names (green names near arrows; for details see the software documentation [30,31]). For explanation of acronyms in various boxes see the Abbreviations list above.

References

1. Hofmann-Wellenhof, B.; Lichtenegger, H.; Wasle, E. *GNSS—Global Navigation Satellite Systems*; Springer: Wien, NY, USA, 2008.
2. Teunissen, P.J.; Montenbruck, O. *Springer Handbook of Global Navigation Satellite Systems*; Springer: Cham, Switzerland, 2017. [CrossRef]
3. Kursinski, E.R.; Hajj, G.A.; Schofield, J.T.; Linfield, R.P.; Hardy, K.R. Observing Earth's atmosphere with radio occultation measurements using the Global Positioning System. *J. Geophys. Res.* **1997**, *102*, 23429–23465. [CrossRef]
4. Syndergaard, S. Retrieval Analysis and Methodologies in Atmospheric Limb Sounding Using the GNSS Radio Occultation Technique. Ph.D. Thesis, Danish Meteorological Institute, Copenhagen, Denmark, 1999.
5. Hajj, G.A.; Kursinski, E.R.; Romans, L.J.; Bertiger, W.I.; Leroy, S.S. A technical description of atmospheric sounding by GPS occultation. *J. Atmos. Solar-Terr. Phys.* **2002**, *64*, 451–469. [CrossRef]
6. Anthes, R.A. Exploring Earth's atmosphere with radio occultation: Contributions to weather, climate, and space weather. *Atmos. Meas. Tech.* **2011**, *4*, 1077–1103. [CrossRef]
7. Steiner, A.K.; Lackner, B.C.; Ladstädter, F.; Scherllin-Pirscher, B.; Foelsche, U.; Kirchengast, G. GPS radio occultation for climate monitoring and change detection. *Radio Sci.* **2011**, *46*. [CrossRef]
8. Leroy, S.S.; Dykema, J.A.; Anderson, J.G. Climate benchmarking using GNSS occultation. In *Atmosphere and Climate: Studies by Occultation Methods*; Foelsche, U., Kirchengast, G., Steiner, A.K., Eds.; Springer: Berlin/Heidelberg, Germany, 2006; pp. 287–301. [CrossRef]
9. Foelsche, U.; Scherllin-Pirscher, B.; Ladstädter, F.; Steiner, A.K.; Kirchengast, G. Refractivity and temperature climate records from multiple radio occultation satellites consistent within 0.05%. *Atmos. Meas. Tech.* **2011**, *4*, 2007–2018. [CrossRef]
10. Steiner, A.K.; Ladstädter, F.; Ao, C.O.; Gleisner, H.; Ho, S.P.; Hunt, D.; Schmidt, T.; Foelsche, U.; Kirchengast, G.; Kuo, Y.H.; et al. Consistency and structural uncertainty of multi-mission GPS radio occultation records. *Atmos. Meas. Tech. Discuss.* **2019**. [CrossRef]

11. Bojinski, S.; Verstraete, M.; Peterson, T.C.; Richter, C.; Simmons, A.; Zemp, M. The concept of Essential Climate Variables in support of climate research, applications, and policy. *Bull. Am. Meteor. Soc.* **2014**, *95*, 1431–1443. [CrossRef]
12. National Research Council. *Earth Science and Applications from Space: National Imperatives for the Next Decade and Beyond (Decadal Survey)*; The National Academies Press: Washington, DC, USA, 2007. [CrossRef]
13. GCOS. *Status of the Global Observing System for Climate—Full Report*; GCOS-195; WMO: Geneva, Switzerland, 2015.
14. Scherllin-Pirscher, B.; Steiner, A.K.; Kirchengast, G.; Kuo, Y.H.; Foelsche, U. Empirical analysis and modeling of errors of atmospheric profiles from GPS radio occultation. *Atmos. Meas. Tech.* **2011**, *4*, 1875–1890. [CrossRef]
15. Scherllin-Pirscher, B.; Kirchengast, G.; Steiner, A.K.; Kuo, Y.H.; Foelsche, U. Quantifying uncertainty in climatological fields from GPS radio occultation: An empirical-analytical error model. *Atmos. Meas. Tech.* **2011**, *4*, 2019–2034. [CrossRef]
16. Angerer, B.; Ladstädter, F.; Scherllin-Pirscher, B.; Schwärz, M.; Steiner, A.K.; Foelsche, U.; Kirchengast, G. Quality aspects of the WEGC multi-satellite GPS radio occultation record OPSv5.6. *Atmos. Meas. Tech.* **2017**, *10*, 4845–4863. [CrossRef]
17. Ho, S.P.; Hunt, D.; Steiner, A.K.; Mannucci, A.J.; Kirchengast, G.; Gleisner, H.; Heise, S.; von Engeln, A.; Marquardt, C.; Sokolovskiy, S.; et al. Reproducibility of GPS radio occultation data for climate monitoring: Profile-to-profile inter-comparison of CHAMP climate records 2002 to 2008 from six data centers. *J. Geophys. Res.* **2012**, *117*. [CrossRef]
18. Steiner, A.K.; Hunt, D.; Ho, S.P.; Kirchengast, G.; Mannucci, A.J.; Scherllin-Pirscher, B.; Gleisner, H.; von Engeln, A.; Schmidt, T.; Ao, C.; et al. Quantification of structural uncertainty in climate data records from GPS radio occultation. *Atmos. Chem. Phys.* **2013**, *13*, 1469–1484. [CrossRef]
19. Kirchengast, G.; Schwärz, M.; Schwarz, J.; Scherllin-Pirscher, B.; Pock, C.; Innerkofler, J.; Proschek, V.; Steiner, A.K.; Danzer, J.; Ladstädter, F.; et al. The reference occultation processing system approach to interpret GNSS radio occultation as SI-traceable planetary system refractometer. Presented at the OPAC-IROWG International Workshop, Seggau/Leibnitz, Austria, 8–14 September 2016. Available online: http://wegcwww.uni-graz.at/opacirowg2016 (accessed on 23 March 2020).
20. Kirchengast, G.; Schwärz, M.; Angerer, B.; Schwarz, J.; Innerkofler, J.; Proschek, V.; Ramsauer, J.; Fritzer, J.; Scherllin-Pirscher, B.; Rieckh, T. *Reference OPS DAD—Reference Occultation Processing System (rOPS) Detailed Algorithm Description*; Tech. Rep. for ESA and FFG No. 1/2018, Doc-Id: WEGC–rOPS–2018–TR01, Issue 2.0; Wegener Center, Univ. of Graz: Graz, Austria, 2018.
21. Schwarz, J.C.; Kirchengast, G.; Schwaerz, M. Integrating uncertainty propagation in GNSS radio occultation retrieval: From bending angle to dry-air atmospheric profiles. *Earth Space Sci.* **2017**, *4*, 200–228. [CrossRef]
22. Schwarz, J.C.; Kirchengast, G.; Schwaerz, M. Integrating uncertainty propagation in GNSS radio occultation retrieval: From excess phase to atmospheric bending angle profiles. *Atmos. Meas. Tech.* **2018**, *11*, 2601–2631. [CrossRef]
23. Innerkofler, J.; Pock, C.; Kirchengast, G.; Schwärz, M.; Jäggi, A.; Andres, Y.; Marquardt, C.; Schwarz, J. Multi-Mission Multi-Center Level 1 Data Inter-Validation towards Wegener Center Reference Occultation System Reprocessing. Presented at the EUMETSAT ROM SAF-IROWG International Workshop Helsingør, Denmark, 19–25 September 2019. Available online: https://www.romsaf.org/romsaf-irowg-2019/en/content/21/program-agenda-by-day (accessed on 23 March 2020).
24. Rocken, C.; Anthes, R.; Exner, M.; Hunt, D.; Sokolovskiy, S.; Ware, R.; Gorbunov, M.; Schreiner, W.; Feng, D.; Herman, B.; et al. Analysis and validation of GPS/MET data in the neutral atmosphere. *J. Geophys. Res.* **1997**, *102*, 29849–29866. [CrossRef]
25. Wickert, J.; Galas, R.; Beyerle, G.; König, R.; Reigber, C. GPS ground station data for CHAMP radio occultation measurements. *Phys. Chem. Earth* **2001**, *26*, 503–511. [CrossRef]
26. Wickert, J. Das CHAMP-Radiookkultationsexperiment: Algorithmen, Prozessierungssystem und erste Ergebnisse. Ph.D. Thesis, GeoForschungsZentrum Potsdam, Potsdam, Germany, 2002; Scientific Tech. Rep. STR02/07.

27. Wickert, J.; Schmidt, T.; Michalak, G.; Heise, S.; Arras, C.; Beyerle, G.; Falck, C.; König, R.; Pingel, D.; Rothacher, M. GPS radio occultation with CHAMP, GRACE-A, SAC-C, TerraSAR-X, and FORMOSAT-3/COSMIC: Brief review of results from GFZ. In *New Horizons in Occultation Research: Studies in Atmosphere and Climate*; Steiner, A.K., Pirscher, B., Foelsche, U., Kirchengast, G., Eds.; Springer: Berlin/Heidelberg, Germany, 2009; pp. 3–16.
28. Montenbruck, O.; Andres, Y.; Bock, H.; van Helleputte, T.; van den Ijssel, J.; Loiselet, M.; Marquardt, C.; Silvestrin, P.; Visser, P.; Yoon, Y. Tracking and orbit determination performance of the GRAS instrument on MetOp-A. *GPS Solut.* **2008**, *12*, 289–299. [CrossRef]
29. Montenbruck, O.; Hauschild, A.; Andres, Y.; von Engeln, A.; Marquardt, C. (Near-)real-time orbit determination for GNSS radio occultation processing. *GPS Solut.* **2013**, *17*, 199–209. [CrossRef]
30. Dach, R.; Andritsch, F.; Arnold, D.; Bertone, S.; Fridez, P.; Jäggi, A.; Jean, Y.; Maier, A.; Mervart, L.; Meyer, U.; et al. *Bernese GNSS Software Version 5.2, User Manual*; Astron. Inst., Univ. of Bern: Bern, Switzerland, 2015. [CrossRef]
31. Springer, T.A. *NAPEOS—Mathematical Models and Algorithms*; DOPS-SYS-TN-0100-OPS-GN; European Space Operation Centre, European Space Agency: Darmstadt, Germany, 2009.
32. Jean, Y.; Dach, R. *International GNSS Service Technical Report 2015*; IGS Annual Report; IGS Central Bureau and University of Bern: Bern, Switzerland, 2016. [CrossRef]
33. Dow, J.M.; Neilan, R.E.; Rizos, C. The International GNSS Service in a changing landscape of Global Navigation Satellite Systems. *J. Geod.* **2009**, *83*, 191–198. [CrossRef]
34. Wickert, J.; Beyerle, G.; König, R.; Heise, S.; Grunwaldt, L.; Michalak, G.; Reigber, C.; Schmidt, T. GPS radio occultation with CHAMP and GRACE: A first look at a new and promising satellite configuration for global atmospheric sounding. *Ann. Geophys.* **2005**, *23*, 653–658. [CrossRef]
35. Klaes, D.; Lugert, M.; Bojkov, B.; Ackermann, J.; Borde, R.; Coppens, D.; Guedj, S.; Linow, S.; August, T.; Marquardt, C.; et al. Metop Science Update and the Metop-C Mission of the Eumetsat Polar System (EPS). Presented at the AMS 2019 Joint Satellite Conference, Boston, MA, USA, 28 September–4 October 2019. Available online: https://ams.confex.com/ams/JOINTSATMET/meetingapp.cgi/Paper/359586 (accessed on 23 March 2020).
36. Reigber, C.; Lühr, H.; Schwintzer, P. Status of the CHAMP Mission. In *Towards an Integrated Global Geodetic Observing System (IGGOS)*; Rummel, R., Drewes, H., Bosch, W., Hornik, H., Eds.; Springer: Berlin/Heidelberg, Germany, 2000; pp. 63–65.
37. Montenbruck, O.; Kroes, R. In-flight performance analysis of the CHAMP BlackJack GPS Receiver. *GPS Solut.* **2003**, *7*, 74–86. [CrossRef]
38. Beutler, G.; Jäggi, A.; Hugentobler, U.; Mervart, L. Efficient satellite orbit modelling using pseudo-stochastic parameters. *J. Geod.* **2006**, *80*, 353–372. [CrossRef]
39. Wickert, J.; Reigber, C.; Beyerle, G.; König, R.; Marquardt, C.; Schmidt, T.; Grunwaldt, L.; Galas, R.; Meehan, T.; Melbourne, W.; et al. Atmosphere sounding by GPS radio occultation: First results from CHAMP. *Geophys. Res. Lett.* **2001**, *28*, 3263–3266. [CrossRef]
40. Jørgensen, J.L. In Orbit Performance of a Fully Autonomous Star Tracker. In *ESA 4th Symposion on Spacecraft Guidance Navigation and Control*; ESTEC, European Space Agency: Noordwijk, Netherlands, 1999.
41. Jørgensen, P.S.; Jørgensen, J.L.; Denver, T.; Betto, M. In-flight quality and accuracy of attitude measurements from the CHAMP advanced stellar compass. *Acta Astron.* **2005**, *56*, 181–186. [CrossRef]
42. Neubert, R.; Grunwaldt, L.; Neubert, J. The Retro-Reflector for the CHAMP Satellite: Final Design and Realization. In Proceedings of the 11th International Workshop on Laser Ranging, Deggendorf, Germany, 21–25 September 1998; pp. 260–270.
43. Grunwaldt, L.; Neubert, R. First Results of Laser Ranging to the CHAMP Retroreflector. In Proceedings of the 12th International Workshop on Laser Ranging, Matera, Italy, 13–17 November 2000.
44. Arnold, D.; Montenbruck, O.; Hackel, S.; Sośnica, K. Satellite laser ranging to low Earth orbiters: Orbit and network validation. *J. Geodesy* **2018**. [CrossRef]
45. Tapley, B.D.; Bettadpur, S.; Watkins, M.; Reigber, C. The gravity recovery and climate experiment: Mission overview and early results. *Geophys. Res. Lett.* **2004**, *31*. [CrossRef]
46. Tapley, B.; Watkins, M.; Flechtner, F.; Reigber, C.; Bettadpur, S.; Rodell, M.; Sasgen, I.; Famiglietti, J.; Landerer, F.; Chambers, D.; et al. Contributions of GRACE to understanding climate change. *Nat. Clim. Chang.* **2019**, *5*. [CrossRef]

47. Kim, J.; Lee, S.W. Flight performance analysis of GRACE K-band ranging instrument with simulation data. *Acta Astron.* **2009**, *65*, 1571–1581. [CrossRef]
48. Dunn, C.; Bertiger, W.; Franklin, G.; Harris, I.; Kruizinga, G.; Meehan, T. The instrument on NASA's GRACE mission: Augmentation of GPS to achieve unprecedented gravity field measurements. In Proceedings of the 15th International Technical Meeting of the Satellite Division of the Institute of Navigation (ION GPS 2002), Portland, Oregon, 24–27 September 2002; pp. 724–730.
49. Beyerle, G.; Schmidt, T.; Michalak, G.; Heise, S.; Wickert, J.; Reigber, C. GPS radio occultation with GRACE: Atmospheric profiling utilizing the zero difference technique. *Geophys. Res. Lett.* **2005**, *32*. [CrossRef]
50. Flechtner, F.; Morton, P.; Watkins, M.; Webb, F. Status of the GRACE Follow-On Mission. In *Gravity, Geoid and Height Systems*; Marti, U., Ed.; Springer International Publishing: Cham, Switzerland, 2014; pp. 117–121. [CrossRef]
51. Kornfeld, R.P.; Arnold, B.W.; Gross, M.A.; Dahya, N.T.; Klipstein, W.M.; Gath, P.F.; Bettadpur, S. GRACE-FO: The Gravity Recovery and Climate Experiment Follow-On Mission. *J. Spacecr. Rocket.* **2019**, *56*, 931–951. [CrossRef]
52. Klaes, K.D.; Cohen, M.; Buhler, Y.; Schlüssel, P.; Munro, R.; Luntama, J.P.; von Engeln, A.; Clérigh, E.Ó.; Bonekamp, H.; Ackermann, J.; et al. An Introduction to the EUMETSAT Polar system. *Bull. Am. Meteor. Soc.* **2007**, *88*, 1085–1096. [CrossRef]
53. Loiselet, M.; Stricker, N.; Menard, Y.; Luntama, J.P. GRAS—MetOp's GPS-based atmospheric sounder. *ESA Bull.* **2000**, *102*, 38–44.
54. Silvestrin, P.; Bagge, R.; Bonnedal, M.; Carlström, A.; Christensen, J.; Hägg, M.; Lindgren, T. Spaceborne GNSS Radio Occultation Instrumentation for Operational Applications. In Proceedings of the 13th ION-GPS Meeting, Salt Lake City, UT, USA, 19–22 September 2000.
55. Bonnedal, M.; Christensen, J.; Carlström, A.; Berg, A. Metop-GRAS in-orbit instrument performance. *GPS Solut.* **2010**, *14*, 109–120. [CrossRef]
56. von Engeln, A.; Healy, S.; Marquardt, C.; Andres, Y.; Sancho, F. Validation of operational GRAS radio occultation data. *Geophys. Res. Lett.* **2009**, *36*. [CrossRef]
57. Pearlman, M.; Degnan, J.; Bosworth, J. The International Laser Ranging Service. *Adv. Space Res.* **2002**, *30*, 135–143. [CrossRef]
58. Pearlman, M.R.; Noll, C.E.; Pavlis, E.C.; Lemoine, F.G.; Combrink, L.; Degnan, J.J.; Kirchner, G.; Schreiber, U. The ILRS: Approaching 20 years and planning for the future. *J. Geodesy* **2019**. [CrossRef]
59. Susnik, A.; Dach, R.; Villiger, A.; Maier, A.; Arnold, D.; Schaer, S.; Jäggi, A. *CODE Reprocessing Product Series*; Astronomical Institute, University of Bern: Bern, Switzerland, 2016. [CrossRef]
60. Griffiths, J.; Ray, J. On the precision and accuracy of IGS orbits. *J. Geod.* **2009**, *83*. [CrossRef]
61. Kouba, J. *A Guide to Using International GNSS Service (IGS) Products*; Technical Report; IGS: Pasadena, CA, USA, 2009.
62. Ray, J. Precision, Accuracy, and Consistency of GNSS Products. In *Encyclopedia of Geodesy*; Grafarend, E., Ed.; Springer International Publishing: Cham, Switzerland, 2016; pp. 1–5. [CrossRef]
63. Griffiths, J. Combined orbits and clocks from IGS second reprocessing. *J. Geod.* **2019**, *93*, 177–195. [CrossRef]
64. Bock, H.; Dach, R.; Jäggi, A.; Beutler, G. High-rate GPS clock corrections from CODE: Support of 1 Hz applications. *J. Geod.* **2009**, *83*, 1083–1094. [CrossRef]
65. Arnold, D.; Meindl, M.; Beutler, G.; Dach, R.; Schaer, S.; Lutz, S.; Prange, L.; Sośnica, K.; Mervart, L.; Jäggi, A. CODE's new solar radiation pressure model for GNSS orbit determination. *J. Geod.* **2015**, *89*. [CrossRef]
66. Gurtner, W. RINEX: The Receiver Independent Exchange Format. *GPS World* **1994**, *5*, 48–52.
67. Case, K.; Kruizinga, G.; Wu, S.C. *GRACE Level 1B Data Product User Handbook*; D-22027; JPL: Pasadena, CA, USA, 2010.
68. Jäggi, A.; Hugentobler, U.; Beutler, G. Pseudo-Stochastic Orbit Modeling Techniques for Low-Earth Orbiters. *J. Geod.* **2006**, *80*, 47–60. [CrossRef]
69. Jäggi, A. Pseudo-Stochastic Orbit Modeling of Low Earth Satellites Using the Global Positioning System. Ph.D. Thesis, Schweizerische Geodätische Kommission/Swiss Geodetic Commission, Zürich, Switzerland, 2007.
70. Švehla, D.; Rothacher, M. Kinematic Orbit Determination of LEOs Based on Zero or Double-difference Algorithms Using Simulated and Real SST GPS Data. In *Vistas for Geodesy in the New Millennium*; Ádám, J., Schwarz, K.P., Eds.; Springer: Berlin/Heidelberg, Germany, 2002; pp. 322–328.

71. Zehentner, N.; Mayer-Gürr, T. Precise orbit determination based on raw GPS measurements. *J. Geod.* **2016**, *90*, 275–286. [CrossRef]
72. Švehla, D.; Rothacher, M. Kinematic Precise Orbit Determination for Gravity Field Determination. In *A Window on the Future of Geodesy*; Sansò, F., Ed.; Springer: Berlin/Heidelberg, Germany, 2005; pp. 181–188.
73. Schutz, B.E.; Tapley, B.D.; Abusali, P.A.M.; Rim, H.J. Dynamic orbit determination using GPS measurements from TOPEX/POSEIDON. *Geophys. Res. Lett.* **1994**, *21*, 2179–2182. [CrossRef]
74. Wu, S.C.W.; Yunck, T.P.; Thornton, C.L. Reduced-dynamic technique for precise orbit determination of low earth satellites. *J. Guid. Control Dynam.* **1991**, *14*, 24–30. [CrossRef]
75. Yunck, T.P.; Bertiger, W.I.; Wu, S.C.; Bar-Sever, Y.E.; Christensen, E.J.; Haines, B.J.; Lichten, S.M.; Muellerschoen, R.J.; Vigue, Y.; Willis, P. First assessment of GPS-based reduced dynamic orbit determination on TOPEX/Poseidon. *Geophys. Res. Lett.* **1994**, *21*, 541–544. [CrossRef]
76. Montenbruck, O.; van Helleputte, T.; Kroes, R.; Gill, E. Reduced dynamic orbit determination using GPS code and carrier measurements. *Aerosp. Sci. Technol.* **2005**, *9*, 261–271. [CrossRef]
77. Peter, H.; Jäggi, A.; Fernández, J.; Escobar, D.; Ayuga, F.; Arnold, D.; Wermuth, M.; Hackel, S.; Otten, M.; Simons, W.; et al. Sentinel-1A—First precise orbit determination results. *Adv. Space Res.* **2017**, *60*, 879–892. [CrossRef]
78. Bancroft, S. An Algebraic Solution of the GPS Equations. *IEEE Trans. Aerosp. Electron. Syst.* **1985**, *AES-21*, 56–59. [CrossRef]
79. Jäggi, A.; Beutler, G.; Hugentobler, U. Efficient Stochastic Orbit Modeling Techniques using Least Squares Estimators. In *A Window on the Future of Geodesy*; Sansò, F., Ed.; Springer: Berlin/Heidelberg, Germany, 2005; pp. 175–180.
80. IERS. IERS Conventions (2010). In *International Earth Rotation and Reference Systems Service*; IERS technical note no. 36; Gérard Petit and Brain Luzum, Ed.; IERS: Frankfurt am Main, Germany, 2010.
81. IERS. IERS Conventions (2003). In *International Earth Rotation and Reference Systems Service*; IERS Technical note no. 32; McCarthy, D.D., Petit, G., Eds.; IERS: Frankfurt am Main, Germany, 2004.
82. Altamimi, Z.; Collilieux, X.; Métivier, L. ITRF2008: An improved solution of the international terrestrial reference frame. *J. Geod.* **2011**, *85*, 457–473. [CrossRef]
83. Schmid, R.; Dach, R.; Collilieux, X.; Jäggi, A.; Schmitz, M.; Dilssner, F. Absolute IGS antenna phase center model igs08.atx: Status and potential improvements. *J. Geod.* **2016**, *90*, 343–364. [CrossRef]
84. Pavlis, N.K.; Holmes, S.A.; Kenyon, S.C.; Factor, J.K. The development and evaluation of the Earth Gravitational Model 2008 (EGM2008). *J. Geophys. Res.* **2012**, *117*. [CrossRef]
85. Rudenko, S.; Dettmering, D.; Esselborn, S.; Schöne, T.; Förste, C.; Lemoine, J.M.; Ablain, M.; Alexandre, D.; Neumayer, K.H. Influence of time variable geopotential models on precise orbits of altimetry satellites, global and regional mean sea level trends. *Adv. Space Res.* **2014**, *54*, 92–118. [CrossRef]
86. Lyard, F.; Lefevre, F.; Letellier, T.; Francis, O. Modelling the global ocean tides: Modern insights from FES2004. *Ocean Dynam.* **2006**, *56*, 394–415. [CrossRef]
87. Standish, E.M. *JPL Planetary and Lunar Ephemerides*; DE405/LE405. Interoffice Memorandum (IOM), 98, 048; Jet Propulsion Laboratory: Pasadena, CA, USA, 1998.
88. Hedin, A.E. Extension of the MSIS thermosphere model into the middle and lower atmosphere. *J. Geophys. Res.* **1991**, *96*, 1159–1172. [CrossRef]
89. Hwang, C.; Tseng, T.P.; Lin, T.; Švehla, D.; Schreiner, B. Precise orbit determination for the FORMOSAT-3/COSMIC satellite mission using GPS. *J. Geod.* **2009**, *83*, 477–489. [CrossRef]
90. Schreiner, W.S.; Rocken, C.; Sokolovskiy, S.; Hunt, D. Quality assessment of COSMIC/FORMOSAT-3 GPS radio occultation data derived from single- and double-difference atmospheric excess phase processing. *GPS Solut.* **2010**, *14*, 13–22. [CrossRef]
91. EUMETSAT. *GRAS Level 1B Bending Angle Climate Data Record Release 1—Metop-A*; European Organisation for the Exploitation of Meteorological Satellites: Darmstadt, Germany, 2017. [CrossRef]
92. Prange, L.; Jäggi, A.; Dach, R.; Bock, H.; Beutler, G.; Mervart, L. AIUB-CHAMP02S: The influence of GNSS model changes on gravity field recovery using spaceborne GPS. *Adv. Space Res.* **2010**, *45*, 215–224. [CrossRef]
93. Jäggi, A.; Dach, R.; Montenbruck, O.; Hugentobler, U.; Peter, H.; Beutler, G. Phase center modeling for LEO GPS receiver antennas and its impact on precise orbit determination. *J. Geod.* **2009**, *83*, 1145–1162. [CrossRef]

94. Pock, C. Low Earth Orbit Determination for GNSS Radio Occultation with Aspects of Uncertainty Estimation. Master's Thesis, Wegener Center Verlag Graz: Graz, Austria, 2015. Sci. Rep. 66-2015.
95. Combrinck, L. Satellite Laser Ranging. In *Sciences of Geodesy - I: Advances and Future Directions*; Xu, G., Ed.; Springer: Berlin/Heidelberg, Germany, 2010; pp. 301–338. [CrossRef]
96. Wilkinson, M.; Schreiber, K.; Prochazka, I.; Moore, C.; Degnan, J.; Kirchner, G.; Zhongping, Z.; Dunn, P.; Shargorodskiy, V.; Sadovnikov, M.; et al. The next generation of satellite laser ranging systems. *J. Geodesy* **2018**. [CrossRef]
97. Strugarek, D.; Sośnica, K.; Jäggi, A. Characteristics of GOCE orbits based on Satellite Laser Ranging. *Adv. Space Res.* **2019**, *63*, 417–431. [CrossRef]
98. JCGM. *Evaluation of Measurement Data—Guide to the Expression of Uncertainty in Measurement*; Rep. JCGM 100:2008; Joint Committee for Guides in Metrology, Office BIPM, Paris, France, 2008.
99. Schwarz, J.C. Benchmark Quality Processing of Radio Occultation Data with Integrated Uncertainty Propagation. Ph.D. Thesis, Wegener Center Verlag Graz: Graz, Austria, 2018; Sci. Rep. 77-2018.
100. Scaramuzza, S.; Dach, R.; Beutler, G.; Arnold, D.; Sušnik, A.; Jäggi, A. Dependency of geodynamic parameters on the GNSS constellation. *J. Geod.* **2018**, *92*, 93–104. [CrossRef]
101. Urschl, C.; Gurtner, W.; Hugentobler, U.; Schaer, S.; Beutler, G. Validation of GNSS orbits using SLR observations. *Adv. Space Res.* **2005**, *36*, 412–417. [CrossRef]
102. Sośnica, K.; Thaller, D.; Dach, R.; Steigenberger, P.; Beutler, G.; Arnold, D.; Jäggi, A. Satellite laser ranging to GPS and GLONASS. *J. Geod.* **2015**, *89*, 725–743. [CrossRef]
103. Anthes, R.A.; Bernhardt, P.A.; Chen, Y.; Cucurull, L.; Dymond, K.F.; Ector, D.; Healy, S.B.; Ho, S.P.; Hunt, D.C.; Kuo, Y.H.; et al. The COSMIC/FORMOSAT-3 mission: Early results. *Bull. Am. Meteor. Soc.* **2008**, *89*, 313–333. [CrossRef]
104. Sun, Y.; Bai, W.; Liu, C.; Liu, Y.; Du, Q.; Wang, X.; Yang, G.; Liao, M.; Yang, Z.; Zhang, X.; et al. The FengYun-3C radio occultation sounder GNOS: A review of the mission and its early results and science applications. *Atmos. Meas. Tech.* **2018**, *11*, 5797–5811. [CrossRef]
105. Masters, D.; Irisov, V.; Nguyen, V.; Duly, T.; Nogués-Correig, O.; Tan, L.; Yuasa, T.; Ringer, J.; Sikarin, R.; Gorbunov, M.; et al. Status and plans for Spire's commercial constellation of GNSS science CubeSats, 2019. Presented at the EUMETSAT ROM SAF-IROWG International Workshop, Helsingør, Denmark, 19–25 September 2019. Available online: https://www.romsaf.org/romsaf-irowg-2019/en/content/21/program-agenda-by-day (accessed on 23 March 2020).
106. Schreiner, B.; Sokolovskiy, S.; Weiss, J.; Braun, J.; Anthes, R.; Kuo, Y.H.; Hunt, D.; Zeng, Z.; Wee, T.K.; VanHove, T.; et al. Performance Assessment and Requirement Verification of COSMIC-2 Neutral Atmospheric Radio Occultation Data, 2019. Presented at the EUMETSAT ROM SAF-IROWG International Workshop, Helsingør, Denmark, 19–25 September 2019. Available online: https://www.romsaf.org/romsaf-irowg-2019/en/content/21/program-agenda-by-day (accessed on 23 March 2020).



© 2020 by the authors. Licensee MDPI, Basel, Switzerland. This article is an open access article distributed under the terms and conditions of the Creative Commons Attribution (CC BY) license (http://creativecommons.org/licenses/by/4.0/).

5. Paper 2: GNSS radio occultation excess phase processing for climate applications including uncertainty estimation

Innerkofler, J., Kirchengast, G., Schwärz, M., Marquardt, C., and Andres, Y. (2023). "GNSS radio occultation excess-phase processing for climate applications including uncertainty estimation". *Atmos. Meas. Tech.* 16, 5217–5247. DOI: 10.5194/amt-16-5217-2023

Atmos. Meas. Tech., 16, 5217–5247, 2023
https://doi.org/10.5194/amt-16-5217-2023
© Author(s) 2023. This work is distributed under
the Creative Commons Attribution 4.0 License.

Atmospheric Measurement Techniques
Open Access
EGU

GNSS radio occultation excess-phase processing for climate applications including uncertainty estimation

Josef Innerkofler[1,2], **Gottfried Kirchengast**[1,2,3], **Marc Schwärz**[1,3], **Christian Marquardt**[4], **and Yago Andres**[4]

[1]Wegener Center for Climate and Global Change (WEGC), University of Graz, Graz, Austria
[2]Doctoral Programme Climate Change, University of Graz, Graz, Austria
[3]Institute of Physics, University of Graz, Graz, Austria
[4]European Organisation for the Exploitation of Meteorological Satellites (EUMETSAT), Darmstadt, Germany

Correspondence: Josef Innerkofler (josef.innerkofler@uni-graz.at)

Received: 10 February 2023 – Discussion started: 10 March 2023
Revised: 29 August 2023 – Accepted: 30 August 2023 – Published: 7 November 2023

Abstract. Earth observation from space provides a highly valuable basis for atmospheric and climate science, in particular also through climate benchmark data from suitable remote sensing techniques. Measurements by global navigation satellite system (GNSS) radio occultation (RO) qualify to produce such benchmark data records as they globally provide accurate and long-term stable datasets for essential climate variables (ECVs) such as temperature. This requires a rigorous processing of the raw RO measurements to ECVs, with narrow uncertainties. In order to fully exploit this potential, Wegener Center's Reference Occultation Processing System (rOPS) Level 1a (L1a) processing subsystem includes uncertainty estimation in both precise orbit determination (POD) and excess-phase profile derivation.

Here we introduce the new rOPS L1a excess-phase processing, the first step in the RO profiles retrieval down to atmospheric profiles, which extracts the atmospheric excess phase from raw SI-traceable RO measurements. This excess-phase processing, for itself algorithmically concise, includes integrated quality control and uncertainty estimation, requiring a complex framework of various subsystems that we first introduce before describing the implementation of the core algorithms. The quality control and uncertainty estimation, computed per RO event, are supported by reliable forward-modeled excess-phase profiles based on the POD orbit arcs and collocated short-range forecast profiles of the European Centre for Medium-Range Weather Forecasts (ECMWF) Reanalysis (ERA5). The quality control removes or alternatively flags excess-phase profiles of insufficient or degraded quality. The uncertainty estimation accounts both for relevant random- and systematic-uncertainty components, and the resulting (total) uncertainty profiles serve as a starting point for the subsequent uncertainty propagation through the retrieval processing chain down to the atmospheric ECV profiles.

We also evaluated the quality and reliability of the resulting excess-phase profiles based on Metop-A/B/C (Meteorological Operational) RO datasets for three 3-month periods in 2008, 2013, and 2020 by way of a sensitivity analysis for three representative atmospheric layers (tropo-, strato-, mesosphere), investigating consistency with ERA5-derived profiles, influences of different orbit and clock inputs, and consistency across the different Metop satellites. These consistencies range from centimeter to submillimeter levels, indicating that the new processing can provide highly accurate and robust excess-phase profiles. Furthermore, cross-evaluation and intercomparison with excess-phase data from the established data providers EUMETSAT (European Organisation for the Exploitation of Meteorological Satellites) and UCAR (University Corporation for Atmospheric Research) revealed subtle discrepancies but overall very close agreement, with larger differences compared to UCAR in the boundary layer. The new rOPS L1a processing can hence be considered capable of producing reliable long-term data records including uncertainty estimation for the benefit of climate applications.

Published by Copernicus Publications on behalf of the European Geosciences Union.

1 Introduction

Satellite-based remote sensing observations of the atmosphere, throughout the troposphere and stratosphere, constitute an important backbone for contemporary atmospheric and climate science. With global warming ongoing and its worldwide environmental and socioeconomic implications, improvement in the observational foundation of Earth's climate system has become more important than ever (IPCC, 2021). The Global Climate Observing System (GCOS) therefore aims for the establishment and preservation of climate benchmark data records for the detection, projection, and attribution of changes in the climate system as essential (GCOS, 2021).

By observing essential climate variables (ECVs) (National Research Council, 2007; GCOS, 2021; Bojinski et al., 2014), the global navigation satellite system (GNSS) radio occultation (RO) measurements (e.g., Kursinski et al., 1996; Syndergaard, 1999; Hajj et al., 2002) qualify to provide benchmark data records, as they provide accurate and precise monitoring of ECVs, such as temperature and pressure over the troposphere and stratosphere, and tropospheric water vapor, with global coverage, long-term stability, and essentially all-weather capability (Anthes, 2011; Steiner et al., 2011, 2020).

During an occultation measurement, signals emitted by a GNSS satellite scan the atmosphere in limb-sounding geometry and arrive with a time delay at the receiving RO satellite in low Earth orbit (LEO), which occurs due to the signal's refraction in Earth's atmosphere. A vertical setting or rising occultation event is observed depending on whether the GNSS transmitter satellite sets or rises behind Earth's horizon, from the viewpoint of the rapidly moving LEO receiver satellite.

The raw phase change measurements, obtained by a GNSS receiver aboard the LEO satellite, fundamentally can be traced to the SI seconds, a requirement for RO measurements to serve as a fundamental climate data record (FCDR) (GCOS, 2021). This is ensured by atomic clocks aboard the GNSS satellites, which are linked to a ground-based atomic clock network for monitoring and correction of the space-based clocks. In order to maintain traceability of the less stable oscillators of the LEO satellite, the clock bias is estimated along with the position and velocity of the satellite within the precise orbit determination (POD) process (Montenbruck et al., 2008; Innerkofler et al., 2020). This allows for accurate georeferencing of the measurements in order to isolate the phase delay induced by the atmosphere. This so-called *excess phase* serves as a key FCDR variable available from the RO measurements. Within the RO retrieval, this FCDR can be processed further to vertical atmospheric profiles of bending angle and refractivity, as well as subsequently to ECVs, namely temperature, pressure, and tropospheric water vapor.

The assessment of the quality and uncertainty in RO data, caused by measurement and retrieval errors, is also affected by the use of external data that facilitate the retrieval (Wee and Kuo, 2015). The inclusion of auxiliary information in the retrieval and its influence advances with each step of the retrieval and hence partially degrades the fundamental SI traceability of the measurements. Evaluation of basic (low-level) RO data, in particular the excess-phase data record, benefits from very little influence of external data in its determination and therefore offers the possibility of obtaining highly accurate FCDRs.

For this reason the RO processing at the Wegener Center for Climate and Global Change (WEGC) underwent a substantial revision with the decisive change to start processing from raw measurement data and to independently perform POD of the LEO receiver satellites (Innerkofler et al., 2020). Prior to those changes, OPSv5.6 (Angerer et al., 2017), the former WEGC processing system, started with the supply of excess-phase data along with already interpolated orbit and clock data from the COSMIC (Constellation Observing System for Meteorology Ionosphere and Climate) Data Analysis and Archive Center (CDAAC). The current Reference Occultation Processing System (rOPS) (Kirchengast et al., 2016, 2018) now aims to process raw RO phase measurements into ECVs in a way which is SI-traceable to the universal time standard and which includes rigorous uncertainty propagation. This climate quality rOPS comprises the *occultation data processing* (ODP) from raw RO measurement data (Level 0) to excess phase (Level 1a), atmospheric bending angles (Level 1b), refractivity and dry-air profiles (Level 2a), and finally thermodynamic ECV profiles, as outlined in Fig. 1 (red box). As a basis for supporting ODP, the *daily system modeling* (DSM; green box) for observation geometry and atmospheric-background modeling and the *event system modeling* (ESM; orange box) for RO event geometry and environment modeling, as well as the simulation of RO profiles, were added.

Within this study the new rOPS implementation of Level 1a excess-phase processing within rOPS is introduced, closing the gap between the calculation of precise orbit positions, velocities, and clock estimates (Innerkofler et al., 2020); the retrieval of bending angles (Schwarz et al., 2018); and, subsequently, refractivity and atmospheric profiles (Schwarz et al., 2017; Schwarz, 2018; Li et al., 2019). This includes the uncertainty estimation at the excess-phase level provided by rOPS for each individual RO event.

The random- and systematic-uncertainty estimates at the excess-phase level are then propagated through the entire ODP retrieval chain in order to provide the final ECVs with their associated uncertainties. Additionally, the uncertainties quantified are employed in part of the retrieval operators of rOPS to improve the derivation of variables (e.g., ionosphere correction, statistical optimization, moist-air retrieval). For details on the uncertainty propagation along this chain, starting from the estimates at excess-phase level, see Schwarz et al. (2018, 2017), Schwarz (2018), and Li et al. (2019).

Quality assessment of the algorithms is carried out based on RO data from the EUMETSAT (European Organisa-

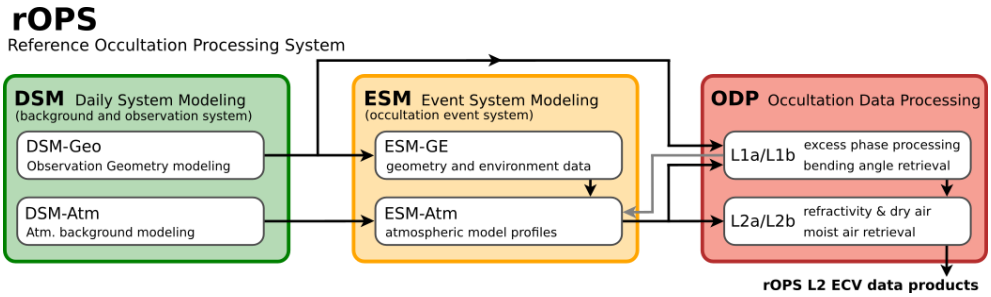


Figure 1. General schematic overview of parts of WEGC's rOPS relevant to this study, comprising the daily system modeling (DSM; green), the event system modeling (ESM; orange), and the occultation data processing (ODP; red). The latter outlines the main Level 1 and Level 2 retrieval steps (L1a to L1b) from the excess phase to ECVs.

tion for the Exploitation of Meteorological Satellites) Polar System (EPS) Meteorological Operational (Metop) satellite series (Luntama et al., 2008). Metop satellites provide a stable data record of RO measurements over more than a decade, which is routinely processed by two renowned processing centers: EUMETSAT as the operator of the mission (von Engeln et al., 2009) and CDAAC as an independent party (Schreiner et al., 2011). Simulated profiles extracted from European Centre for Medium-Range Weather Forecasts (ECMWF) ERA5 data (Hersbach et al., 2020) support this evaluation, which is subdivided into sensitivity, statistical, and uncertainty analysis (Sect. 4).

The Metop satellite series consists of three flight models, Metop-A/B/C, which were launched into orbit sequentially in time (Metop-A: 19 October 2006, Metop-B: 17 September 2012, Metop-C: 7 November 2018). All three satellites are equipped on board with the GNSS Receiver for Atmospheric Sounding (GRAS) RO instrument, developed by Saab Ericsson Space (SAAB, 2004; Klaes et al., 2007; Loiselet et al., 2000). Metop-A was then decommissioned by November 2021 (https://www.eumetsat.int/plans-metop-end-life, last access: 29 September 2023), while Metop-B and Metop-C are still in orbit and operational. The GRAS instrument provides dual-frequency navigation and occultation tracking at 12×3 channels for L1 C/A (coarse/acquisition) and L1/L2 P(Y) code. Besides a zenith-looking antenna providing navigation tracking data for POD, two high-gain antennas looking in the flight velocity and anti-velocity direction share 4 out of the 12 channels for recording setting and rising occultations, respectively. GRAS supports closed-loop (50 Hz) and open-loop (1 kHz) measurements (Bonnedal et al., 2010). RO data from EPS are limited to GPS observations, while EPS-SG (Second Generation) will be capable of tracking GPS, Galileo, and BeiDou signals (https://www.eumetsat.int/eps-sg-radio-occultation, last access: 29 September 2023). Hence, the scope of the new algorithm's evaluation in this study focuses on GPS RO data.

Following this introduction, in Sect. 2, the processing setup is described, the input data and their sources are summarized (Sect. 2.1), and the POD and background data modeling are introduced (Sect. 2.2). Subsequently, the excess-phase processing and algorithmic description are provided (Sect. 3.1), complemented by a description of the quality control and estimation of measurement uncertainties (Sect. 3.2). The results are presented and discussed in Sect. 4, before ending with a conclusion section (Sect. 5).

2 Processing setup and system modeling

Processing raw RO measurements to atmospheric excess-phase profiles, also termed Level 1a (L1a) processing, follows a basic algorithmic sequence sometimes also referred to as "calibration" of the measurements (Hajj et al., 2002). In practice, the inclusion of rigorous quality control, uncertainty estimation, and proper data preparation for the subsequent Level 1b (L1b) bending-angle retrieval algorithm make this L1a processing a fairly complex task. Within rOPS, the excess-phase processing is divided into two parts: (1) the derivation of the raw excess phase (the main calibration algorithm) and (2) the quality control and uncertainty estimation of the derived excess-phase profiles. Along with these two subprocesses, a series of steps, involving ESM-GE and ESM-Atm (cf. Fig. 1), complement the excess-phase computation.

Figure 2 summarizes the relations and workflow between those rOPS subsystems most relevant to the L1a excess-phase processing. In a first step, external input data have to be acquired and prepared to satisfy the rOPS data interface. DSM supplies precise and accurate orbit and clock data of LEO receiver and GNSS transmitter satellites, including estimates of systematic and random uncertainty. Subsequently, the ESM-GE models reference locations of all possible RO events and provides additional information on the geometry and environment, while the raw excess-phase profile processing delivers vertical profiles of measured RO data. With the event information and the raw L1a data, atmospheric excess-phase model profiles can be provided by ESM-Atm. These model profiles are then used for the L1a quality control and uncertainty estimation, yielding "final" quality-controlled excess-phase profiles, which serve as in-

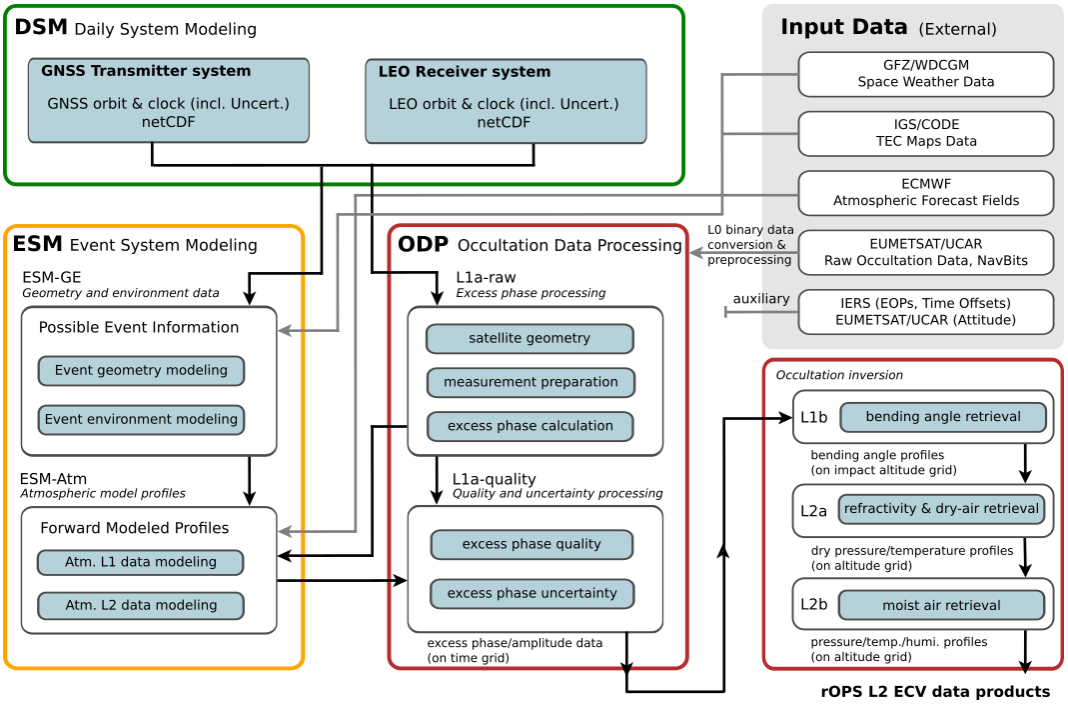


Figure 2. Schematic overview of parts of WEGC's rOPS relevant to this study, comprising the daily system modeling (DSM; green), the event system modeling (ESM; orange), and the occultation data processing (ODP; red). Main details of subsystems are identified, with a focus on the ODP L1a processor, together with the major input data sources and output flow towards the L1b and L2 (L2a, L2b) retrieval chain from the excess phase to ECVs. GFZ: German Research Centre for Geosciences. WDCGM: World Data Center for Geomagnetism (Kyoto). IGS: International GNSS Service. CODE: Center for Orbit Determination in Europe. ECMWF: European Centre for Medium-Range Weather Forecasts. EUMETSAT: European Organisation for the Exploitation of Meteorological Satellites. UCAR: University Corporation for Atmospheric Research. IERS: International Earth Rotation and Reference Systems Service. EOPs: Earth orientation parameters.

put for the ODP L1b retrieval processing. In the following, we take a closer look at each of these steps relevant to the L1a processing after summarizing the relevant input data.

2.1 Input data preparation

The RO data processing in general and, more specifically to this study, the WEGC ODP L1a excess-phase data processing rely on various input data sources. Besides the main observational data measured by the satellite's occultation antenna(s), space weather data, atmospheric reanalysis and forecast data, satellite antenna specifications, GNSS navigation bit data, and auxiliary data comprising Earth orientation data and time offsets are also necessary input data for RO excess-phase processing and its supporting ESM system. Table 1 provides a concise overview of these external data sources used for the L1a processing within rOPS and is followed by a description of the application of these data.

In this study we used three multi-month time periods as the basis for the assessment, each comprising 3 months: July to September 2008 (Metop-A; 2008-JAS), July to September 2013 (Metop-A/B; 2013-JAS), and December 2019 to February 2020 (Metop-A/B/C; 2020-DJF). These are representative of different solar cycle and summer/winter conditions over more than a decade from 2008 to 2020. As a cross-check, we also investigated data in the main season of equatorial plasma bubbles (September 2013 to March 2014), which involves particularly challenging geophysical conditions, but found no appreciable differences in comparison to the three time periods chosen. Data availability of the respective study periods is limited by the different launch dates of Metop satellites A, B, and C (cf. Sect. 1).

Compared to other RO receivers, the GRAS receiver on board the Metop satellites delivers raw-level measurement data in the form of chunks of numerically controlled oscillator (NCO) time-tagged phase as well as in-phase and quadrature (I/Q) components, instead of already connected phase and amplitude as a function of time (SAAB, 2004; Schreiner et al., 2011). Since the computation of these variables is time intensive and some data distribution limitations for original Level 0 data by EUMETSAT do apply, WEGC decided to reconstruct the raw variables from the EUMETSAT L1a data (EUMETSAT, 2016). This includes reconstruction of the raw measurement time stamps and undifferencing of the NCO phase. It was validated against processing based on EUMETSAT Level 0 data that such correctly performed raw-level measurement reconstruction does not show any non-

Table 1. External input data used by the different subsystems of the rOPS ODP L1a processing system. Data are provided by the Crustal Dynamics Data Information System (CDDIS), German Research Centre for Geosciences (GFZ), Geomagnetic Laboratory (GEOLAB) of Natural Resources Canada, ECMWF, International GNSS Service (IGS), EUMETSAT, and International Earth Rotation and Reference Systems Service (IERS). For details on the specific data types, see the text. n/a: not applicable.

Data type	Provider	Resources (last access: 29 September 2023)
ESM-GE		
TEC maps	IGS, CDDIS	https://cddis.nasa.gov/archive/gnss/products/ionex; Hernández-Pajares et al. (2009)
Kp index	GFZ	ftp://ftp.gfz-potsdam.de/pub/home/obs/kp-ap; Matzka et al. (2021)
Solar flux F10.7	GEOLAB	ftp://ftp.seismo.nrcan.gc.ca/spaceweather/solar_flux/daily_flux_values/fluxtable.txt; Tapping (2013)
DSM-Atm		
Atmospheric fields	ECMWF	Climate Data Store (CDS) Application Program Interface; ECMWF (2019), Hersbach et al. (2023)
ODP L1a (raw processing)		
GNSS ANTEX	IGS	https://files.igs.org/pub/station/general/igs14.atx; Rebischung and Schmid (2016)
LEO ANTEX	n/a	from satellite providers; format: https://files.igs.org/pub/station/general/antex14.txt
Occultation data	EUMETSAT	https://eoportal.eumetsat.int, EUMETSAT (2016)
Navigation bit data	EUMETSAT	https://eoportal.eumetsat.int, EUMETSAT (2018)
Auxiliary		
EOP, time offsets, etc.	IERS	https://datacenter.iers.org/eop.php

negligible differences compared to the original data. We note that CDAAC developed their own phase and amplitude calculation for GRAS data, which also shows good agreement with data generated by EUMETSAT (Schreiner et al., 2011).

For evaluation of the calculated atmospheric excess-phase profiles, inter alia also of the proper implementation of the rOPS ODP L1a processing, a careful intercomparison with independently calculated profiles is indispensable. In this study publicly available excess-phase profiles from EUMETSAT (https://eoportal.eumetsat.int, last access: 29 September 2023; 2008-JAS and 2013-JAS: https://doi.org/10.15770/EUM_SEC_CLM_0029 (EUMETSAT, 2020), processor: Yaros 1.4; 2020-DJF: operational, processor: GRAS-4.6.2) and CDAAC (Metop-A: https://doi.org/10.5065/789w-m137 (CDAAC, 2023a), version: 2016.0120; Metop-B: https://doi.org/10.5065/1k0w-2272 (CDAAC, 2023b), version: 2016.0120; Metop-C: https://doi.org/10.5065/p8es-mc74 (CDAAC, 2023c), version: 2019.2580) have been used for such intercomparison (Sect. 4.2). Additionally, forward-modeled profiles computed from ERA5 reanalysis data (Hersbach et al., 2023) served as a reference for a sensitivity analysis for the excess-phase profiles calculated with rOPS (Sect. 4.1.1).

Reanalysis data are widely used in atmospheric sciences applications and also serve as an integral component in WEGC's rOPS system. The reference dataset used in this study is the ERA5 reanalysis dataset, computed with the Integrated Forecasting System (IFS) of the ECMWF (ECMWF, 2016, 2019; Hersbach et al., 2019, 2020). Within rOPS, ERA5 short-range *forecast* data are used for the provision of model and background profiles in order to facilitate the ODP retrieval and to derive quality measures and support estimation of the uncertainty in the observed profiles at each step of the retrieval, while the ERA5 *analysis* data are used for the provision of reference profiles in part of the sensitivity analysis of the RO retrieval.

The employed short-range forecast is essentially a pure model state carrying no direct information from assimilated observational data. This is an important aspect in order to keep the final rOPS ECVs uncorrelated with the evaluation (analysis) dataset, given that RO data are assimilated into ECMWF's (re)analyses as of late 2006 (Healy, 2007; Schmidt et al., 2008; Hersbach et al., 2020). Although the assimilation of RO data has an influence on the ERA5 analysis data, we consider this analysis suitable for supporting the task of evaluation of the quality and robustness of the implemented excess-phase processing in this study. We note that for the actual validation of data, which is not the focus here, further independent datasets should be used. With a horizontal resolution of about 30 km, with 137 vertical levels from the surface up to about 80 km, the ERA5 reanalysis data suit the RO measurement characteristics well. The interpolation strategy to produce collocated model, background, and reference profiles is summarized in Sect. 2.2.3.

For the ESM-GE processing, ionosphere and space weather information are incorporated to complement the environment information for each RO event. These data comprise total electron content (TEC) maps, Kp indices describing disturbances of Earth's magnetic field, and solar flux data measuring the radio emission from the Sun at a wavelength of 10.7 cm as a proxy for solar activity. These can support quality evaluation and, in particular, serve as an in-

put for higher-order ionospheric correction in L1b processing (Danzer et al., 2020, 2021; Liu et al., 2020). In addition, GNSS and LEO antenna offset information is used to accurately model the event locations in ESM-GE and to correct the location of the observations in ODP L1a. For the GNSS, these data are provided by the International GNSS Service (IGS) using the antenna exchange format (ANTEX; https://files.igs.org/pub/data/format/antex14.txt, last access: 29 September 2023).

For the LEO receiver satellites, different sources need to be exploited depending on the RO mission and satellite data provider. At WEGC all relevant LEO antenna information is merged in a custom receiver antenna file, using the ANTEX format as well. GNSS navigation bit data for measurement signal demodulation are obtained from EUMETSAT (EUMETSAT, 2018). Variable Earth geodetic data, such as Earth orientation parameters (EOPs), leap seconds, and time offsets, serve as general input in support of coordinate and time transformations performed as part of the rOPS L1a processing.

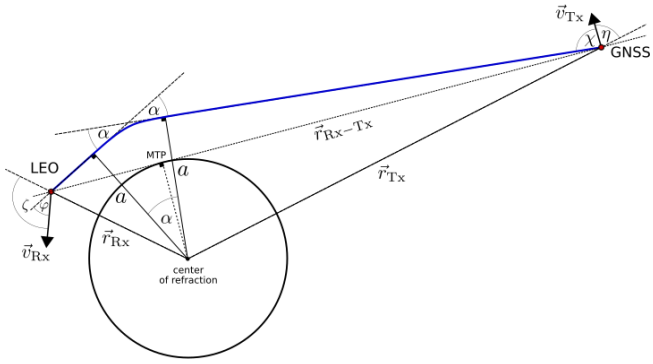


Figure 3. Occultation event geometry, defining important location and angular variables of an RO event. Adapted from Pirscher (2010). The schematic depicts the occultation event at the time when the straight-line connection between GNSS and the LEO satellite is tangent to Earth's ellipsoidal and defines the mean tangent point (MTP) in this way.

2.2 Daily and event-based system modeling

The system modeling part of rOPS, in preparation for the ODP core system, consists of two main components: (1) DSM, the daily system modeling of the *observation system geometry* and preparation of *atmospheric-background* fields, and (2) ESM, the occultation event modeling of *geometry and environment* modeling and derivation of corresponding *atmospheric-model profiles* (Fig. 2).

2.2.1 Observation geometry modeling

Accurate and precise knowledge of the location and time of GNSS signal transmission and reception is fundamental to RO processing and the subsequent derivation of highly accurate and long-term stable ECVs. For this reason, a novel multi-system setup for POD was introduced by Innerkofler et al. (2020) that builds on independent orbit solutions from three different processing runs for each day. Embedded in the DSM observation geometry modeling of rOPS, the system also provides attributed measures for quality and estimated uncertainties, in order to enable long-term stable and highly consistent LEO orbit processing and analysis.

Within DSM-Geo, the LEO POD of RO receiver satellites is performed in parallel by employing the two independent software packages of Bernese v5.2 (Dach et al., 2015) and NAPEOS v3.3.1 (NAvigation Package for Earth Observation Satellites) (Springer, 2009). The calculations are based on GNSS pseudorange and carrier phase measurements obtained by the RO satellite's zenith antenna and GNSS orbit and clock data products from the Center for Orbit Determination in Europe (CODE). One additional orbit solution is derived with transmitter orbit and clock data from the International GNSS Service (IGS) using Bernese. This POD setup enables mutual consistency checks of the calculated orbit solutions and is used for monitoring the quality of the "primary" orbit solution (the one derived with Bernese–CODE used for further RO processing) as well as for position and velocity uncertainty estimation, including estimated systematic and random uncertainties. In general, the combined 3D-estimated position and velocity uncertainties for the Metop satellite series account for around 1.9 cm and 0.02 mm s^{-1} (random) and 5.0 cm and 0.05 mm s^{-1} (systematic), respectively. For more details on this rOPS POD processing, the reader is referred to Innerkofler et al. (2020).

The additional uncertainty output produced by DSM-Geo exceeds the limitation of the well-established format definitions used for the exchange of orbit data, e.g., SP3 (Standard Product 3; https://files.igs.org/pub/data/format/sp3c.txt, last access: 29 September 2023). We therefore store the final output data of the POD in a specially designed netCDF file that contains orbit and clock data for each daily 24 h orbit arc per satellite. In total this results nominally in 32 GPS transmitter and 1 RO receiver satellite file per day. The content comprises the center-of-mass (COM) satellite positions and velocities in an Earth-centered, Earth-fixed (ECEF) coordinate system as well as satellite clock biases. Adequate for the intended purpose of RO processing (confirmed by comprehensive sensitivity checks), the GNSS orbit data are stored with a sampling rate of 15 min, whereas the clock bias data and LEO orbit data are stored at a sampling rate of 30 s. All these daily orbit arc data are stored together with their estimated random and systematic uncertainty.

Table 2 provides an overview of the core variables supplied by the DSM-Geo POD processing, which subsequently serve as input for the ODP L1a processing. For the excess-phase processing these data need to be aligned in time (interpolation of RO measurement time stamps and correction of clock biases) and location (application of RO antenna off-

sets). The preparation and necessary steps for this processing are discussed further in Sect. 3.1.

2.2.2 Event system modeling

Provided the positions and velocities of the transmitter and receiver satellites, calculated by DSM-Geo, a reference event location of an occultation is determined in rOPS by geometrical constraints only, independent of any atmospheric state or RO measurement data. The selected reference location of an event is defined on Earth's ellipsoidal surface at the time when the straight-line connection between receiver and transmitter satellite is tangent to Earth's surface (WGS-84 EGM2008; World Geodetic System, Earth Gravitational Model; cf. Fig. 3 for measurement geometry). This uniquely defined point in space and time, also referred to as the *mean tangent point* of the RO event, is determined after the GNSS orbit is interpolated to the 30 s sampled LEO orbit time stamps (and locally using fine interpolation for accurately determining the point). For compact identification, each event is uniquely encoded using a 64-bit integer representation compiled from the mean event time, transmitter system, and transmitting-satellite identifier, as well as the receiver identifier.

The event geometry modeling is complemented by the event environment modeling comprising surface and atmosphere data, as well as ionosphere and space weather information extracted for each reference location. Apart from the mean tangent point, which per definition is at a straight-line tangent height (SLTH) of 0 km, the same information can be additionally retrieved for any other non-zero SLTH. In rOPS this is done additionally at an SLTH of 90, 80, 70, 60, and −250 km, respectively. Extracted parameters and variables at these auxiliary locations visited during the RO event is valuable for contextual grouping of events, event distribution analyses, and ionosphere/space weather sensitivity analyses and is also needed in the subsequent ODP processing, e.g., as part of higher-ionospheric correction (Danzer et al., 2021; Liu et al., 2020).

The mean tangent point location derived in this way has been proven to be very adequate and corresponds to real RO event tangent point trajectory locations near the tropopause (Foelsche et al., 2011). This offers the advantage that purely geometrical analyses, like those for geographic RO event distributions, can be done independent of RO data, and it enables rigorous location consistency of forward modeling (simulating RO profiles) and retrievals (analyzing observed profiles) for each and for all individual events. Figure 4 illustrates the global RO event distribution for Metop-A/B on 1 July 2013. In principle the number of modeled events exceeds the number of observed events. The calculated data of ESM-GE are provided as a dedicated output file of rOPS and then are further used by the subsequent ESM subsystems and the ODP L1a processing.

2.2.3 Atmospheric-model profiles

With knowledge of the simulated but realistic event location of the measurements from ESM-GE, corresponding atmospheric profiles can be forward-modeled upward along the ODP processing chain from Level 2 to Level 1. Figure 5 illustrates the forward-modeled results, extracted from ERA5 data at the respective locations, for the three example events (see Fig. 4 and Table 3), for refractivity (N), bending angle (α), and excess phase (L), respectively, as well as the difference profiles between the forward-modeled and related observed excess-phase data. These example profiles serve to represent standard (STD), tropical (TRO), and sub-arctic winter (SAW) conditions. Given the simulated event locations, it is ensured that for each observed RO event, a corresponding consistent set of forward-modeled profiles is made available at each step from refractivity to the excess phase.

The ERA5 reanalysis fields, introduced in Sect. 2.1 above, globally provide temperature, pressure, and water vapor information at any desired location and time of interest. Hence, starting from ERA5 fields, atmospheric profiles of these variables are extracted by interpolation in time and space to the RO event location (mean tangent point location, extracting vertical profiles at these locations). Since the ERA5 fields are used in a 6-hourly resolved form, the closest time layer happens to always be within 3 h of the occurrence of the mean RO event time, a time difference which is sufficient to model the semi-diurnal cycle (Scherllin-Pirscher et al., 2011b, a). Horizontal interpolation is performed by using a four-point cubic-polynomial interpolation technique (for a detailed description, see Appendix A.3 of Lackner, 2010). For vertical interpolation of temperature T, pressure $\ln(p)$, and specific humidity q, several interpolation methods were compared (linear, cubic spline, and Savitzky–Golay filter). Based on this, those providing the most robust fit through the nodes of the ECMWF altitude levels were selected. As a result, the vertical interpolation to the fixed-altitude grid z is performed for T and $\ln(p)$ using a natural cubic-spline interpolation, while q profiles are interpolated linearly.

Refractivity profiles are then derived, based on the interpolated variables, employing the ionosphere-free first-order relationship (Smith and Weintraub, 1953; Kursinski et al., 1997). Given the refractivity profile as a function of the fixed vertical grid $N(z)$, Level 1 profiles of bending angle α, Doppler shift D, and excess phase L can be calculated.

In a first step impact altitude grid $z_a(z) = z + 10^{-6}N(z) \cdot (z + U_G + R_C)$ and impact parameter grid $a_z(z_a) = z_a(z) + U_G + R_C$ are computed consistently with altitude grid z, with geoid undulation U_G and radius of curvature R_C both at the occultation event location. Additionally log-refractive index profile $n^{\ln}(a_z) = \ln(1 + 10^{-6}N(z))$ and its gradient profile $n^{\ln}_{\mathrm{d}a}(a_z)$ are calculated at the consistent grids.

Using the refractive index gradient profile the bending-angle profile $\alpha(a_z)$ is then derived using an inverse Abelian integral transformation (Fjeldbo and Eshleman,

Table 2. Orbit and clock data output from the rOPS POD processing, including the associated sampling rates and corresponding estimates of random (u_r) and systematic uncertainty (u_s).

	Variable	Unit	Description
LEO	r^r	m	COM position of LEO satellite, each 30 s including estimates of $r^r_{u_r}$, $r^r_{u_s}$
	v^r	$m\,s^{-1}$	COM velocity of LEO satellite, each 30 s including estimates of $v^r_{u_r}$, $v^r_{u_s}$
	δt^r	s	clock bias (30 s) including $\delta t^r_{u_r}$
GNSS	r^t	m	COM position of LEO satellite, each 15 min including estimates of $r^t_{u_r}$, $r^t_{u_s}$
	v^t	$m\,s^{-1}$	COM velocity of LEO satellite, each 15 min including estimates of $v^t_{u_r}$, $v^t_{u_s}$
	δt^t	s	clock bias (30 s) including $\delta t^t_{u_r}$

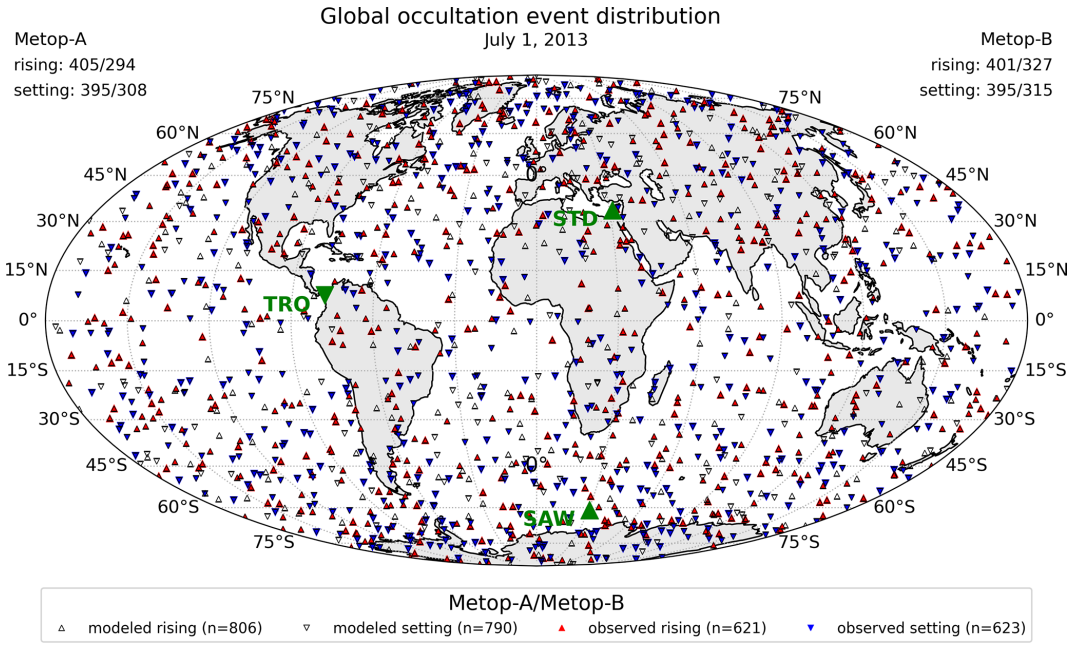


Figure 4. Global distribution of Metop-A/B RO events on 1 July 2013. Setting events (upside-down triangles) and rising events (upright triangles) are separately identified, and the number of modeled/processed events is noted as part of the legend information. Three example events used for illustrating the subsequent description and results are separately identified (large green triangles) as well, with more information on them summarized in Table 3).

1965; Fjeldbo et al., 1971), solving for all grid levels a_i from $a(z_{top})$ to $a(z_{bot})$. The actual calculation is performed using the implementation in rOPS (Syndergaard and Kirchengast, 2016) in combination with the baseband method (cf. Kirchengast et al., 2018). Subsequently, the bending-angle profile is mapped to a strict 50 Hz measurement grid including a vertical mapping from impact altitude $\alpha(a)$ to time $\alpha(t)$. This mapping requires knowledge of the orbit position of the transmitter (r_{Tx}) and receiver (r_{Rx}) satellites at the measurement time and demands an iterative numerical solution (Proschek et al., 2011).

The mapped bending angle $\alpha(t)$ is then used to calculate the Doppler shift, which can in turn be further integrated to the excess phase. Based on the occultation geometry (cf. Fig. 3) and the corresponding angles χ, η, φ, and ζ, as well as the position and velocity of the receiver (r_{Rx}, v_{Rx}) and transmitter (r_{Tx}, v_{Tx}) satellites and their distance to each other dr_{RxTx}, the Doppler shift can be calculated as follows:

$$D(t_i) = [v_{Rx}\cos\varphi(a_i) - v_{Tx}\cos\chi(a_i)] - \frac{dr_{RxTx}(t_i)}{dt}, \quad (1)$$

with

$$\chi(a_i) = (\pi - \eta) - \arcsin\left(\frac{a_i}{r_{Tx}}\right)$$

and

$$\varphi(a_i) = \zeta - \arcsin\left(\frac{a_i}{r_{Rx}}\right). \quad (2)$$

Modeled Doppler shift $D(t_i)$ is limited to the proportion of the entire Doppler shift, which is induced by the atmo-

Table 3. Selected Metop-A RO example events, representing standard (STD), tropical (TRO), and sub-arctic winter (SAW) conditions.

No.	Label	GPS ID	Mission	Latitude	Longitude	Time	Characterization
1	STD	03	Metop-A	33.54° N	31.24° E	17:36:19	standard atmosphere
2	TRO	20	Metop-A	7.45° N	77.96° W	13:22:12	tropical atmosphere
3	SAW	14	Metop-A	60.84° S	30.61° E	06:42:07	southern atm. winter

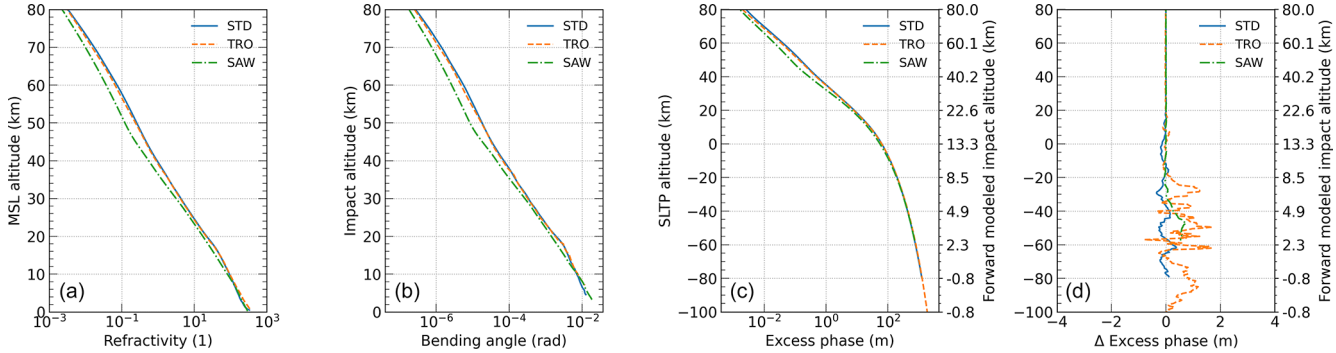


Figure 5. (a–c) Forward-modeled example profiles from **(a)** refractivity to **(b)** the bending angle and **(c)** the excess phase, respectively, and **(d)** the difference between modeled and observed excess phase. Results for all three example events defined in Table 3 are shown. MSL: mean sea level. SLTP: straight-line tangent point.

sphere, while those parts which come from the movement of the satellites relative to each other are not considered.

Finally, modeled excess phase $L(t_i)$ can be calculated as a function of time by using the relation with the previously calculated Doppler shift $D(t_i)$:

$$L(t_i) = \int_{t_{\mathrm{top}}}^{t^{\mathrm{bot}}} D(t_i)\mathrm{d}t + L\left(t_{\mathrm{top}}\right). \tag{3}$$

To integrate the excess-phase change (or Doppler shift), in order to obtain the excess-phase path, we apply Simpson's rule for the numerical integration of Eq. (3). The integration starts at the top of the measurement, where D is very small and errors in the initialization almost vanish relative to contributions at lower-atmospheric levels. Scale height H multiplied by the bending angle α at the uppermost level serves as integration constant $L(t_{\mathrm{top}}) = H_{\mathrm{top}} \cdot \alpha_{\mathrm{top}}$, which is considered an adequate approximation for the integration of the excess phase (Rieder and Kirchengast, 2001; Kirchengast et al., 2018).

3 Excess-phase processing and algorithmic description

3.1 Excess-phase processing

Numerous studies have described the RO retrieval chain in detail (e.g., Kursinski et al., 1997; Rieder and Kirchengast, 2001; Hajj et al., 2002; Kuo et al., 2004) and have shown the high accuracy of RO data, particularly in the upper-troposphere and lower-stratosphere region (e.g., Rocken et al., 1997; Gobiet et al., 2007; Ho et al., 2012; Steiner et al., 2020). More specifically, RO Level 1a processing data from raw occultation measurements and precise orbit and clock data of the transmitter and receiver satellites to the excess phase have been discussed in detail (e.g., Hajj et al., 2002; Beyerle et al., 2005; Schreiner et al., 2010; Bai et al., 2018), since accurate and precise excess-phase data are the indispensable basis for SI traceability and co-determine the quality of derived ECVs. Here the implementation of WEGC's new rOPS ODP L1a excess-phase processing is described, preceded by a short discussion of GNSS signal structure and signal-tracking modes.

3.1.1 GNSS observables

In principle, the concept of GNSS measurements relies on measurements of ranges between the transmitter and receiver which are derived from measured time (code pseudoranges) or phase differences (phase pseudoranges) relative to the transmitted electromagnetic signal. Since the measured ranges are affected by transmitter and receiver satellite clock errors, they are labeled pseudoranges. Also, more commonly simply referred to as code and (carrier) phase measurements, those observables constitute basic measurements made by GNSS receivers aboard RO satellites, where the latter (carrier phase) are more precise and therefore favored in RO processing. This is intrinsic to the chip length of the code modulated onto the carrier phase (e.g., GPS, coarse/acquisition (C/A) code: $\lambda \approx 293$ m; precision (P) code: $\lambda \approx 29$ m), which is accurate to 1 %–0.1 %, while carrier phase measurements of a typical GNSS wavelength (e.g., GPS, L1: $\lambda \approx 0.19$ m; L2:

$\lambda \approx 0.24$ m) allow for millimeter precision (Teunissen and Montenbruck, 2017; Hofmann-Wellenhof et al., 2008).

The enhanced precision of the carrier phase measurements comes with the disadvantage of ambiguity of the measurement, since at the time of the initial signal acquisition the number of full carrier wave cycles ("integer cycles") between the receiver and the transmitting satellite is not known. Although this is a problem for classical navigation and positioning applications, for atmospheric RO, interested in the relative change in the signal for vertical atmospheric profiling, it does not pose a problem (Teunissen and Montenbruck, 2017).

Phase measurements are generally performed using a phase-locked loop (PLL), where the receiver generates an internal replica of the GNSS signal, aligns it with the incoming carrier phase, and measures it while keeping track of the changes in full cycles and the fractional shift (I/Q). Within PLL tracking, the internally generated signal is adjusted using a feedback loop on the basis of previous measurements, which works fine with a sufficiently high signal-to-noise ratio (SNR) and weak atmospheric disturbances in the atmospheric regions above the lower troposphere. In the lower troposphere, however, the complicated structure of RO signals, caused by multipath propagation or even ducting in the moist lower troposphere, leads to a loss of lock or to biases in the measured signals as well as to late signal acquisitions for rising occultations that may miss the moist lower troposphere (Sokolovskiy, 2001; Sokolovskiy et al., 2006; Ao et al., 2009).

In order to overcome these issues, RO signals are measured using a delay-locked loop (DLL) when disturbed atmospheric conditions interfere with closed-loop (CL) tracking using a PLL. This OL-tracking (open-loop) mode is not supported with a feedback loop including the measured signal (and is therefore less prone to be affected by disturbed atmospheric conditions) but is model-aided based on orbit, receiver clock drift, and estimated Doppler shift and delay, deduced from a real-time navigation solution (e.g., Ao et al., 2009). This onboard computation of the OL model, including the prediction of the code pseudorange, is employed by the majority of GNSS RO receivers currently in space. Note that RO measurements performed using OL tracking need to be demodulated from GNSS navigation data in postprocessing (Sokolovskiy, 2001; Sokolovskiy et al., 2006).

The GRAS receiver, in contrast, continues C/A code tracking in OL mode and only uses an OL model for carrier phase tracking. This can lead to data gaps when the C/A code tracking loses lock caused by challenging tracking conditions in the lower troposphere (Schreiner et al., 2011). Therefore, in order not to degrade SI traceability, we restrict the processed data to the longest continuous CL and raw-sampling (RS) data segments, not allowing for any gaps between these two data segments. Another method to overcome the shortcomings of CL tracking in the lower troposphere is to use moderate wideband digital recording, a technique which features a sufficient bandwidth to capture the spectrum of the excess Doppler in the lower troposphere (Ao et al., 2009). For GRAS on board Metop (Bonnedal et al., 2010) this was realized by the implementation of the RS-tracking mode, scanning the GNSS signal with a frequency of 1 kHz (SAAB, 2004; Gorbunov et al., 2011; Zus et al., 2011). This bears the advantage that only geometric effects need to be modeled in the tracking loop, but at the same time data storage requirements increase significantly compared to 50 Hz OL tracking featuring narrowband digital recording (Sokolovskiy, 2001; Ao et al., 2009).

Independent of the tracking mode employed, the RO technique aims to extract atmospheric and ionospheric delays from the total measured phase. The measured phase between the GNSS transmitter and LEO receiver satellites, denoted with the superscript t and the subscript r, respectively, can be modeled for a given GNSS signal frequency, summing up the following terms as a function of signal reception time t_r at the LEO satellite and transmission time t^t at the GNSS satellite (Schreiner et al., 2010):

$$\begin{aligned} L_\mathrm{r}^\mathrm{t}(t_\mathrm{r}) = {} & \rho_\mathrm{r}^\mathrm{t}(t_\mathrm{r}, t^\mathrm{t}) + c\left[\delta t_\mathrm{r}(t_\mathrm{r}) + \delta t_\mathrm{r,rel}(t_\mathrm{r})\right] \\ & - c\left[\delta t^\mathrm{t}(t^\mathrm{t}) + \delta t_\mathrm{rel}^\mathrm{t}(t^\mathrm{t})\right] + \lambda N_\mathrm{r,amb}^\mathrm{t} - \delta\rho_\mathrm{r,ion}^\mathrm{t}(t_\mathrm{r}) \\ & + \delta\rho_\mathrm{r,atm}^\mathrm{t}(t_\mathrm{r}) + \delta t_\mathrm{r,rel}^\mathrm{t}(t_\mathrm{r}, t^\mathrm{t}) + \epsilon, \end{aligned} \tag{4}$$

where $L_\mathrm{r}^\mathrm{t}(t_\mathrm{r})$ denotes the total observed carrier phase in units of length, $\rho_\mathrm{r}^\mathrm{t}(t_\mathrm{r}, t^\mathrm{t})$ denotes the geometrical distance between the transmitter and receiver satellites, $\delta t_\mathrm{r}(t_\mathrm{r})$ denotes the receiver clock error (or bias/offset), $\delta t^\mathrm{t}(t^\mathrm{t})$ denotes the transmitter clock bias (or offset), $\delta t_\mathrm{r,rel}(t_\mathrm{r})$ denotes the special relativistic effect on the receiver clock, $\delta t_\mathrm{rel}^\mathrm{t}(t^\mathrm{t})$ denotes the special relativistic effect on the transmitter clock, $\delta\rho_\mathrm{r,ion}^\mathrm{t}(t_\mathrm{r})$ denotes the ionospheric delay, $\delta\rho_\mathrm{r,atm}^\mathrm{t}(t_\mathrm{r})$ denotes the neutral atmosphere delay, $\delta_\mathrm{r,rel}^\mathrm{t}(t_\mathrm{r}, t^\mathrm{t})$ denotes the general-relativistic gravitational delay, and $\lambda N_\mathrm{r,amb}^\mathrm{t}$ denotes the integer phase ambiguity, with the signal wavelength λ, speed of light in a vacuum c, and ϵ of the phase noise and residual errors.

3.1.2 Atmospheric and ionospheric excess phase

For the purpose of remote sensing of Earth's atmosphere, the atmospheric influences, comprising effects of the neutral atmosphere $\delta\rho_\mathrm{r,atm}^\mathrm{t}$ and the ionosphere $\delta\rho_\mathrm{r,ion}^\mathrm{t}$, need to be separated from the phase model as specified above. Thus, all terms in Eq. (4) apart from the neutral atmosphere delay and ionospheric delay need to be modeled or removed in order to isolate the atmospheric and ionospheric excess phase:

$$\begin{aligned} \Delta L_\mathrm{r}^\mathrm{t}(t_\mathrm{r}) = {} & \delta\rho_\mathrm{r,atm}^\mathrm{t}(t_\mathrm{r}) - \delta\rho_\mathrm{r,ion}^\mathrm{t}(t_\mathrm{r}) + \epsilon = L_\mathrm{r}^\mathrm{t}(t_\mathrm{r}) \\ & - \rho_\mathrm{r}^\mathrm{t}(t_\mathrm{r}) - c\left[\delta t_\mathrm{r}(t_\mathrm{r}) + \delta t_\mathrm{r,rel}(t_\mathrm{r})\right] \\ & + c\left[\delta t^\mathrm{t}(t^\mathrm{t}) + \delta t_\mathrm{rel}^\mathrm{t}(t^\mathrm{t})\right] - \delta t_\mathrm{r,rel}^\mathrm{t}(t_\mathrm{r}) - \lambda N_\mathrm{r,amb}^\mathrm{t}. \end{aligned} \tag{5}$$

The ionospheric part can then later on be removed using a linear combination of the dual-frequency measurements

(Schreiner et al., 2010) or more refined RO-tailored corrections at the bending-angle level (Vorob'ev and Krasil'nikova, 1994; Ladreiter and Kirchengast, 1996; Liu et al., 2013; Healy and Culverwell, 2015; Liu et al., 2020). As depicted in Fig. 6, the separation of the excess phase includes a series of corrections to the measurement geometry and the measured signal itself. In the following the necessary steps for the excess-phase calculation and the implementation in rOPS are discussed in more detail.

3.1.3 Satellite geometry – orbit and clock corrections

As a first step of the ODP L1a excess-phase determination, the accurate space–time points of the signal's transmission and reception need to be determined. Therefore, the low-rate GNSS and LEO orbit data need to be corrected and then interpolated to the high-rate RO measurement time stamps. This process includes the removal of receiver and transmitter clock biases, relativistic corrections, the calculation of the signal travel time, proper coordinate transformation of the antenna offsets and addition to the satellite's COM, and the calculation of the geometric distance between receiver and transmitter satellite antennas (see Fig. 6).

At the beginning of the ODP L1a processing, all the necessary input data (cf. Sect. 2.1) are read and checked for their consistency. Starting with precise orbit and clock data from ESM-Geo, the coordinate and time systems of the data are examined. The positions and velocities of the satellites are converted from an Earth-centered, Earth-fixed (ECEF) to an Earth-centered inertial (ECI) reference frame. That way, all calculations are independent of Earth's rotation correction (Sagnac effect; Ashby, 2004), which has to be taken into account when working in a rotating, Earth-fixed reference frame. More specifically, we use the J2000 coordinate system as a realization of the ECI reference frame for all calculations.

The atomic clocks aboard the GNSS satellites are considered stable over the short duration of an occultation event of approximately 1 to 2 min, with 1 s stability (Allan deviation) at a level of between 10^{-11} and 10^{-12}, while more up-to-date clocks feature even higher accuracy (Griggs et al., 2015; Hauschild et al., 2013). In contrast to the GNSS satellites, the RO LEO missions do not carry atomic clocks on board; hence timing is in principle less accurate. However, among other RO missions, the Metop-A/B/C satellites use ultra-stable quartz oscillators that are likewise highly accurate over the short term of RO events. LEO clock errors δt_r (bias estimates along time) are estimated along with the orbit determination process at WEGC, while GNSS clock bias estimates δt^t are provided as part of the orbit data products by the CODE (or IGS) analysis center. The selection of a suitable differencing method, applied later in the excess-phase calculation (see Sect. 3.1.4), is dependent on the stability of the LEO clock.

Satellites and their clocks move with considerable speed in Earth's gravity field and orbit at fairly high altitudes above the surface, and hence effects of Einstein's theory of special and general relativity need to be taken into account. The reduced gravitational influence in orbit, compared to Earth's surface, causes a blue shift and satellite clocks to tick a little faster, whereas time dilation, induced by the motion of the satellites, reduces clock frequency (Ashby, 2003). At higher orbit altitude, such as for GNSS clocks, the former effect prevails. Therefore, these atomic clocks are intentionally slowed down prior to the GNSS satellite's launch by a certain clock frequency shift, in order to compensate for their time acceleration in orbit (Ashby, 2014; Mudrak et al., 2015). An additional periodically varying gravitational frequency shift and second-order Doppler shift, induced by the eccentricity of the satellite orbit, are modeled based on the LEO position r_r and velocity v_r at the signal reception time and the GNSS position r^t and velocity v^t at the signal transmission time, respectively (Kouba, 2015, 2004):

$$\delta t_{\mathrm{r,rel}} = -2\frac{r_\mathrm{r}\cdot v_\mathrm{r}}{c^2}, \delta t^\mathrm{t}_\mathrm{rel} = -2\frac{r^\mathrm{t}\cdot v^\mathrm{t}}{c^2}. \tag{6}$$

By convention, GNSS clock products provided by IGS and CODE analysis centers do not contain this so-called eccentricity correction (Kouba, 2015), and for this reason it needs to be applied to the transmitter clock in RO excess-phase processing. For LEO satellites, however, such a convention does not exist, and the correction might be handled differently in POD processing. At WEGC, Bernese (v5.2) by default does not explicitly model this correction, whereas we had to modify NAPEOS to align the processing strategy between the two POD software packages. In practice, if the effect is not explicitly modeled, it is absorbed in the POD clock error estimate and $\delta t_{\mathrm{r,rel}}$ is set to 0. However, explicit modeling of the eccentricity correction of the LEO clock can reduce variability and therefore slightly enhance interpolation residuals.

In addition to the relativistic effects acting on the satellite clocks we model the far smaller gravitational time delay acting on the GNSS signals transmitted between the GNSS and LEO satellites as follows:

$$\delta\rho^\mathrm{t}_{\mathrm{r,rel}} = \frac{2GM_\mathrm{E}}{c^2}\ln\left(\frac{r^\mathrm{t}+r_\mathrm{r}+\rho^\mathrm{t}_\mathrm{r}}{r^\mathrm{t}+r_\mathrm{r}-\rho^\mathrm{t}_\mathrm{r}}\right), \tag{7}$$

where G is the gravitational constant, M_E is the mass of Earth, and r^t and r_r are the satellite and receiver radial position at signal transmission and reception times (Ashby, 2014; Mudrak et al., 2015). This effect is also referred to as the Shapiro time delay.

The GNSS and LEO orbits are provided with the satellite's mass center as a reference point and hence need to be corrected for the antenna offsets (from COM) in order to reflect the proper locations of the RO signal's transmission and reception. In general, those antenna offsets are composed by the geometric antenna reference point (ARP); the elec-

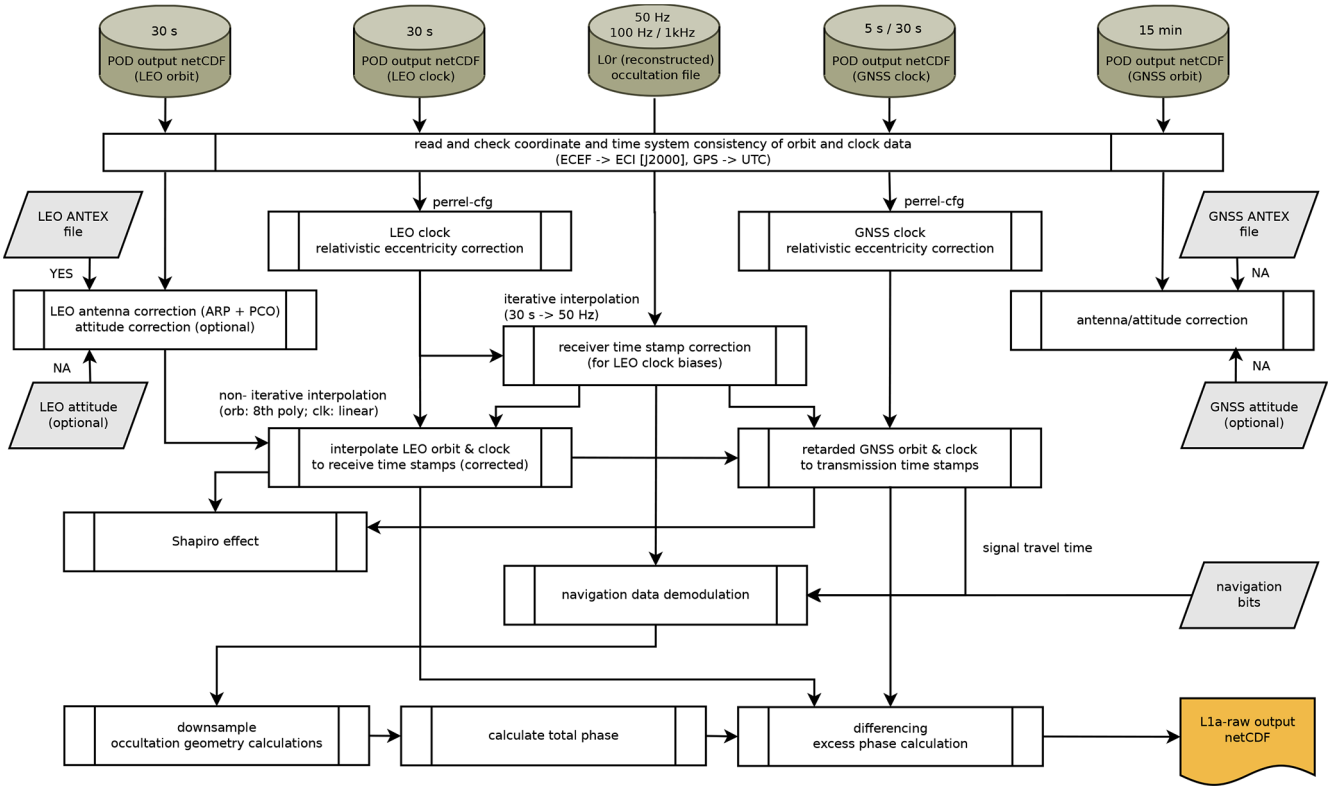


Figure 6. rOPS ODP L1a excess-phase processing algorithm workflow. For description and explanations, see the text. NA: not applied.

tromagnetic phase center offset (PCO) accounting for deviation from the geometric ARP; and, dependent on the signal's incoming direction, the phase center variation (PCV). As the PCV is a rather small effect, considering the short duration of an occultation event, it can be disregarded in RO processing (Hajj et al., 2002). The LEO RO antenna offsets (ARP and PCO) are applied using definitions provided in the so-called ANTEX format (cf. Sect. 2.1) and common coordinate transformation from the satellite body frame to ECI (EUMETSAT, 2005). Corrections for the changing orientation of the satellite in space and the deviation from nominal attitude during orbital revolution are not yet implemented in rOPS. However, although for missions with a stable orientation like Metop, this correction is small, it was found that not applying the correction introduces a small residual bias in bending-angle data (Alemany et al., 2022). Therefore, it is treated as a priority to include this correction in a future version of rOPS. On the GNSS transmitter side, neither GNSS antenna offsets nor their attitude is modeled, since they have a far smaller effect on RO processing than the LEO antenna offsets (Hunt et al., 2018).

After the correct handling of the relativistic eccentricity corrections and application of LEO antenna offsets, we can proceed and interpolate the LEO clock corrections, available at a low 30 s sampling rate, to the high-rate (50 Hz) RO measurement time stamps. This is done in an iterative procedure using a linear interpolation method until it converges at an empirically determined precision threshold. Once the corrected high-rate receive time is available, the LEO orbit and clock data from the POD-derived DSM-Geo orbit arcs are well interpolated to these time stamps, using an eighth-order polynomial Lagrange interpolation for satellite positions and velocities and a linear interpolation for its clock biases.

While the reception time of RO signals is recorded by the receiver and its biases are modeled and estimated, the signal transmission time of phase measurements needs to be reconstructed in order to allow for extraction of corresponding GNSS orbit and clock data. Assuming a straight-line propagation in a vacuum medium of the signal is considered sufficient to infer signal travel time τ, which elapsed during the signal's transmission at the GNSS satellite and the reception by RO receiver on the LEO satellite, with an iterative approach starting with $\tau_0 = 0$,

$$\tau^{\mathrm{t}}_{\mathrm{r},n} = \frac{\rho^{\mathrm{t}}_{\mathrm{r}}}{c} = \frac{|r_{\mathrm{r}}(t_{\mathrm{r}}) - r^{\mathrm{t}}(t_{\mathrm{r}} - \tau^{\mathrm{t}}_{\mathrm{r},n-1})|}{c}, \text{ if } \tau^{\mathrm{t}}_{\mathrm{r},n} - \tau^{\mathrm{t}}_{\mathrm{r},n-1} < \text{threshold then abort, } n \in \{0,1,2,...\}, \quad (8)$$

and therefore signal transmission time $t^{\mathrm{t}} = t_{\mathrm{r}} - \tau^{\mathrm{t}}_{\mathrm{r}}$. Within the signal travel time calculation routine, the GNSS orbit positions are also updated and interpolated to t^{t}. Once the iterative calculation of the signal transmission time converged, the GNSS velocity and clock data are interpolated the same

way as was performed for the LEO satellite. Note that the retrieved geometric distance ρ_r^t, required for the extraction of the RO excess phases, is a function of two time system variables t^t and t_r.

3.1.4 Measurement correction and preparation and differencing

At this point we have available all the correction terms necessary for the excess-phase calculation in Eq. (5): geometric distance between corrected GNSS and LEO satellites at signal receive time $\rho_r^t\ (t_r)$, interpolated clock bias estimates $\delta t^t\ (t^t)$ and $\delta t_r\ (t_r)$, corresponding relativistic eccentricity correction terms $\delta t_{r,rel}\ (t_r)$ and $\delta t_{rel}^t\ (t^t)$, and relativistic Shapiro effect $\delta t_{r,rel}^t\ (t_r)$. Effects not modeled, such as antenna phase wind-up (Bai et al., 2014, 2018), and residual errors are accounted for in error budget ϵ, which we will discuss in Sect. 3.2. However, depending on the RO receiver type, the raw measurements recorded in CL, OL, or RS tracking are also subject to corrections and preparatory steps before total phase $L_r^t\ (t_r)$ can be used in the calculation: the navigation data demodulation, downsampling to a nominal measurement frequency (i.e., 50 Hz) of higher-sampled tropospheric measurements (e.g., Metop GRAS 1 kHz RS), and assembling of the total phase.

GNSS signals are modulated with a binary $[0, \pi]$ navigation data message (NDM) providing useful information, such as ephemeris, clock, ionospheric, and service parameters, but at the same time introducing carrier phase flips to the signal. In CL tracking, these phase changes of π are corrected in real time at the RO receiver in orbit, whereas in lower-troposphere tracking (OL, RS) the NDM must be demodulated in postprocessing on the ground by either (Sokolovskiy et al., 2006) (1) the internal removal by detection of phase switches between adjacent samples or (2) the application of an externally provided NDM data stream (see Sect. 2.1; EUMETSAT, 2018). In general, as well as at WEGC, the latter strategy is preferred, in particular for climate application, because increasing disturbances in the lower troposphere can exceed the NDM-induced phase flips and introduce substantial retrieval errors if performing internal NDM removal (Sokolovskiy et al., 2009). Note that the previously calculated signal travel time τ is used to align the measurement data and the NDM bits at the signal transmission time, which are then used directly to revert the phase flips in the measured residual I/Q components.

Measurement data exceeding the 50 Hz sampling rate for RO CL measurements are downsampled to this nominal sampling frequency. Schreiner et al. (2011) investigated different downsampling target rates for Metop GRAS 1 kHz RS data and suggested using a sampling of 100 Hz for RO measurements in the lower troposphere, but also 50 Hz data lead to very similar results (Gorbunov et al., 2011). So far a sampling rate of 100 Hz has been realized for COSMIC-2 (Schreiner et al., 2020) and FengYun-3 (FY-3) GNOS (GNSS Occultation Sounder) (Bai et al., 2018). For GRAS RS data specifically, we calculate the arithmetic mean of 20 adjacent samples in order to obtain downsampled RO signal at 50 Hz. The SNR is then recalculated from the raw I/Q components with amplitude $A = \sqrt{I^2 + Q^2}$, while the NCO phase L_{nco} is interpolated linearly to 50 Hz.

With the corrected in-phase and quadrature I/Q signal components and the receiver model phase, the total measured phase can be constructed. First the ith sample of the residual phase in radians is calculated by $L_{rsd,i} = \mathrm{atan}_2(Q_i, I_i)$ for all four quadrants, before unwrapping the signal so that adjacent samples of the residual phase are always within $\pm\pi$:

$$L_{rsd,i} = L_{rsd,i} + 2k_i\pi \qquad \text{with} \quad k \in [-1, 0, 1], \tag{9}$$

where k_i is defined by minimization of $|L_{rsd,i} - L_{rsd,i-1}|$. Finally, the total phase is obtained by $L_i = L_{nco,i} + \lambda\frac{1}{2\pi}L_{rsd,i}$, where division by 2π converts the residual phase from radians to cycles and λ denotes the wavelength of the GNSS signal in question.

With all terms available, we now can calculate excess phase ΔL_r^t following Eq. (5), representing a zero-differencing approach. This means that no clock differencing method is applied and the receiver clock bias estimates are employed directly in the differencing equation. This is the preferred option, introducing the lowest amount of noise in the processing, but is only practical for RO missions with a sufficiently stable LEO clock (ultra-stable quartz oscillators; e.g., Metop; GRACE, Gravity Recovery and Climate Experiment; FengYun-3). For other missions with less stable LEO clocks (e.g., CHAMP, Challenging Minisatellite Payload; COSMIC), the receiver clocks biases are removed by introducing a reference clock from a non-occulting GNSS satellite link in a so-called single-differencing approach (Schreiner et al., 2010; Beyerle et al., 2005; Bai et al., 2018). This alternative differencing is not applied in this study.

3.2 Quality control and uncertainty estimation

Following the calculation of excess-phase profiles as a function of time – including SLTP altitudes as an initial vertical-level variable – by the ODP L1a *raw* processor, the quality and uncertainty in these profiles are assessed in the ODP L1a *quality* processing. ESM-Atm provides modeled excess phases for each measured RO event, which serve as an important input to ODP L1a quality (cf. Fig. 2). Following the sequence we implemented, we will first discuss the quality assessment of the excess-phase profiles, including possible rejection, before addressing the associated uncertainty estimation.

3.2.1 Quality control

The rOPS L1a quality control (QC) process flags or (optionally) excludes unphysical or low-quality excess-phase profiles from further processing in order to provide a standardized input for the uncertainty estimation and to ensure the highest quality in the subsequent retrieval steps towards thermodynamic variables. If an event is not entirely rejected, specific QC flags are set (and written to a separate monitoring file) for data which are not passing the various quality checks or for which certain parts of the measurement are truncated at basically reliable top and bottom altitude levels. Key variables of the QC system are the observed excess-phase profiles and the independent forward-modeled excess-phase profiles as well as their delta profiles with suitable low- and high-pass filtering applied.

Central to the quality checks performed is the evaluation of the observed excess-phase data against the independent forward-modeled data. Since the modeled excess-phase profiles are free from ionospheric influences, we derive the ionosphere-corrected excess-phase profile by the classical first-order linear combination of the observed dual-frequency GNSS excess phases, e.g., for GPS (Schreiner et al., 2011),

$$L_c = L_1 + \frac{f_2^2}{f_1^2 - f_2^2}(L_1 - L_2), \tag{10}$$

with f_1 and f_2 being the GPS carrier frequencies of the corresponding L_1 and L_2 excess-phase profiles. Figure 7 (left) illustrates such profiles.

The signal strength and thus the penetration depth in the troposphere differs among the different GNSS signals involved in Eq. (10). Hence, the derived L_c profile is restricted to the altitude range covered by the shorter of the two signals. To overcome this limitation we artificially extend the shorter signal using a linear extrapolation downwards to match the reach of the stronger signal. This is realized by determination of the linear gradient of the difference profile of both signals over a sufficiently long altitude range (10 km) above the end of the shorter weak signal, with the lowest-allowed altitude of 15 km, to avoid the usage of data with a low SNR. The extrapolated part is then obtained by subtraction from the leading signal to obtain the extended weaker signal. The extended ionosphere-corrected excess-phase profile L_c in this form serves just as an auxiliary variable for the L1a QC. The ionospheric correction as part of RO retrieval is performed in a more advanced manner at the ODP L1b bending-angle level, including also higher-order correction (Danzer et al., 2021; Liu et al., 2020).

Within rOPS and specifically also for the ODP L1a quality control, the analysis and processing on delta profiles play a central role. Following the so-called *baseband approach*, with the subtraction of background model profile L_m (ESM-Atm) from retrieved profile L (ODP L1a), biases from the (near) exponentially varying RO profiles can be removed. This also leads to very small residual numerical errors in operators such as filters and derivatives: $\delta L_{BB} = L - L_m$. Residual noise in the high-frequency domain of baseband excess phase δL_{BB} can be suppressed by a low-pass filter, leading to a delta phase profile without noise and smaller variations, which better displays the large-scale effects of the atmosphere. We use a Blackman windowed sinc (BWS; Smith, 1999) low-pass filter $\boldsymbol{F}^{BWS}$ with a cutoff frequency f_c at 0.5 Hz. With a sampling rate of $f_s = 50$ Hz the suitable window size is $2 \cdot f_s/f_c + 1 = 201$ data points, which corresponds to an effective filtering window size of 100 points or 2 s. For a more detailed description and discussion of advantages of a BWS filter over moving-average boxcar filters, see Schwarz et al. (2018, their Appendix 1.2). The low-pass-filtered baseband excess phase is then obtained as $\delta L_{LFBB} = \boldsymbol{F}^{BWS} \delta L_{BB}$. Subtraction of the low-pass-filtered baseband excess phase from the baseband excess phase leads to a high-pass-filtered baseband excess phase: $\delta L_{HFBB} = \delta L_{BB} - \delta L_{LFBB}$. This double-delta profile is virtually unbiased down to the lowest altitudes and contains almost only information about the noise level, which allows for inspection of the noise level, as well as of potential outliers, of the individual excess-phase profiles.

Based on these derived delta phase profiles (cf. Fig. 7), the quality check procedure is summarized in Table 4, providing a concise overview of the main quality checks performed. Note that parameters listed are tailored for Metop GRAS data and might require some modification for other RO missions.

The QC process starts from raw excess-phase data (raw signal) with some basic data preparation steps and initial checks for physical plausibility of the measurement. Initially, all the profiles are cropped to a minimum of $z_{SLTP}^{min} = -250$ km and a maximum of $z_{SLTP}^{max} = 90$ km altitude, respectively. Subsequently, the measurements, recorded at irregular measurement times, are interpolated to a strict equidistant time grid of 50 Hz based on the model grid. Additionally, the sampling rate consistency and drift are checked to be within the plausible maximum limits of 0.015 s and 10^{-5} s min^{-1}, respectively, over the entire cropped altitude range. The interpolated and cropped excess-phase profiles are written to the output used for further L1b processing; all subsequent steps solely serve the quality control and are stored as interim output.

For further processing, profiles which do not span over a minimum altitude range from $z_{SLTP}^{bot} = 23$ km to $z_{SLTP}^{top} = 70$ km are dismissed or optionally flagged. In a next step the entire profile is normalized to the median value of an SLTP altitude between 60 and 70 km. In order to eliminate obviously unphysical profile behaviors, delta profile δL_{BB} for any signal profile is not allowed to exceed 500 m (an empirically determined value for sorting out gross outliers) over the minimum SLTP altitude range defined above.

Highly important to the QC, as well as for safeguarding the further processing, is the outlier detection performed on baseband delta excess phase δL_{BB} for each signal pro-

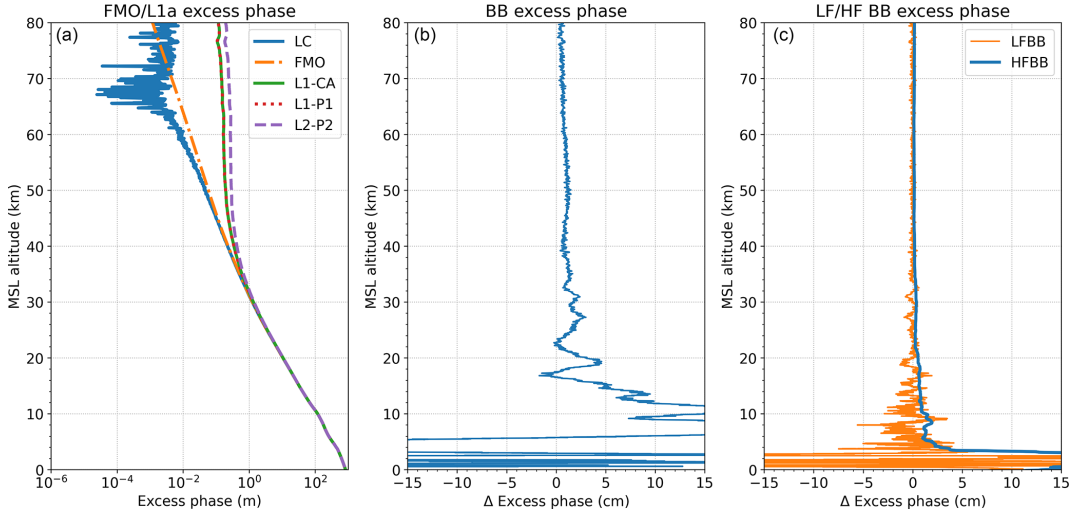


Figure 7. (a) Illustration of forward-modeled (FMO), observed coarse/acquisition code (L1–CA), precise codes (L1–P1 and L2–P2), and linearly ionosphere-corrected (LC) excess-phase profiles, all as a function of (forward-modeled) MSL altitude. Additionally shown are **(b)** the derived baseband (BB) delta excess phase and **(c)** the low-pass-filtered (LF) BB and high-pass-filtered (HF) BB delta excess-phase profiles. These different phase profile examples are shown for an exemplary setting RO event from Metop-A (1 July 2008, 00:01 UTC; lat −72.3°, long 37.6°).

Table 4. Overview of the rOPS L1a quality processing. All parameters apply to Metop GRAS data. Middle column separates the total data rejection rate f_{QC} of 4.17 % for all data (9 months) processed by WEGC for this study in rejection fractions for every single quality control step. n/a: not applicable.

Task	f_{QC}	Description
Background check	0.15 %	check if corresponding background file exists
Crop profiles	n/a	cut profiles at minimum z^{min}_{SLTP} (−250 km) and maximum z^{max}_{SLTP} (90 km) SLTP altitude
Equidistant grid	n/a	interpolate irregular measurement time stamps from L to the strict 50 Hz stamps from L_m
Sampling check	0 %	check consistency and rate drift of interpolated excess phase L
Altitude check	1.96 %	check coverage of minimum required height range of an SLTP altitude from 23 to 70 km
Normalization	n/a	basic normalization to median phase of an SLTP altitude of between 60 and 70 km
Raw phase check	0.28 %	check baseband delta excess phase δL_{BB} to be within ± 500 m
Outlier check	0 %	check outliers based on δL_{BB} using $\pm 5\sigma$ bounds
SD check	1.60 %	check standard deviation range of baseband excess phase $\delta L_{c,BB}$ (top) and $\delta L_{c,HFBB}$ (bottom)
Bounds check	0.18 %	check bounds of delta phase based on $\delta L_{c,HFBB}$
Smoothness check	0 %	check delta phase gradient based on $\delta L_{c,HFBB}$

file separately. This baseband delta excess phase allows for a very robust outlier check, since the forward-modeled excess phase is a noise-free reference, in order to focus on potential irregular spikes and patterns in the data themselves. The outlier detection criteria are based on a moving-median-referenced percentile-based detection calculation. The 16th and 84th percentile are used for an estimation of the standard deviation ($\pm\sigma$). A data point is considered an outlier if it is greater than the 5-fold value of this standard deviation around the median; if more than 3 % of outlier values are detected across the profile, the entire profile gets rejected.

Since values are not distributed symmetrically around the median, an adequate window size of $2 \times f_s + 1 = 101$ data points was found as a result of sensitivity tests that evaluated statistics and counted the number of profiles with at least one detected outlier, while employing different window sizes (Seidl, 2018). At this stage of the processing, outliers are only detected, while in the early part of the ODP L1b processing outliers are then (statistically) corrected, because further calculations including averages and standard deviations respond very sensitively to outliers. That correction replaces any detected outlier value by a statistically reasonable value randomly drawn from a normal distribution with standard deviation $\sigma = \frac{1}{2}(p_{84} - p_{16})$ within the interval $[-3\sigma, +3\sigma]$.

Next, inspection of the moving standard deviation of delta excess-phase profiles, using a window size of $2 \times f_s + 1 = 101$ data points to estimate it, helps to estimate reliable top and

bottom altitude levels, within which the quality of the excess-phase data is considered sufficiently reliable to retrieve sufficiently accurate variables in the subsequent geometric-optics bending-angle retrieval. For the determination of a reliable top altitude level in the mesosphere, we apply a moving standard deviation to baseband delta excess phase $\delta L_{\mathrm{c,BB}}$ and check where a threshold of 3 cm (an empirically determined reasonable value) is exceeded for the first time when searching upwards.

For determination of the bottom altitude level, the standard deviation of high-pass-filtered baseband delta excess phase δL_{HFBB} of L_1, L_2, and L_c profiles are checked, now searching downwards, for the maximum of either a fixed value (3 cm) or a relative value (0.1 %), the latter relative to forward-modeled excess phase L_m. If the moving standard deviation thresholds are found to be exceeded already within the minimum-required altitude region from $z^{\mathrm{bot}}_{\mathrm{SLTP}}$ to $z^{\mathrm{top}}_{\mathrm{SLTP}}$, then the respected profile (and whole RO event) is either discarded or flagged. The top and bottom altitude levels determined are stored for later use, such as for optionally cutting the profiles to their best-quality range before further retrieval steps.

A final pair of fundamental QC checks for the physical plausibility of a processed excess-phase profile is done by checking the bounds and smoothness of delta excess-phase profiles of L_c. The bounds are checked on baseband delta excess phase $\delta L_{\mathrm{c,BB}}$ with defined limits derived from sensitivity studies and using general physical knowledge for expected magnitudes in different atmospheric altitude regions. Specifically, every data point of $\delta L_{\mathrm{c,BB}}$ is checked to be within a threshold of 15 cm in the mesosphere from 50 km upwards and the maximum $\max[30\,\mathrm{cm}, 0.01 \cdot L_\mathrm{m}]$ for altitudes from 30 km downwards, respectively. For altitudes in between (upper stratosphere), the bound is defined by linearly increasing between the lower-stratospheric and mesospheric bounds, i.e., from 30 to 15 cm (Seidl, 2018).

The smoothness check is based on a five-point derivative of high-pass-filtered baseband delta excess phase $\delta L_{\mathrm{c,HFBB}}$, yielding a delta phase derivative profile used for detection of rapidly fluctuating noise or spikes with unphysical magnitude. The smoothness bound is set such that no point in the derivative profile shall exceed $7.5\,\mathrm{m\,s^{-1}}$. Additionally, it is cross-checked to fall within a relative limit of 75 % of the five-point derivative of L_m. Profiles failing the bounds check and/or smoothness check within the minimum-required altitude range are discarded.

3.2.2 Characterization of excess-phase uncertainty

Following the QC of the RO events initially processed by the ODP L1a processor (raw), the uncertainty in the excess-phase profiles found to be of adequate quality (i.e., passing the QC) is characterized and empirically estimated as the next step of the processing. This new approach to assess the uncertainty in each individual RO event is conducted following the Guide to the Expression of Uncertainty in Measurement (GUM; JCGM2008, JCGM2012) and its proposed handling and terminology of uncertainties. Overall the GUM is considered the standard guideline for the uncertainty estimation and propagation in rOPS, as already realized in parts of the retrieval (Innerkofler et al., 2020; Schwarz et al., 2017, 2018; Schwarz, 2018; Li et al., 2019).

As summarized by Schwarz et al. (2018) we categorize uncertainties into estimated random uncertainties and estimated systematic uncertainties, the latter with differentiation between basic and apparent systematic uncertainties. Effects included in the estimated random-uncertainty budget are of unpredictable or stochastic temporal and spatial variability in repeated observations. These effects are essentially stationary in a statistical sense so that we can estimate their statistics also from individual RO event data, given the high noise-resolving sampling rate along the vertical profile.

Systematic effects (biases), which can not be quantified using statistical data analysis based on just one individual RO profile, are estimated and corrected for if known, as recommended by the GUM. The remaining residual biases are assumed to stay within a (conservative) bound estimate, which we refer to as estimated systematic uncertainty. Depending on their nature, we distinguish two types: (1) estimated basic systematic uncertainties which appear and will remain systematic despite averaging over individual RO events and (2) estimated apparent systematic uncertainties which will essentially behave as random uncertainties in ensemble averaging over many RO events. It is important to distinguish these two subtypes, since the former will not average out and therefore fundamentally limit the (absolute) accuracy of ensemble averages such as climatologies.

With respect to the phase observations (Eq. 4) a total uncertainty budget for the GNSS excess-phase measurements can be approached as

$$u_{\mathrm{tot}} = \sqrt{u^2_{\mathrm{atm}} + u^2_{\mathrm{ion}} + u^2_{\mathrm{r,clk}} + u^2_{\mathrm{t,clk}} + u^2_{\mathrm{vel}} + u^2_{\mathrm{therm}} + u^2_{\mathrm{mult}} + u^2_{\mathrm{cycle}} + u^2_{\mathrm{phase}}}, \quad (11)$$

where u_{tot} denotes the total uncertainty assigned to the excess-phase profile, u_{atm} denotes the uncertainty inferred from the neutral atmosphere influences, u_{ion} denotes the uncertainty inferred from the ionospheric influences, $u_{\mathrm{r,clk}}$ denotes the receiver clock uncertainty, $u_{\mathrm{t,clk}}$ denotes the transmitter clock uncertainty, u_{vel} denotes the velocity drift uncertainty, u_{therm} denotes the thermal noise, u_{mult} denotes uncertainty due to local spacecraft multipath, u_{cycle} denotes the cycle slip uncertainty, and u_{phase} denotes the phase noise comprising residual error influences.

Remaining error sources, such as phase wind-up and tide and ocean loading effects, which are not considered in Eq. (11), are expected to be below the order of 10^{-6} in relative errors and are therefore disregarded in the uncertainty budget. Not yet taken into account is the spacecraft's attitude uncertainty which will be addressed in more detail once

the attitude correction in rOPS is included and verified. For larger spacecrafts like the Metop satellites this effect caused by attitude jitter is expected to be small, however. Also interpolation and the smoothing of data introduce errors in the calculations, e.g., by disregarding terms of a higher order in an approximation or through the imperfect representation of numerical values. Within the excess-phase processing these errors are mostly attributable to the interpolation of the receiver and transmitter orbits and clocks. The magnitude of these errors was empirically determined and found to be smaller than the order of 10^{-5} in relative errors and hence is also considered negligible compared to the other components in the error budget.

The uncertainties in the transmitter and receiver clocks are modeled based on their 1 s Allan deviation, using typical values for atomic clocks and quartz clocks of GNSS and LEO satellites, respectively (cf. Sect. 3.1.3). The relative frequency error for white frequency noise averaged over the sampling time is simply simulated as a random number between -1 and 1 (Harting, 1996). To achieve the correct 1 s Allan deviation of the final calculated clock noise, the 1 s Allan deviation has to be corrected for the used sampling rate. The relative frequency error for the sampling period therefore becomes

$$y_n = \sqrt{6}\, A_{1\mathrm{sec}}\, \mathrm{rand}_n\, \frac{c}{\sqrt{\tau_\mathrm{s}}}, \tag{12}$$

where y_n is the relative frequency error averaged over the sampling period τ_s, $A_{1\mathrm{sec}}$ is the 1 s Allan deviation, rand_n is the random number between -1 and 1, and c is the speed of light in a vacuum. For spaceborne single differencing, a flicker frequency noise is added to the clock uncertainty.

Thermal noise denotes the errors due to the random movements of electrons in the electronic components of a GNSS receiver. For carrier phase signals of nominal strength, the thermal noise in the carrier-tracking phase-locked loop (PLL) of a GNSS receiver can be modeled as

$$\sigma_\mathrm{PLL} = \frac{\lambda}{2\pi}\sqrt{\frac{B_\mathrm{L}}{C/N_0}}, \tag{13}$$

where B_L is the carrier loop noise bandwidth, C/N_0 is the carrier-to-noise power density ratio, and λ is the carrier phase wavelength. In a realistic approximation, with $C/N_0 = 45\,\mathrm{dB\,Hz}$ and $B_\mathrm{L} = 2\,\mathrm{Hz}$, the thermal noise for the GPS L1 signal is 0.2 mm (Langley, 1997). Accounting for the weaker GNSS signals and non-optimal conditions in the lower atmosphere, where open-loop tracking is also used, we safely assume a conservative bound for the influence of the thermal noise on phase measurements of 1 mm for all measured GNSS signals.

The random velocity error, estimated along with the POD processing (Sect. 2.2.1), also contributes to the total uncertainty budget. It introduces a linear drift to the measurement and is therefore categorized as estimated apparent systematic uncertainty. Assuming a random velocity uncertainty in $v^\mathrm{r}_{u_r} = 0.02\,\mathrm{mm\,s^{-1}}$ of the receiver satellite orbit,

$$u_\mathrm{vel} = v^\mathrm{r}_{u_r} \cdot \left(|t_\mathrm{top} - t_\mathrm{bot}|\right), \tag{14}$$

where the total uncertainty introduced by the velocity drift uncertainty u_vel would account for 1.2 mm after a typical RO event duration of 60 s from the time of the highest altitude t_top to the lowest altitude t_bot.

As stated in Sect. 3.1.1, phase ambiguities do not pose a problem in the excess-phase processing since constant terms can be eliminated from the observation equation. However, an undetected cycle slip can introduce a phase shift of half or full carrier wave cycles on the order of several centimeters, depending on the wavelength of the GNSS frequency. With decreasing altitude the ratio between the absolute value of the excess phase and the magnitude of possible cycle slips increases, and additionally propagation media effects in the troposphere require a DLL measurement mode, which makes cycle slips occur more frequently and leaves them undetected. Therefore, to account for these undetected cycle slips as an estimated basic uncertainty, we include change-rate factor $c = 1\,\mathrm{mm\,s^{-1}}$, reflecting a 1 % slip fraction per second relative to the half-cycle length. This leads to a gradual excess-phase decrease (cumulative negative bias) with decreasing altitude from the time of highest altitude $t^\mathrm{DLL}_\mathrm{top}$ to lowest altitude $t^\mathrm{DLL}_\mathrm{bot}$ in the DLL measurement mode:

$$u_\mathrm{cycle} = c \cdot \left(|t^\mathrm{DLL}_\mathrm{top} - t^\mathrm{DLL}_\mathrm{bot}|\right). \tag{15}$$

A local spacecraft multipath occurs when the incoming signals at the receiver satellite are reflected and scattered before reaching the vicinity of the GNSS antenna, and thus signals with different paths are detected simultaneously at the receiver. The effect depends on the spacecraft geometry, the occultation viewing geometry, and the electrical properties in the vicinity of the receiver antenna (Kursinski et al., 1997). The possible phase shifts of up to a few centimeters, introduced by the local spacecraft multipath, can be reduced by proper platform design and the use of directional antennas. Additionally, local multipath effects can be reduced by dismissing incoming left-hand polarized signals, since the right-hand circular-polarized GNSS signals are left-hand polarized after reflection at the surface of the LEO. The residual local multipath error effects on the phase measurements are modeled using a sinusoidal model, for representative broad beam antennas used in GNSS RO (Steiner and Kirchengast, 2005; Ramsauer and Kirchengast, 2001; Syndergaard, 1999). The sinusoidally shaped function is defined with a multipath phase error amplitude of 0.5 mm and period set to 60 s, resulting in multipath errors up to 1 mm, following GRAS-type error specifications (Carrascosa-Sanz et al., 2003). We classify this effect as apparent systematic uncertainty, since with a changing viewing geometry from occultation to occultation, the local spacecraft multipath errors will average down when regional and temporal averages are calculated (Kursinski et al., 1997).

The influence of the propagation media (neutral atmosphere and ionosphere) itself cannot be quantified directly because ionospheric scintillations and atmospheric turbulence lead to variations in the properties of the atmosphere which can be hardly captured by models. However, if we assume that the defined uncertainty budget in Eq. (11) includes all possible major error sources, the uncertainty arising from the neutral atmosphere and ionosphere can be inferred from an empirical estimate of the total random uncertainty and subtraction of the terms categorized as contributors to the random uncertainty:

$$u^2_{\mathrm{atm+ion}} = u^2_{\mathrm{atm}} + u^2_{\mathrm{ion}} = u^2_{\mathrm{emp}} - u^2_{\mathrm{r,\,clk}} - u^2_{\mathrm{t,\,clk}} - u^2_{\mathrm{thermal}}. \quad (16)$$

The empirical uncertainty estimate is determined based on the double-delta excess-phase profiles δL_{HFBB} smoothed with a moving standard deviation with a window size of $2 \cdot f_{\mathrm{s}} + 1 = 101$, like we already used in in the QC processing (Sect. 3.2.1).

As the final output, the combined estimated random, basic systematic, and apparent systematic uncertainties are appended to the L1a output, while the individual uncertainty estimates are stored in a "monitoring file" together with the QC output. Figure 8 illustrates the daily component-wise and combined uncertainty estimates. The overall estimated excess-phase uncertainties then serve as input to the subsequent uncertainty propagation in the ODP L1b bending-angle retrieval (Schwarz et al., 2018). An evaluation of the uncertainty estimation can be found in the results in Sect. 4.3.

4 Results and discussion

In this section we evaluate a set of three 3-monthly periods of RO data at the excess-phase level, the summers of 2008 and 2013 (both July–August–September, JAS) and the winter of 2019/20 (December–January–February, DJF), for the Metop-A/B/C RO data as available given their launch times. Starting with a sensitivity analysis of the excess phases computed by rOPS, we analyzed how the measured profiles compare against forward-modeled profiles, how a different orbit solution input influences the L1a excess-phase processing, and how the evaluated differences in collocated profiles agree between the three Metop missions and their GRAS receivers.

Subsequently, we present a statistical ensemble evaluation of WEGC's rOPS data in comparison to the excess-phase data processed and provided by EUMETSAT and UCAR. The last subsection discusses results related to uncertainty estimation of the excess-phase profiles processed at WEGC.

The number of profiles for each study period per Metop satellite is depicted in Fig. 9. All data are available in the rOPS-L1a file format, where the external excess-phase data from EUMETSAT and UCAR underwent a basic conversion routine. Overall, on average, the daily number of profiles amounts to 647 profiles (Metop-A), 610 profiles (Metop-B), and 559 profiles (Metop-C). For the later 2020 JAS period EUMETSAT input data contain files with a missing closed loop (either L2 or both frequencies), which reduces the number of processed events in this later study period, with reduced numbers in the later periods. In the following evaluation, differences between observations of rising or setting RO events or differences from geographic regions (zonal bands) are discussed whenever worthwhile to take into account.

4.1 Sensitivity analysis

In order to evaluate the quality of processed excess phases and their sensitivity to certain effects we considered their difference to selected reanalysis data, their sensitivity to different orbit inputs and different measurement geometries, and their dependency on the specific Metop satellite. For a comprehensive and very comparative analysis we focused on three vertical atmospheric regions and their layer averages (calculated from the vertical statistical measures, i.e., mean, median, SD, and percentiles, by obtaining the average over all values within the corresponding altitude layer):

- *Middle troposphere (3–7 km)*. This atmospheric region in the lowermost section of the atmosphere was selected for representation of the (moist) middle to lower troposphere. With the restriction of being above 3 km, the boundary layer and its special behavior that requires separate study (e.g., Gorbunov et al., 2021; Gorbunov and Kirchengast, 2018; Zeng et al., 2016) were disregarded.

- *Lower stratosphere (20–25 km)*. This region represents the lower-stratosphere region of RO soundings, with narrow uncertainty and minimal influence of background data or of any tropospheric or tropopause effects in the retrieval.

- *Lower mesosphere (50–60 km)*. This region represents the lower mesosphere with small absolute excess phases only on the order of 10 cm left but still without major ionospheric influences that start higher. The layer thickness of this region is increased compared to the tropospheric and stratospheric layers for increasing averaging in view of the less dense atmosphere at these higher altitudes.

4.1.1 Atmospheric-background modeled profiles: $O - B$

The observed RO data, processed to the excess-phase level by WEGC's rOPS, are compared to forward-modeled excess-phase background profiles from ECMWF ERA5 reanalyses (Sect. 2.2.3) in an observation minus background ($O - B$) comparison. Since per construction there is a corresponding reference profile extracted from the highly resolved ECMWF data for each observed RO event, the number of profile pairs is high.

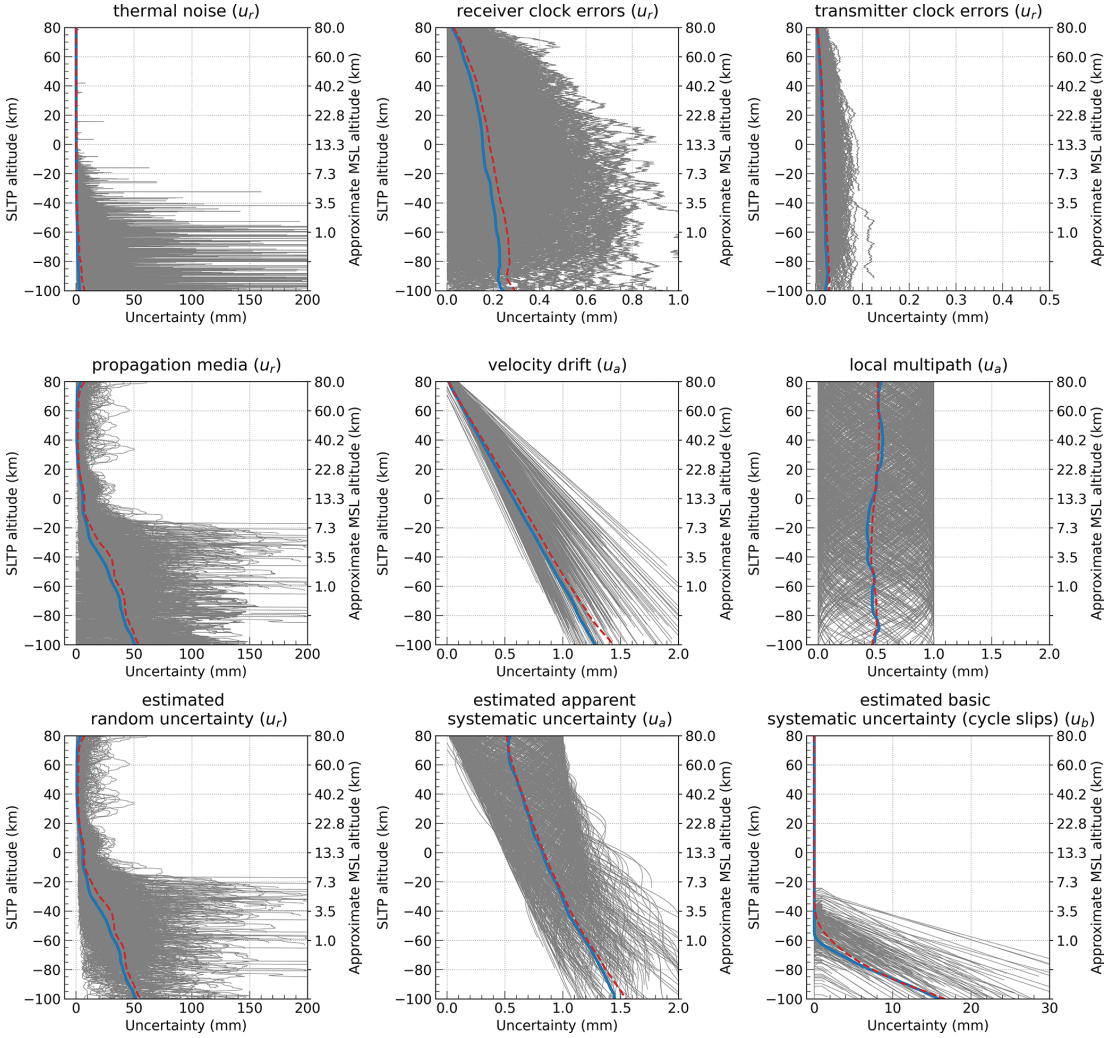


Figure 8. Overview of exemplary estimated random u_r, basic systematic u_b, and apparent systematic u_a uncertainty components, respectively, from rOPS ODP L1a processing for Metop-A on 1 July 2008. For each component, individual estimates for each of the 781 events (thin grey profiles) are shown together with the daily median (highlighted thick blue) and mean (highlighted dashed red) uncertainty profile.

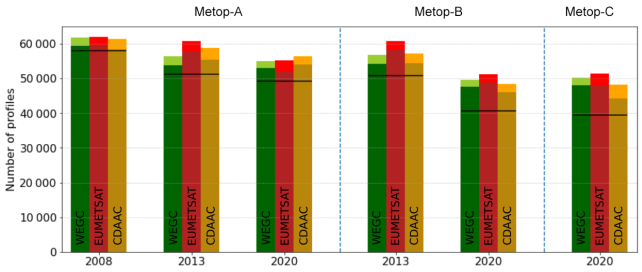


Figure 9. Number of RO events per time period (2008-JAS, 2013-JAS, 2020-DJF) processed at WEGC (green) and converted from EUMETSAT (red) and CDAAC (orange) to the rOPS format. Darker shaded area of the bars indicates profiles which successfully passed quality control. The black line indicates the number of profiles matched by the event identifier and common to all three processing centers.

Statistical evaluation of WEGC processing against the forward-modeled atmospheric-background profiles is shown in Fig. 10. In general the median of the intercomparison is seen at the millimeter level for all atmospheric regions and Metop satellites considered. The spread of the data increases due to higher variability and model imperfections at lower altitudes in the troposphere, where also a portion of skewed data can be seen. Differences between rising and setting RO events and differences in geographic distribution (not shown) are found to be very small with median differences of a few millimeters.

4.1.2 Orbit sensitivity

Various studies have documented that the accuracy of the orbit and, in particular, the velocities and estimated clock biases, co-determine the quality of the derived excess-phase

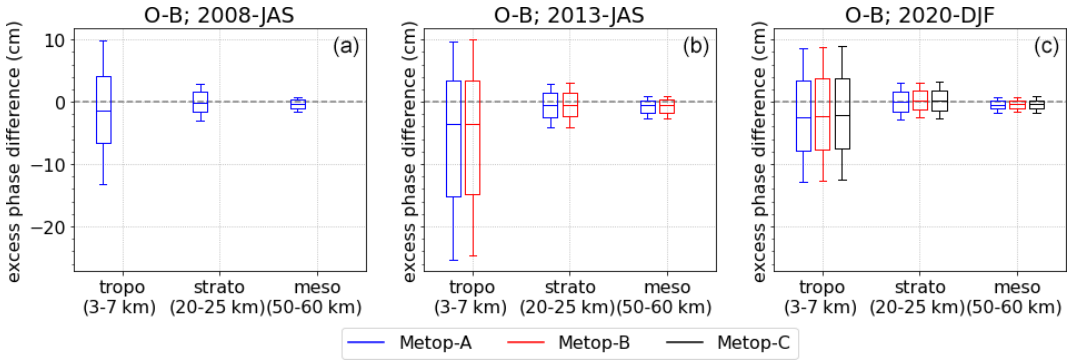


Figure 10. Sensitivity analysis results from comparing WEGC rOPS L1a excess-phase profiles from Metop-A (blue), Metop-B (red), and Metop-C (black) against collocated forward-modeled profiles from ERA5, for the three 3-month periods (2008, 2013, 2020; **a** to **c**) and three representative altitude layers (**a** to **c** within each panel), with the box and whiskers depicting the median (mid-line), 16 %–84 % range (box), and 5 %–95 % range (whiskers).

profiles (e.g., Kursinski et al., 1997; Montenbruck et al., 2008). For this reason, WEGC implemented a novel system routinely evaluating the quality of the calculated orbits which was introduced by Innerkofler et al. (2020). In this study we conducted the WEGC L1a excess-phase processing based on three different orbit solutions, from WEGC, EUMETSAT, and UCAR, respectively.

The comparison results of these independently computed orbit solutions are summarized in Table 5. These results focus on 2013-JAS and 2020-DJF, since data from 2008 were not available from EUMETSAT for this study part. In order to ensure a stable orbit geometry and excess-phase comparison, one generally aims for a daily 3D rms (root mean square) threshold of 5 cm in position and 0.05 mm s^{-1} in velocity (Innerkofler et al., 2020). This is generally satisfied for the WEGC orbit solutions in comparison to EUMETSAT, whereas UCAR exhibits slightly higher deviations as part of this intercomparison.

Comparison results of rOPS-processed excess phases based on WEGC–Bernese and orbit processing against using EUMETSAT POD exhibit a similar agreement across all vertical layers, time periods, and satellites. As depicted in Fig. 11, the median of the comparison experiences a slight positive bias and is enclosed by a stable percentile envelope, which is only slowly increasing when moving towards lower-atmospheric regions. Overall, the 5th–95th percentile range stays below about 1 cm. Setting events show a tendency, at the millimeter level, towards smaller averages and rising events towards larger averages, compared to the total median statistic.

4.1.3 Sensitivity of sensors

In order to investigate the influence and difference between the very similar receivers and satellite platforms, profiles of the three Metop satellites were co-located and binned together, before these differences were also calculated for statistical inspection. Though the satellites are essentially identical in construction, different firmware, a shift in orbital planes, different satellite lifetimes, and the degradation of instruments and hardware may influence the differences between profiles of different satellites.

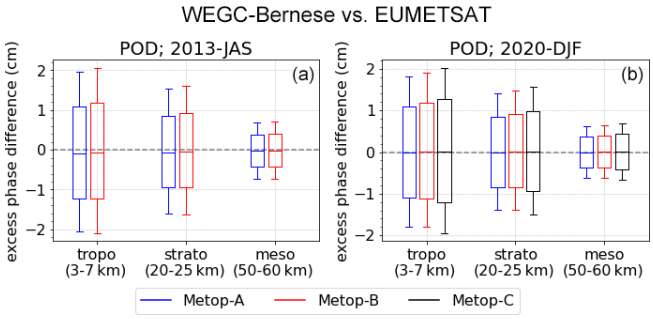


Figure 11. Sensitivity analysis results from comparing WEGC rOPS L1a excess-phase profiles from Metop-A (blue), Metop-B (red), and Metop-C (black) based on WEGC–Bernese orbits minus excess-phase profiles based on EUMETSAT POD solutions, for the two 3-month periods (2013, 2020; **a** to **b**) and three representative altitude layers (**a** to **b** within each panel), with the box and whiskers depicting the median (mid-line), 16 %–84 % range (box), and 5 %–95 % range (whiskers).

For the evaluation of platform-dependent differences the collocation algorithm was restricted to match profiles within 2 h in time and 200 km in space. In addition to this, we limited the analysis to the period where at least the first two satellites launched, Metop-A and Metop-B, were already in space. This results in an adequate number of co-located profiles for robust statistics: 2708 (2013-JAS) and 1641 (2020-DJF) for Metop-B vs. Metop-A and 1797 (2020-DJF) for Metop-C vs. Metop-A.

Figure 12 shows that the resulting differences are generally larger compared to strictly collocated profile-to-profile comparisons, particularly in the troposphere, where the

Table 5. Metop orbit intercomparisons for position and velocity in terms of 3D rms for different orbit solutions for the 2013-JAS and 2020-DJF periods, compared to the EUMETSAT–NAPEOS POD solution used as a reference. Days flagged to exceed 20 cm in 3D rms (about 3 d per satellite and 3-month period) have been excluded from the statistics.

	2013-JAS		2020-DJF	
ID	Position (cm)	Velocity (mm s^{-1})	Position (cm)	Velocity (mm s^{-1})
Metop-A vs. EUMETSAT–NAPEOS				
WEGC–Bernese	3.86 ± 0.37	0.036 ± 0.004	5.22 ± 1.84	0.049 ± 0.021
WEGC–NAPEOS	4.22 ± 0.49	0.031 ± 0.005	4.55 ± 1.62	0.039 ± 0.016
UCAR–Bernese	5.80 ± 0.47	0.067 ± 0.004	8.31 ± 2.18	0.088 ± 0.021
Metop-B vs. EUMETSAT–NAPEOS				
WEGC–Bernese	3.67 ± 0.26	0.040 ± 0.004	5.19 ± 1.74	0.053 ± 0.015
WEGC–NAPEOS	3.95 ± 0.52	0.032 ± 0.006	4.93 ± 1.58	0.044 ± 0.016
UCAR–Bernese	5.57 ± 0.55	0.062 ± 0.005	9.81 ± 2.02	0.108 ± 0.022
Metop-C vs. EUMETSAT–NAPEOS				
WEGC–Bernese	–	–	5.12 ± 1.17	0.089 ± 0.026
WEGC–NAPEOS	–	–	4.46 ± 0.91	0.048 ± 0.011
UCAR–Bernese	–	–	8.78 ± 3.20	0.038 ± 0.011

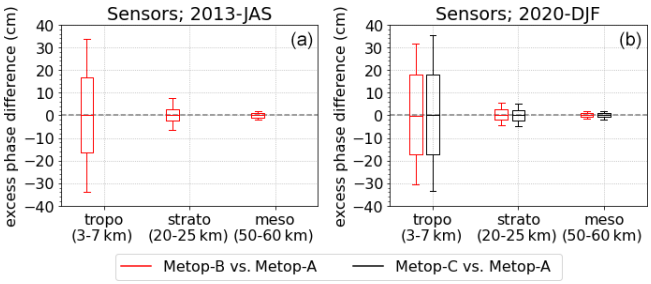


Figure 12. Sensitivity analysis results from comparing co-located WEGC rOPS L1a excess-phase profiles from Metop-B (red) and Metop-C (black) against Metop-A, selected as a representative reference, for two 3-month periods (2013, 2020: **a** to **b**) and three representative altitude layers (**a** to **b** within each panel), with the box and whiskers depicting the median (mid-line), 16 %–84 % range (box) and 5 %–95 % range (whiskers).

space–time mislocation of the RO event locations grossly dominate the (quasi-random) differences. However, the results exhibit a stable median, which is well centered at 0 (centimeter-level consistency) for all altitude layers. Only for Metop-C in winter 2020 is a small positive deviation from 0 visible for the tropospheric layer, which is due to the high overall variability that cannot be interpreted in more detail based on these statistics.

4.2 Statistical analysis

In order to evaluate the performance and ensure the highest-quality profiles by the new rOPS L1a processing, the excess-phase profiles calculated at WEGC were also evaluated against profiles from EUMETSAT (von Engeln et al., 2009) and UCAR CDAAC (Schreiner et al., 2011), the latter serving as an additional independent data source. Prior to comparison and the calculation of profile differences, the external L1a profiles from EUMETSAT and UCAR were converted to the rOPS-L1a format, including the calculation of a consistent and unambiguous event information identifier and some format alignments of the datasets (Sect. 2.2). This enables reliably matching the RO events from the three different processing centers.

For a thorough analysis we separated the profiles into a combined mesospheric and stratospheric section, using MSL altitude (mapped using the corresponding forward-modeled profiles) as a vertical coordinate from 10 to 80 km. In this range, absolute phase and differences are comparatively small. Second, a tropospheric region using SLTP altitudes from 0 to −100 km was defined, wherein loss of lock of the tracking usually occurs and where open-loop tracking introduces larger differences. Considering a standard-atmosphere model, this approximately equals an MSL altitude from about 13 km down to the last few hundred meters above Earth's surface within the boundary layer.

Although several profiles reach down to an SLTP altitude of −250 km, the number of profiles significantly decreases below an SLTP altitude of about −100 km, which is why we focused the tropospheric statistics down to this level. Furthermore, strong refraction, possibly super-refraction, and other disturbances complicate an overall statistical comparison at the very low-altitude levels below an SLTP altitude of −100 km.

Figure 13 shows the number of available matched profiles from WEGC and CDAAC vs. EUMETSAT for 2008-JAS, 2013-JAS, and 2020-DJF, for all RO events from

Metop-A/B/C and additionally separated for rising and setting events. In comparison, generally the number of profile differences from setting events, compared to rising events, is higher for all time periods and also shows an overall deeper penetration.

The inter-center comparison results at the excess-phase level between WEGC and UCAR against EUMETSAT (the latter used as a reference) are shown in Fig. 14 for the stratosphere-/mesosphere-focused region and in Fig. 15 for the troposphere-focused region, respectively.

A closer look at these 3-monthly excess-phase difference statistics as a function of MSL altitude (see Fig. 14) shows good agreement and robust difference statistics. The systematic difference between WEGC and EUMETSAT shows a virtually bias-free consistency (differences within 1 mm), apart from the 2013 period, where a salient kink can be observed at an MSL altitude of around 11 km. More detailed investigation showed that this behavior occurs for all time periods considered, although the altitude at which it can be observed is slightly below an MSL altitude of 10 km for the other time periods and hence outside the focus region shown in Fig. 14.

This characteristic can be attributed to a weakness in the transition from closed-loop to open-loop data for rising events in the WEGC processing, a matter which is currently under refinement. Systematic differences between UCAR and EUMETSAT show a positive bias, up to 2 to 3 mm, around the tropopause, which is most pronounced for setting events. Interestingly, in 2020-DJF the biases for rising events prevail. With increasing excess-phase magnitude, with decreasing height, the standard deviation of the comparison of WEGC with EUMETSAT also gradually increases, from 80 km down to 10 km in a linear and fairly symmetrical manner. The standard deviation of the differences corresponds to an envelope of about ± 6 and ± 8 mm (somewhat increased in 2020), demonstrating millimeter-level consistency of the random deviations. With UCAR as the candidate dataset, slightly increased standard deviations on the order of 1 cm can be observed near an altitude of 10 km.

The statistical intercomparison in the troposphere, depicted in Fig. 15, shows a good agreement between WEGC and EUMETSAT excess-phase profiles, with an almost bias-free comparison down to about an SLTP altitude of -80 km and a slightly increased systematic difference below. Separate investigation of rising and setting events reveals increased systematic differences starting already at about -50 km for rising events. However, the contribution to the overall statistics is limited because of the lower number of rising profile differences in that altitude region (cf. Fig. 13).

For the intercomparison statistics of UCAR against EUMETSAT, increased systematic differences are found starting at about -40 km in 2013-JAS and 2020-DJF, a characteristic only found below about -80 km in 2008. The biases observed are similar for all Metop satellites and most pronounced for setting events in 2020-DJF. At about -100 km, their magnitude is on the order of about 4 times the signal's wavelength, while rising events feature smaller but positive biases.

Although these characteristics arise in the (deep) boundary layer, where proper signal tracking is challenging, the salient deviations between UCAR excess phases and EUMETSAT and WEGC processing results point to remaining issues in the different processing approaches. However, such further investigation is beyond the scope of this study and will be addressed in follow-on intercomparison work.

The standard deviation of the comparison statistics shows an increase in the spread of the data with the onset at an SLTP altitude of about -20 km for the comparisons from WEGC and UCAR against EUMETSAT, along with a decreasing number of difference-pair profiles. For setting events considered separately, however, the standard deviation for WEGC against EUMETSAT is narrower and starts to increase from an SLTP altitude of -50 km downwards. In general, the standard deviation amounts to about ± 80 cm in most cases at an SLTP altitude of -100 km, with increased values for UCAR compared to WEGC as a candidate dataset in the lowest hundreds of meters of the boundary layer close to Earth's surface.

4.3 Uncertainty analysis

As described in Sect. 3.2.2, the empirical uncertainty estimation at the excess-phase level delivers estimated random uncertainty and, separately, estimated basic and apparent systematic uncertainties for each individual RO event. Related to this Fig. 16 provides, as a synthesis result, a concise overview of daily mean estimates of these uncertainties, for a representative example day of each of the three 3-month periods investigated.

In the mesosphere and upper stratosphere, the estimated random- and systematic-uncertainty components are small at the millimeter level, while towards lower altitudes, where the absolute excess phase increases rapidly, the estimated random-uncertainty component amounts to several centimeters (which is still very small at levels below 0.02 % in relative terms in the troposphere, though). The estimated systematic-uncertainty component is seen to be very small at the millimeter level and increases with decreasing altitude to reach about 2 cm in the deep troposphere.

Overall, the daily averages of the uncertainty estimates as depicted in Fig. 16 show similar characteristics for all three time periods and for all the three different Metop satellites. However, between an SLTP altitude of -20 and -40 km, the two later periods exhibit a slight kink in the estimated random uncertainty compared to the 2008 period. This is presumably connected to the different structure of the corresponding numbers of profiles as a function of altitude shown in the lower panel of Fig. 13 and changes in the receiver tracking.

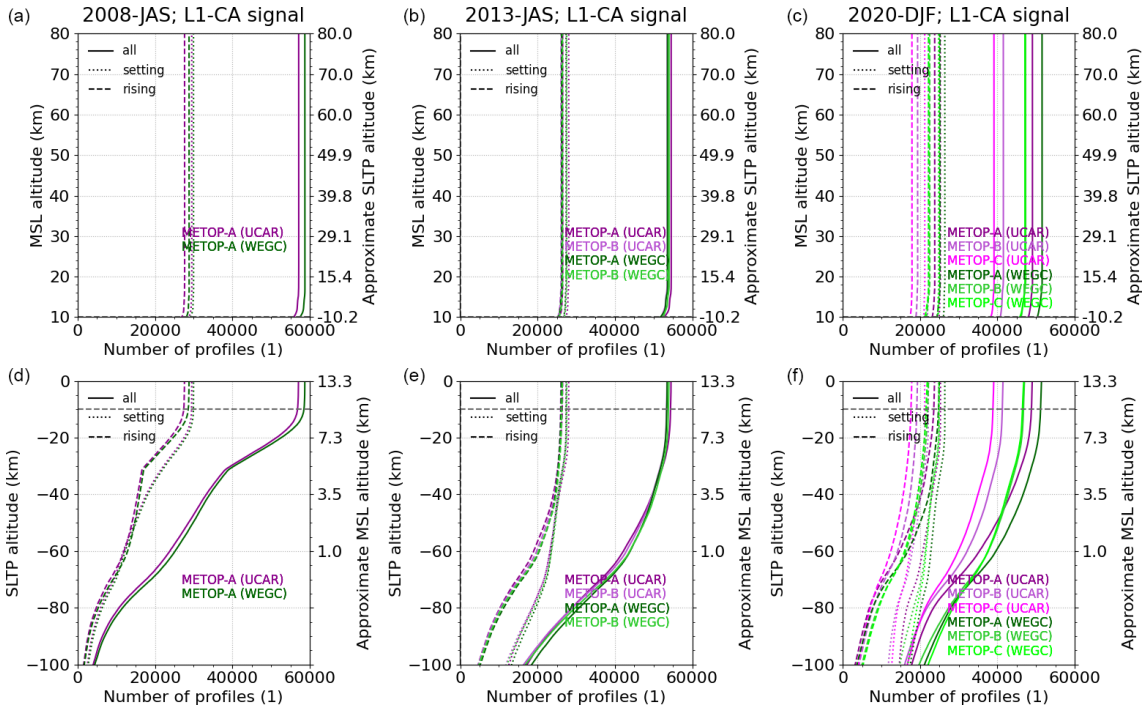


Figure 13. Number of excess-phase difference-pair profiles used for the ensemble statistics for WEGC vs. EUMETSAT (green) and WEGC vs. UCAR (purple), with a focus on **(a–c)** the stratosphere and mesosphere region and **(d–f)** the troposphere region. Difference-pair profile numbers are shown for L1–CA excess-phase profiles, featuring the deepest penetration and being most relevant for the subsequent L1b retrieval.

5 Summary and conclusions

The derivation of climate benchmark data from RO measurements requires a rigorous processing from the raw GNSS signal occultation measurements (including their georeferencing in space–time) to essential climate variables (ECVs), such as temperature, with narrow uncertainties. In order to encompass the entire RO data processing, the new rOPS processing system at WEGC has recently seen major advancements in Level 1a (L1a) processing, with the integration of the POD processing (Innerkofler et al., 2020) as well as the excess-phase processing including uncertainty estimation that was presented and evaluated in this study.

The rOPS L1a excess-phase processing, itself algorithmically concise, is complemented by integrated quality control and uncertainty estimation, which requires an advanced framework of various subsystems, which we introduced in a step-by-step manner in Sect. 2. Starting with the input data preparation we discussed the various input data sources. Building on the POD processing, integrated in rOPS, the DSM (daily system modeling) subsystem delivers daily LEO receiver and GNSS transmitter satellite orbit and clock data. The observation geometry setup computed by ESM (event system modeling) facilitates the provision of basic event-based geometry and environmental context information. Complemented by atmospheric profiles modeling, ESM also provides reliable forward-modeled excess-phase profiles based on collocated (re)analysis data such as from the ECMWF Reanalysis (ERA5). These forward-modeled profiles, including a forward mapping of mean sea level (MSL) altitudes to the RO event's time grid, are found to be highly valuable for the quality control and for supporting the uncertainty estimation.

After the introduction of the rOPS L1a processing framework, we provided an in-depth description of the main processing algorithms for the derivation of excess-phase profiles in addition to a due account of the GNSS observables and corresponding receiver-tracking modes. Subsequently, an elaborated quality control, to a major extent supported by forward-modeled excess-phase profiles, removes or alternatively flags profiles of insufficient or degraded quality. The primary addition, however, is the component-wise estimation of excess-phase uncertainty profiles for each individual RO event, which serve as a starting point for the uncertainty propagation in the subsequent RO retrieval chain down to the atmospheric ECV profiles.

The validation of the new processing was based on three 3-month periods (in 2008, 2013, and 2020) for achieving a robust statistical analysis. In a sensitivity analysis for inspecting the quality and reliability of the resulting excess phases, we focused on three atmospheric layers – lower mesosphere (50–60 km), lower stratosphere (20–25 km), and middle tro-

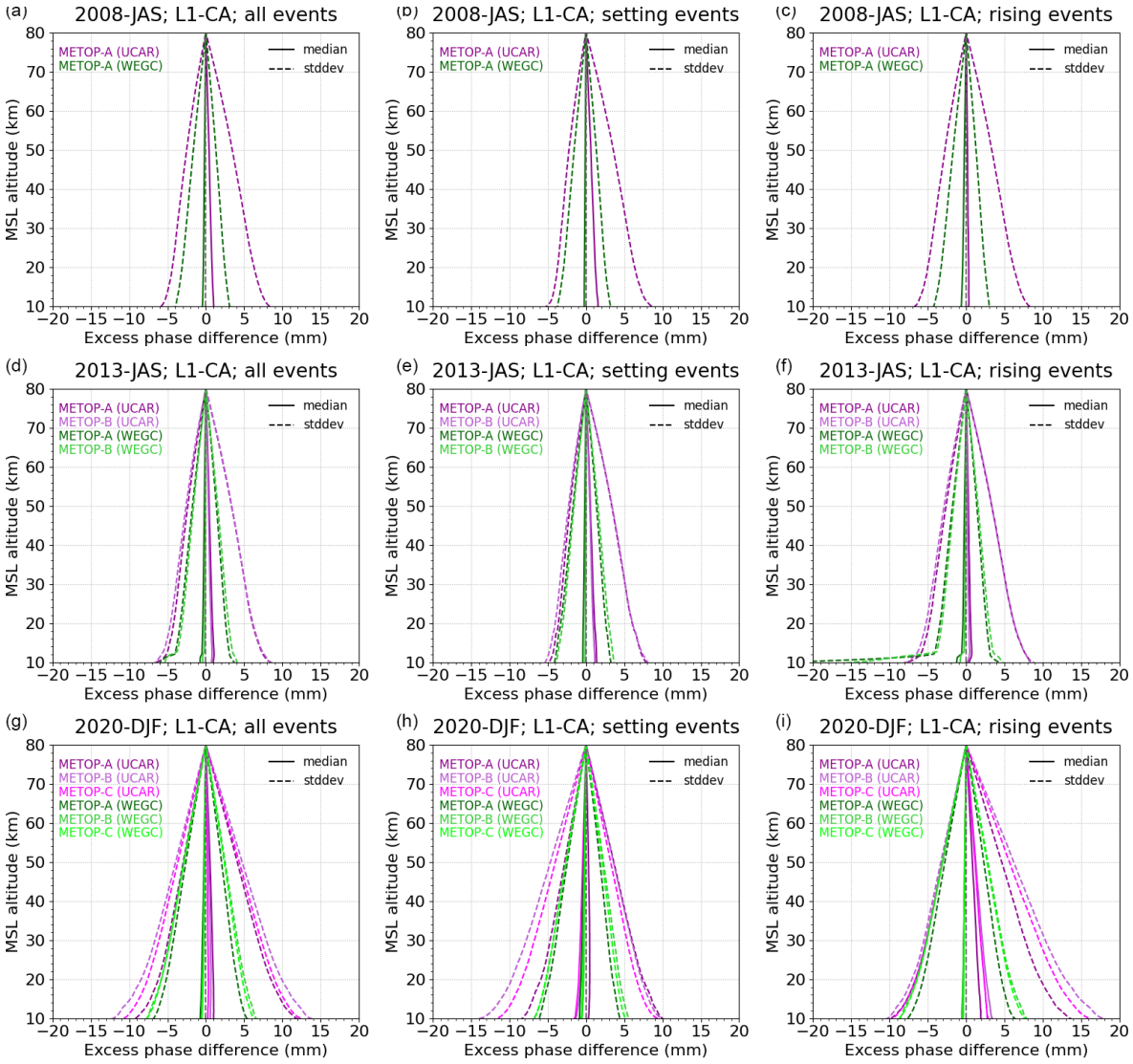


Figure 14. Systematic difference (median) and standard deviation (16th and 84th percentile) profiles from the statistical ensemble differences between excess-phase profiles from WEGC (green) and UCAR/CDAAC (magenta) compared to EUMETSAT. **(a, d, g)** All events, **(b, e, h)** setting events, and **(c, f, i)** rising events are shown for **(a–c)** 2008-JAS to **(g–i)** 2020-DJF. The altitude range focuses on an MSL altitude of 10–80 km.

posphere (3–7 km) – investigating differences between observed and collocated ERA5-derived profiles, the influence of different orbit and clock inputs, and a cross-platform comparison between profiles from the different Metop satellites.

The comparison against forward-modeled profiles revealed small systematic differences mostly of the millimeter level only, based on the multi-monthly statistics. The exchange of WEGC LEO orbit solutions with orbit solutions from EUMETSAT or UCAR (all of adequate quality within about 5 cm in position and 0.05 mm s^{-1} in velocity in an orbit intercomparison) in the rOPS processing led to negligible differences in the results of the different time periods and Metop satellites. Intercomparing matched observations between different Metop satellites, using collocation criteria of 2 h in time and 200 km in space, revealed larger differences dominated by the space–time differences in the RO event locations, but still the median difference results, found at millimeter-level deviation, confirmed an overall statistically very tight consistency across the different Metop receiver platforms.

An inter-center comparison of WEGC- and UCAR-processed excess phases against EUMETSAT-processed data focused on an upper- (MSL altitudes of 10–80 km) and lower-atmospheric (SLTP altitude from 0 to −100 km) region, respectively. While this analysis revealed some small discrepancies in the processing of rising RO events at WEGC, the excess phases processed with rOPS show better agreement to EUMETSAT excess phases than to UCAR

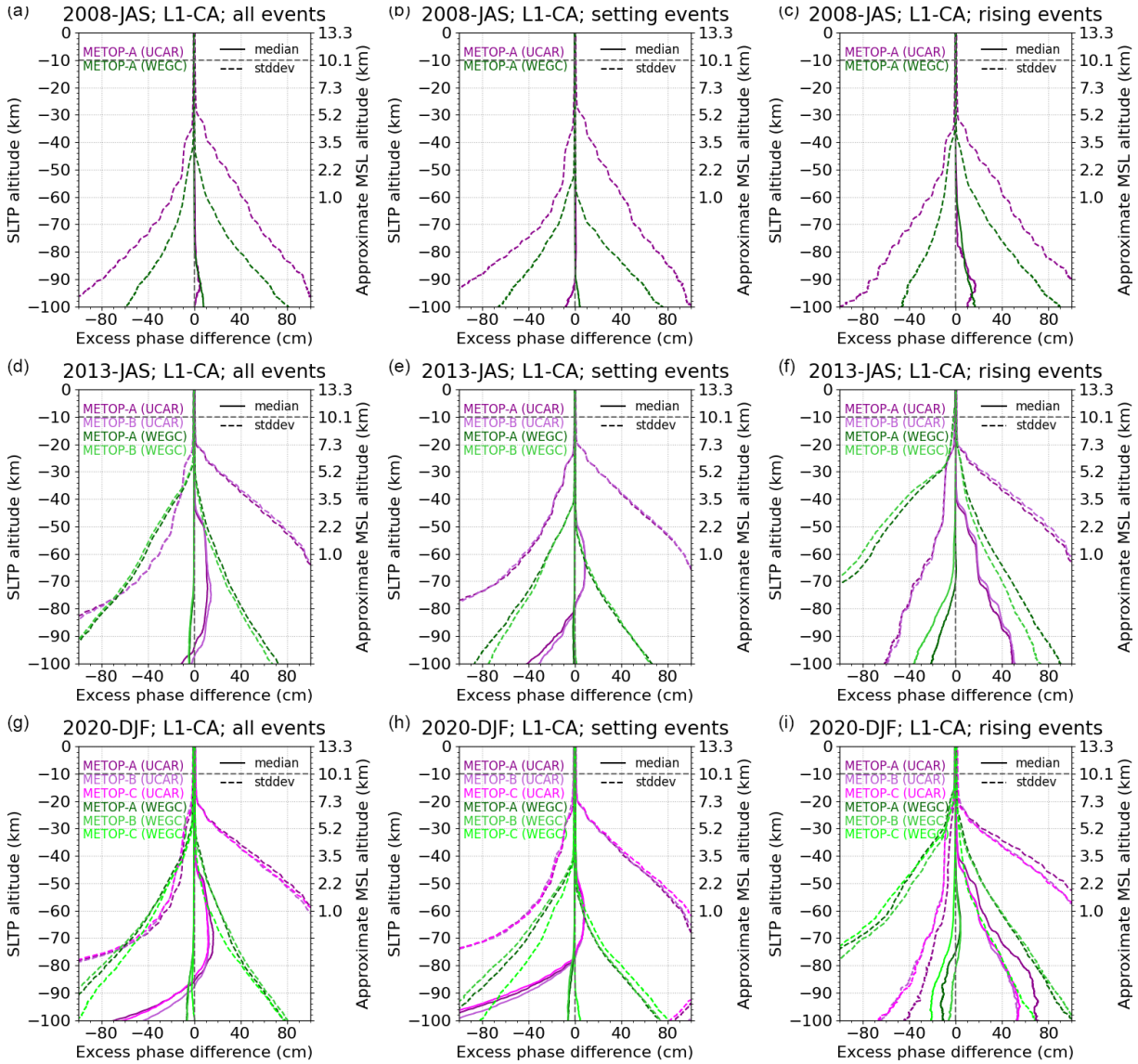


Figure 15. Systematic differences (median) and standard deviation (16th and 84th percentile) profiles from the statistical ensemble differences between excess-phase profiles from WEGC (green) and UCAR/CDAAC (magenta) compared to EUMETSAT. **(a, d, g)** All events, **(b, e, h)** setting events, and **(c, f, i)** rising events are shown for **(a–c)** 2008-JAS to **(g–i)** 2020-DJF. The altitude range focuses on an SLTP altitude of −100–0 km.

ones. In the stratosphere-/mesosphere-focused region, the differences between WEGC and EUMETSAT amount to 1 ± 6 mm, compared to 3 ± 8 mm for UCAR against EUMETSAT. In the troposphere-focused region, differences stay small down to an SLTP altitude of about −80 km, with a standard deviation increase to near ± 80 cm, still corresponding to very small relative differences. Larger deviations of UCAR excess phases at lower altitudes suggest noticeable differences compared to the processing strategies at WEGC and EUMETSAT.

A sensitivity check of the stability of the uncertainty processing, based on daily averages of example days from the study time periods, showed closely consistent systematic- and random-uncertainty estimates across all time periods and the three Metop satellites. Both the estimated random and estimated systematic uncertainties stay at the (sub)millimeter level in the stratosphere and mesosphere, while at tropospheric altitudes in the dense atmosphere with large excess phases, where signal tracking is challenged, the random-uncertainty estimates increase up to several centimeters.

We note that the results from the intercomparison between excess-phase data processed by EUMETSAT, WEGC, and UCAR experience larger differences in the lower troposphere than we quantified in the uncertainty budget. This indicates additional structural uncertainties arising from different processing schemes not captured in the estimated uncertainties

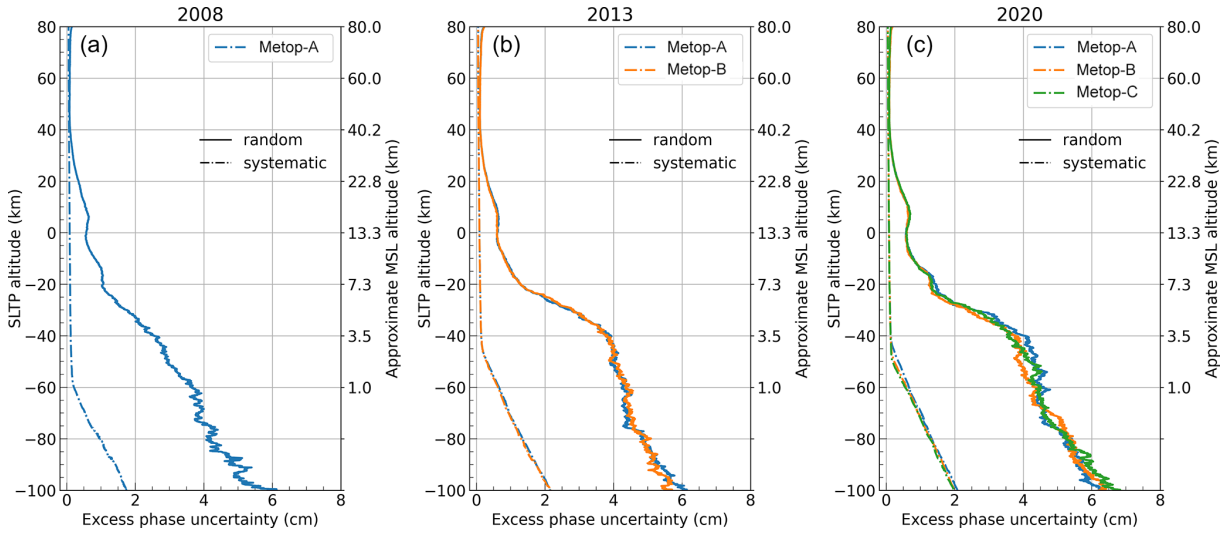


Figure 16. Daily averages (median) of estimated random and estimated systematic (combined basic and apparent) uncertainties based on uncertainty profiles of an individual RO event for the example days of 1 July 2008 (Metop-A; **a**), 1 July 2013 (Metop-A/B; **b**), and 2 January 2020 (Metop-A/B/C; **c**).

in the observational data. In order to address this substantial differences, a broader inter-center comparison study is advised.

In follow-on work we will investigate the long-time evolution of the uncertainty budget and compare the characteristics to those of other RO missions. The approach of the uncertainty estimations of various components at the excess-phase level is also subject to repeated improvements and refinements. Overall the results provide evidence for the rOPS L1a processing's capability to provide valuable uncertainty estimates for further processing, supported by rigorous quality control for climate quality data-processing demands. Demonstrating the delivery of robust and accurate excess-phase profiles, the results indicate that the rOPS L1a subsystem is a reliable new excess-phase processor, which is versatile also in the sense that it can handle multiple different input data sources, such as orbit and excess-phase data also from other processing centers.

While this study focused on a thorough introduction and careful initial evaluation based on Metop-A/B/C satellite data, the rOPS L1a processing is set up as a multi-mission system capable of processing RO measurements also from the CHAMP, GRACE, COSMIC, COSMIC-2, FY-3, and Spire RO satellite series. In this way it will support the provision of long-term multi-mission RO data records including uncertainty estimation, for the benefit of climate monitoring and research.

Code availability. The code used to produce the results of this study is available from the corresponding author upon qualified request.

Data availability. The (numeric) data underlying the results of this study are available from the corresponding author upon qualified request. Excess phase data from EUMETSAT supporting this study are available at https://doi.org/10.15770/EUM_SEC_CLM_0029 (EUMETSAT, 2020). Supporting data from UCAR-CDAAC were downloaded from https://doi.org/10.5065/789w-m137 (CDAAC, 2023a), https://doi.org/10.5065/1k0w-2272 (CDAAC, 2023b), and https://doi.org/10.5065/p8es-mc74 (CDAAC, 2023c). Atmospheric field data from ERA5 global reanalysis are available at https://doi.org/10.24381/cds.143582cf (Hersbach et al., 2023).

Author contributions. The conceptualization and methodology were provided by JI and GK, embedded into the Reference Occultation Processing System (rOPS) framework conceived by GK. JI elaborated the detailed algorithms, performed the computational implementation and the analysis, prepared the figures, and wrote the first draft of the paper. GK supported this work with the provision of detailed design input and advice on all aspects of the study and significant contributions to the writing of the paper. The computational implementation was extensively supported by MS. MS, CM, and YA advised on a range of technical and scientific aspects and contributed through writing (review and editing). All authors participated in the consolidation of the paper for submission and towards publication.

Competing interests. The contact author has declared that none of the authors has any competing interests.

Disclaimer. Publisher's note: Copernicus Publications remains neutral with regard to jurisdictional claims made in the text, published maps, institutional affiliations, or any other geographical representation in this paper. While Copernicus Publications makes ev-

ery effort to include appropriate place names, the final responsibility lies with the authors.

Special issue statement. This article is part of the special issue "Observing atmosphere and climate with occultation techniques – results from the OPAC-IROWG 2022 workshop". It is a result of the International Workshop on Occultations for Probing Atmosphere and Climate, Leibnitz, Austria, 8–14 September 2022.

Acknowledgements. We thank EUMETSAT (Darmstadt) and UCAR–CDAAC (Boulder) for access to their RO excess-phase and orbit data and ECMWF (Reading) for access to their analysis and forecast data. We also thank Veronika Proschek from WEGC for technical support and valuable discussions and Doug Hunt and Bill Schreiner from UCAR for valuable advice.

Financial support. This research has been supported by the Radio Occultation Meteorology Satellite Application Facility (ROM SAF) Fourth-Phase (CDOP-4) Climate Research and Monitoring project (ROMSAF4P/ROMSAF4CLIM) funded by EUMETSAT (ROMSAF4P, project no. PO4500023609/UG-WEGC); the Austrian Research Promotion Agency (FFG) through the Austrian Space Applications Programme (ROMSAF4CLIM, project no. 892287; predecessor projects ATROMSAF1 and ATROMSAF2, project nos. 859771 and 873696) endowed by the Federal Ministry for Climate Action, Environment, Energy, Mobility, Innovation and Technology (BMK); and the University of Graz. Furthermore, funding was provided by the Austrian Science Fund (FWF; research grant no. W1256-G15; Doctoral Programme Climate Change – Uncertainties, Thresholds and Coping Strategies) and the publication cost support programme of the University of Graz.

Review statement. This paper was edited by Peter Alexander and reviewed by three anonymous referees.

References

Alemany, F. M., Marquardt, C., von Engeln, A., Padovan, S., Paolella, S., Notarpietro, R., Sancho, F., Andres, Y., and Butenko, L.: EUMETSAT GRAS reprocessing activities, presentation at OPAC-IROWG International Workshop, 8–14 September 2022, Leibnitz/Seggau, Austria, https://static.uni-graz.at/fileadmin/veranstaltungen/opacirowg2022/programme/08.9.22/AM/Session_2/OPAC-IROWG-2022_Alemany.pdf (last access: 29 September 2023), 2022.

Angerer, B., Ladstädter, F., Scherllin-Pirscher, B., Schwärz, M., Steiner, A. K., Foelsche, U., and Kirchengast, G.: Quality aspects of the WEGC multi-satellite GPS radio occultation record OPSv5.6, Atmos. Meas. Tech., 10, 4845–4863, https://doi.org/10.5194/amt-10-4845-2017, 2017.

Anthes, R. A.: Exploring Earth's atmosphere with radio occultation: contributions to weather, climate, and space weather, Atmos. Meas. Tech., 4, 1077–1103, https://doi.org/10.5194/amt-4-1077-2011, 2011.

Ao, C. O., Hajj, G. A., Meehan, T. K., Dong, D., Iijima, B. A., Mannucci, A. J., and Kursinski, E. R.: Rising and setting GPS occultations by the use of open-loop tracking, J. Geophys. Res., 114, D04101, https://doi.org/10.1029/2008JD010483, 2009.

Ashby, N.: Relativity in the Global Positioning System, Living Rev. Relativity, 6, 1, https://doi.org/10.12942/lrr-2003-1, 2003.

Ashby, N.: The Sagnac effect in the Global Positioning System, in: Relativity in Rotating Frames: Relativistic Physics in Rotating Reference Frames, edited by: Rizzi, G. and Ruggiero, M. L., 11–28, Springer Netherlands, Dordrecht, https://doi.org/10.1007/978-94-017-0528-8_3, 2004.

Ashby, N.: Relativity in GNSS, in: Springer Handbook of Spacetime, edited by: Ashtekar, A. and Petkov, V., m 509–525, Springer Berlin Heidelberg, Berlin, Heidelberg, https://doi.org/10.1007/978-3-642-41992-8_24, 2014.

Bai, W., Liu, C., Meng, X., Sun, Y., Kirchengast, G., Du, Q., Wang, X., Yang, G., Liao, M., Yang, Z., Zhao, D., Xia, J., Cai, Y., Liu, L., and Wang, D.: Evaluation of atmospheric profiles derived from single- and zero-difference excess phase processing of BeiDou radio occultation data from the FY-3C GNOS mission, Atmos. Meas. Tech., 11, 819–833, https://doi.org/10.5194/amt-11-819-2018, 2018.

Bai, W. H., Sun, Y. Q., Du, Q. F., Yang, G. L., Yang, Z. D., Zhang, P., Bi, Y. M., Wang, X. Y., Cheng, C., and Han, Y.: An introduction to the FY3 GNOS instrument and mountain-top tests, Atmos. Meas. Tech., 7, 1817–1823, https://doi.org/10.5194/amt-7-1817-2014, 2014.

Beyerle, G., Schmidt, T., Michalak, G., Heise, S., Wickert, J., and Reigber, C.: GPS radio occultation with GRACE: Atmospheric profiling utilizing the zero difference technique, Geophys. Res. Lett., 32, L13806, https://doi.org/10.1029/2005GL023109, 2005.

Bojinski, S., Verstraete, M., Peterson, T. C., Richter, C., Simmons, A., and Zemp, M.: The concept of Essential Climate Variables in support of climate research, applications, and policy, B. Am. Meteorol. Soc., 95, 1431–1443, https://doi.org/10.1175/BAMS-D-13-00047.1, 2014.

Bonnedal, M., Christensen, J., Carlström, A., and Berg, A.: Metop-GRAS in-orbit instrument performance, GPS Solut., 14, 109–120, https://doi.org/10.1007/s10291-009-0142-3, 2010.

Carrascosa-Sanz, C., Fernández-Pérez, L., Salcedo, J.-M., Modrego-Contreras, D., Loiselet, M., Christensen, J., and Hägg, M.: Analysis of the performances in retrieved atmospheric profiles with radio-occultation methods by considering different sources of error and different processing techniques, Atmospheric Remote Sensing using Satellite Navigation Systems Workshop, Matera, Italy, https://esamultimedia.esa.int/docs/metop/Matera_oct2003_analysis.pdf (last access: 29 September 2023), 2003.

CDAAC: GNSS Radio Occultation Datasets – Metop-A, COSMIC Data Analysis and Archive Center [data set], https://doi.org/10.5065/789w-m137, 2023a.

CDAAC: GNSS Radio Occultation Datasets – Metop-B, COSMIC Data Analysis and Archive Center [data set], https://doi.org/10.5065/1k0w-2272, 2023b.

CDAAC: GNSS Radio Occultation Datasets – Metop-C, COSMIC Data Analysis and Archive Center [data set], https://doi.org/10.5065/p8es-mc74, 2023c.

Dach, R., Andritsch, F., Arnold, D., Bertone, S., Fridez, P., Jäggi, A., Jean, Y., Maier, A., Mervart, L., Meyer, U., Orliac, E., Ortiz-Geist, E., Prange, L., Scaramuzza, S., Schaer, S., Sidorov, D., Sušnik, A., Villiger, A., Walser, P., Baumann, C., Beutler, G., Bock, H., Gäde, A., Lutz, S., Meindl, M., Ostini, L., Sośnica, K., Steinbach, A., and Thaller, D.: Bernese GNSS Software Version 5.2, User manual, Astron. Inst., University of Bern, Bern, Switzerland, https://doi.org/10.7892/boris.72297, 2015.

Danzer, J., Schwaerz, M., Kirchengast, G., and Healy, S. B.: Sensitivity analysis and impact of the kappa-correction of residual ionospheric biases on radio occultation climatologies, Earth Space Sci., 7, e2019EA000942, https://doi.org/10.1029/2019EA000942, 2020.

Danzer, J., Haas, S. J., Schwaerz, M., and Kirchengast, G.: Performance of the ionospheric kappa-correction of radio occultation profiles under diverse ionization and solar activity conditions, Earth Space Sci., 8, e2020EA001581, https://doi.org/10.1029/2020EA001581, 2021.

ECMWF: Changes in ECMWF model, http://www.ecmwf.int/en/forecasts/documentation-and-support/changes-ecmwf-model (last access: 29 September 2023), 2016.

ECMWF: ERA-5 Documentation, https://confluence.ecmwf.int/display/CKB/ERA5%3A+data+documentation (last access: 29 September 2023), 2019.

EUMETSAT: EPS Mission Conventions Document, EUMETSAT Doc. No. EPS/SYS/SPE/990002, EUMETSAT, Darmstadt, Germany, Issue 1.2, https://www.eumetsat.int/media/8191 (last access: 29 September 2023), 2005.

EUMETSAT: Radio Occultation Level 1 Product Format Specification, EUMETSAT Doc. No. EUM/TSS/SPE/16/817861, EUMETSAT, Darmstadt, Germany, Issue v1A, 55 pp., https://www-cdn.eumetsat.int/files/2022-04/Radio%20Occultation%20Level%201%20Product%20Format%20Specification-1.pdf (last access: 29 September 2023), 2016.

EUMETSAT: GNSS Navigation Bit Product Format Specification, EUMETSAT Doc. No. EUM/TSS/SPE/17/953527, EUMETSAT, Darmstadt, Germany, Issue v1C, 26 pp., 2018.

EUMETSAT: GRAS Level 1B Bending Angle Climate Data Record Release 2 – Metop-A and -B, European Organisation for the Exploitation of Meteorological Satellites [data set], https://doi.org/10.15770/EUM_SEC_CLM_0029, 2020.

Fjeldbo, G. and Eshleman, V. R.: The bistatic radar-occultation method for the study of planetary atmospheres, J. Geophys. Res., 70, 3217–3225, 1965.

Fjeldbo, G., Kliore, A. J., and Eshleman, V. R.: The neutral atmosphere of Venus as studied with the Mariner V radio occultation experiments, The Astro. J., 76, 123–140, https://doi.org/10.1086/111096, 1971.

Foelsche, U., Syndergaard, S., Fritzer, J., and Kirchengast, G.: Errors in GNSS radio occultation data: relevance of the measurement geometry and obliquity of profiles, Atmos. Meas. Tech., 4, 189–199, https://doi.org/10.5194/amt-4-189-2011, 2011.

GCOS: The Status of the Global Climate Observing System 2021: The GCOS Status Report, GCOS-240, WMO, Geneva, https://ane4bf-datap1.s3.eu-west-1.amazonaws.com/wmod8_gcos/s3fs-public/gcos-status_report_full_text-240_lr_compressed.pdf (last access: 29 September 2023), 2021.

Gobiet, A., Kirchengast, G., Manney, G. L., Borsche, M., Retscher, C., and Stiller, G.: Retrieval of temperature profiles from CHAMP for climate monitoring: intercomparison with Envisat MIPAS and GOMOS and different atmospheric analyses, Atmos. Chem. Phys., 7, 3519–3536, https://doi.org/10.5194/acp-7-3519-2007, 2007.

Gorbunov, M. E. and Kirchengast, G.: Wave-optics uncertainty propagation and regression-based bias model in GNSS radio occultation bending angle retrievals, Atmos. Meas. Tech., 11, 111–125, https://doi.org/10.5194/amt-11-111-2018, 2018.

Gorbunov, M. E., Lauritsen, K. B., Benzon, H.-H., Larsen, G. B., Syndergaard, S., and Sørensen, M. B.: Processing of GRAS/METOP radio occultation data recorded in closed-loop and raw-sampling modes, Atmos. Meas. Tech., 4, 1021–1026, https://doi.org/10.5194/amt-4-1021-2011, 2011.

Gorbunov, M. E., Kirchengast, G., and Lauritsen, K. B.: Generalized canonical transform method for radio occultation sounding with improved retrieval in the presence of horizontal gradients, Atmos. Meas. Tech., 14, 853–867, https://doi.org/10.5194/amt-14-853-2021, 2021.

Griggs, E., Kursinski, E. R., and Akos, D.: Short-term GNSS satellite clock stability, Radio Sci., 50, 813–826, https://doi.org/10.1002/2015RS005667, 2015.

Hajj, G. A., Kursinski, E. R., Romans, L. J., Bertiger, W. I., and Leroy, S. S.: A technical description of atmospheric sounding by GPS occultation, J. Atmos. Solar-Terr. Phys., 64, 451–469, https://doi.org/10.1016/S1364-6826(01)00114-6, 2002.

Harting, A.: Considering clock errors in numerical simulations, IEEE T. Instrum. Meas., 45, 715–720, https://doi.org/10.1109/19.494587, 1996.

Hauschild, A., Montenbruck, O., and Steigenberger, P.: Short-term analysis of GNSS clocks, GPS Solut., 17, 295–307, https://doi.org/10.1007/s10291-012-0278-4, 2013.

Healy, S.: Operational assimilation of GPS radio occultation measurements at ECMWF, ECMWF Newsletter, 111, 6–11, 2007.

Healy, S. B. and Culverwell, I. D.: A modification to the standard ionospheric correction method used in GPS radio occultation, Atmos. Meas. Tech., 8, 3385–3393, https://doi.org/10.5194/amt-8-3385-2015, 2015.

Hernández-Pajares, M., Juan, J. M., Sanz, J., Orus, R., Garcia-Rigo, A., Feltens, J., Komjathy, A., Schaer, S. C., and Krankowski, A.: The IGS VTEC mpas: a reliable source of ionospheric information since 1998, J. Geodesy, 83, 263–275, https://doi.org/10.1007/s00190-008-0266-1, 2009.

Hersbach, H., Bell, B., Berrisford, P., Hirahara, S., Horányi, A., Muñoz-Sabater, J., Nicolas, J., Peubey, C., Radu, R., Schepers, D., Simmons, A., Soci, C., Abdalla, S., Abellan, X., Balsamo, G., Bechtold, P., Biavati, G., Bidlot, J., Bonavita, M., De Chiara, G., Dahlgren, P., Dee, D., Diamantakis, M., Dragani, R., Flemming, J., Forbes, R., Fuentes, M., Geer, A., Haimberger, L., Healy, S., Hogan, R. J., Hólm, E., Janisková, M., Keeley, S., Laloyaux, P., Lopez, P., Lupu, C., Radnoti, G., de Rosnay, P., Rozum, I., Vamborg, F., Villaume, S., and Thépaut, J.-N.: Complete ERA5 from 1940: Fifth generation of ECMWF atmospheric reanalyses of the global climate, Copernicus Climate Change Service (C3S) Data Store (CDS) [data set], https://doi.org/10.24381/cds.143582cf, 2023.

Hersbach, H., Bell, B., Berrisford, P., Horányi, A., Sabater, J. M., Nicolas, J., Radu, R., Schepers, D., Simmons, A., Soci, C., and Dee, D.: Global reanalysis: goodbye ERA-Interim, hello ERA5, ECMWF Newsletter, 159, 17–24, 2019.

Hersbach, H., Bell, B., Berrisford, P., Hirahara, S., Horányi, A., Muñoz-Sabater, J., Nicolas, J., Peubey, C., Radu, R., Schepers, D., Simmons, A., Soci, C., Abdalla, S., Abellan, X., Balsamo, G., Bechtold, P., Biavati, G., Bidlot, J., Bonavita, M., De Chiara, G., Dahlgren, P., Dee, D., Diamantakis, M., Dragani, R., Flemming, J., Forbes, R., Fuentes, M., Geer, A., Haimberger, L., Healy, S., Hogan, R. J., Hólm, E., Janisková, M., Keeley, S., Laloyaux, P., Lopez, P., Lupu, C., Radnoti, G., de Rosnay, P., Rozum, I., Vamborg, F., Villaume, S., and Thépaut, J.-N.: The ERA5 global reanalysis, Q. J. Roy. Meteorol. Soc., 146, 1999–2049, https://doi.org/10.1002/qj.3803, 2020.

Ho, S.-P., Hunt, D., Steiner, A. K., Mannucci, A. J., Kirchengast, G., Gleisner, H., Heise, S., von Engeln, A., Marquardt, C., Sokolovskiy, S., Schreiner, W., Scherllin-Pirscher, B., Ao, C., Wickert, J., Syndergaard, S., Lauritsen, K., Leroy, S., Kursinski, E. R., Kuo, Y.-H., Foelsche, U., Schmidt, T., and Gorbunov, M.: Reproducibility of GPS radio occultation data for climate monitoring: Profile-to-profile inter-comparison of CHAMP climate records 2002 to 2008 from six data centers, J. Geophys. Res., 117, D18111, https://doi.org/10.1029/2012JD017665, 2012.

Hofmann-Wellenhof, B., Lichtenegger, H., and Wasle, E.: GNSS – Global Navigation Satellite Systems, Springer, Wien New York, 516 pp., ISBN 978-3-211-73012-6, 2008.

Hunt, D., Innerkofler, J., and Sokolovskiy, S.: Honing in on atmospheric excess phase computation for radio occultation, Fourth ICGPSRO 2018 and Eleventh FORMOSAT-3/COSMIC Data Users Workshop 2018, 18–20 April 2018: Taipei, Taiwan, https://static.uni-graz.at/fileadmin/urbi-zentren/Wegcenter/3.Forschen/1.Forschungsgruppen/Arsclisys/Publikationen/2018_Hunt-Innerkofler-Sokolvskiy_Atmospheric-Exess-Phase-Computation.pdf (last access: 29 September 2023), 2018.

Innerkofler, J., Kirchengast, G., Schwärz, M., Pock, C., Jäggi, A., Andres, Y., and Marquardt, C.: Precise orbit determination for climate applications of GNSS radio occultation including uncertainty estimation, Remote Sens., 12, 1180, https://doi.org/10.3390/rs12071180, 2020.

IPCC: Climate Change 2021: The Physical Science Basis. Contribution of Working Group I to the Sixth Assessment Report of the Intergovernmental Panel on Climate Change, Cambridge University Press, Cambridge, United Kingdom and New York, NY, USA, 2204 pp., https://doi.org/10.1017/9781009157896, 2021.

Kirchengast, G., Schwärz, M., Schwarz, J., Scherllin-Pirscher, B., Pock, C., Innerkofler, J., Proschek, V., Steiner, A. K., Danzer, J., Ladstädter, F., and Foelsche, U.: The reference occultation processing system approach to interpret GNSS radio occultation as SI-traceable planetary system refractometer, presentation at OPAC-IROWG International Workshop 8–14 September 2016, Seggau/Leibnitz, Austria, > Scient. Programme > Mon, 12 September, http://wegcwww.uni-graz.at/opacirowg2016 (last access: 29 September 2023), 2016.

Kirchengast, G., Schwärz, M., Angerer, B., Schwarz, J., Innerkofler, J., Proschek, V., Ramsauer, J., Fritzer, J., Scherllin-Pirscher, B., Rieckh, T., Danzer, J., and Leuprecht, A.: Reference OPS DAD – Reference Occultation Processing System (rOPS) Detailed Algorithm Description, Tech. Rep. for ESA and FFG No. 1/2018, Doc-Id: WEGC–rOPS–2018–TR01, Issue 2.0, Wegener Center, Universitz of Graz, Austria, 181 pp., 2018.

Klaes, K. D., Cohen, M., Buhler, Y., Schlüssel, P., Munro, R., Luntama, J.-P., von Engeln, A., Clérigh, E. Ó., Bonekamp, H., Ackermann, J., and Schmetz, J.: An introduction to the EUMETSAT Polar System, B. Am. Meteorol. Soc., 88, 1085–1096, https://doi.org/10.1175/BAMS-88-7-1085, 2007.

Kouba, J.: Improved relativistic transformations in GPS, GPS Solut., 8, 170–180, https://doi.org/10.1007/s10291-004-0102-x, 2004.

Kouba, J.: A guide to using International GNSS Service (IGS) products, Tech. rep., IGS, https://files.igs.org/pub/resource/pubs/UsingIGSProductsVer21_cor.pdf (last access: 29 September 2023), 2015.

Kuo, Y.-H., Wee, T.-K., Sokolovskiy, S., Rocken, C., Schreiner, W., Hunt, D., and Anthes, R. A.: Inversion and error estimation of GPS radio occultation data, J. Meteor. Soc. Japan, 82, 507–531, 2004.

Kursinski, E. R., Hajj, G. A., Bertiger, W. I., Leroy, S. S., Meehan, T. K., Romans, L. J., Schofield, J. T., McCleese, D. J., Melbourne, W. G., Thornton, C. L., Yunck, T. P., Eyre, J. R., and Nagatani, R. N.: Initial results of radio occultation observations of Earth's atmosphere using the Global Positioning System, Science, 271, 1107–1110, https://doi.org/10.1126/science.271.5252.1107, 1996.

Kursinski, E. R., Hajj, G. A., Schofield, J. T., Linfield, R. P., and Hardy, K. R.: Observing Earth's atmosphere with radio occultation measurements using the Global Positioning System, J. Geophys. Res., 102, 23429–23465, https://doi.org/10.1029/97JD01569, 1997.

Lackner, B. C.: Exploring trend indicators of climate change from radio occultation and optimal trend detection (PhD thesis), Scientific Report No. 38-2010, Wegener Center Verlag, University of Graz, Austria, 181 pp., ISBN 978-3-9502940-5-7, https://wegcwww.uni-graz.at/publ/wegcreports/2010/WCV-SciRep-No38-BCLackner-Jul2010.pdf (last access: 6 October 2023), 2010.

Ladreiter, H. P. and Kirchengast, G.: GPS/GLONASS sensing of the neutral atmosphere: Model independent correction of ionospheric influences, Radio Sci., 31, 877–891, https://doi.org/10.1029/96RS01094, 1996.

Langley, R. B.: GPS Receiver System Noise, GPS World, 8, 40–45, 1997.

Li, Y., Kirchengast, G., Scherllin-Pirscher, B., Schwaerz, M., Nielsen, J. K., Ho, S.-p., and Yuan, Y.-b.: A new algorithm for the retrieval of atmospheric profiles from GNSS radio occultation data in moist air and comparison to 1DVar retrievals, Remote Sens., 11, 2729, https://doi.org/10.3390/rs11232729, 2019.

Liu, C., Kirchengast, G., Syndergaard, S., Schwaerz, M., Danzer, J., and Sun, Y.: New higher-order correction of GNSS RO bending angles accounting for ionospheric asymmetry: Evaluation of performance and added value, Remote Sens., 12, 3637, https://doi.org/10.3390/rs12213637, 2020.

Liu, C.-L., Kirchengast, G., Zhang, K., Norman, R., Li, Y., Zhang, S. C., Carter, B., Fritzer, J., Schwaerz, M., Choy, S. L., Wu, S. Q., and Tan, Z. X.: Characterisation of residual ionospheric errors in bending angles using GNSS RO end-to-end simulations, Adv. Space Res., 52, 821–836, https://doi.org/10.1016/j.asr.2013.05.021, 2013.

Loiselet, M., Stricker, N., Menard, Y., and Luntama, J.-P.: GRAS – MetOp's GPS-based atmospheric sounder, ESA Bulletin, 102, 38–44, 2000.

Luntama, J.-P., Kirchengast, G., Borsche, M., Foelsche, U., Steiner, A., Healy, S. B., von Engeln, A., O'Clerigh, E., and Marquardt, C.: Prospects of the EPS GRAS mission for operational atmospheric applications, B. Am. Meteorol. Soc., 89, 1863–1875, https://doi.org/10.1175/2008BAMS2399.1, 2008.

Matzka, J., Stolle, C., Yamazaki, Y., Bronkalla, O., and Morschhauser, A.: The geomagnetic Kp index and derived indices of geomagnetic activity, Space Weather, 19, e2020SW002641, https://doi.org/10.1029/2020SW002641, 2021.

Montenbruck, O., Andres, Y., Bock, H., van Helleputte, T., van den Ijssel, J., Loiselet, M., Marquardt, C., Silvestrin, P., Visser, P., and Yoon, Y.: Tracking and orbit determination performance of the GRAS instrument on MetOp-A, GPS Solut., 12, 289–299, https://doi.org/10.1007/s10291-008-0091-2, 2008.

Mudrak, A., De Simone, P., and Lisi, M.: Relativistic corrections in the European GNSS Galileo, Aerotec. Missili Spaz., 94, 139–144, https://doi.org/10.1007/BF03404697, 2015.

National Research Council: Earth Science and Applications from Space: National Imperatives for the Next Decade and Beyond (Decadal Survey), The National Academies Press, Washington, D.C., 456 pp., https://doi.org/10.17226/11820, 2007.

Pirscher, B.: Multi-satellite climatologies of fundamental atmospheric variables from radio occultation and their validation (PhD thesis), Scientific Report No. 33-2010, Wegener Center Verlag, University of Graz, Austria, 218 pp., ISBN 978-3-9502940-3-3, https://wegcwww.uni-graz.at/publ/wegcreports/2010/WCV-SciRep-No33-BPirscher-Mai2010.pdf (last access: 6 October 2023), 2010.

Proschek, V., Kirchengast, G., and Schweitzer, S.: Greenhouse gas profiling by infrared-laser and microwave occultation: retrieval algorithm and demonstration results from end-to-end simulations, Atmos. Meas. Tech., 4, 2035–2058, https://doi.org/10.5194/amt-4-2035-2011, 2011.

Ramsauer, J. and Kirchengast, G.: Sensitivity of atmospheric profiles retrieved from GNSS radio occultation data to instrumental errors, IGAM/UG Technical Report for ESA/ESTEC No. 6/2001, Institute for Geophysics, Astrophysics, and Meteorology, University of Graz, Austria, 62 pp., https://wegcwww.uni-graz.at/publ/users/gki/web/arsclisys/publications/publ2001/JRandGK-IGAMTechRepfESA-62p-n6y2001.pdf (last access: 6 October 2023), 2001.

Rebischung, P. and Schmid, R.: IGS14/igs14.atx: a new framework for the IGS products, in: AGU Fall Meeting 2016, 12–16 December 2016, San Francisco, CA, USA, American Geophysical Union, https://www.researchgate.net/publication/311654495_IGS14igs14atx_a_new_framework_for_the_IGS_products (last access: 29 September 2023), 2016.

Rieder, M. J. and Kirchengast, G.: Error analysis and characterization of atmospheric profiles retrieved from GNSS occultation data, J. Geophys. Res., 106, 31755–31770, 2001.

Rocken, C., Anthes, R., Exner, M., Hunt, D., Sokolovskiy, S., Ware, R., Gorbunov, M., Schreiner, W., Feng, D., Herman, B., Kuo, Y.-H., and Zuo, X.: Analysis and validation of GPS/MET data in the neutral atmosphere, J. Geophys. Res., 102, 29849–29866, https://doi.org/10.1029/97JD02400, 1997.

SAAB: METOP-GRAS Measurement Data Interpretation and Description, P-GRM-SPC-0036-SE, Saab Ericsson Space, Göteborg, Sweden, issue 7, 94 pp., 2004.

Scherllin-Pirscher, B., Kirchengast, G., Steiner, A. K., Kuo, Y.-H., and Foelsche, U.: Quantifying uncertainty in climatological fields from GPS radio occultation: an empirical-analytical error model, Atmos. Meas. Tech., 4, 2019–2034, https://doi.org/10.5194/amt-4-2019-2011, 2011a.

Scherllin-Pirscher, B., Steiner, A. K., Kirchengast, G., Kuo, Y.-H., and Foelsche, U.: Empirical analysis and modeling of errors of atmospheric profiles from GPS radio occultation, Atmos. Meas. Tech., 4, 1875–1890, https://doi.org/10.5194/amt-4-1875-2011, 2011b.

Schmidt, T., Wickert, J., Heise, S., Flechtner, F., Fagiolini, E., Schwarz, G., Zenner, L., and Gruber, T.: Comparison of ECMWF analyses with GPS radio occultations from CHAMP, Ann. Geophys., 26, 3225–3234, https://doi.org/10.5194/angeo-26-3225-2008, 2008.

Schreiner, W., Sokolovskiy, S., Hunt, D., Rocken, C., and Kuo, Y.-H.: Analysis of GPS radio occultation data from the FORMOSAT-3/COSMIC and Metop/GRAS missions at CDAAC, Atmos. Meas. Tech., 4, 2255–2272, https://doi.org/10.5194/amt-4-2255-2011, 2011.

Schreiner, W., Weiss, J., Anthes, R., Braun, J., Chu, V., Fong, J., Hunt, D., Kuo, Y.-H., Meehan, T., Serafino, W., Sjoberg, J., Sokolovskiy, S., Talaat, E., Wee, T., and Zeng, Z.: COSMIC-2 radio occultation constellation: first results, Geophys. Res. Lett., 47, e2019GL086841, https://doi.org/10.1029/2019GL086841, 2020.

Schreiner, W. S., Rocken, C., Sokolovskiy, S., and Hunt, D.: Quality assessment of COSMIC/FORMOSAT-3 GPS radio occultation data derived from single- and double-difference atmospheric excess phase processing, GPS Solut., 14, 13–22, https://doi.org/10.1007/s10291-009-0132-5, 2010.

Schwarz, J. C.: Benchmark quality processing of radio occultation data with integrated uncertainty propagation, PhD thesis, Wegener Center Verlag, University of Graz, Austria, Scientific Report No. 77-2018, 194 pp., ISBN 978-3-9504501-5-6, https://wegcwww.uni-graz.at/publ/wegcreports/2018/WCV-SciRep-No77-JSchwarz-July2018.pdf (last access: 6 October 2023), 2018.

Schwarz, J. C., Kirchengast, G., and Schwaerz, M.: Integrating uncertainty propagation in GNSS radio occultation retrieval: from bending angle to dry-air atmospheric profiles, Earth Space Sci., 4, 200–228, https://doi.org/10.1002/2016EA000234, 2017.

Schwarz, J. C., Kirchengast, G., and Schwaerz, M.: Integrating uncertainty propagation in GNSS radio occultation retrieval: from excess phase to atmospheric bending angle profiles, Atmos. Meas. Tech., 11, 2601–2631, https://doi.org/10.5194/amt-11-2601-2018, 2018.

Seidl, V.: Quality control and evaluation for atmospheric profiles from GNSS radio occultation reference processing, MSc thesis, Graz University of Technology and University of Graz, Austria, 101 pp., https://diglib.tugraz.at/quality-control-and-evaluation-for-atmospheric-profiles-from-gnss-radio-occultation-reference-processing-2018 (last access: 6 October 2023), 2018.

Smith, E. and Weintraub, S.: The constants in the equation for atmospheric refractive index at radio frequencies, Proc. IRE, 41, 1035–1037, 1953.

Smith, S. W.: The Scientist and Engineer's Guide to Digital Signal Processing, 2nd edn., California Technical Publishing, 688 pp., ISBN 0-9660176-6-8, 1999.

Sokolovskiy, S., Rocken, C., Hunt, D., Schreiner, W., Johnson, J., Masters, D., and Esterhuizen, S.: GPS profiling of the lower troposphere from space: Inversion and demodulation of the open-loop radio occultation signals, Geophys. Res. Lett., 33, L14816, https://doi.org/10.1029/2006GL026112, 2006.

Sokolovskiy, S., Rocken, C., Schreiner, W., Hunt, D., and Johnson, J.: Postprocessing of L1 GPS radio occultation signals recorded in open-loop mode, Radio Sci., 44, RS2002, https://doi.org/10.1029/2008RS003907, 2009.

Sokolovskiy, S. V.: Tracking tropospheric radio occultation signals from low Earth orbit, Radio Sci., 36, 483–498, 2001.

Springer, T. A.: NAPEOS – Mathematical Models and Algorithms, DOPS-SYS-TN-0100-OPS-GN, European Space Operation Centre, European Space Agency, Darmstadt, Germany, 150 pp., http://navigation-office.esa.int/attachments/32834429/1/NAPEOS_MathModels_Algorithms.pdf (last access: 29 September 2023), 2009.

Steiner, A. K. and Kirchengast, G.: Error analysis of GNSS radio occultation data based on ensembles of profiles from end-to-end simulations, J. Geophys. Res., 110, D15307, https://doi.org/10.1029/2004JD005251, 2005.

Steiner, A. K., Lackner, B. C., Ladstädter, F., Scherllin-Pirscher, B., Foelsche, U., and Kirchengast, G.: GPS radio occultation for climate monitoring and change detection, Radio Sci., 46, RS0D24, https://doi.org/10.1029/2010RS004614, 2011.

Steiner, A. K., Ladstädter, F., Ao, C. O., Gleisner, H., Ho, S.-P., Hunt, D., Schmidt, T., Foelsche, U., Kirchengast, G., Kuo, Y.-H., Lauritsen, K. B., Mannucci, A. J., Nielsen, J. K., Schreiner, W., Schwärz, M., Sokolovskiy, S., Syndergaard, S., and Wickert, J.: Consistency and structural uncertainty of multi-mission GPS radio occultation records, Atmos. Meas. Tech., 13, 2547–2575, https://doi.org/10.5194/amt-13-2547-2020, 2020.

Syndergaard, S.: Retrieval analysis and methodologies in atmospheric limb sounding using the GNSS radio occultation technique (PhD thesis), Danish Meteorological Institute, Copenhagen, Denmark, 89 pp., ISBN 87-7478-394-7, 1999.

Syndergaard, S. and Kirchengast, G.: An Abel transform for deriving line-of-sight wind profiles from LEO-LEO infrared laser occultation measurements, J. Geophys. Res., 121, 2525–2541, https://doi.org/10.1002/2015JD023535, 2016.

Tapping, K. F.: The 10.7 cm solar radio flux (F10.7), Space Weather, 11, 394–406, https://doi.org/10.1002/swe.20064, 2013.

Teunissen, P. J. and Montenbruck, O.: Springer Handbook of Global Navigation Satellite Systems, Springer, https://doi.org/10.1007/978-3-319-42928-1, 2017.

von Engeln, A., Healy, S., Marquardt, C., Andres, Y., and Sancho, F.: Validation of operational GRAS radio occultation data, Geophys. Res. Lett., 36, L17809, https://doi.org/10.1029/2009GL039968, 2009.

Vorob'ev, V. V. and Krasil'nikova, T. G.: Estimation of the accuracy of the atmospheric refractive index recovery from Doppler shift measurements at frequencies used in the NAVSTAR system, Izv. Atmos. Ocean. Phys., 29, 602–609, 1994.

Wee, T.-K. and Kuo, Y.-H.: A perspective on the fundamental quality of GPS radio occultation data, Atmos. Meas. Tech., 8, 4281–4294, https://doi.org/10.5194/amt-8-4281-2015, 2015.

Zeng, Z., Sokolovskiy, S., Schreiner, W., Hunt, D., Lin, J., and Kuo, Y.-H.: Ionospheric correction of GPS radio occultation data in the troposphere, Atmos. Meas. Tech., 9, 335–346, https://doi.org/10.5194/amt-9-335-2016, 2016.

Zus, F., Beyerle, G., Heise, S., Schmidt, T., Wickert, J., and Marquardt, C.: Validation of refractivity profiles derived from GRAS raw-sampling data, Atmos. Meas. Tech., 4, 1541–1550, https://doi.org/10.5194/amt-4-1541-2011, 2011.

6. Paper 3: Evaluation of excess phase and bending angle data from FengYun-3 radio occultation based on two independent processing chains

Innerkofler, J., Liu, C., Kirchengast, G., Schwärz, M., Meng, X., Bai, W., Hu, P., Sun, Y., Liao, M., Hu, X. (2024). "Evaluation of excess phase and bending angle data from FengYun-3 radio occultation based on two independent processing chains". *Res. Square*, Research Article Preprint. DOI: 10.21203/rs.3.rs-4400072/v1

Evaluation of excess phase and bending angle data from FengYun-3 radio occultation based on two independent processing chains

Josef Innerkofler[1,4], Congliang Liu[2,4], Gottfried Kirchengast[1,3,4], Marc Schwärz[1,3,4], Xiangguan Meng[2,4], Weihua Bai[2,4], Peng Hu[2,4], Yueqiang Sun[2,4], Mi Liao[5], and Xiuqing Hu[5]

[1]Wegener Center for Climate and Global Change (WEGC), University of Graz, Graz, Austria
[2]Beijing Key Laboratory of Space Environment Exploration, National Space Science Center, Chinese Academy of Sciences (NSSC/CAS), Beijing, China
[3]Institute of Physics, University of Graz, Graz, Austria
[4]International Laboratory on Climate and Atmosphere Research with Occultation & Reflectometry Observing Systems (ICAROS) of NSSC/CAS, German Research Centre for Geosciences (GFZ) and University of Graz, Graz, Austria
[5]National Satellite Meteorological Center, China Meteorological Administration (NSMC/CMA), Beijing, China

Correspondence: Josef Innerkofler (josef.innerkofler@uni-graz.at)

Abstract.

With long-term mission planning extending well into the next decade, the Chinese FengYun-3 (FY-3) meteorological satellite series acts as an important backbone for the provision of radio occultation (RO) data for climate science and numerical weather prediction (NWP). Independent evaluation is an essential part for considerate application of the data. Here we present results of the first cross-evaluation of RO low-level data, obtained by the GNSS occultation sounder (GNOS) onboard of FY-3 satellites, from two independent processing chains (Wegener Center, Graz; National Space Science Center–National Satellite Meteorological Center, Beijing). We analyzed and compared the orbit solutions, atmospheric excess phase, and bending angle profiles, for 3-month evaluation periods of FY-3C and FY-3D data in 2014 (FY-3C only) and 2019. We found the orbit data to be within requirements for high-quality RO data processing. Cross-comparison at excess phase level as well showed high-quality consistency overall, while some differences were revealed in the closed-loop to open-loop transition of FY-3D data. The cross-evaluation of bending angle profiles against European Centre for Medium-Range Weather Forecasts (ECMWF) forecast data also showed good agreement and adequate quality in general, while some distinct deviations occurred below 26 km altitude in the early FY-3C rising event data in 2014. The results underscore the high basic quality of the GNOS data for applications in climate research and NWP. At the same time they valuably inform subsequent work to resolve remaining biases, improve current processing algorithms, and include data from FY-3E, FY-3F, and FY-3G satellites.

Posted date. May 24th, 2024

DOI. https://doi.org/10.21203/rs.3.rs-4400072/v1

Copyright statement. This work is licensed under a Creative Commons Attribution 4.0 International License.

Additional declarations. No competing interests reported.

1 Introduction

Consistent and long-term stable observations of the Earth's atmosphere constitute an important backbone for contemporary atmospheric and climate sciences. Global navigation satellite system (GNSS) radio occultation (RO) (e.g., Kursinski et al., 1997; Syndergaard, 1999; Hajj et al., 2002) is a highly valuable satellite based measurement technique providing global and long-time stable observations the free atmosphere (Anthes, 2011; Steiner et al., 2020). Providing measurements with high accuracy and vertical resolution of essential climate variables (ECVs; Bojinski et al., 2014), such as temperature and pressure over the tropo- and stratosphere, and tropospheric water vapor, RO qualifies to provide benchmark data records. In order to fulfill the requirements for RO observations to be used as benchmark data in numerical weather prediction, for independent validation of other observing systems, or for climate model analysis, rigorous assessment of the data quality is indispensable.

With a long-term mission plan (https://fy4.nsmc.org.cn/nsmc/en/satellite/index.html) the GNSS Occultation Sounder (GNOS) RO missions on the Chinese meteorological FengYun-3 (FY-3) satellite series (Cai et al., 2017; Sun et al., 2018) constitutes an important part of the global RO observing system within this decade and beyond, which makes safeguarding the quality of the measurements from the SI-tied measurements to ECVs an important task. So far, the FY-3C and FY-3D GNOS missions, launched in 2013 and 2017, respectively, have acquired longer time records. As with other RO sensors, the GNOS anti-velocity (velocity) antenna enables to obtain setting (rising) occultation measurements based on L-band microwave signals emitted by GNSS satellites setting or rising behind Earth's horizon from the viewpoint of the rapidly moving FY-3 satellite in low Earth orbit (LEO). In this limb sounding geometry, the atmosphere is scanned from the top of the mesosphere down into the boundary layer (or vice versa for rising events), providing high-resolution vertical profiles within the short duration of such RO events (approximately 1-2 minutes).

The basic observables of a GNSS RO receiver such as GNOS are phase differences relative to the transmitted GNSS signals (replicated within the receiver), induced by the refraction of the electromagnetic waves in the atmosphere (e.g., Sun et al. (2018)). Relying on atomic clocks of the GNSS space and ground segments, RO measurements can be traced to the fundamental time standard of the SI-second (Leroy et al., 2006). The less stable LEO oscillator errors can be either eliminated using the clock biases estimated within the precise orbit determination (zero-differencing) or by introducing a reference clock from a non-occulting GNSS satellite link (single-differencing). Introducing lowest noise in the processing, zero-differencing is the preferred option and applicable to FY-3, which is equipped with an ultra-stable oscillator with 1 s stability (Allan deviation) at the level of 10^{-12} (Bai et al., 2018).

The calculation of precise orbit positions, velocities, and clock bias estimates, together with the calculation of the atmospheric phase delay, the so-called excess phase, constitute the first steps of the RO retrieval chain of WEGC's reference occultation processing system (rOPS; Kirchengast et al., 2016, 2018; Innerkofler et al., 2020, 2023). Subsequently, based on the excess phase profiles, bending angle profiles are derived (Schwarz et al., 2018), before retrieving refractivity and atmospheric profiles of ECVs (Schwarz et al., 2017; Li et al., 2019).

So far, the FY-3C and FY-3D GNOS measurements and atmospheric and ionospheric data products have been evaluated, validated, and used for atmosphere and ionosphere related scientific applications in various studies, e.g., Liao et al. (2016,

2019); Bai et al. (2018); Wei et al. (2020). However, a thorough evaluation of the RO data quality by independent processing systems, starting from the low-level observation data, has not been conducted yet. Within the international cooperation between NSSC and WEGC, including also the National Satellite Meteorological Center of the China Meteorological Administration (NSMC/CMA) as the FY-3 GNOS data provider, several test months of low-level RO datasets from the FY-3C and FY-3D satellites were delivered to WEGC, and the rOPS software prepared to process these data. Based on this, this study focuses on inter-comparing and evaluating NSSC/NSMC processed excess phase and bending angle data, obtained from the FengYun satellite data center (NSMC, https://satellite.nsmc.org.cn/), against the corresponding independently processed retrieval results obtained by WEGC. This evaluation, for the first time, closes the gap in the assessment of FY-3C and FY-3D RO from the SI-tied low-level data to bending angle data, which so far did not involve any inter-comparison between independent processing chains between different processing centers.

In the following we introduce the FY-3 missions and data used in this study in Section 2.1 and outline the validation setup in Section 2.2. The results are presented and discussed in Section 3, before ending with a conclusion section (Section 4).

2 Data and methods

2.1 FengYun-3 mission and data

The Chinese FY-3 series comprises the deployment of 5 operational meteorological satellites in LEO with the capability to provide RO soundings of the neutral atmosphere and ionosphere beginning with the launch of the second batch of the series. This includes the flight model FY-3C, which was launched in September 2013, followed by FY-3D in November 2017 and more recently FY-3E (Zhang et al., 2022) in July 2021, and FY-3G and FY-3F in April and August 2023, respectively. The onboard GNOS (Bai et al., 2014) is compatible with two GNSS's: BeiDou navigation satellite system (BDS) and the GPS. While the FY-3C satellite is equipped with the first generation of the GNOS receiver, starting with FY-3E the enhanced second generation GNOS II receiver is mounted on the satellite platforms (Sun et al., 2017; Du et al., 2018). The receiver is capable of tracking L1 C/A, L2P, and L2C (if available) GPS signals and B1 and B2 BDS signals (Bai et al., 2014). All signals are recorded in closed loop (CL) tracking (50 Hz) except from GPS L1 C/A which also features open loop (OL) tracking (100 Hz) for sounding with higher penetration depth. The GNOS instrument on the FY-3 satellite platforms provides both rising and setting occultations (Bai et al., 2018).

The data provision from NSSC/CAS for this study covered 3 months of data from the early measurement period of FY-3C in June, July, and August 2014 and 3 months FY-3C and FY-3D data in July, August, and September 2019, including input data required for independent POD processing at WEGC. The other data provided comprised FY-3 orbit and clock solutions from the POD processing at NSSC and decoded GNOS measurement data for the L1a excess phase and subsequent L1b bending angle processing at WEGC, as well as L1a and L1b data for comparison delivered by NSSC/CAS. Although the GNOS receivers are the first scientific receivers enabling BDS occultations, this study is limited to GPS observations only. On average about 500 GPS occultations per day are recorded by a single satellite.

2.2 Validation setup

For proper FY-3 data analysis several steps need to be performed in preparation for a profile-to-profile inter-center comparison of excess phase (level 1a) and bending angle (level 1b) data. On the one hand FY-3 L1a/L1b data provided by NSSC/NSMC—used as reference data in this study—need to be converted to WEGC rOPS data formats to allow comparability. On the other hand independent RO processing at WEGC is conducted starting from the FY-3 RO measurement data provided by NSSC. In addition to that we perform quality control of the NSSC-converted and WEGC-processed data, rejecting un-physical and low quality profiles following the algorithmic described in Innerkofler et al. (2023). Figure 1 provides a schematic overview over the WEGC validation setup for NSSC/NSMC FY-3 data.

The input data for the two independent processing streams, realized at NSSC and WEGC, comprise 1 Hz navigation tracking data from the satellite's zenith antenna for precise orbit determination and high-rate GNOS occultation tracking data from the fore and aft atmospheric sounding antennae. The intercomparison of FY-3 orbit products is performed as a sanity check for a reasonable foundation of the following excess phase comparison. For more details on the methodology the reader is referred to Innerkofler et al. (2020).

In order to facilitate intercomparison of FY-3 excess phase and bending angle data within the WEGC validation system, the external data from NSSC/NSMC need to be converted into rOPS data format. As an auxiliary intermediate step forward-modeled reference profiles for each NSSC/NSMC-converted or WEGC-processed profile was extracted from data of the integrated forecasting system (IFS) of the European Center for Medium Range Weather Forecasts (ECMWF). In particular we used ECMWF ERA5 reanalysis forecast data (Hersbach et al., 2020) in support of the quality control at excess phase level, as described by Innerkofler et al. (2023), and additionally used those profiles as independent reference for the validation of NSSC and WEGC L1b bending angle data.

The intercomparison of atmospheric profiles is then based on L1a/L1b profiles calculated at WEGC and corresponding profiles acquired from NSSC. In addition modeled bending angle profiles are used for validation at bending angle level. The individual profiles are interpolated to a common altitude grid before calculating the differences for each corresponding profile pair. Those individual profile differences are then averaged per time bin t_i and for each height level z_k, for a robust statistical evaluation:

$$\bar{L}\left(t_i, z_{\mathrm{SLTP},k}\right) = \frac{1}{n_{prof}} \sum_{n=1}^{n_{prof}} L_n \quad \text{and} \quad \bar{\alpha}\left(t_i, z_{a,k}\right) = \frac{1}{n_{prof}} \sum_{n=1}^{n_{prof}} \alpha_n, \tag{1}$$

where n denotes the profile index for the specific time bin and zonal band, and n_{prof} the total number of profiles for this specific time and spatial domain. The altitude is either represented as straight-line-tangent point altitude z_{SLTP} or impact altitude z_a. Results of the intercomparison of FY3 data are reported in Section 3.3 for L1a excess phase data and in Section 3.4 for L1b bending angle data, respectively.

For a comprehensive and well comparative analysis we additionally focused on four vertical atmospheric regions and their layer averages (calculated from the vertical statistical measures, i.e., mean, median, stddev, percentiles, by obtaining the average over all values within the corresponding altitude layer):

- lower troposphere (LT, 2-5 km): this atmospheric region in the lowermost section of the atmosphere was selected for representation of the (moist) lower troposphere. With the restriction to above 2 km, the boundary layer and its special behavior that requires separate study (e.g., Gorbunov et al., 2021; Gorbunov and Kirchengast, 2018; Zeng et al., 2016) was disregarded.
- upper troposphere (UT, 7-10 km): in this layer of the atmosphere, tracking of the RO signals is increasingly impeded by the downward increasing air density, moisture and inhomogeneities in the atmosphere, making the use of an open loop tracking technique necessary.
- lower stratosphere (LS, 15-25 km): representing the lower stratosphere region of RO soundings, with narrow uncertainty and minimal influence of tropospheric or tropopause effects in the retrieval.
- upper stratosphere (US, 40-45 km): representing the upper stratosphere with small absolute excess phases but still without major ionospheric influences that start higher.

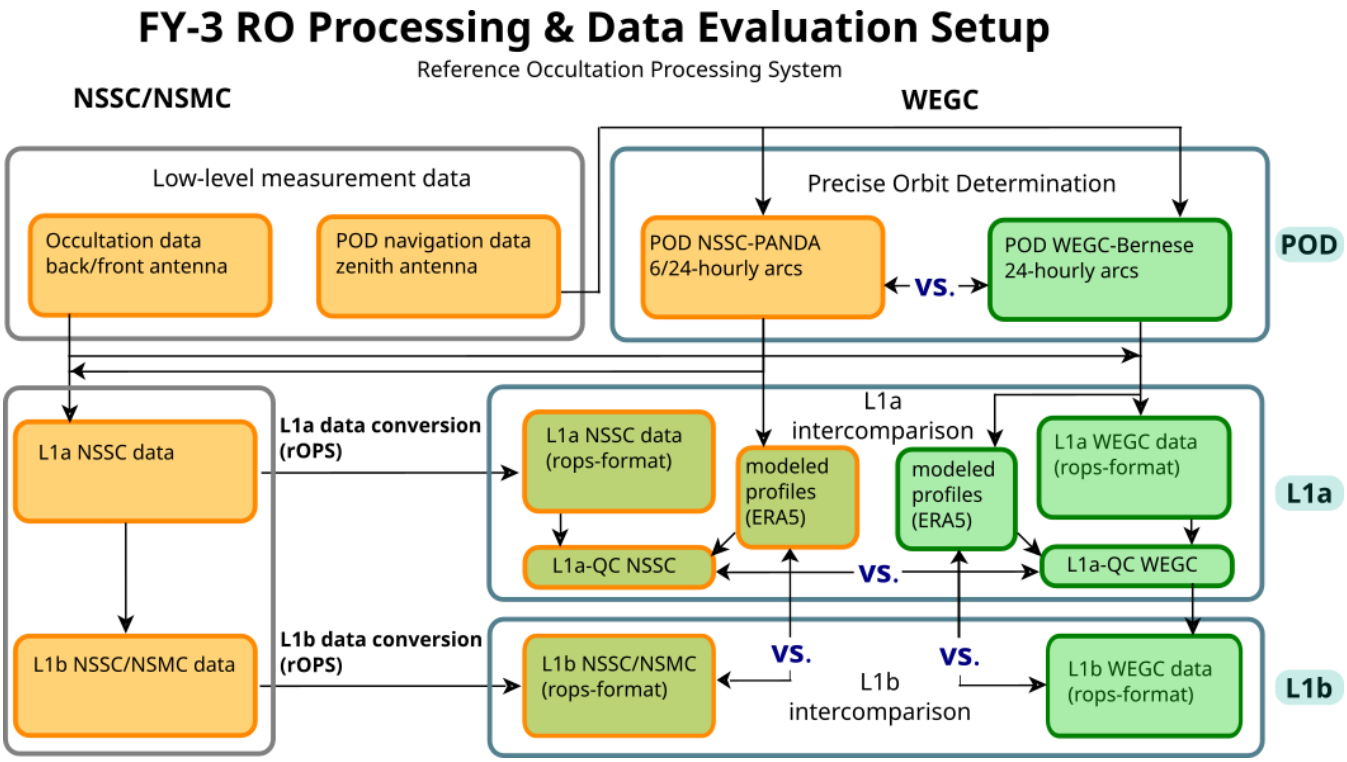


Figure 1. Schematic overview of the WEGC evaluation strategy and setup for the NSSC/NSMC FY-3 GNOS data evaluation. Low-level measurement data processed and provided by NSSC (orange) are used as input for WEGC's rOPS POD and L1a processing (green). NSSC/NSMC data (L1a/L1b) are converted to WEGC rOPS format (olive "interface" boxes), to be ingestible to the WEGC cross-evaluation system.

3 Results

In the following we present a cross-evaluation of FY-3 LEO orbit data calculated at NSSC and WEGC as sanity check for an established basis for the analysis at excess phase and bending angle data level. We investigate the number of profiles in Section 3.2 provided as input from NSSC/NSMC and the converted NSSC and processed WEGC data in preparation of the subsequent evaluation of the excess phases in Section 3.3 and bending angles in Section 3.4.

3.1 Precise orbit determination cross-evaluation

Figure 2 shows the results of the orbit comparison between NSSC-POD and the orbit processing at WEGC for FY-3C and FY-3D as daily radial, transverse, and cross-track component-wise orbit differences. For all periods investigated a reasonable 3D-RMS of 4.20 cm for FY-3C from June to August 2014 and of 5.72 cm (FY-3C) and 3.31 cm (FY-3D) from July to September can be found. Orbit comparison for FY-3C is less representative since NSSC orbits were calculated as 6-hourly arcs while WEGC follows a daily processing approach (Innerkofler et al., 2020).

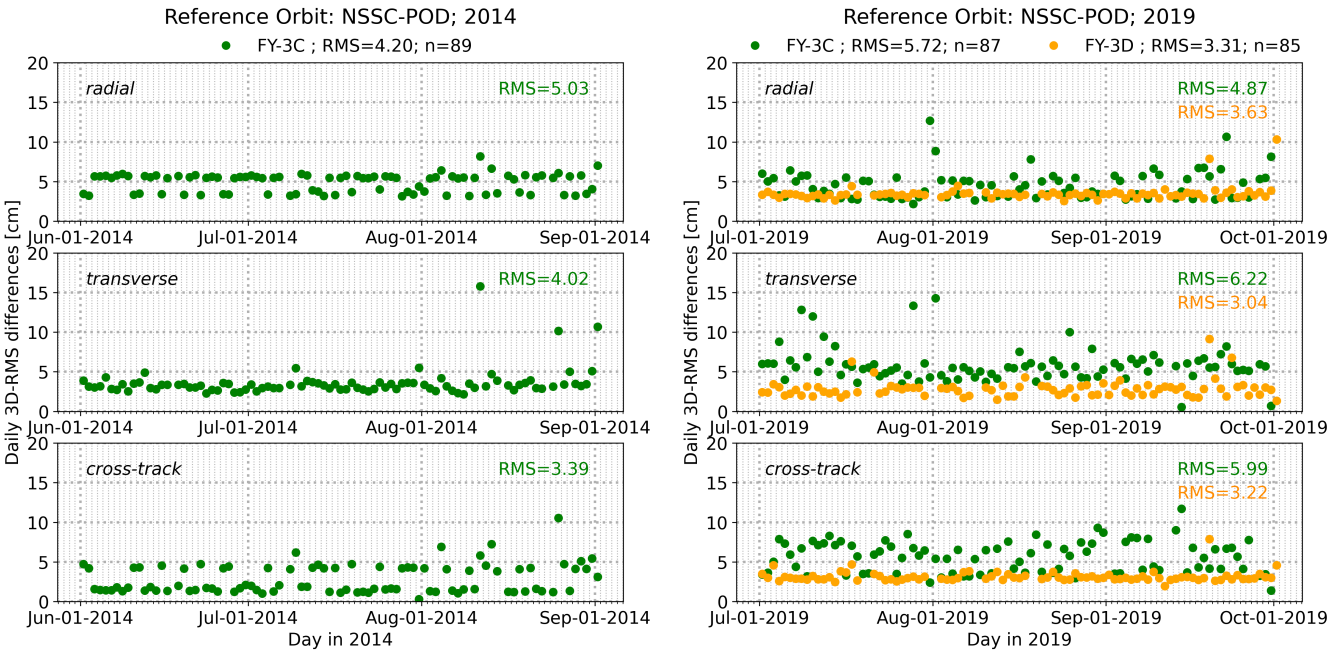


Figure 2. Daily radial, transverse, and cross-track orbit comparison between WEGC and NSSC POD processing for FY-3C from June to August 2014 (left) and for FY-3C/D from July to September 2019 (right). Rare outliers exceeding 20 cm in 3D-RMS difference (9 days total for all four satellites) have been disregarded for the calculation of the overall RMS (noted as part of the legend; units cm). The number of total days included in the calculation for each period and satellite also noted (number "n" in subtitles).

3.2 Excess phase and bending angle profile statistics

Before considering profile-to-profile comparison we contrast the number of converted NSSC/NSMC and processed WEGC profiles on basis of the input data provided by NSSC. Figure 3 shows the number of profiles (setting and rising occultations separated) for each satellite and time period investigated, from the low-level observations, to the number of inferred excess phase profiles (before and after quality control), to the number of bending angle profiles, obtained from the NSMC FengYun satellite data center.

Overall, the different test periods for FY-3C (2014-JJA, 2019-JAS) and FY-3D (2019-JAS) show different quality in the numbers of processed data. In 2019 for instance, one can observe a significant drop from the number of low-level input data to level 1a provided by NSSC for FY-3D, in contrast to lower rejection rates observed in FY-3C data in 2014 and 2019 (cf. left block of each panel in Figure 3). Furthermore, the number of NSSC L1a profiles is reduced in the conversion process to rOPS since profiles, found to have no valid measurement at one out of all frequencies, are rejected. This is most pronounced for FY-3D data. Also, in the excess phase quality control process of WEGC-processed data, a relatively high number of profiles gets rejected, an issue currently under investigation at WEGC (most pronounced for FY-3D data). Overall a balanced ratio between setting and rising occultations is found.

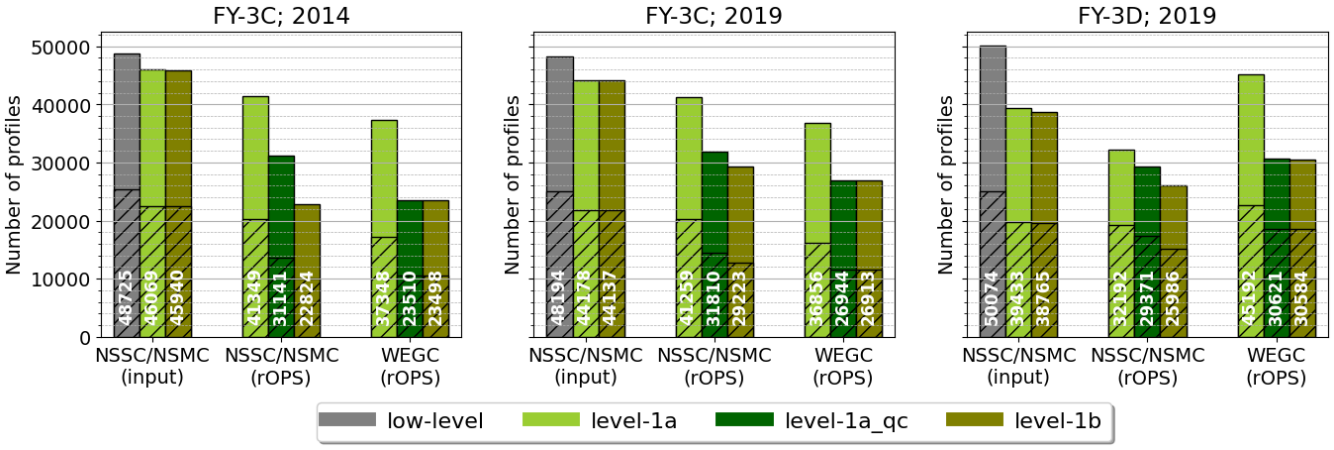


Figure 3. Numbers of FY-3C (left and middle panel) and FY-3D (right panel) low-level RO event data (low-level, gray), excess phase data (level-1a, light green) and corresponding quality checked profiles (level-1a_qc, dark green), as well as bending angle data (level-1b, olive). In each panel, the input profile numbers delivered by NSSC/NSMC are shown as the left histogram-stack ("NSSC/NSMC-input"), the converted and quality-checked NSSC/NSMC data in the middle ("NSSC/NSMC-rOPS"), and the WEGC-processed data at the right ("WEGC-rOPS"). For each histogram bar, the number of rising events (hatched part) is indicated separately from the setting one (non-hatched part on top).

3.3 Excess phase cross-evaluation

Based on the quality checked level 1a excess phase profiles obtained by NSSC and WEGC, we performed a cross-evaluation of the data as a measure for their consistency. For thorough analysis we separated the profiles into a combined mesospheric and stratospheric section, using MSL altitude (mapped using the corresponding forward-model profiles) as vertical coordinate from 10 km to 80 km. In this range absolute phase and differences are comparatively small. Second, a tropospheric region using SLTP altitudes from 0 km to −100 km was defined, where open loop tracking introduces larger differences. Considering a standard atmosphere model, this approximately equals an MSL altitude from about 13 km down to the last few hundred meters above Earth's surface within the boundary layer.

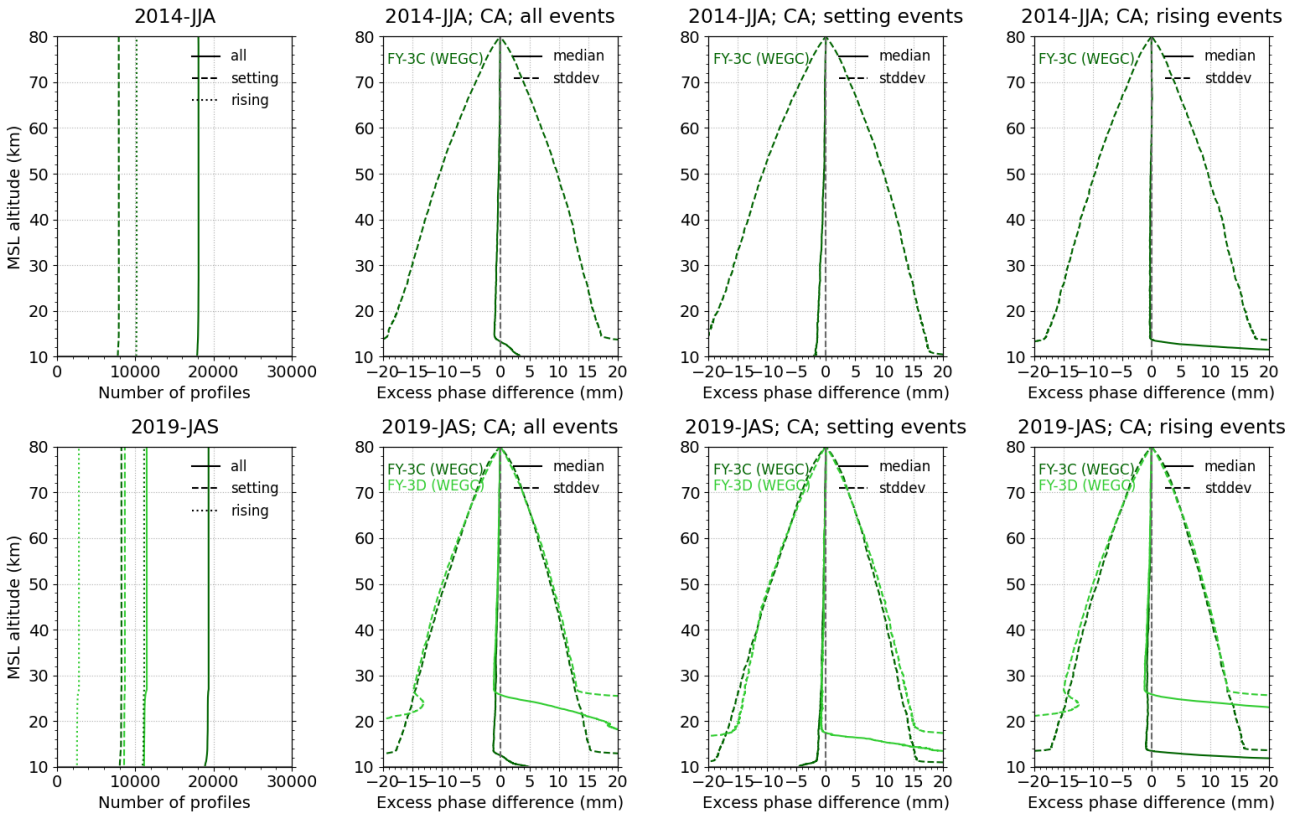


Figure 4. Systematic difference profiles (median) and standard deviation profile estimates (stddev; 16% and 84% percentiles) as function of MSL altitude (focus here above troposphere; 10−80 km), from the statistical ensemble of difference profiles between the excess phase profiles of WEGC and NSSC (i.e., the latter serving as reference dataset here), for the FY-3C JJA 2014 (upper row) and FY-3C and FY-3D JAS 2019 data (lower row). Together with the number of profiles as a function of altitude (left column) shown for context, the statistical results are depicted for all events (middle-left), setting events (middle-right), and rising events (right), respectively.

The inter-center comparison results at excess phase level between WEGC and NSSC (the latter used as reference) are shown in Figure 4 with focus on the stratosphere/mesosphere region and in Figure 5 with focus on the troposphere region, respectively. The evaluation at MSL altitude shows good agreement in the inter-center comparison for FY-3C data with maximum 2 mm to 3 mm bias towards the tropopause, although rising events in 2014-JJA feature a distinct kink at about 12 km. For FY-3D data in 2019-JAS, however, such a distinctive kink is observable at altitudes of about 18 km and 26 km, for setting and rising events, respectively. The standard deviation (16% and 84% percentiles) features similar characteristics in all cases increasing with decreasing altitude, reaching values up to about ±20 mm at altitudes of 10 km height.

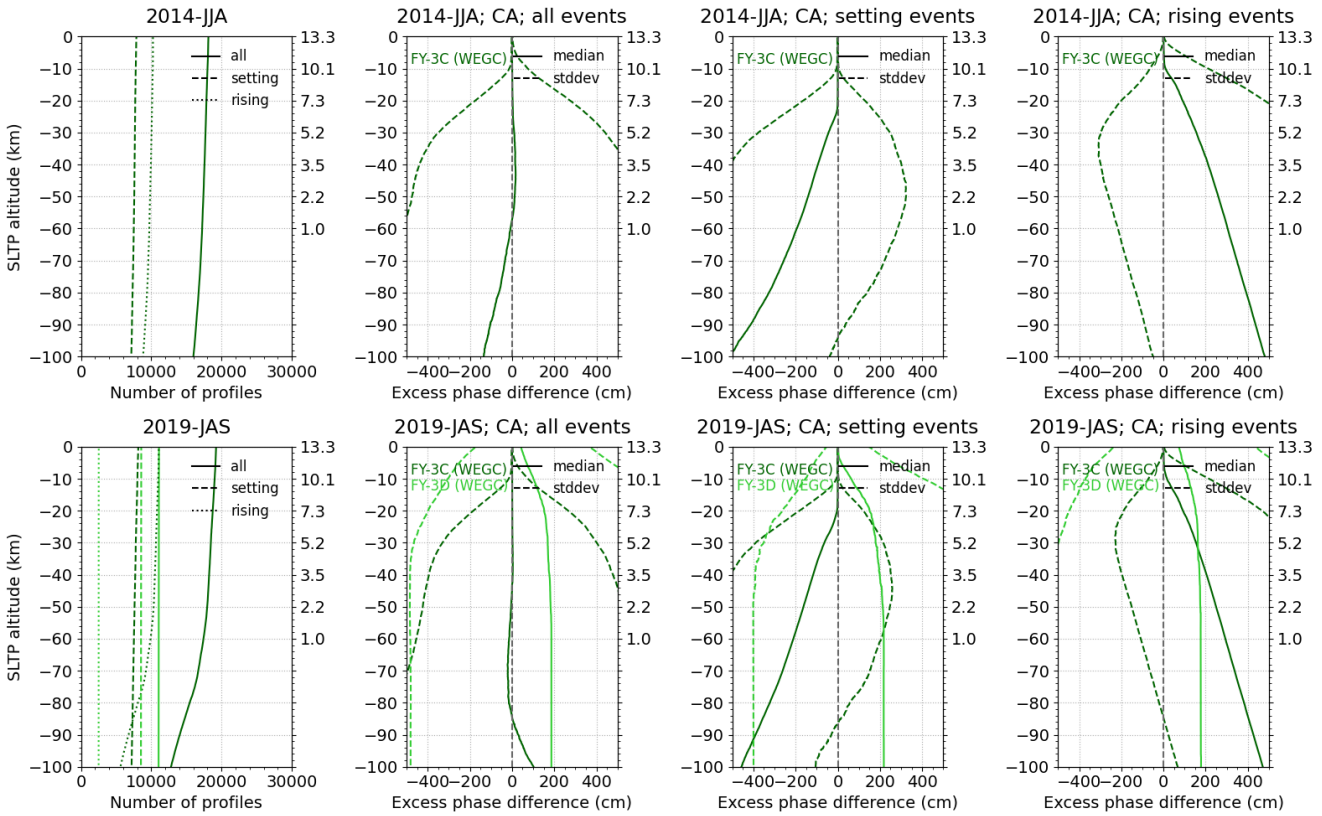


Figure 5. Systematic difference profiles (median) and standard deviation profile estimates (stddev; 16% and 84% percentiles) as function of SLTP altitude (focus here on troposphere below ∼13 km; see approximate MSL altitudes labeled at right side of panels), from the statistical ensemble of difference profiles between the excess phase profiles of WEGC and NSSC (i.e., the latter serving as reference dataset here), for the FY-3C JJA 2014 (upper row) and FY-3C and FY-3D JAS 2019 data (lower row). Together with the number of profiles as a function of altitude (left column) shown for context, the statistical results are depicted for all events (middle-left), setting events (middle-right), and rising events (right), respectively.

The comparison results in the troposphere, best represented as function of SLTP altitude in Figure 5, start to deviate from essentially zero-difference for FY-3C data downwards to -25 km and -10 km for setting and rising events, respectively. Below these altitudes, differences increase up to several meters towards the lower troposphere and in the boundary layer, where proper signal tracking is challenging. As already observed in the evaluation using MSL altitude as vertical coordinate the FY-3D data shows increased differences compared to FY-3C. By separate intercomparison with model profiles from ERA5 (not shown), it was possible to attribute the distinct deviation to be inherent to NSSC data processing. Further investigation showed that those differences arise from different transition criteria applied in the combination algorithms of closed and open loop data by WEGC and NSSC.

3.4 Bending angle cross-evaluation

Here we present the cross-evaluation results of the NSMC and WEGC processed bending angle data for the later 2019-JAS period in comparison to corresponding forward-modeled ECMWF ERA5 bending angle profiles, as depicted in Figure 6. Results for the 2014 data were excluded here, due to constraints in the early FY-3C data processing at NSMC's FengYun satellite data center, where these early data have not been reprocessed yet. With regard to the penetration depth, the NSMC bending angle data features more soundings deeper into the lower troposphere/boundary layer compared to WEGC. This limitation in WEGC FY-3 data processing is under further inspection and improvement for the future.

In general, the bending angle data feature almost no bias between around 5 km and 35 km for data from both processing centers. Above, at higher altitudes, systematic differences against ERA5 data increase and so does the standard deviation of the statistic. Looking at the number of profiles as a function of altitude in Figure 6 we can observe small kinks in the profile statistic at about 25 km and about 15 km, which are also visible at about 25 km in the median and standard deviation of the comparison of NSMC data against ECMWF. We note that this discontinuity observed here does no longer occur in the latest improved processing version for FY-3E and FY-3F data processing at NSSC/NSMC.

As a complement to the bending angle evaluation results presented in Figure 6, we specifically analyzed four vertical atmospheric regions (lower troposphere: LT, upper troposphere: UT, lower stratosphere: LS, upper stratosphere: US), as introduced in Section 2.2. Based on the statistical measures of the vertical bending angle profiles, we investigate the performance of the data processing systems with respect to the different atmospheric regions. Table 1 lists the statistical results averaged within the respective altitude layer, for the combined setting and rising WEGC and NSMC bending angle data versus forward-modeled collocated profiles extracted from ERA5 forecast data.

We observe best comparison results with small biases and narrow standard deviation in the differences in the lower troposphere and upper troposphere regions, where RO measurements are known to provide best results. Below, in the lower troposphere, the spread of the data increases due to higher variability and model imperfections. Above, in the upper stratosphere, a small positive systematic difference between the RO data and the ECMWF reanalysis data prevails, for data from both processing centers and for all time periods considered, which is presumably a small bias feature of the ECMWF data (e.g., Hersbach et al., 2020; Steiner et al., 2020).

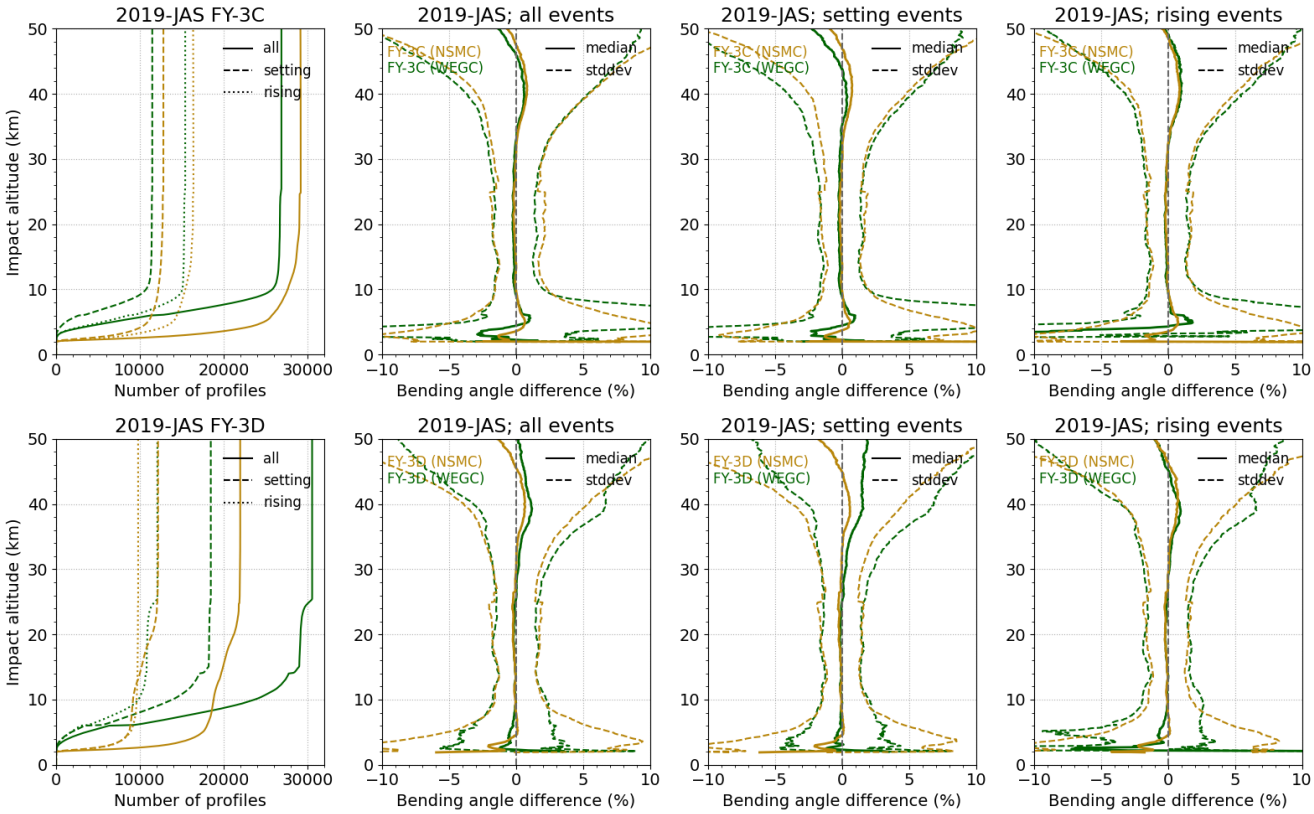


Figure 6. Systematic difference profiles (median) and standard deviation profile estimates (stddev; 16% and 84% percentiles) as function of impact altitude, from the statistical ensemble of difference profiles between the bending angle profiles of WEGC (green) and NSMC (orange) compared to matching forward-modeled ERA5 profiles (serving as reference dataset here), respectively, for the FY-3C JAS 2019 (upper row) and FY-3D JAS 2019 data (lower row). Together with the number of profiles as a function of altitude (left column) shown for context, the statistical results are depicted for all events (middle-left), setting events (middle-right), and rising events (right), respectively.

Table 1. Bending angle intercomparison results, complementary to Fig. 6, for the FY-3C and FY-3D 2019 JAS period data, for four representative altitude layers: lower troposphere (LT, 2-5 km), upper troposphere (UT, 7-10 km), lower stratosphere (LS, 15-25 km), upper stratosphere (US, 40-45 km), shown as relative differences in %. First value of each entry represents the mean within the respective altitude layer and the corresponding standard deviation estimates (16% and 84% percentiles) in brackets.

level	**periods**	**troposphere**		**stratosphere**	
		LT	**UT**	**LS**	**US**
WEGC vs.	FY-3C 2019	−1.13 (−12.40 to 6.60)	0.10 (−1.82 to 4.51)	−0.21 (−1.62 to 1.28)	0.47 (−5.08 to 5.98)
ERA5	FY-3D 2019	−0.29 (−3.99 to 3.10)	−0.09 (−2.08 to 2.12)	−0.13 (−1.58 to 1.38)	0.84 (−4.79 to 6.26)
NSMC vs.	FY-3C 2019	−0.30 (−7.66 to 8.76)	0.12 (−1.87 to 3.11)	−0.13 (−1.72 to 1.78)	0.71 (−4.18 to 6.03)
ERA5	FY-3D 2019	−0.99 (−8.94 to 7.01)	−0.01 (−1.97 to 2.45)	−0.19 (−1.74 to 1.53)	0.49 (−5.76 to 6.03)

4 Conclusions

The Chinese polar-orbiting operational meteorological FengYun-3 satellite series is an important complement to the global contemporary weather and climate observing system using radio occultation. Within this study FY-3C and FY-3D GNOS low level data streams where prepared to interface and be processed with rOPS and further analyzed against NSSC/NSMC processed data to ensure suitable quality of the data for the use of benchmark climate data. The evaluation of the excess phase and bending angle processing of two independent processing centers, namely NSSC and WEGC, is unprecedented for FY-3 RO data and closes the gap in the assessment of FY-3 data from the SI-tied low-level data to bending angle data.

Basic cross-evaluation of the data ingestion was performed at POD and L1a excess phase data level, while thorough analysis was conducted at L1b bending angle data level. The analyzed data comprised the periods from June to September 2014 and July to August 2019. The comparison of orbit solutions provided by NSSC and calculated at WEGC showed good agreement with on average a 3D-RMS of 4.20 cm for FY-3C in 2014 and of 5.72 cm for FY-3C and 3.31 cm for FY-3D in 2019, a solid basis for subsequent excess phase processing.

Intercomparison of excess phase data between WEGC and NSSC was analyzed for two distinctive altitude domains: a combined mesospheric and stratospheric region using MSL altitude as vertical coordinate (10 km to 80 km), and secondly a tropospheric region as function of SLTP altitude (0 km to -100 km). In general, the evaluation showed small differences at millimetric level in the upper atmosphere domain, but revealed some differences in the combination of closed and open loop data applied in the calibration algorithms at the two processing chains, causing increased deviations, most pronounced for FY-3D data at an MSL altitude near 18 km and 26 km, for setting and rising events, respectively. In the tropospheric domain larger differences due to more challenging signal tracking can be observed.

Validation of bending angle data showed that NSMC data from the FengYun satellite data center and WEGC-processed FY-3 data show almost no systematic differences between 5 km and 35 km, compared to collocated forward-modeled ECMWF ERA5 bending angle profiles. At the same time, we found larger differences for FY-3C in the early 2014-JJA NSMC-processed data, due to constraints in their early-stage processing version for these data. On the other hand, WEGC data provides a limited number of profiles penetrating the lower part of the troposphere and the boundary layer. These are valuable findings to inform further improvements towards long-term climate-quality data processing.

Concluding, the cross-comparison of L1a excess phase data showed good agreement and high consistency for FY-3C and also FY-3D data in most respects; the latter also showed some remaining deviations which help to further improve the processing chains. In general the validation results of L1b bending angle data are promising, although a state-of-the-art reprocessing of the early FY-3C data at the FengYun satellite data center would be of high value for climate applications. Overall, the results based on the selected 3-monthly periods are promising and justify the use of FY-3 data (after robust quality control) and provide a good base in order to ensure a multiyear re-processing of FY-3 data with adequate quality and consistency to serve climate-quality data processing results. In this way it will support the provision of long-term multi-mission RO data records with including uncertainty estimation, for the benefit of climate monitoring and research.

Declarations

Code availability. The code used to produce the results of this study is available from the corresponding author upon qualified request.

Data availability. The datasets underlying the results of this study are available from the corresponding author upon qualified request.

Ethics approval and consent to participate. Not applicable.

Author contributions. Conceptualization was provided by JI and GK, with support also by YS, WB, and XH. Methodology was provided by JI, GK, CL, and XM. JI elaborated the detailed algorithms and evaluation setup. CL and ML conducted the FengYun GNOS data preparation and the format conversion. JI, XM, PH, and CL performed the computational implementation and the analysis. JI prepared the figures and wrote the draft of the paper. GK supported this work with the provision of detailed design input and advice on all aspects of the study and significant contributions to writing of the paper. The computational implementation and analysis was extensively supported by MS. CL and ML advised on a range of technical and scientific aspects of the FengYun satellite data and were responsible for the data provision from NSSC and NSMC. YS and XH provided the supervision to FengYun satellite data processing and analysis work from NSSC and NSMC. All authors participated in the consolidation of the paper for submission and towards publication.

Competing interests. The authors declare that they have no conflict of interest.

Acknowledgements. The authors thank all members of the WEGC rOPS development team for supporting the development of this new processing system, and in particular the former team member V. Proschek for her support and advice during the early work on this study. We are also grateful to the Fengyun Satellite Data Center, China Meteorological Administration (CMA) Beijing, China, for making GNOS radio occultation data publicly available and the European Centre for Medium-Range Weather Forecasts (ECMWF) Reading, UK, for the provision of the ERA5 data (used at native model levels).

Funding. The work at University of Graz was supported by the Radio Occultation Meteorology Satellite Application Facility Fourth-Phase Partnership and Climate Research and Monitoring Project (ROMSAF4P/ROMSAF4CLIM) funded by EUMETSAT (ROMSAF4P, proj. no. PO4500023609/UG-WEGC) and by the Austrian Research Promotion Agency (FFG) through the Austrian Space Applications Programme (pre-project ATROMSAF2, proj. no. 873696; project ROMSAF4CLIM, proj. no. 892287) endowed by the Federal Ministry for Climate Action, Environment, Energy, Mobility, Innovation and Technology (BMK) and the publication costs received financial support by the University of Graz. On the Chinese side, this research was partially funded by the FengYun-3 GNOS development and manufacture project led by NSSC, CAS, the Youth Innovation Promotion Association of the Chinese Academy of Sciences (grant 2019151), the Youth Cross Team Scientific Research Project of the Chinese Academy of Sciences (JCTD-2021-10), and the National Natural Science Foundation of China (grants 41405039, 41775034, 42074042 and 42104032).

References

Anthes, R. A.: Exploring Earth's atmosphere with radio occultation: contributions to weather, climate, and space weather, Atmos. Meas. Tech., 4, 1077–1103, https://doi.org/10.5194/amt-4-1077-2011, 2011.

Bai, W., Liu, C., Meng, X., Sun, Y., Kirchengast, G., Du, Q., Wang, X., Yang, G., Liao, M., Yang, Z., Zhao, D., Xia, J., Cai, Y., Liu, L., and Wang, D.: Evaluation of atmospheric profiles derived from single- and zero-difference excess phase processing of BeiDou radio occultation data from the FY-3C GNOS mission, Atmos. Meas. Tech., 11, 819–833, https://doi.org/10.5194/amt-11-819-2018, 2018.

Bai, W. H., Sun, Y. Q., Du, Q. F., Yang, G. L., Yang, Z. D., Zhang, P., Bi, Y. M., Wang, X. Y., Cheng, C., and Han, Y.: An introduction to the FY3 GNOS instrument and mountain-top tests, Atmos. Meas. Tech., 7, 1817–1823, https://doi.org/10.5194/amt-7-1817-2014, 2014.

Bojinski, S., Verstraete, M., Peterson, T. C., Richter, C., Simmons, A., and Zemp, M.: The concept of Essential Climate Variables in support of climate research, applications, and policy, Bull. Amer. Meteor. Soc., 95, 1431–1443, https://doi.org/10.1175/BAMS-D-13-00047.1, 2014.

Cai, Y., Bai, W., Wang, X., Sun, Y., Du, Q., Zhao, D., Meng, X., Liu, C., Xia, J., Wang, D., Wu, D., Li, W., Wu, C., and Liu, C.: In-orbit performance of GNOS on-board FY3-C and the enhancements for FY3-D satellite, Adv. Space Res., 60, 2812–2821, https://doi.org/10.1016/j.asr.2017.05.001, 2017.

Du, Q., Sun, Y., Bai, W., Wang, X., Wang, D., Meng, X., Cai, Y., Xia, J., Wu, C., Liu, C., Li, W., and Liu, C.: The Advancements in Research of FY-3 GNOS II and Instrument Performance, in: IGARSS 2018 - 2018 IEEE International Geoscience and Remote Sensing Symposium, pp. 3347–3350, https://doi.org/10.1109/IGARSS.2018.8518228, 2018.

Gorbunov, M. E. and Kirchengast, G.: Wave-optics uncertainty propagation and regression-based bias model in GNSS radio occultation bending angle retrievals, Atmos. Meas. Tech., 11, 111–125, https://doi.org/10.5194/amt-11-111-2018, 2018.

Gorbunov, M. E., Kirchengast, G., and Lauritsen, K. B.: Generalized canonical transform method for radio occultation sounding with improved retrieval in the presence of horizontal gradients, Atmos. Meas. Tech., 14, 853–867, https://doi.org/10.5194/amt-14-853-2021, 2021.

Hajj, G. A., Kursinski, E. R., Romans, L. J., Bertiger, W. I., and Leroy, S. S.: A technical description of atmospheric sounding by GPS occultation, J. Atmos. Solar-Terr. Phys., 64, 451–469, https://doi.org/10.1016/S1364-6826(01)00114-6, 2002.

Hersbach, H., Bell, B., Berrisford, P., Hirahara, S., Horányi, A., Muñoz-Sabater, J., Nicolas, J., Peubey, C., Radu, R., Schepers, D., Simmons, A., Soci, C., Abdalla, S., Abellan, X., Balsamo, G., Bechtold, P., Biavati, G., Bidlot, J., Bonavita, M., De Chiara, G., Dahlgren, P., Dee, D., Diamantakis, M., Dragani, R., Flemming, J., Forbes, R., Fuentes, M., Geer, A., Haimberger, L., Healy, S., Hogan, R. J., Hólm, E., Janisková, M., Keeley, S., Laloyaux, P., Lopez, P., Lupu, C., Radnoti, G., de Rosnay, P., Rozum, I., Vamborg, F., Villaume, S., and Thépaut, J.-N.: The ERA5 global reanalysis, Q. J. R. Meteor. Soc., 146, 1999–2049, https://doi.org/10.1002/qj.3803, 2020.

Innerkofler, J., Kirchengast, G., Schwärz, M., Pock, C., Jäggi, A., Andres, Y., and Marquardt, C.: Precise Orbit Determination for Climate Applications of GNSS Radio Occultation including Uncertainty Estimation, Remote Sens., 12, 1180, https://doi.org/10.3390/rs12071180, 2020.

Innerkofler, J., Kirchengast, G., Schwärz, M., Marquardt, C., and Andres, Y.: GNSS radio occultation excess phase processing for climate applications including uncertainty estimation, Atmos. Meas. Tech. Discuss., pp. 1–46, https://doi.org/10.5194/amt-2023-28, 2023.

Kirchengast, G., Schwärz, M., Schwarz, J., Scherllin-Pirscher, B., Pock, C., Innerkofler, J., Proschek, V., Steiner, A. K., Danzer, J., Ladstädter, F., and Foelsche, U.: The reference occultation processing system approach to interpret GNSS radio occultation as SI-traceable planetary

system refractometer, presentation at OPAC-IROWG International Workshop 8–14 September 2016, Seggau/Leibnitz, Austria, available online at http://wegcwww.uni-graz.at/opacirowg2016 > Scient. Programme > Mon, Sep 12, 2016.

Kirchengast, G., Schwärz, M., Angerer, B., Schwarz, J., Innerkofler, J., Proschek, V., Ramsauer, J., Fritzer, J., Scherllin-Pirscher, B., and Rieckh, T.: Reference OPS DAD—Reference Occultation Processing System (rOPS) Detailed Algorithm Description, Tech. Rep. for ESA and FFG No. 1/2018, Doc-Id: WEGC–rOPS–2018–TR01, Issue 2.0, Wegener Center, Univ. of Graz, 2018.

Kursinski, E. R., Hajj, G. A., Schofield, J. T., Linfield, R. P., and Hardy, K. R.: Observing Earth's atmosphere with radio occultation measurements using the Global Positioning System, J. Geophys. Res., 102, 23 429–23 465, https://doi.org/10.1029/97JD01569, 1997.

Leroy, S. S., Dykema, J. A., and Anderson, J. G.: Climate benchmarking using GNSS occultation, in: Atmosphere and Climate: Studies by Occultation Methods, edited by Foelsche, U., Kirchengast, G., and Steiner, A. K., pp. 287–301, Springer, Berlin Heidelberg, https://doi.org/10.1007/3-540-34121-8_24, 2006.

Li, Y., Kirchengast, G., Scherllin-Pirscher, B., Schwaerz, M., Nielsen, J. K., Ho, S.-p., and Yuan, Y.-b.: A New Algorithm for the Retrieval of Atmospheric Profiles from GNSS Radio Occultation Data in Moist Air and Comparison to 1DVar Retrievals, Remote Sens., 11, 2729, https://doi.org/10.3390/rs11232729, 2019.

Liao, M., Zhang, P., Yang, G.-L., Bi, Y.-M., Liu, Y., Bai, W.-H., Meng, X.-G., Du, Q.-F., and Sun, Y.-Q.: Preliminary validation of the refractivity from the new radio occultation sounder GNOS/FY-3C, Atmos. Meas. Tech., 9, 781–792, https://doi.org/10.5194/amt-9-781-2016, 2016.

Liao, M., Healy, S., and Zhang, P.: Processing and quality control of FY-3C GNOS data used in numerical weather prediction applications, Atmos. Meas. Tech., 12, 2679–2692, https://doi.org/10.5194/amt-12-2679-2019, 2019.

Schwarz, J. C., Kirchengast, G., and Schwaerz, M.: Integrating uncertainty propagation in GNSS radio occultation retrieval: from bending angle to dry-air atmospheric profiles, Earth Space Sci., 4, 200–228, https://doi.org/10.1002/2016EA000234, 2017.

Schwarz, J. C., Kirchengast, G., and Schwaerz, M.: Integrating uncertainty propagation in GNSS radio occultation retrieval: from excess phase to atmospheric bending angle profiles, Atmos. Meas. Tech., 11, 2601–2631, https://doi.org/10.5194/amt-11-2601-2018, 2018.

Steiner, A. K., Ladstädter, F., Ao, C. O., Gleisner, H., Ho, S.-P., Hunt, D., Schmidt, T., Foelsche, U., Kirchengast, G., Kuo, Y.-H., Lauritsen, K. B., Mannucci, A. J., Nielsen, J. K., Schreiner, W., Schwärz, M., Sokolovskiy, S., Syndergaard, S., and Wickert, J.: Consistency and structural uncertainty of multi-mission GPS radio occultation records, Atmos. Meas. Tech., 13, 2547–2575, https://doi.org/10.5194/amt-13-2547-2020, 2020.

Sun, Y., Liu, C., Du, Q., Wang, X., Bai, W., Kirchengast, G., Xia, J., Meng, X., Wang, D., Cai, Y., Zhao, D., Wu, C., Li, W., and Liu, C.: Global Navigation Satellite System Occultation Sounder II (GNOS II), in: 2017 IEEE International Geoscience and Remote Sensing Symposium (IGARSS), pp. 1189–1192, https://doi.org/10.1109/IGARSS.2017.8127170, 2017.

Sun, Y., Bai, W., Liu, C., Liu, Y., Du, Q., Wang, X., Yang, G., Liao, M., Yang, Z., Zhang, X., Meng, X., Zhao, D., Xia, J., Cai, Y., and Kirchengast, G.: The FengYun-3C radio occultation sounder GNOS: a review of the mission and its early results and science applications, Atmos. Meas. Tech., 11, 5797–5811, https://doi.org/10.5194/amt-11-5797-2018, 2018.

Syndergaard, S.: Retrieval analysis and methodologies in atmospheric limb sounding using the GNSS radio occultation technique (Ph.D. thesis), Danish Meteorological Institute, Copenhagen, Denmark, 1999.

Wei, J., Li, Y., Zhang, K., Liao, M., Bai, W., Liu, C., Liu, Y., and Wang, X.: An Evaluation of Fengyun-3C Radio Occultation Atmospheric Profiles Over 2015–2018, Remote Sens., 12, 2116, https://doi.org/10.3390/rs12132116, 2020.

Zeng, Z., Sokolovskiy, S., Schreiner, W., Hunt, D., Lin, J., and Kuo, Y.-H.: Ionospheric correction of GPS radio occultation data in the troposphere, Atmos. Meas. Tech., 9, 335–346, https://doi.org/10.5194/amt-9-335-2016, 2016.

Zhang, P., Hu, X., Lu, Q., Zhu, A., Lin, M., Sun, L., Chen, L., and Xu, N.: FY-3E: The First Operational Meteorological Satellite Mission in an Early Morning Orbit, Adv. Atmos. Sci., 39, 1–9, https://doi.org/10.1007/s00376-021-1304-7, 2022.

Part III.

Summary and conlusions

7. Summary and conclusions

A beginning and an ending suggest the existence of a journey. Remove either and you've lost all three.

— Craig D. Lounsbrough

Considering the ongoing anthropogenic climate change and its implications (IPCC 2021) it is the responsibility of climate sciences to provide high-quality observations for monitoring the Earth's climate system. This work helps to solve the global climate monitoring problem (GCOS 2021) by contributing to the establishment of climate benchmark data records for detection, projection, and attribution of changes in the climate system. Satellite remote sensing data from GNSS RO qualify as reference climate data, due to their global coverage, high accuracy, long-term stability and by measuring ECVs, which can be tied to irrefutable standards (SI-second).

With the aim to establish SI-traceable climate benchmark data records WEGC's RO processing system underwent a major redesign by starting its processing from the raw measurement data rather than using existing excess phase data from other data centers. This was realized in this work within rOPS, comprising the novel implementation and embedment of a climate-quality POD processing setup (Paper 1; Innerkofler et al. 2020b) and RO excess phase processing system (Paper 2; Innerkofler et al. 2023) complementing the existing RO retrieval at WEGC. In the implementation we particularly focused on the derivation of uncertainty estimates attributed to the calculated orbit solutions and RO excess phase profiles. These estimated uncertainties further serve the uncertainty propagation within the rOPS along the RO retrieval chain to final ECVs as vertical profiles of atmospheric temperature, pressure, and humidity.

The successful realization of the POD and excess phase subsystems was tested on various RO datasets comprising data from the CHAMP, GRACE, and Metop missions, employing the derived uncertainty estimates and the quality control within rOPS (also implemented within this work). Additionally, orbit solutions

and excess phase profiles from other processing centers were used to evaluate the processing at WEGC. This also included forward-modeled data from ECMWF ERA5 at excess phase and bending angle level. In the final study of this thesis (Paper 3; Innerkofler et al. 2024) we used the newly developed system to evaluate RO low-level data from the Chinese FY-3 meteorological satellite series for the first time by intercomparison of results of two independent processing systems used at WEGC and NSSC/NSMC.

In the following (Section 7.1.1 to 7.1.3), I summarize the main results from the three research articles comprised within this work, before providing an overall synthesis of the conclusions and future prospects.

7.1. Main results of research articles

7.1.1. Summary and conclusions for Paper 1

Derivation of atmospheric state variables (ECVs) from RO measurements relies on precise positions, velocities, and clock biases of the GNSS transmitter and LEO receiver satellites. Within RO processing these highly accurate and reliable orbit data of proven quality co-determine the quality of the derived atmospheric excess phase profiles and subsequently of the final ECVs.

In Paper 1 (Innerkofler et al. 2020b) we presented a novel setup for the POD within the rOPS, which routinely and in parallel performs the LEO POD with the two independent software packages Bernese (v5.2) and NAPEOS (v3.3.1), employing two different GNSS orbit data products. This POD setup enables mutual consistency checks of the calculated orbit solutions and is used for position and velocity uncertainty estimation, including estimated systematic and random uncertainties.

The implementation of the new POD processing setup was evaluated based on a multi-month, multi-satellite POD result statistics from the CHAMP, GRACE, and Metop RO missions. By evaluation of the calculated orbits with satellite laser tracking data and the cross-validation against orbit solutions by other international processing centers we could acknowledge the good agreement of the calculated orbit solutions within the rOPS daily system modeling. The overall high consistency of uncertainty estimates within RO target specifications of 5 cm in position and $0.05\,\mathrm{mm\,s^{-1}}$ in velocity satisfies the requirements for highly accurate climate-quality RO processing. Furthermore, the system allows identification of periods with increased uncertainties in turn leading to RO profiles of somewhat reduced

quality, a potential benefit for adequate further use of the data in climate monitoring and research.

7.1.2. Summary and conclusions for Paper 2

Building on the work conducted in Paper 1 (Innerkofler et al. 2020b), the follow-on work presented in Paper 2 (Innerkofler et al. 2023), employed the input of WEGC's POD subsystem to derive atmospheric excess phase profiles from the raw RO measurement data. This work not only comprised the implementation of the excess phase processing, but also the conceptualization and realization of an uncertainty estimation of estimated random and estimated systematic uncertainties as basis for a rigorous quality control of the calculated excess phase profiles.

In particular within Paper 2 (Innerkofler et al. 2023) we focused on a comprehensive algorithmic description of the excess phase processing and the forward-modeling of excess phase profiles from ECMWF ERA5 reanalysis data, not yet published this detailed. The resulting (total) estimated uncertainties for each individual excess phase profile serve as starting point for the subsequent uncertainty propagation along the RO retrieval processing chain downward to the atmospheric ECV profiles.

The implementation of the excess phase processing system within rOPS was evaluated based on the European Metop RO dataset for three 3-month periods in 2008, 2013, and 2020. This comprised a sensitivity analysis for three representative atmospheric layers (tropo-, strato-, mesosphere), investigating consistency with ERA5-derived profiles, influences of different orbit and clock inputs, and consistency across the different Metop satellites. With these consistencies ranging from centimeter to submillimeter levels, we could acknowledge that the new processing can provide highly accurate and robust excess phase profiles. Further cross-evaluation with excess phase data from established data providers, such as EUMETSAT and UCAR, revealed subtle discrepancies but overall very close agreement, with larger differences found in the boundary layer compared to UCAR data. The new rOPS excess phase processing can hence be considered capable of producing reliable long-term data records including uncertainty estimation for the benefit of climate applications.

7.1.3. Summary and conclusions for Paper 3

Paper 3 (Innerkofler et al. 2024) used the established systems within the previous two publications and applied them to the Chinese FY-3 RO satellite data, thereby closing the gap between the raw measurements towards the bending angle processing. In this paper we presented results of the first cross-evaluation of RO low-level data,

obtained by the GNSS radio-occultation sounder (GNOS) instrument on board of FY-3 satellites, by analyses of results from the two independent processing chains at WEGC and NSSC/NSMC.

The 3-month evaluation periods of FY-3C and FY-3D data in 2014 (FY-3C only) and 2019 were used for comparison of the orbit solutions, atmospheric excess phases, and bending angle profiles. With adequate quality of the underlying orbit solutions of the two processing systems the excess phase cross-comparison showed high-quality consistency overall, while some differences were revealed in the closed-loop to open-loop transition of FY-3D data. At bending angle level cross-evaluation against ECMWF ERA5 modeled profiles, the analysis also showed good agreement and adequate quality in general, while some distinct deviations occurred below 26 km altitude in the early FY-3C rising event data in 2014.

This comparison of the two independent processing chains showed the high basic quality of the GNOS data for applications in climate research and NWP. At the same time the results provide valuable information for subsequent work to resolve remaining biases, improve current processing algorithms, and for including data from FY-3E, FY-3F, and FY-3G satellites.

7.2. Synthesis conclusions and prospects

Overall, we invested a substantial amount of work and dedication in the proper implementation of the POD (Paper 1; Innerkofler et al. 2020b) and excess phase processing (Paper 2; Innerkofler et al. 2023) subsystems within WEGC's RO processing system. The technical implementation of both subsystems and the included derivation of estimated random and estimated systematic uncertainties was accompanied by careful evaluation of the results at both processing levels, respectively.

By doing so, we could successfully accomplish the initial goal to tie the final derived ECV products to the SI-traceable input data, by closing the gap towards the existing RO bending angle retrieval of rOPS. Especially the implementation of uncertainty estimates at each level supports a rigorous quality control which enables to support climate analysis of the rOPS processed data. With the availability of estimated uncertainty at individual profile level, this also passes improvements on to derived climatologies, a major benefit for future data handling and climate trend analysis.

Furthermore, with the establishment of an FCDR at excess phase level, this work sets the stage to tackle the hypothesis by Yuan et al. 1993 three decades ago that monitoring trends in RO excess phase data records could be particularly

suitable to detect global and regional climate change. As a further consequence of this work and in support of the RO community, rOPS, now independent of externally pre-processed input data, represents a highly valuable software utility for cross-evaluation of existing RO processing systems, the identification of structural uncertainties in RO data, and the evaluation of future RO missions to come.

List of Acronyms

Symbols

COSMIC-1 Constellation Observing System for Meteorology, Ionosphere, and Climate-1. 26, 32

COSMIC-2 Constellation Observing System for Meteorology, Ionosphere, and Climate-2. 26

FY-3 FengYun-3 [satellite series]. 26, 106, 123

A

AC Analysis Center. 73

AIRS Atmospheric Infrared Sounder. 24

AIUB Astronomical Institute at the University of Bern. 73

AMSU Advanced MSU. 24

ARP Antenna Reference Point. 106

ASAP Austrian Space Applications Programme. 73

ASC Advanced Star Camera. 73

ATMS Advanced Technology Microwave Sounder. 24

B

BB Baseband. 106

BDS BeiDou Navigation Satellite System. 26, 123

BIPM Bureau International des Poids et Mesures. 30

BMVIT Ministry for Transport, Innovation, and Technology. 73

C

CA California. 106

CAS Chinese Academy of Sciences. 123

CB Conservative Bound. 73

CDAAC COSMIC Data Analysis and Archive Center. 73, 106

CDDIS Crustal Dynamics Data Information System. 106

CDR Climate Data Record. 28

CDS Climate Data Store. 106

CHAMP Challenging Mini-Satellite Payload. 26, 27, 32, 33, 73

CICERO Community Initiative for Continuous Earth Remote Observation. 26

CL Closed Loop. 106, 123

CMA Chinese Meteorological Administration. 123

CO_2 Carbon Dioxide. 19

CODE Center for Orbit Determination. 45, 73, 106, 131

COM Center-of-Mass. 106

COSMIC Constellation Observing System for Meteorology, Ionosphere, and Climate. 106, 129, 130

CrIS Cross-track Infrared Sounder. 24

D

DLL Delay-locked Loop. 106

DLR Deutsches Zentrum für Luft und Raumfahrt. 73

DSM Daily System Modeling. 45, 73, 106

DTU Technical University of Denmark. 73

E

ECEF Earth-centered, Earth-fixed. 106

ECI Earth Centered Inertial reference frame. 106

ECMWF European Centre for Medium-Range Weather Forecasts. 42, 106, 123, 131

ECOM Empirical CODE Orbit Model. 73

ECV Essential Climate Variable. 19, 20, 25–28, 41, 73, 106

EOP Earth Observation Parameters. 73, 106

EPS EUMETSAT Polar System. 106

ERA5 ECMWF Re-Analysis Version 5. 106

ESA European Space Agency. 73

ESM Event System Modeling. 106

ESOC European Space Operations Centre. 73

EUMETSAT European Organization for the Exploitation of Meteorological Satellites. 73, 106, 131

F

FCDR Fundamental Climate Data Record. 19, 20, 34, 73, 106

FMO Forward-Modeled. 106

FWF Austrian Science Fund (Fonds zur Förderung der wissenschaftlichen Forschung). 73

G

Galileo Galileo Navigation Satellite System. 26

GCOS Global Climate Observing System. 19, 20, 23–28, 30, 106, 132

GEOLAB Geomagnetic Laboratory. 106

GFZ German Research Centre for Geosciences [former GeoForschungsZentrum]. 73, 106, 123

GLONASS Global'naya Navigatsionnaya Sputnikovaya Sistema/Global Navigation Satellite System. 26

GNOS GNSS radio-occultation sounder. 106, 123

GNSS Global Navigation Satellite System. 20, 26, 27, 30, 31, 42, 45, 73, 106, 123, 132

GPS Global Positioning System. 26, 27, 33, 73, 123, 132

GPS/MET Global Positioning System/Meteorology [experiment]. 27

GRACE Gravity Recovery and Climate Experiment. 32, 73

GRAS Global Navigation Satellite Systems Receiver for Atmospheric Sounding. 73, 106

GRUAN GCOS Reference Upper Air Network. 24

GUM Guide to the Expression of Uncertainty in Measurement. 106

H

HF High-Pass-Filtered. 106

HQ Headquarters. 73

I

IASI Infrared Atmospheric Sounding Interferometer. 24

ICAROS International Laboratory on Climate and Atmosphere Research with Occultation & Reflectometry Observing Systems. 123

IERS International Earth Rotation and Reference Systems Service. 73, 106

IFS Integrated Forecasting System. 106, 123

IGS International GNSS Service. 45, 73, 106

ILRS International Laser Ranging Service. 73

IPCC Intergovernmental Panel on Climate Change. 19, 106

IR Infrared. 73

ITRF International Terrestrial Reference Frame. 73

J

JCGM Joint Committee for Guides in Metrology. 73

JPL Jet Propulsion Laboratory. 73

L

LC Linearly Ionosphere-corrected. 106

LEO Low Earth Orbit. 24, 26, 31, 40, 42, 45, 73, 106, 123

LF Low-Pass-Filtered. 106

LRR Laser Retroreflector. 73

LS Lower Stratosphere. 123

LT Local Time. 123

M

Metop Meteorological Operational [satellite series]. 26, 32, 73, 106

MSL Mean Sea Level. 106, 123

MSU Microwave Sounding Unit. 24, 129

MTP Mean Tangent Point. 106

N

NAPEOS Navigation Package for Earth Orbiting Satellites (POD Software). 106

NASA National Aeronautics and Space Administration. 73

NCO Numerically Controlled Oscillator. 106

NDM Navigation Data Message. 106

NRT Near Real Time. 38

NSMC National Satellite Meteorological Center. 123

NSSC National Space Science Center. 123

NWP Numerical Weather Prediction. 123

O

ODP Occultation Data Processing. 45, 73, 106

OL Open Loop. 106, 123

P

PCO Phase Center Offset. 73, 106

PCV Phase Center Variation. 73, 106

PLL Phase Locked Loop. 106

POD Precise Orbit Determination. 20, 31, 32, 36, 40, 45, 73, 106, 133

Q

QC Quality Control. 106

R

RAOB Radiosonde Observation (Rawinsonde Observation). 106

RCB Receiver Clock Bias. 73

RINEX Receiver Independent Exchange Format. 73

RMS Root Mean Square [error]. 73, 106

RO Radio Occultation. 20, 23, 25–31, 33, 36, 38, 40, 42, 43, 73, 106, 123, 137

rOPS Reference Occultation Processing System. 20, 34, 37–39, 45, 73, 106

RTN Radial-Transverse-Normal. 73

S

S/A Selective Availability. 33

SAW Sub-arctic Winter. 106

SG Second Generation. 106

SI International System of Units. 19, 20, 106

SLR Satellite Laser Ranging. 73

SLTH Straight-line Tangent Height. 106

SLTP Straight Line Tangent Point. 123

SP3 Standard Product 3 [orbit file format]. 73, 106

Spire Spire Global, Inc.. 26

STD Standard. 106

T

TEC Total Electron Content. 106

U

UCAR University Corporation for Atmospheric Research. 73, 106

US United States. 123

UT Universal Time. 123

W

WEGC Wegener Center for Climate and Global Change [University of Graz]. 20, 37, 39, 73, 106, 123

WMO World Meteorological Organization. 19

List of Figures

Part I. Synopsis

2.1. Illustration of space-qualified GNSS atomic clocks 17
2.2. Representative Allan deviation versus averaging time for a variety of GNSS flight clocks 18
2.3. Schematic of RO measurement principle 19

3.1. Schematic view of the RO observing geometry with real proportions 24
3.2. Overview of the rOPS as functional block diagram 28
3.3. Number of OPSv5.6 RO profiles from 2001 to 2020 31
3.4. Distribution of COSMIC-1 RO profiles based on latitude and local time 33

Part II. Research articles

Paper 1: Precise orbit determination for climate applications of GNSS radio occultation including uncertainty estimation

1. Schematic overview of parts of the rOPS with focus on the daily system modeling 41
2. Propagated random position and velocity uncertainty estimates from Bernese for Metop-A (1 July, 2013) 48
3. Propagated random position and velocity uncertainty estimates from Bernese for the GPS constellation (12 March, 2016) 49
4. Daily 3D-RMS orbit differences between the WEGC-Bernese (CODE) primary solution and WEGC-Bernese (JPL), WEGC-Napeos, UCAR, EUMETSAT, and AIUB orbit solutions for CHAMP and GRACE-A (Jul-Sep 2008) and Metop-A/B (Jul-Sep 2013 50
5. SLR residuals of CHAMP and GRACE-A orbits for 12 high-quality SLR stations (Jul-Sep 2008) 52

6. Daily position and velocity uncertainty estimates for the WEGC-Bernese primary orbit for CHAMP and GRACE-A (Jul-Sep 2008), Metop-A/B (Jul-Sep 2013) and GPS-23/24 (Jul-Sep 2013) 54
7. Schematic illustration of the orbit processing setup of the Bernese and NAPEOS software packages used in this study for the LEO POD 57

Paper 2: GNSS radio occultation excess phase processing for climate applications including uncertainty estimation

1. General schematic overview of WEGC's rOPS subsystems 67
2. Detailed Schematic overview of parts of WEGC's rOPS relevant to this study 68
3. Occultation event geometry, defining important location and angular variables of an RO event 70
4. Global distribution of Metop-A/B RO events on 1 July 2013 . . . 72
5. Forward-modeled example profiles from refractivity to bending angle and excess phase and difference between modeled and observed excess phase 73
6. L1a excess-phase processing algorithm workflow of the rOPS ODP 76
7. Illustration of forward-modeled and retrieved excess-phase profiles and the derived baseband delta excess phase, and the low-pass-filtered and high-pass-filtered baseband delta excess-phase profiles 79
8. Overview of exemplary estimated random, basic systematic, and apparent systematic uncertainty components for Metop-A on 1 July 2008 83
9. Number of RO events per time period (2008-JAS, 2013-JAS, 2020-DJF) processed at WEGC and converted from EUMETSAT and CDAAC to the rOPS format 83
10. Sensitivity analysis results from comparing WEGC rOPS L1a excess-phase profiles from Metop-A/B/C against collocated forward-modeled profiles from ERA5 84
11. Sensitivity analysis results from comparing WEGC rOPS L1a excess-phase profiles from Metop-A/B/C based WEGC–Bernese orbits minus excess-phase profiles based on EUMETSAT POD solutions . 84
12. Sensitivity analysis results from comparing co-located WEGC rOPS L1a excess-phase profiles from Metop-A/B/C 85
13. Number of excess-phase difference-pair profiles used for the ensemble statistics for the stratosphere and mesosphere region and the troposphere region 87

14. Systematic difference and standard deviation profiles as a function of MSL altitude from the statistical ensemble differences between excess-phase profiles from WEGC and UCAR/CDAAC compared to EUMETSAT 88
15. Systematic difference and standard deviation profiles as a function of SLTP altitude from the statistical ensemble differences between excess-phase profiles from WEGC and UCAR/CDAAC compared to EUMETSAT 89
16. Daily averages of estimated random and estimated systematic uncertainties based on uncertainty profiles of an individual RO event for the example days 90

Paper 3: Evaluation of excess phase and bending angle data from FengYun-3 radio occultation based on two independent processing chains

1. Schematic overview of the WEGC evaluation strategy and setup for the NSSC/NSMC FY-3 GNOS data evaluation 103
2. Daily radial, transverse, and cross-track orbit comparison between WEGC and NSSC POD processing for FY-3C (Jun-Aug 2014) and FY-3C/D (Jul to Sep 2019) 104
3. Numbers of FY-3C/D low-level RO event data, excess phase data, and bending angle data) 105
4. Systematic difference profiles and standard deviation profile estimates as function of MSL altitude between WEGC and NSSC excess phase profiles 106
5. Systematic difference profiles and standard deviation profile estimates as function of SLTP altitude between WEGC and NSSC excess phase profiles 107
6. Systematic difference profiles and standard deviation profile estimates as function of impact altitude between WEGC/NSSC bending angle profiles compared forward-modeled ERA5 profiles 109

List of Tables

Part I. Synopsis

2.1. Overview on Essential Climate Variables 12
2.2. The seven SI base units and their corresponding defining constants 16

Part II. Research articles

Paper 1: Precise orbit determination for climate applications of GNSS radio occultation including uncertainty estimation

1. Summary of orbit processing models, parameters, and data 45
2. Orbit solutions and metadata used in this study 46
3. Orbit comparison for position and velocity (radial, along-track, cross-track, and 3D-RMS) for different orbit solution compared to WEGC-Bernese primary orbit 51
4. Mean and standard deviation of SLR residuals for the full set of SLR stations and selected high-quality stations for CHAMP and GRACE-A (Jun-Aug 2008) 52
5. Random and systematic 3D and component-wise position uncertainty estimates 52

Paper 2: GNSS radio occultation excess phase processing for climate applications including uncertainty estimation

1. External input data used by the different subsystems of the rOPS ODP L1a processing system 69
2. Orbit and clock data output from the rOPS POD processing . . . 72
3. Selected Metop-A RO example events, representing standard, tropical, and sub-arctic winter conditions 73
4. Overview of the rOPS L1a quality processing steps 79

5. Metop orbit intercomparisons for position and velocity for different orbit solutions for the 2013-JAS and 2020-DJF periods, compared to the EUMETSAT–NAPEOS POD solution 85

Paper 3: Evaluation of excess phase and bending angle data from FengYun-3 radio occultation based on two independent processing chains

1. FY-3C/D Bending angle intercomparison results for four representative altitude layers (Jun-Sep 2019) 109

Bibliography

Alemany, F. M., C. Marquardt, A. von Engeln, S. Padovan, S. Paolella, R. Notarpietro, F. Sancho, Y. Andres, and L. Butenko (2022). *EUMETSAT GRAS reprocessing activities*. Presentation at OPAC-IROWG International Workshop 8–14 September 2022, Leibnitz/Seggau, Austria. URL: https://static.uni-graz.at/fileadmin/veranstaltungen/opacirowg2022/programme/08.9.22/AM/Session_2/OPAC-IROWG-2022_Alemany.pdf (visited on 06/27/2024).

Altamimi, Z., X. Collilieux, and L. Métivier (Aug. 2011). "ITRF2008: an improved solution of the international terrestrial reference frame". *J. Geodesy* 85, pp. 457–473. DOI: 10.1007/s00190-011-0444-4.

Angerer, B., F. Ladstädter, B. Scherllin-Pirscher, M. Schwärz, A. K. Steiner, U. Foelsche, and G. Kirchengast (2017). "Quality aspects of the WEGC multi-satellite GPS radio occultation record OPSv5.6". *Atmos. Meas. Tech.* 10, pp. 4845–4863. DOI: 10.5194/amt-10-4845-2017.

Angling, M. J., S. Elvidge, and S. B. Healy (2018). "Improved model for correcting the ionospheric impact on bending angle in radio occultation measurements". *Atmos. Meas. Tech.* 11, pp. 2213–2224. DOI: 10.5194/amt-11-2213-2018,.

Anthes, R. A. (2011). "Exploring Earth's atmosphere with radio occultation: contributions to weather, climate, and space weather". *Atmos. Meas. Tech.* 4, pp. 1077–1103. DOI: 10.5194/amt-4-1077-2011.

Anthes, R. A., P. A. Bernhardt, Y. Chen, L. Cucurull, K. F. Dymond, D. Ector, S. B. Healy, S.-P. Ho, D. C. Hunt, Y.-H. Kuo, H. Liu, K. Manning, C. McCormick, T. K. Meehan, W. J. Randel, C. Rocken, W. S. Schreiner, S. V. Sokolovskiy, S. Syndergaard, D. C. Thompson, K. E. Trenberth, T.-K. Wee, N. L. Yen, and Z. Zeng (2008). "The COSMIC/FORMOSAT-3 mission: Early results". *Bull. Amer. Meteor. Soc.* 89, pp. 313–333. DOI: 10.1175/BAMS-89-3-313.

Anthes, R. A., C. Marquardt, B. Ruston, and H. Shao (2024). "Radio Occultation Modeling Experiment (ROMEX): Determining the impact of radio occultation observations on numerical weather prediction". *Bull. Amer. Meteor. Soc.* 105, E1552–E1568. DOI: 10.1175/BAMS-D-23-0326.1.

Ao, C. O., G. A. Hajj, T. K. Meehan, D. Dong, B. A. Iijima, A. J. Mannucci, and E. R. Kursinski (2009). "Rising and setting GPS occultations by the use of open-loop tracking". *J. Geophys. Res.* 114, D04101. DOI: 10.1029/2008JD010483.

Arnold, D., M. Meindl, G. Beutler, R. Dach, S. Schaer, S. Lutz, L. Prange, K. Sośnica, L. Mervart, and A. Jäggi (May 2015). "CODE's new solar radiation pressure model for GNSS orbit determination". *J. Geodesy* 89. DOI: 10.1007/s00190-015-0814-4.

Arnold, D., O. Montenbruck, S. Hackel, and K. Sośnica (2018). "Satellite laser ranging to low Earth orbiters: orbit and network validation". *J. Geodesy*. ISSN: 1432-1394. DOI: 10.1007/s00190-018-1140-4.

Ashby, N. (2003). "Relativity in the Global Positioning System". *Living Rev. Relativity* 6. DOI: 10.12942/lrr-2003-1.

– (2004). "The Sagnac Effect in the Global Positioning System". In: *Relativity in Rotating Frames: Relativistic Physics in Rotating Reference Frames*. Ed. by G. Rizzi and M. L. Ruggiero. Dordrecht: Springer Netherlands, pp. 11–28. ISBN: 978-94-017-0528-8. DOI: 10.1007/978-94-017-0528-8_3.

– (2014). "Relativity in GNSS". In: *Springer Handbook of Spacetime*. Ed. by A. Ashtekar and V. Petkov. Berlin, Heidelberg: Springer Berlin Heidelberg, pp. 509–525. ISBN: 978-3-642-41992-8. DOI: 10.1007/978-3-642-41992-8_24.

Bai, W., C. Liu, X. Meng, Y. Sun, G. Kirchengast, Q. Du, X. Wang, G. Yang, M. Liao, Z. Yang, D. Zhao, J. Xia, Y. Cai, L. Liu, and D. Wang (2018). "Evaluation of atmospheric profiles derived from single- and zero-difference excess phase processing of BeiDou radio occultation data from the FY-3C GNOS mission". *Atmos. Meas. Tech.* 11, pp. 819–833. DOI: 10.5194/amt-11-819-2018.

Bai, W. H., Y. Q. Sun, Q. F. Du, G. L. Yang, Z. D. Yang, P. Zhang, Y. M. Bi, X. Y. Wang, C. Cheng, and Y. Han (2014). "An introduction to the FY3 GNOS instrument and mountain-top tests". *Atmos. Meas. Tech.* 7, pp. 1817–1823. DOI: 10.5194/amt-7-1817-2014.

Bancroft, S. (Jan. 1985). "An Algebraic Solution of the GPS Equations". *IEEE T. Aero. Elec. Sys.* AES-21, pp. 56–59. DOI: 10.1109/TAES.1985.310538.

Bauer, P., E. Andersson, and D. Richardson (2015). "The quiet revolution of numerical weather prediction". *Nature* 525, pp. 47–55. DOI: 10.1038/nature14956.

Baum, W. A. and A. D. Code (1953). "A photometric observation of the occultation of σ ARIETIS by Jupiter". *Astronomical Journal* 58, pp. 108–112. DOI: 10.1086/106829.

Beutler, G., A. Jäggi, U. Hugentobler, and L. Mervart (Oct. 2006). "Efficient satellite orbit modelling using pseudo-stochastic parameters". *J. Geodesy* 80, pp. 353–372. DOI: 10.1007/s00190-006-0072-6.

Beyerle, G., T. Schmidt, G. Michalak, S. Heise, J. Wickert, and C. Reigber (2005). "GPS radio occultation with GRACE: Atmospheric profiling utilizing the zero difference technique". *Geophys. Res. Lett.* 32, L13806. DOI: 10.1029/2005GL023109.

Bize, S. (2019). "The unit of time: Present and future directions". *C. R. Phys.* 20. The new International System of Units, pp. 153–168. DOI: 10.1016/j.crhy.2019.02.002.

Bock, H., R. Dach, A. Jäggi, and G. Beutler (Nov. 2009). "High-rate GPS clock corrections from CODE: Support of 1 Hz applications". *J. Geodesy* 83, pp. 1083–1094. DOI: 10.1007/s00190-009-0326-1.

Bodeker, G. E., S. Bojinski, D. Cimini, R. J. Dirksen, M. Haeffelin, J. W. Hannigan, D. F. Hurst, T. Leblanc, F. Madonna, M. Maturilli, A. C. Mikalsen, R. Philipona, T. Reale, D. J. Seidel, D. G. H. Tan, P. W. Thorne, H. Vömel, and J. Wang (2016). "Reference Upper-Air Observations for Climate: From Concept to Reality". *Bull. Amer. Meteor. Soc.* 97, pp. 123–135. DOI: 10.1175/BAMS-D-14-00072.1.

Bojinski, S., M. Verstraete, T. C. Peterson, C. Richter, A. Simmons, and M. Zemp (2014). "The concept of Essential Climate Variables in support of climate research, applications, and policy". *Bull. Amer. Meteor. Soc.* 95, pp. 1431–1443. DOI: 10.1175/BAMS-D-13-00047.1.

Boldbaatar, E., D. Grant, S. Choy, S. Zaminpardaz, and L. Holden (2023). "Evaluating Optical Clock Performance for GNSS Positioning". *Sensors* 23, 5998. DOI: 10.3390/s23135998.

Bonnedal, M., J. Christensen, A. Carlström, and A. Berg (2010). "Metop-GRAS in-orbit instrument performance". *GPS Solut.* 14, pp. 109–120. DOI: 10.1007/s10291-009-0142-3.

Born, M. and E. Wolf (1999). *Principles of Optics. Electromagnetic theory of propagation, interference and diffraction of light*. 7th ed. Cambridge, New York: Cambridge University Press.

Bureau International des Poids et Mesures (2019). *The International System of Units (SI)*. 9th edition. URL: https://www.bipm.org/en/publications/si-brochure (visited on 06/27/2024).

Cai, Y., W. Bai, X. Wang, Y. Sun, Q. Du, D. Zhao, X. Meng, C. Liu, J. Xia, D. Wang, D. Wu, W. Li, C. Wu, and C. Liu (2017). "In-orbit performance of GNOS on-board FY3-C and the enhancements for FY3-D satellite". *Adv. Space Res.* 60, pp. 2812–2821. ISSN: 0273-1177. DOI: 10.1016/j.asr.2017.05.001.

Carrascosa-Sanz, C., L. Fernández-Pérez, J.-M. Salcedo, D. Modrego-Contreras, M. Loiselet, J. Christensen, and M. Hägg (Oct. 2003). *Analysis of the Performances in Retrieved Atmospheric Profiles with Radio-Occultation Methods by Considering Different Sources of Error and Different Processing Techniques*. Atmospheric Remote Sensing using Satellite Navigation Systems Workshop, Matera, Italy. URL: https://esamultimedia.esa.int/docs/metop/Matera_oct2003_analysis.pdf (visited on 06/27/2024).

Case, K., G. Kruizinga, and S.-C. Wu (2010). *GRACE Level 1B Data Product User Handbook*. D-22027. Pasadena, CA: JPL. 62 pp. URL: https://podaac.jpl.nasa.gov/gravity/grace-documentation (visited on 06/27/2024).

Cirac-Claveras, G. (2019). "Weather Satellites: Public, Private and Data Sharing. The Case of Radio Occultation Data". *Space Policy* 47, pp. 94–106. ISSN: 0265-9646. DOI: 10.1016/j.spacepol.2018.08.002.

Combrinck, L. (2010). "Satellite Laser Ranging". In: *Sciences of Geodesy - I: Advances and Future Directions*. Ed. by G. Xu. Berlin, Heidelberg: Springer Berlin Heidelberg, pp. 301–338. ISBN: 978-3-642-11741-1. DOI: 10.1007/978-3-642-11741-1_9.

Comité International des Poids et Mesures (CIPM) (1967). *Comptes rendus de la CGPM (1967/68) (1969) 103*. DOI: 10.59161/CGPM1967RES1E.

Council, N. R. (2007). *Earth Science and Applications from Space: National Imperatives for the Next Decade and Beyond (Decadal Survey)*. The National Academies Press, Washington, D.C. ISBN: 978-0-309-10387-9. DOI: 10.17226/11820.

Dach, R., F. Andritsch, D. Arnold, S. Bertone, P. Fridez, A. Jäggi, Y. Jean, A. Maier, L. Mervart, U. Meyer, E. Orliac, E. Ortiz-Geist, L. Prange, S. Scaramuzza, S. Schaer, D. Sidorov, A. Sušnik, A. Villiger, P. Walser, C. Baumann, G. Beutler, H. Bock, A. Gäde, S. Lutz, M. Meindl, L. Ostini, K. Sośnica, A. Steinbach, and D. Thaller (2015). *Bernese GNSS Software Version 5.2, User manual*. Ed. by R. Dach, S. Lutz, P. Walser, and P. Fridez. Astron. Inst., Univ. of Bern. Bern, Switzerland: Bern Open Publishing. ISBN: 978-3-906813-05-9. DOI: 10.7892/boris.72297.

Danzer, J., M. Schwaerz, G. Kirchengast, and S. B. Healy (2020). "Sensitivity Analysis and Impact of the Kappa-Correction of Residual Ionospheric Biases on Radio Occultation Climatologies". *Earth Space Sci.* 7. e2019EA000942. DOI: 10.1029/2019EA000942.

Danzer, J., S. J. Haas, M. Schwaerz, and G. Kirchengast (2021). "Performance of the Ionospheric Kappa-Correction of Radio Occultation Profiles Under Diverse Ionization and Solar Activity Conditions". *Earth Space Sci.* 8. e2020EA001581. DOI: 10.1029/2020EA001581.

Dow, J. M., R. E. Neilan, and C. Rizos (Mar. 2009). "The International GNSS Service in a changing landscape of Global Navigation Satellite Systems". *J. Geodesy* 83, pp. 191–198. ISSN: 1432-1394. DOI: 10.1007/s00190-008-0300-3.

Du, Q., Y. Sun, W. Bai, X. Wang, D. Wang, X. Meng, Y. Cai, J. Xia, C. Wu, C. Liu, W. Li, and C. Liu (2018). "The Advancements in Research of FY-3 GNOS II and Instrument Performance". In: *IGARSS 2018 - 2018 IEEE International Geoscience and Remote Sensing Symposium*, pp. 3347–3350. DOI: 10.1109/IGARSS.2018.8518228.

Dunn, C., W. Bertiger, G. Franklin, I. Harris, G. Kruizinga, and T. Meehan (Jan. 2002). "The instrument on NASA's GRACE mission: Augmentation of GPS to achieve unprecedented gravity field measurements". In: *Proceedings of the 15th international technical meeting of the satellite division of the institute of navigation (ION GPS 2002)*, pp. 724–730.

ECMWF (2016). *Changes in ECMWF model*. URL: http://www.ecmwf.int/en/forecasts/documentation-and-support/changes-ecmwf-model (visited on 06/27/2024).

– (2019). *ERA-5 Documentation*. URL: https://confluence.ecmwf.int/display/CKB/ERA5%3A+data+documentation (visited on 06/27/2024).

Elachi, C. and J. van Zyl (2006). *Introduction to the Physics and Techniques of Remote Sensing*. 2nd ed. John Wiley & Sons, Inc. Publication. DOI: 10.1002/0471783390.

Eshleman, V. R. (1973). "The radio occultation method for the study of planetary atmospheres". *Planet. Space Sci.* 21, pp. 1521–1531. DOI: 10.1016/0032-0633(73)90059-7.

EUMETSAT (Oct. 2005). *EPS Mission Conventions Document*. EUMETSAT Doc. No. EPS/SYS/SPE/990002. Issue 1.2. Darmstadt, Germany: EUMETSAT. URL:

https://www-cdn.eumetsat.int/files/2020-04/pdf_ten_990002-eps-mission-cnv.pdf (visited on 06/27/2024).

EUMETSAT (2016). *Radio Occultation Level 1 Product Format Specification*. EUMETSAT Doc. No. EUM/TSS/SPE/16/817861. Issue v1A. Darmstadt, Germany: EUMETSAT.

– (2017). *GRAS Level 1B Bending Angle Climate Data Record Release 1 - Metop-A*. European Organisation for the Exploitation of Meteorological Satellites. Darmstadt, Germany. DOI: 10.15770/EUM_SEC_CLM_0015.

– (2018). *GNSS Navigation Bit Product Format Specification*. EUMETSAT Doc. No. EUM/TSS/SPE/17/953527. Issue v1C. Darmstadt, Germany: EUMETSAT.

Fjeldbo, G. and V. R. Eshleman (1965). "The Bistatic Radar-Occultation Method for the Study of Planetary Atmospheres". *J. Geophys. Res.* 70, pp. 3217–3225. DOI: 10.1029/JZ070i013p03217.

– (1968). "The atmosphere of Mars analyzed by integral inversion of the Mariner IV occultation data". *Planet. Space Sci.* 16, pp. 1035–1059. DOI: 10.1016/0032-0633(68)90020-2.

Fjeldbo, G., A. J. Kliore, and V. R. Eshleman (1971). "The neutral atmosphere of Venus as studied with the Mariner V radio occultation experiments". *The Astronomical Journal* 76, pp. 123–140. DOI: 10.1086/111096.

Fjeldbo, G., A. Kliore, D. Sweetnam, P. Esposito, B. Seidel, and T. Howard (1976). "The occultation of Mariner 10 by Mercury". *ICARUS* 29, pp. 439–444. DOI: 10.1016/0019-1035(76)90063-4.

Flechtner, F., P. Morton, M. Watkins, and F. Webb (2014). "Status of the GRACE Follow-On Mission". In: *Gravity, Geoid and Height Systems*. Ed. by U. Marti. Springer International Publishing, pp. 117–121. DOI: 10.1007/978-3-319-10837-7_15.

Foelsche, U., G. Kirchengast, M. Borsche, B. Pirscher, and A. K. Steiner (2008). "Creating a consistent radio occultation data base for climate studies in the upper troposphere and lower stratosphere". In: *Proc. of the ECMWF GRAS-SAF Workshop on Applications of Radio Occultation Measurements*. Reading, UK: ECMWF, pp. 151–165.

Foelsche, U., B. Scherllin-Pirscher, F. Ladstädter, A. K. Steiner, and G. Kirchengast (2011a). "Refractivity and temperature climate records from multiple radio occultation satellites consistent within 0.05 %". *Atmos. Meas. Tech.* 4, pp. 2007–2018. DOI: 10.5194/amt-4-2007-2011.

Foelsche, U., S. Syndergaard, J. Fritzer, and G. Kirchengast (2011b). "Errors in GNSS radio occultation data: relevance of the measurement geometry and obliquity of profiles". *Atmos. Meas. Tech.* 4, pp. 189–199. DOI: 10.5194/amt-4-189-2011.

Fritzer, J., G. Kirchengast, and M. Pock (2009). *EGOPS 5.5/SUM, End-to-End Generic Occultation Performance Simulation and Processing System, Version 5.5, Software User Manual*. WEGC-IGAM/Uni Graz Technical Report for ESA/ESTEC No. 1/2009, Doc-Id: WEGC–EGOPS–2009–TR01. Version 1. University of Graz, Austria: WEGC and IGAM.

Fujiwara, M., G. L. Manney, L. J. Gray, and J. S. Wright (2022). *SPARC Reanalysis Intercomparison Project (S-RIP) Final Report*. Tech. rep. 10th assessment report of the SPARC project, published by the International Project Office at DLR-IPA. also: WCRP Report 6/2021. WCRP. URL: https://elib.dlr.de/148623/ (visited on 06/27/2024).

GCOS (2003). *The second report on the adequacy of the global observing systems for climate in support of the UNFCCC*. WMO-TD/No. 1143. GCOS-82. Geneva: WMO. 85 pp. URL: https://library.wmo.int/idurl/4/41396 (visited on 06/27/2024).

– (2007). *GCOS Reference Upper-Air Network (GRUAN): Justification, requirements, siting and instrumentation options*. WMO-TD/No. 1379. GCOS-112. Geneva: WMO. 42 pp. URL: https://library.wmo.int/idurl/4/48112 (visited on 06/27/2024).

– (2010a). *Guideline for the Generation of Datasets and Products Meeting GCOS Requirements*. WMO-TD/No. 1530. GCOS-143, update to GCOS-128. Geneva: WMO. 12 pp. URL: https://library.wmo.int/idurl/4/39563 (visited on 06/27/2024).

– (2010b). *Implementation plan for the global observing system for climate in support of the UNFCCC (2010 update)*. WMO-TD/No. 1523. GCOS-138, update to GCOS-92. Geneva: WMO. 186 pp. URL: https://library.wmo.int/idurl/4/58703 (visited on 06/27/2024).

– (2011). *Systematic Observation Requirements for Satellite-based Products for Climate (2011 Update)*. GCOS-154, supplement to GCOS-138, update to GCOS-107. Geneva: WMO. 138 pp. URL: https://library.wmo.int/idurl/4/48411 (visited on 06/27/2024).

– (2015). *Status of the Global Observing System for Climate – Full Report*. GCOS-195. Geneva: WMO. 358 pp. URL: https://library.wmo.int/idurl/4/54812 (visited on 06/27/2024).

GCOS (2021). *The Status of the Global Climate Observing System 2021: The GCOS Status Report*. GCOS-240. Geneva: WMO. 384 pp. URL: https://library.wmo.int/idurl/4/57596 (visited on 06/27/2024).

Gobiet, A., G. Kirchengast, G. L. Manney, M. Borsche, C. Retscher, and G. Stiller (2007). "Retrieval of temperature profiles from CHAMP for climate monitoring: Intercomparison with Envisat MIPAS and GOMOS and different atmospheric analyses". *Atmos. Chem. Phys.* 7, pp. 3519–3536. DOI: 10.5194/acp-7-3519-2007.

Gorbunov, M. E., K. B. Lauritsen, H.-H. Benzon, G. B. Larsen, S. Syndergaard, and M. B. Sørensen (2011). "Processing of GRAS/METOP radio occultation data recorded in closed-loop and raw-sampling modes". *Atmos. Meas. Tech.* 4, pp. 1021–1026. DOI: 10.5194/amt-4-1021-2011.

Gorbunov, M. E., H.-H. Benzon, A. S. Jensen, M. S. Lohmann, and A. S. Nielsen (2004). "Comparative analysis of radio occultation processing approaches based on Fourier integral operators". *Radio Sci.* 39, RS6004. DOI: 10.1029/2003RS002916.

Gorbunov, M. E. and G. Kirchengast (2018). "Wave-optics uncertainty propagation and regression-based bias model in GNSS radio occultation bending angle retrievals". *Atmos. Meas. Tech.* 11, pp. 111–125. DOI: 10.5194/amt-11-111-2018.

Gorbunov, M. E., G. Kirchengast, and K. B. Lauritsen (2021). "Generalized canonical transform method for radio occultation sounding with improved retrieval in the presence of horizontal gradients". *Atmos. Meas. Tech.* 14, pp. 853–867. DOI: 10.5194/amt-14-853-2021.

Griffiths, J. and J. Ray (2009). "On the precision and accuracy of IGS orbits". *J. Geodesy* 83. DOI: 10.1007/s00190-008-0237-6.

Griffiths, J. (Feb. 2019). "Combined orbits and clocks from IGS second reprocessing". *J. Geodesy* 93, pp. 177–195. DOI: 10.1007/s00190-018-1149-8.

Griggs, E., E. R. Kursinski, and D. Akos (2015). "Short-term GNSS satellite clock stability". *Radio Sci.* 50, pp. 813–826. DOI: 10.1002/2015RS005667.

Grunwaldt, L. and R. Neubert (2000). "First Results of Laser Ranging to the CHAMP Retroreflector". In: *Proceedings of the 12th International Workshop on Laser Ranging*. Matera, Italy.

Gurtner, W. (1994). "RINEX: The Receiver Independent Exchange Format". *GPS World* 5, pp. 48–52.

Hajj, G. A., E. R. Kursinski, L. J. Romans, W. I. Bertiger, and S. S. Leroy (2002). "A technical description of atmospheric sounding by GPS occultation". *J. Atmos. Solar-Terr. Phys.* 64, pp. 451–469. DOI: 10.1016/S1364-6826(01)00114-6.

Hajj, G. A. and L. J. Romans (1998). "Ionospheric electron density profiles obtained with the Global Positioning System: Results from the GPS/MET experiment". *Radio Sci.* 33, pp. 175–190. DOI: 10.1029/97RS03183.

Harting, A. (1996). "Considering clock errors in numerical simulations". *IEEE Transactions on Instrumentation and Measurement* 45, pp. 715–720. DOI: 10.1109/19.494587.

Hauschild, A., O. Montenbruck, and P. Steigenberger (July 2013). "Short-term analysis of GNSS clocks". *GPS Solut.* 17, pp. 295–307. DOI: 10.1007/s10291-012-0278-4.

Healy, S. (2007). "Operational assimilation of GPS radio occultation measurements at ECMWF". *ECMWF Newsletter* 111, pp. 6–11.

Healy, S. B. and I. D. Culverwell (2015). "A modification to the standard ionospheric correction method used in GPS radio occultation". *Atmos. Meas. Tech.* 8, pp. 3385–3393. DOI: 10.5194/amt-8-3385-2015.

Hedin, A. E. (1991). "Extension of the MSIS thermosphere model into the middle and lower atmosphere". *J. Geophys. Res.* 96, pp. 1159–1172. DOI: 10.1029/90JA02125.

Hernández-Pajares, M., J. M. Juan, J. Sanz, R. Orus, A. Garcia-Rigo, J. Feltens, A. Komjathy, S. C. Schaer, and A. Krankowski (2009). "The IGS VTEC mpas: a reliable source of ionospheric information since 1998". *J. Geodesy* 83, pp. 263–275. DOI: 10.1007/s00190-008-0266-1.

Hersbach, H., B. Bell, P. Berrisford, A. Horányi, J. M. Sabater, J. Nicolas, R. Radu, D. Schepers, A. Simmons, C. Soci, and D. Dee (2019). "Global reanalysis: goodbye ERA-Interim, hello ERA5". *ECMWF Newsletter* 159, pp. 17–24.

Hersbach, H. et al. (2020). "The ERA5 global reanalysis". *Q. J. R. Meteor. Soc.* 146, pp. 1999–2049. DOI: 10.1002/qj.3803.

Ho, S.-P., D. Hunt, A. K. Steiner, A. J. Mannucci, G. Kirchengast, H. Gleisner, S. Heise, A. von Engeln, C. Marquardt, S. Sokolovskiy, W. Schreiner, B. Scherllin-Pirscher, C. Ao, J. Wickert, S. Syndergaard, K. Lauritsen, S. Leroy, E. R. Kursinski, Y.-H. Kuo, U. Foelsche, T. Schmidt, and M. Gorbunov (2012). "Reproducibility of GPS radio occultation data for climate monitoring: Profile-

to-profile inter-comparison of CHAMP climate records 2002 to 2008 from six data centers". *J. Geophys. Res.* 117, D18111. DOI: 10.1029/2012JD017665.

Hofmann-Wellenhof, B., H. Lichtenegger, and E. Wasle (2008). *GNSS—Global Navigation Satellite Systems*. Wien New York: Springer. 516 pp. ISBN: 978-3-211-73012-6.

Hollberg, L. (2020). "Atomic Clocks for GNSS". In: *Position, Navigation, and Timing Technologies in the 21st Century*. John Wiley & Sons, Ltd. Chap. 47, pp. 1497–1519. ISBN: 9781119458555. DOI: 10.1002/9781119458555.ch47.

Hunt, D., J. Innerkofler, and S. Sokolovskiy (2018). *Honing in on atmospheric excess phase computation for Radio Occultation*. Fourth ICGPSRO 2018 and Eleventh FORMOSAT-3/COSMIC Data Users Workshop 2018, 18–20 April 2018: Taipei, Taiwan. URL: https://static.uni-graz.at/fileadmin/urbi-zentren/Wegcenter/3.Forschen/1.Forschungsgruppen/Arsclisys/Publikationen/2018_Hunt-Innerkofler-Sokolvskiy_Atmospheric-Exess-Phase-Computation.pdf (visited on 07/20/2023).

Hwang, C., T.-P. Tseng, T. Lin, D. Švehla, and B. Schreiner (May 2009). "Precise orbit determination for the FORMOSAT-3/COSMIC satellite mission using GPS". *J. Geodesy* 83, pp. 477–489. DOI: 10.1007/s00190-008-0256-3.

IERS (2004). *IERS Conventions (2003)*. IERS Technical Note No. 32. Dennis D. McCarthy and Gérard Petit (eds.) Frankfurt am Main, Germany: International Earth Rotation and Reference Systems Service. 127 pp.

– (Jan. 2010). *IERS Conventions (2010)*. IERS Technical Note No. 36. Gérard Petit and Brain Luzum (eds.) Frankfurt am Main, Germany: International Earth Rotation and Reference Systems Service. 180 pp.

IGS (2024). *International GNSS Service: Technical Report 2023*. IGS Annual Report. Dach, R. and Brockmann, E. (eds.) IGS Central Bureau and University of Bern. DOI: 10.48350/191991.

Innerkofler, J., G. Kirchengast, M. Schwärz, E. Wappis, C.-L. Liu, W.-H. Bai, Y.-Q. Sun, V. Irisov, V. Nguyen, and D. Masters (2020a). *Evaluation of the Climate Quality of FY-3 and Spire Radio Occultation Excess Phase Data*. Technical Report for FFG No. 2/2020, Doc-Id: WEGC–FFG–CLIMRECORD–TR–02–2020, Issue 1.0. University of Graz, Austria: WEGC. 40 pp.

Innerkofler, J., G. Kirchengast, M. Schwärz, C. Marquardt, and Y. Andres (2023). "GNSS radio occultation excess-phase processing for climate applications in-

cluding uncertainty estimation". *Atmos. Meas. Tech.* 16, pp. 5217–5247. DOI: 10.5194/amt-16-5217-2023.

Innerkofler, J., G. Kirchengast, M. Schwärz, C. Pock, A. Jäggi, Y. Andres, and C. Marquardt (2020b). "Precise Orbit Determination for Climate Applications of GNSS Radio Occultation including Uncertainty Estimation". *Remote Sens.* 12, 1180. DOI: 10.3390/rs12071180.

Innerkofler, J., C. Liu, G. Kirchengast, M. Schwärz, X. Meng, W. Bai, P. Hu, Y. Sun, M. Liao, and X. Hu (May 2024). "Evaluation of excess phase and bending angle data from FengYun-3 radio occultation based on two independent processing chains". *Res. Square*. Research Article Preprint. DOI: 10.21203/rs.3.rs-4400072/v1.

Innerkofler, J., C. Pock, G. Kirchengast, M. Schwärz, A. Jäggi, Y. Andres, C. Marquardt, and J. Schwarz (2019). *Multi-Mission Multi-Center Level 1 Data Inter-Validation towards Wegener Center Reference Occultation System Reprocessing*. Presentation at EUMETSAT ROM SAF-IROWG International Workshop 19–25 September 2019, Helsingør, Denmark. URL: https://rom-saf.eumetsat.int/romsaf-irowg-2019/en/open/1570629948.ef13300996e166e8fac3e3c5525e1169.pdf/Innerkofler__IROWG2019_final.pdf (visited on 06/27/2024).

IPCC (2021). *Climate Change 2021: The Physical Science Basis. Contribution of Working Group I to the Sixth Assessment Report of the Intergovernmental Panel on Climate Change*. Ed. by M.-D. V., P. Zhai, A. Pirani, S. L. Connors, C. Péan, S. Berger, N. Caud, Y. Chen, L. Goldfarb, M. I. Gomis, M. Huang, K. Leitzell, E. Lonnoy, J. B. R. Matthews, T. K. Maycock, T. Waterfield, O. Yelekçi, R. Yu, and B. Zhou. Cambridge, United Kingdom and New York, NY, USA: Cambridge University Press. 2204 pp. DOI: 10.1017/9781009157896.

J. L. Elliot (1996). "Probing Planetary Atmospheres with Stellar Occultations". *Ann. Rev. Earth Planet. Sci* 24, pp. 89–124. DOI: 10.1146/annurev.earth.24.1.89.

Jaduszliwer, B. and J. Camparo (2021). "Past, present and future of atomic clocks for GNSS". *GPS Solut.* 25. DOI: 10.1007/s10291-020-01059-x.

Jäggi, A., G. Beutler, and U. Hugentobler (2005). "Efficient Stochastic Orbit Modeling Techniques using Least Squares Estimators". In: *A Window on the Future of Geodesy*. Ed. by F. Sansò. Berlin, Heidelberg: Springer Berlin Heidelberg, pp. 175–180. ISBN: 978-3-540-27432-2.

Jäggi, A., R. Dach, O. Montenbruck, U. Hugentobler, H. Peter, and G. Beutler (Dec. 2009). "Phase center modeling for LEO GPS receiver antennas and its

impact on precise orbit determination". *J. Geodesy* 83, pp. 1145–1162. DOI: 10.1007/s00190-009-0333-2.

Jäggi, A., U. Hugentobler, and G. Beutler (Apr. 2006). "Pseudo-Stochastic Orbit Modeling Techniques for Low-Earth Orbiters". *J. Geodesy* 80, pp. 47–60. ISSN: 1432-1394. DOI: 10.1007/s00190-006-0029-9.

Jäggi, A. (2007). "Pseudo-Stochastic Orbit Modeling of Low Earth Satellites Using the Global Positioning System". PhD Thesis. AIUB.

JCGM (2008a). *Evaluation of Measurement Data – Guide to the Expression of Uncertainty in Measurement*. Rep. JCGM 100:2008. Joint Committee for Guides in Metrology, Office BIPM, Paris. DOI: 10.59161/JCGM100-2008E.

– (2008b). *Evaluation of Measurement Data – Supplement 1 to the "Guide to the Expression of Uncertainty in Measurement" – Propagation of distributions using a Monte Carlo method*. Rep. JCGM 101:2008. Joint Committee for Guides in Metrology, Office BIPM, Paris. DOI: 10.59161/JCGM101-2008.

– (2023). *Guide to the expression of uncertainty in measurement – Part 1: Introduction*. Rep. JCGM GUM-1:2023. Joint Committee for Guides in Metrology, Office BIPM, Paris. DOI: 10.59161/JCGMGUM-1-2023.

Jean, Y. and R. Dach (2016). *International GNSS Service Technical Report 2015*. IGS Annual Report. IGS Central Bureau and University of Bern. DOI: 10.7892/boris.80307.

Jones, H. (2018). "The recent large reduction in space launch cost". In: *International Conference on Environmental Systems*. 48th International Conference on Environmental Systems. URL: http://hdl.handle.net/2346/74082 (visited on 06/27/2024).

Jørgensen, J. L. (1999). "In Orbit Performance of a Fully Autonomous Star Tracker". In: *ESA 4th Symposion on Spacecraft Guidance Navigation and Control*. Noordwijk, Netherlands: ESTEC, European Space Agency.

Jørgensen, P. S., J. L. Jørgensen, T. Denver, and M. Betto (2005). "In-flight quality and accuracy of attitude measurements from the CHAMP advanced stellar compass". *Acta Astron.* 56. 4th IAA International Symposium on Small Satellites for Earth Observation, pp. 181–186. DOI: 10.1016/j.actaastro.2004.09.012.

Kim, J. and S. W. Lee (2009). "Flight performance analysis of GRACE K-band ranging instrument with simulation data". *Acta Astron.* 65, pp. 1571–1581. DOI: 10.1016/j.actaastro.2009.04.010.

Kirchengast, G. (2018). *Innovating GNSS and LEO occultations for weather and climate: three keys to next breakthroughs*. Presentation at IGL-1 International Workshop 6–11 September 2018, Beijing, China.

Kirchengast, G., J. Fritzer, and M. Pock (2012). *EGOPS 5.6 DDD – End-to-End Occultation Performance Simulation and Processing System Version 5.6 Detailed Design Document*. WEGC–IGAM/Uni Graz Technical Report for ESA/ESTEC No. 02/2012, Doc-Id: WEGC–EGOPS–2012–TR02, Issue 1.1. WEGC and IGAM.

Kirchengast, G., M. Schwärz, B. Angerer, J. Schwarz, J. Innerkofler, V. Proschek, J. Ramsauer, J. Fritzer, B. Scherllin-Pirscher, and T. Rieckh (2018). *Reference OPS DAD—Reference Occultation Processing System (rOPS) Detailed Algorithm Description*. Tech. Rep. for ESA and FFG No. 1/2018, Doc-Id: WEGC–rOPS–2018–TR01, Issue 2.0. Wegener Center, Univ. of Graz. 182 pp.

Kirchengast, G., M. Schwärz, J. Schwarz, B. Scherllin-Pirscher, C. Pock, J. Innerkofler, V. Proschek, A. K. Steiner, J. Danzer, F. Ladstädter, and U. Foelsche (2016). *The reference occultation processing system approach to interpret GNSS radio occultation as SI-traceable planetary system refractometer*. Presentation at OPAC-IROWG International Workshop 8–14 September 2016, Seggau/Leibnitz, Austria. URL: https://wegccon.uni-graz.at/opacirowg2016/data/public/files/opacirowg2016_Gottfried_Kirchengast_presentation_261.pdf (visited on 06/27/2024).

Klaes, D., M. Lugert, B. Bojkov, J. Ackermann, R. Borde, D. Coppens, S. Guedj, S. Linow, T. August, C. Marquardt, C. Anderson, R. Lang, R. Munro, A. Cacciari, G. Williams, A. Gatti, R. Broughton, G. Bruni, M. Tschimmel, and J. Wilson (2019). *Metop Science Update and the Metop-C Mission of the Eumetsat Polar System (EPS)*. Presentation at AMS 2019 Joint Satellite Conference 28 September – 04 October 2019, Boston, MA, USA. URL: https://ams.confex.com/ams/JOINTSATMET/meetingapp.cgi/Paper/359586 (visited on 06/27/2024).

Klaes, K. D., M. Cohen, Y. Buhler, P. Schlüssel, R. Munro, J.-P. Luntama, A. von Engeln, E. Ó. Clérigh, H. Bonekamp, J. Ackermann, and J. Schmetz (2007). "An Introduction to the EUMETSAT Polar system". *Bull. Amer. Meteor. Soc.* 88, pp. 1085–1096. DOI: 10.1175/BAMS-88-7-1085.

Kornfeld, R. P., B. W. Arnold, M. A. Gross, N. T. Dahya, W. M. Klipstein, P. F. Gath, and S. Bettadpur (2019). "GRACE-FO: The Gravity Recovery and Climate Experiment Follow-On Mission". *J. Spacecraft Rockets* 56, pp. 931–951. DOI: 10.2514/1.A34326.

Kouba, J. (2004). "Improved relativistic transformations in GPS". *GPS Solut.* 8, pp. 170–180. ISSN: 1521-1886. DOI: 10.1007/s10291-004-0102-x.

– (Apr. 2009). *A guide to using International GNSS Service (IGS) products*. Tech. rep. IGS. 34 pp. URL: http://acc.igs.org/UsingIGSProductsVer21.pdf (visited on 06/27/2024).

– (Sept. 2015). *A guide to using International GNSS Service (IGS) products*. Tech. rep. IGS. 34 pp. URL: https://files.igs.org/pub/resource/pubs/UsingIGSProductsVer21_cor.pdf (visited on 06/27/2024).

Kuo, Y.-H., T.-K. Wee, S. Sokolovskiy, C. Rocken, W. Schreiner, D. Hunt, and R. A. Anthes (2004). "Inversion and error estimation of GPS radio occultation data". *J. Meteor. Soc. Japan* 82, pp. 507–531. DOI: 10.2151/jmsj.2004.507.

Kursinski, E. R., G. A. Hajj, W. I. Bertiger, S. S. Leroy, T. K. Meehan, L. J. Romans, J. T. Schofield, D. J. McCleese, W. G. Melbourne, C. L. Thornton, T. P. Yunck, J. R. Eyre, and R. N. Nagatani (1996). "Initial Results of Radio Occultation Observations of Earth's Atmosphere Using the Global Positioning System". *Science* 271, pp. 1107–1110. DOI: 10.1126/science.271.5252.1107.

Kursinski, E. R., G. A. Hajj, J. T. Schofield, R. P. Linfield, and K. R. Hardy (1997). "Observing Earth's atmosphere with radio occultation measurements using the Global Positioning System". *J. Geophys. Res.* 102, pp. 23429–23465. DOI: 10.1029/97JD01569.

Lackner, B. C. (2010). *Exploring trend indicators of climate change from radio occultation and optimal trend detection (Ph.D. thesis)*. Sci. Rep. 38-2010. Austria: Wegener Center Verlag Graz. ISBN: 978-3-9502940-5-7.

Ladreiter, H. P. and G. Kirchengast (1996). "GPS/GLONASS sensing of the neutral atmosphere: Model independent correction of ionospheric influences". *Radio Sci.* 31, pp. 877–891. DOI: 10.1029/96RS01094.

Ladstädter, F., A. K. Steiner, U. Foelsche, L. Haimberger, C. Tavolato, and G. Kirchengast (2011). "An assessment of differences in lower stratospheric temperature records from (A)MSU, radiosondes, and GPS radio occultation". *Atmos. Meas. Tech.* 4, pp. 1965–1977. DOI: 10.5194/amt-4-1965-2011.

Ladstädter, F., A. K. Steiner, M. Schwärz, and G. Kirchengast (2015). "Climate intercomparison of GPS radio occultation, RS90/92 radiosondes and GRUAN from 2002 to 2013". *Atmos. Meas. Tech.* 8, pp. 1819–1834. DOI: 10.5194/amt-8-1819-2015.

Langley, R. B. (1997). "GPS Receiver System Noise". *GPS World* 8, pp. 40–45.

Leroy, S. S., J. A. Dykema, and J. G. Anderson (2006). "Climate benchmarking using GNSS occultation". In: *Atmosphere and Climate: Studies by Occultation Methods*. Ed. by U. Foelsche, G. Kirchengast, and A. K. Steiner. Berlin Heidelberg: Springer, pp. 287–301. DOI: 10.1007/3-540-34121-8_24.

Li, Y., G. Kirchengast, B. Scherllin-Pirscher, M. Schwaerz, J. K. Nielsen, S.-p. Ho, and Y.-b. Yuan (2019). "A New Algorithm for the Retrieval of Atmospheric Profiles from GNSS Radio Occultation Data in Moist Air and Comparison to 1DVar Retrievals". *Remote Sens.* 11, 2729. ISSN: 2072-4292. DOI: 10.3390/rs11232729.

Liao, M., S. Healy, and P. Zhang (2019). "Processing and quality control of FY-3C GNOS data used in numerical weather prediction applications". *Atmos. Meas. Tech.* 12, pp. 2679–2692. DOI: 10.5194/amt-12-2679-2019.

Liao, M., P. Zhang, G.-L. Yang, Y.-M. Bi, Y. Liu, W.-H. Bai, X.-G. Meng, Q.-F. Du, and Y.-Q. Sun (2016). "Preliminary validation of the refractivity from the new radio occultation sounder GNOS/FY-3C". *Atmos. Meas. Tech.* 9, pp. 781–792. DOI: 10.5194/amt-9-781-2016.

Liu, C.-L., G. Kirchengast, K. Zhang, R. Norman, Y. Li, S. C. Zhang, B. Carter, J. Fritzer, M. Schwaerz, S. L. Choy, S. Q. Wu, and Z. X. Tan (2013). "Characterisation of residual ionospheric errors in bending angles using GNSS RO end-to-end simulations". *Adv. Space Res.* 52, pp. 821–836. DOI: 10.1016/j.asr.2013.05.021.

Liu, C., G. Kirchengast, S. Syndergaard, M. Schwaerz, J. Danzer, and Y. Sun (2020). "New Higher-Order Correction of GNSS RO Bending Angles Accounting for Ionospheric Asymmetry: Evaluation of Performance and Added Value". *Remote Sens.* 12, 3637. DOI: 10.3390/rs12213637.

Loiselet, M., N. Stricker, Y. Menard, and J.-P. Luntama (2000). "GRAS—MetOp's GPS-based atmospheric sounder". *ESA Bulletin* 102, pp. 38–44.

Luntama, J.-P. (2009). "Radio occultation soundings in ionosphere and space weather applications: Achievements and prospects". In: *New Horizons in Occultation Research: Studies in Atmosphere and Climate*. Ed. by A. K. Steiner, B. Pirscher, U. Foelsche, and G. Kirchengast. Berlin, Heidelberg: Springer-Verlag, pp. 63–76. DOI: 10.1007/978-3-642-00321-9_6.

Luntama, J.-P., G. Kirchengast, M. Borsche, U. Foelsche, A. Steiner, S. B. Healy, A. von Engeln, E. O'Clerigh, and C. Marquardt (2008). "Prospects of the EPS GRAS mission for operational atmospheric applications". *Bull. Amer. Meteor. Soc.* 89, pp. 1863–1875. DOI: 10.1175/2008BAMS2399.1.

Lyard, F., F. Lefevre, T. Letellier, and O. Francis (Dec. 2006). "Modelling the global ocean tides: modern insights from FES2004". *Ocean Dynam.* 56, pp. 394–415. ISSN: 1616-7228. DOI: 10.1007/s10236-006-0086-x.

Marquardt, C., A. von Engeln, A. Nardo, and Y. Andres (2020). *EUMETSAT Assessment of Spire Commercial RO Data*. Doc. No. EUM/TSS/TEN/20/1179103. EUMETSAT. 50 pp.

Masters, D., V. Nyuen, V. Irisov, C. Marquardt, A. von Engeln, A. Nardo, Y. Andres, J. Innerkofler, F. Ladstädter, M. Schwärz, and G. Kirchengast (2020). *ESA Evaluation: Spire GNSS-RO Data Quality Assessment by EUMETSAT and WEGC*. Spire Technical Report for ESA Rep. No. SPIRE/ESA-EO/EUMETSAT-WEGC-1. Spire Global, Inc.

Matzka, J., C. Stolle, Y. Yamazaki, O. Bronkalla, and A. Morschhauser (2021). "The Geomagnetic Kp Index and Derived Indices of Geomagnetic Activity". *Space Weather* 19, e2020SW002641. DOI: 10.1029/2020SW002641.

Montenbruck, O., Y. Andres, H. Bock, T. van Helleputte, J. van den Ijssel, M. Loiselet, C. Marquardt, P. Silvestrin, P. Visser, and Y. Yoon (Sept. 2008). "Tracking and orbit determination performance of the GRAS instrument on MetOp-A". *GPS Solut.* 12, pp. 289–299. ISSN: 1521-1886. DOI: 10.1007/s10291-008-0091-2.

Montenbruck, O., A. Hauschild, Y. Andres, A. von Engeln, and C. Marquardt (Apr. 2013). "(Near-)real-time orbit determination for GNSS radio occultation processing". *GPS Solut.* 17, pp. 199–209. DOI: 10.1007/s10291-012-0271-y.

Montenbruck, O., T. van Helleputte, R. Kroes, and E. Gill (2005). "Reduced dynamic orbit determination using GPS code and carrier measurements". *Aerosp. Sci. Technol.* 9, pp. 261–271. DOI: 10.1016/j.ast.2005.01.003.

Montenbruck, O. and R. Kroes (Aug. 2003). "In-flight performance analysis of the CHAMP BlackJack GPS Receiver". *GPS Solut.* 7, pp. 74–86. DOI: 10.1007/s10291-003-0055-5.

Mudrak, A., P. De Simone, and M. Lisi (Aug. 2015). "Relativistic Corrections in the European GNSS Galileo". *Aerotec. Missili Spaz.* 94, pp. 139–144. DOI: 10.1007/BF03404697.

Neubert, R., L. Grunwaldt, and J. Neubert (Sept. 1998). "The Retro-Reflector for the CHAMP Satellite: Final Design and Realization". In: *Proceedings of the 11th International Workshop on Laser Ranging*. Deggendorf, Germany, pp. 260–270.

Pavlis, N. K., S. A. Holmes, S. C. Kenyon, and J. K. Factor (2012). "The development and evaluation of the Earth Gravitational Model 2008 (EGM2008)". *J. Geophys. Res.* 117, B04406. DOI: 10.1029/2011JB008916.

Pearlman, M., J. Degnan, and J. Bosworth (2002). "The International Laser Ranging Service". *Adv. Space Res.* 30, pp. 135–143. ISSN: 0273-1177. DOI: 10.1016/S0273-1177(02)00277-6.

Pearlman, M. R., C. E. Noll, E. C. Pavlis, F. G. Lemoine, L. Combrink, J. J. Degnan, G. Kirchner, and U. Schreiber (Mar. 2019). "The ILRS: approaching 20 years and planning for the future". *J. Geodesy*. ISSN: 1432-1394. DOI: 10.1007/s00190-019-01241-1.

Peter, H., A. Jäggi, J. Fernández, D. Escobar, F. Ayuga, D. Arnold, M. Wermuth, S. Hackel, M. Otten, W. Simons, P. Visser, U. Hugentobler, and P. Féménias (2017). "Sentinel-1A - First precise orbit determination results". *Adv. Space Res.* 60, pp. 879–892. ISSN: 0273-1177. DOI: 10.1016/j.asr.2017.05.034.

Pirscher, B. (2010). *Multi-satellite climatologies of fundamental atmospheric variables from radio occultation and their validation (Ph.D. thesis)*. Sci. Rep. 33-2010. Austria: Wegener Center Verlag Graz. ISBN: 978-3-9502940-3-3.

Pock, C. (2015). *Low Earth Orbit Determination for GNSS Radio Occultation with Aspects of Uncertainty Estimation (M.Sc. thesis)*. Sci. Rep. 66-2015. Austria: Wegener Center Verlag Graz. ISBN: 978-3-9503918-3-1.

Prange, L., A. Jäggi, R. Dach, H. Bock, G. Beutler, and L. Mervart (2010). "AIUB-CHAMP02S: The influence of GNSS model changes on gravity field recovery using spaceborne GPS". *Adv. Space Res.* 45, pp. 215–224. DOI: 10.1016/j.asr.2009.09.020.

Proschek, V., G. Kirchengast, and S. Schweitzer (2011). "Greenhouse gas profiling by infrared-laser and microwave occultation: retrieval algorithm and demonstration results from end-to-end simulations". *Atmos. Meas. Tech.* 4, pp. 2035–2058. DOI: 10.5194/amt-4-2035-2011.

Ramsauer, J. and G. Kirchengast (2001). *Sensitivity of atmospheric profiles retrieved from GNSS radio occultation data to instrumental errors*. IGAM/UG Technical Report for ESA/ESTEC No. 6/2001. Institute for Geophysics, Astrophysics, and Meteorology, University of Graz, pp. 1–62.

Ray, J. (2016). "Precision, Accuracy, and Consistency of GNSS Products". In: *Encyclopedia of Geodesy*. Ed. by E. Grafarend. Springer International Publishing, pp. 1–5. ISBN: 978-3-319-02370-0. DOI: 10.1007/978-3-319-02370-0_97-1.

Rebischung, P. and R. Schmid (2016). "IGS14/igs14.atx: a new framework for the IGS products". In: *AGU Fall Meeting 2016*. American Geophysical Union. San Francisco, CA.

Reigber, C., H. Lühr, and P. Schwintzer (2000). "Status of the CHAMP Mission". In: *Towards an Integrated Global Geodetic Observing System (IGGOS)*. Ed. by R. Rummel, H. Drewes, W. Bosch, and H. Hornik. Berlin, Heidelberg: Springer Berlin Heidelberg, pp. 63–65. ISBN: 978-3-642-59745-9.

Rieder, M. J. and G. Kirchengast (2001). "Error analysis and characterization of atmospheric profiles retrieved from GNSS occultation data". *J. Geophys. Res.* 106, pp. 31755–31770. DOI: 10.1029/2000JD000052.

Rocken, C., R. Anthes, M. Exner, D. Hunt, S. Sokolovskiy, R. Ware, M. Gorbunov, W. Schreiner, D. Feng, B. Herman, Y.-H. Kuo, and X. Zuo (1997). "Analysis and validation of GPS/MET data in the neutral atmosphere". *J. Geophys. Res.* 102, pp. 29849–29866. DOI: 10.1029/97JD02400.

Rocken, C. and C. Meertens (1991). "Monitoring selective availability dither frequencies and their effect on GPS data". *B. Geod.* 65, pp. 162–169. DOI: 10.1007/BF00806345.

Rudenko, S., D. Dettmering, S. Esselborn, T. Schöne, C. Förste, J.-M. Lemoine, M. Ablain, D. Alexandre, and K.-H. Neumayer (2014). "Influence of time variable geopotential models on precise orbits of altimetry satellites, global and regional mean sea level trends". *Adv. Space Res.* 54, pp. 92–118. ISSN: 0273-1177. DOI: 10.1016/j.asr.2014.03.010.

SAAB (2004). *METOP-GRAS Measurement Data Interpretation and Description*. P-GRM-SPC-0036-SE. Issue 7. Göteborg, Sweden: Saab Ericsson Space. 94 pp.

Scaramuzza, S., R. Dach, G. Beutler, D. Arnold, A. Sušnik, and A. Jäggi (Jan. 2018). "Dependency of geodynamic parameters on the GNSS constellation". *J. Geodesy* 92, pp. 93–104. DOI: 10.1007/s00190-017-1047-5.

Scherllin-Pirscher, B., G. Kirchengast, A. K. Steiner, Y.-H. Kuo, and U. Foelsche (2011a). "Quantifying uncertainty in climatological fields from GPS radio occultation: an empirical-analytical error model". *Atmos. Meas. Tech.* 4, pp. 2019–2034. DOI: 10.5194/amt-4-2019-2011.

Scherllin-Pirscher, B., A. K. Steiner, G. Kirchengast, Y.-H. Kuo, and U. Foelsche (2011b). "Empirical analysis and modeling of errors of atmospheric profiles from GPS radio occultation". *Atmos. Meas. Tech.* 4, pp. 1875–1890. DOI: 10.5194/amt-4-1875-2011.

Schmid, R., R. Dach, X. Collilieux, A. Jäggi, M. Schmitz, and F. Dilssner (Apr. 2016). "Absolute IGS antenna phase center model igs08.atx: status and potential improvements". *J. Geodesy* 90, pp. 343–364. ISSN: 1432-1394. DOI: 10.1007/s00190-015-0876-3.

Schmidt, T., J. Wickert, S. Heise, F. Flechtner, E. Fagiolini, G. Schwarz, L. Zenner, and T. Gruber (2008). "Comparison of ECMWF analyses with GPS radio occultations from CHAMP". *Ann. Geophys.* 26, pp. 3225–3234. DOI: 10.5194/angeo-26-3225-2008.

Schreiner, W., S. Sokolovskiy, D. Hunt, C. Rocken, and Y.-H. Kuo (2011). "Analysis of GPS radio occultation data from the FORMOSAT-3/COSMIC and Metop/GRAS missions at CDAAC". *Atmos. Meas. Tech.* 4, pp. 2255–2272. DOI: 10.5194/amt-4-2255-2011.

Schreiner, W., J. Weiss, R. Anthes, J. Braun, V. Chu, J. Fong, D. Hunt, Y.-H. Kuo, T. Meehan, W. Serafino, J. Sjoberg, S. Sokolovskiy, E. Talaat, T. Wee, and Z. Zeng (2020). "COSMIC-2 Radio Occultation Constellation: First Results". *Geophys. Res. Lett.* 47, e2019GL086841. DOI: 10.1029/2019GL086841.

Schreiner, W., C. Rocken, S. Sokolovskiy, S. Syndergaard, and D. Hunt (2007). "Estimates of the precision of GPS radio occultations from the COSMIC/FORMOSAT-3 mission". *Geophys. Res. Lett.* 34, L04808. DOI: 10.1029/2006GL027557.

Schreiner, W. S., C. Rocken, S. Sokolovskiy, and D. Hunt (2010). "Quality assessment of COSMIC/FORMOSAT-3 GPS radio occultation data derived from single- and double-difference atmospheric excess phase processing". *GPS Solut.* 14, pp. 13–22. DOI: 10.1007/s10291-009-0132-5.

Schreiner, W. S., S. V. Sokolovskiy, C. Rocken, and D. C. Hunt (1999). "Analysis and validation of GPS/MET radio occultation data in the ionosphere". *Radio Sci.* 34, pp. 949–966. DOI: 10.1029/1999RS900034.

Schutz, B. E., B. D. Tapley, P. A. M. Abusali, and H. J. Rim (1994). "Dynamic orbit determination using GPS measurements from TOPEX/POSEIDON". *Geophys. Res. Lett.* 21, pp. 2179–2182. DOI: 10.1029/94GL01040.

Schwarz, J. C. (2018). *Benchmark Quality Processing of Radio Occultation Data with Integrated Uncertainty Propagation (Ph.D. thesis)*. Sci. Rep. 77-2018. Austria: Wegener Center Verlag Graz. ISBN: 978-3-9504501-5-6. URL: https://wegcwww.uni-graz.at/publ/wegcreports/2018/WCV-SciRep-No77-JSchwarz-July2018.pdf (visited on 06/27/2024).

Schwarz, J. C., G. Kirchengast, and M. Schwaerz (2017). "Integrating uncertainty propagation in GNSS radio occultation retrieval: from bending angle to dry-air atmospheric profiles". *Earth Space Sci.* 4, pp. 200–228. DOI: 10.1002/2016EA000234.

– (2018). "Integrating uncertainty propagation in GNSS radio occultation retrieval: from excess phase to atmospheric bending angle profiles". *Atmos. Meas. Tech.* 11, pp. 2601–2631. DOI: 10.5194/amt-11-2601-2018.

Seidel, D. J., F. H. Berger, F. Immler, M. Sommer, H. Vömel, H. J. Diamond, J. Dykema, D. Goodrich, W. Murray, T. Peterson, D. Sisterson, P. Thorne, and J. Wang (2009). "Reference Upper-Air Observations for Climate: Rationale, Progress, and Plans". *Bull. Amer. Meteor. Soc.* 90, pp. 361–369. DOI: 10.1175/2008BAMS2540.1.

Seidl, V. (2018). "Quality control and evaluation for atmospheric profiles from GNSS radio occultation reference processing". M.Sc. thesis. Master's thesis. University of Graz, Austria: WEGC and IGAM. 111 pp.

Shen, Z., K. Zhang, Q. He, M. Wan, L. Li, and S. Wu (2021). "Quest over the Sampling Error of COSMIC Radio Occultation Temperature Climatologies". *J. Atmos. Oceanic Technol.* 38, pp. 441–458. DOI: 10.1175/JTECH-D-19-0169.1.

Sicardy, B. (2022). "Study of atmospheres in the solar system, from stellar occultation or planetary transit". *C. R. Phys.* 23, pp. 213–241. DOI: 10.5802/crphys.109.

Silvestrin, P., R. Bagge, M. Bonnedal, A. Carlström, J. Christensen, M. Hägg, and T. Lindgren (Jan. 2000). "Spaceborne GNSS Radio Occultation Instrumentation for Operational Applications". *Proceedings of ION GPS*.

Smith, E. and S. Weintraub (1953). "The Constants in the Equation for Atmospheric Refractive Index at Radio Frequencies". *Proc. IRE* 41, pp. 1035–1037. DOI: 10.1109/JRPROC.1953.274297.

Smith, S. W. (1999). *The Scientist and Engineer's Guide to Digital Signal Processing*. 2nd ed. San Diago, CA, USA: California Technical Publishing. 688 pp. ISBN: 0-9660176-6-8.

Sokolovskiy, S., C. Rocken, W. Schreiner, D. Hunt, and J. Johnson (2009a). "Postprocessing of L1 GPS radio occultation signals recorded in open-loop mode". *Radio Sci.* 44, RS2002. DOI: 10.1029/2008RS003907.

Sokolovskiy, S., C. Rocken, D. Hunt, W. Schreiner, J. Johnson, D. Masters, and S. Esterhuizen (2006). "GPS profiling of the lower troposphere from space: Inversion and demodulation of the open-loop radio occultation signals". *Geophys. Res. Lett.* 33, L14816. DOI: 10.1029/2006GL026112.

Sokolovskiy, S. V. (2001). "Tracking tropospheric radio occultation signals from low Earth orbit". *Radio Sci.* 36, pp. 483–498. DOI: 10.1029/1999RS002305.

Sokolovskiy, S. V., W. S. Schreiner, C. Rocken, and D. Hunt (2009b). "Optimal noise filtering for the ionospheric correction of GPS radio occultation signals". *J. Atmos. Oceanic Technol.* 26, pp. 1398–1403. DOI: 10.1175/2009JTECHA1192.1.

Sośnica, K., D. Thaller, R. Dach, P. Steigenberger, G. Beutler, D. Arnold, and A. Jäggi (2015). "Satellite laser ranging to GPS and GLONASS". *J. Geodesy* 89, pp. 725–743. DOI: 10.1007/s00190-015-0810-8.

Springer, T. A. (2009). *NAPEOS—Mathematical Models and Algorithms*. DOPS-SYS-TN-0100-OPS-GN. Darmstadt, Germany: European Space Operation Centre, European Space Agency. 150 pp.

Standish, E. M. (1998). *JPL Planetary and Lunar Ephemerides, DE405/LE405*. Interoffice Memorandum (IOM), 98, 048. Pasadena, CA, USA: Jet Propulsion Laboratory. 18 pp.

Steiner, A. K., D. Hunt, S.-P. Ho, G. Kirchengast, A. J. Mannucci, B. Scherllin-Pirscher, H. Gleisner, A. von Engeln, T. Schmidt, C. Ao, S. S. Leroy, E. R. Kursinski, U. Foelsche, M. Gorbunov, S. Heise, Y.-H. Kuo, K. B. Lauritsen, C. Marquardt, C. Rocken, W. Schreiner, S. Sokolovskiy, S. Syndergaard, and J. Wickert (2013). "Quantification of structural uncertainty in climate data records from GPS radio occultation". *Atmos. Chem. Phys.* 13, pp. 1469–1484. DOI: 10.5194/acp-13-1469-2013.

Steiner, A. K. and G. Kirchengast (2005). "Error analysis of GNSS radio occultation data based on ensembles of profiles from end-to-end simulations". *J. Geophys. Res.* 110, D15307. DOI: 10.1029/2004JD005251.

Steiner, A. K., G. Kirchengast, and H. P. Ladreiter (1999). "Inversion, error analysis, and validation of GPS/MET occultation data". *Ann. Geophys.* 17, pp. 122–138. DOI: 10.1007/s00585-999-0122-5.

Steiner, A. K., B. C. Lackner, F. Ladstädter, B. Scherllin-Pirscher, U. Foelsche, and G. Kirchengast (2011). "GPS radio occultation for climate monitoring and change detection". *Radio Sci.* 46, RS0D24. DOI: 10.1029/2010RS004614.

Steiner, A. K., F. Ladstädter, C. O. Ao, H. Gleisner, S.-P. Ho, D. Hunt, T. Schmidt, U. Foelsche, G. Kirchengast, Y.-H. Kuo, K. B. Lauritsen, A. J. Mannucci, J. K. Nielsen, W. Schreiner, M. Schwärz, S. Sokolovskiy, S. Syndergaard, and J. Wickert (2019). "Consistency and structural uncertainty of multi-mission GPS

radio occultation records". *Atmos. Meas. Tech. Discuss.* DOI: 10.5194/amt-2019-358.

Steiner, A. K., F. Ladstädter, C. O. Ao, H. Gleisner, S.-P. Ho, D. Hunt, T. Schmidt, U. Foelsche, G. Kirchengast, Y.-H. Kuo, K. B. Lauritsen, A. J. Mannucci, J. K. Nielsen, W. Schreiner, M. Schwärz, S. Sokolovskiy, S. Syndergaard, and J. Wickert (2020). "Consistency and structural uncertainty of multi-mission GPS radio occultation records". *Atmos. Meas. Tech.* 13, pp. 2547–2575. DOI: 10.5194/amt-13-2547-2020.

Strugarek, D., K. Sośnica, and A. Jäggi (2019). "Characteristics of GOCE orbits based on Satellite Laser Ranging". *Adv. Space Res.* 63, pp. 417–431. DOI: 10.1016/j.asr.2018.08.033.

Sun, Y., W. Bai, C. Liu, Y. Liu, Q. Du, X. Wang, G. Yang, M. Liao, Z. Yang, X. Zhang, X. Meng, D. Zhao, J. Xia, Y. Cai, and G. Kirchengast (2018). "The FengYun-3C radio occultation sounder GNOS: a review of the mission and its early results and science applications". *Atmos. Meas. Tech.* 11, pp. 5797–5811. DOI: 10.5194/amt-11-5797-2018.

Sun, Y., C. Liu, Q. Du, X. Wang, W. Bai, G. Kirchengast, J. Xia, X. Meng, D. Wang, Y. Cai, D. Zhao, C. Wu, W. Li, and C. Liu (2017). "Global Navigation Satellite System Occultation Sounder II (GNOS II)". In: *2017 IEEE International Geoscience and Remote Sensing Symposium (IGARSS)*, pp. 1189–1192. DOI: 10.1109/IGARSS.2017.8127170.

Sušnik, A., R. Dach, A. Villiger, A. Maier, D. Arnold, S. Schaer, and A. Jäggi (2016). *CODE reprocessing product series*. Astronomical Institute, University of Bern. DOI: 10.7892/boris.80011.

Švehla, D. and M. Rothacher (2002). "Kinematic Orbit Determination of LEOs Based on Zero or Double-difference Algorithms Using Simulated and Real SST GPS Data". In: *Vistas for Geodesy in the New Millennium*. Ed. by J. Ádám and K.-P. Schwarz. Berlin, Heidelberg: Springer Berlin Heidelberg, pp. 322–328. ISBN: 978-3-662-04709-5.

– (2005). "Kinematic Precise Orbit Determination for Gravity Field Determination". In: *A Window on the Future of Geodesy*. Ed. by F. Sansò. Berlin, Heidelberg: Springer Berlin Heidelberg, pp. 181–188. ISBN: 978-3-540-27432-2.

Syndergaard, S. (1998). "Modeling the impact of the Earth's oblateness on the retrieval of temperature and pressure profiles from limb sounding". *J. Atmos. Solar-Terr. Phys.* 60, pp. 171–180. DOI: 10.1016/S1364-6826(97)00056-4.

– (1999). *Retrieval analysis and methodologies in atmospheric limb sounding using the GNSS radio occultation technique (Ph.D. thesis)*. DMI Sci Rep 99-6. Danish Meteorological Institute, Copenhagen, Denmark. 89 pp. ISBN: 87-7478-394-7.

Syndergaard, S. and G. Kirchengast (2016). "An Abel transform for deriving line-of-sight wind profiles from LEO-LEO infrared laser occultation measurements". *J. Geophys. Res.* 121, pp. 2525–2541. DOI: 10.1002/2015JD023535.

T. P. Yunck, G. F. Lindal, and C. H. Liu (1988). "The role of GPS in precise earth observation". In: *PLANS '88 - IEEE Position Location and Navigation Symposium*, pp. 251–258. DOI: 10.1109/PLANS.1988.195491.

Tapley, B., M. Watkins, F. Flechtner, C. Reigber, S. Bettadpur, M. Rodell, I. Sasgen, J. Famiglietti, F. Landerer, D. Chambers, J. Reager, A. Gardner, H. Save, E. Ivins, S. Swenson, C. Boening, C. Dahle, D. Wiese, H. Dobslaw, and I. Velicogna (Apr. 2019). "Contributions of GRACE to understanding climate change". *Nat. Clim. Change* 5. DOI: 10.1038/s41558-019-0456-2.

Tapley, B. D., S. Bettadpur, M. Watkins, and C. Reigber (2004). "The gravity recovery and climate experiment: Mission overview and early results". *Geophys. Res. Lett.* 31. DOI: 10.1029/2004GL019920.

Tapping, K. F. (2013). "The 10.7 cm solar radio flux (F10.7)". *Space Weather* 11, pp. 394–406. DOI: 10.1002/swe.20064.

Teunissen, P. J. and O. Montenbruck (2017). *Springer Handbook of Global Navigation Satellite Systems*. Springer. 1327 pp. ISBN: 978-3-319-42926-7. DOI: 10.1007/978-3-319-42928-1.

Thorne, P. W., D. E. Parker, J. R. Christy, and C. A. Mears (2005). "Uncertainties in climate trends: Lessons from upper-air temperature records". *Bull. Amer. Meteor. Soc.* 86, pp. 1437–1442. DOI: 10.1175/BAMS-86-10-1437.

Tyler, G. (1987). "Radio propagation experiments in the outer solar system with Voyager". *P. IEEE* 75, pp. 1404–1431. DOI: 10.1109/PROC.1987.13896.

Urschl, C., W. Gurtner, U. Hugentobler, S. Schaer, and G. Beutler (2005). "Validation of GNSS orbits using SLR observations". *Adv. Space Res.* 36, pp. 412–417. DOI: 10.1016/j.asr.2005.03.021.

von Engeln, A., S. Healy, C. Marquardt, Y. Andres, and F. Sancho (2009). "Validation of operational GRAS radio occultation data". *Geophys. Res. Lett.* 36, L17809. DOI: 10.1029/2009GL039968.

Vorob'ev, V. V. and T. G. Krasil'nikova (1994). "Estimation of the accuracy of the atmospheric refractive index recovery from Doppler shift measurements at frequencies used in the NAVSTAR system". *Izv. Atmos. Ocean. Phys.* 29, pp. 602–609.

Wang, W. and C.-Z. Zou (2014). "AMSU-A-Only Atmospheric Temperature Data Records from the Lower Troposphere to the Top of the Stratosphere". *J. Atmos. Oceanic Technol.* 31, pp. 808–825. DOI: 10.1175/JTECH-D-13-00134.1.

Wee, T.-K. and Y.-H. Kuo (2015). "A perspective on the fundamental quality of GPS radio occultation data". *Atmos. Meas. Tech.* 8, pp. 4281–4294. DOI: 10.5194/amt-8-4281-2015.

WEGC EOPAC team (2021). *GNSS Radio Occultation Record (OPS 5.6 2001–2020)*. DOI: 10.25364/WEGC/OPS5.6:2021.1. URL: https://wegcwww.uni-graz.at/data-store/WEGC/OPS5.6:2021.1/.

Wei, J., Y. Li, K. Zhang, M. Liao, W. Bai, C. Liu, Y. Liu, and X. Wang (July 2020). "An Evaluation of Fengyun-3C Radio Occultation Atmospheric Profiles Over 2015–2018". *Remote Sens.* 12, p. 2116. ISSN: 2072-4292. DOI: 10.3390/rs12132116.

Wickert, J. (2002). *Das CHAMP-Radiookkultationsexperiment: Algorithmen, Prozessierungssystem und erste Ergebnisse (Ph.D. thesis)*. Scientific Tech. Rep. STR02/07. GeoForschungsZentrum Potsdam. 149 pp.

Wickert, J., G. Beyerle, G. A. Hajj, V. Schwieger, and C. Reigber (2002). "GPS radio occultation with CHAMP: Atmospheric profiling utilizing the space-based single difference technique". *Geophys. Res. Lett.* 29. DOI: 10.1029/2001GL013982.

Wickert, J., G. Beyerle, R. König, S. Heise, L. Grunwaldt, G. Michalak, C. Reigber, and T. Schmidt (2005). "GPS radio occultation with CHAMP and GRACE: A first look at a new and promising satellite configuration for global atmospheric sounding". *Ann. Geophys.* 23, pp. 653–658. DOI: 10.5194/angeo-23-653-2005.

Wickert, J., R. Galas, G. Beyerle, R. König, and C. Reigber (2001a). "GPS ground station data for CHAMP radio occultation measurements". *Phys. Chem. Earth* 26, pp. 503–511. DOI: 10.1016/S1464-1895(01)00092-8.

Wickert, J., C. Reigber, G. Beyerle, R. König, C. Marquardt, T. Schmidt, L. Grunwaldt, R. Galas, T. Meehan, W. Melbourne, and K. Hocke (2001b). "Atmosphere sounding by GPS radio occultation: First results from CHAMP". *Geophys. Res. Lett.* 28, pp. 3263–3266. DOI: 10.1029/2001GL013117.

Wickert, J., T. Schmidt, G. Michalak, S. Heise, C. Arras, G. Beyerle, C. Falck, R. König, D. Pingel, and M. Rothacher (2009). "GPS radio occultation with

CHAMP, GRACE-A, SAC-C, TerraSAR-X, and FORMOSAT-3/COSMIC: Brief review of results from GFZ". In: *New Horizons in Occultation Research: Studies in Atmosphere and Climate*. Ed. by A. K. Steiner, B. Pirscher, U. Foelsche, and G. Kirchengast. Berlin, Heidelberg: Springer-Verlag, pp. 3–16.

Wilkinson, M., K. Schreiber, I. Prochazka, C. Moore, J. Degnan, G. Kirchner, Z. Zhongping, P. Dunn, V. Shargorodskiy, M. Sadovnikov, C. Courde, and H. Kunimori (Sept. 2018). "The next generation of satellite laser ranging systems". *J. Geodesy*. DOI: 10.1007/s00190-018-1196-1.

Wu, S. C. W., T. P. Yunck, and C. L. Thornton (1991). "Reduced-dynamic technique for precise orbit determination of low earth satellites". *J. Guid. Control Dynam.* 14, pp. 24–30. DOI: 10.2514/3.20600.

Yuan, L. L., R. A. Anthes, R. H. Ware, C. Rocken, W. D. Bonner, M. G. Bevis, and S. Businger (1993). "Sensing climate change using the Global Positioning System". *J. Geophys. Res.* 98, pp. 14925–14937. DOI: 10.1029/93JD00948.

Yunck, T. P., W. I. Bertiger, S. C. Wu, Y. E. Bar-Sever, E. J. Christensen, B. J. Haines, S. M. Lichten, R. J. Muellerschoen, Y. Vigue, and P. Willis (1994). "First assessment of GPS-based reduced dynamic orbit determination on TOPEX/Poseidon". *Geophys. Res. Lett.* 21, pp. 541–544. DOI: 10.1029/94GL00010.

Yunck, T. P. (2002). "An Overview of Atmospheric Radio Occultation". *J. GPS* 1, pp. 58–60.

Yunck, T. P., C.-H. Liu, and R. Ware (2000). "A History of GPS Sounding". *Terr. Atmos. Ocean. Sci.* 11, pp. 1–20. DOI: 10.3319/TAO.2000.11.1.1(COSMIC).

Zehentner, N. and T. Mayer-Gürr (2016). "Precise orbit determination based on raw GPS measurements". *J. Geodesy* 90, pp. 275–286. DOI: 10.1007/s00190-015-0872-7.

Zeng, Z., S. Sokolovskiy, W. Schreiner, and D. Hunt (2019). "Representation of vertical atmospheric structures by radio occultation observations in the UTLS: comparison to high resolution radiosonde profiles". *J. Atmos. Oceanic Technol.* 36, pp. 655–670. DOI: 10.1175/JTECH-D-18-0105.1.

Zeng, Z., S. Sokolovskiy, W. Schreiner, D. Hunt, J. Lin, and Y.-H. Kuo (2016). "Ionospheric correction of GPS radio occultation data in the troposphere". *Atmos. Meas. Tech.* 9, pp. 335–346. DOI: 10.5194/amt-9-335-2016.

Zhang, P., X. Hu, Q. Lu, A. Zhu, M. Lin, L. Sun, L. Chen, and N. Xu (Sept. 2022). "FY-3E: The First Operational Meteorological Satellite Mission in an Early Morning Orbit". *Adv. Atmos. Sci.* 39, pp. 1–9. DOI: 10.1007/s00376-021-1304-7.

Zus, F., G. Beyerle, S. Heise, T. Schmidt, J. Wickert, and C. Marquardt (2011). "Validation of refractivity profiles derived from GRAS raw-sampling data". *Atmos. Meas. Tech.* 4, pp. 1541–1550. DOI: 10.5194/amt-4-1541-2011.

The Intergovernmental Panel on Climate Change (IPCC) states that global warming is an ongoing threat and its worldwide environmental and socioeconomic implications call for a reliable global observational foundation of climate change processes for adequate actions of adaption and mitigation. By observing Essential climate variables (ECVs), such as atmospheric temperature and humidity, from space, the Global Navigation Satellite System (GNSS) radio occultation (RO) measurement technique is highly valuable to support these challenges with the provision of climate benchmark data. Since uncertainties in RO measurements play a significant role in the application for climate monitoring and modeling, this thesis emphasized their better quantification and established a climate-quality processing approach for low-level RO data within the new Reference Occultation Processing System (rOPS) of the Wegener Center for Climate and Global Change.

This approach comprised the implementation of a precise orbit processing subsystem, providing GNSS transmitter and RO receiver orbit and clock data, including estimates of uncertainty and careful quality control. In a subsequent step, based on the orbit and clock data, a new implementation of RO excess phase processing, which was not yet part of rOPS, was realized. Thus, the raw measurement data and their estimated uncertainties can be processed to atmospheric ECVs while ensuring SI-traceability. The integrity of this novel implementation is ensured by extensive evaluation of the uncertainty estimates and by cross-comparison of the atmospheric profiles with data from other international RO processing centers. It also has been used for the evaluation of new RO mission data.

As an important benefit of this work, rOPS, now independent of externallypre-processed input data, represents a highly valuable software utility for the cross-evaluation of existing RO processing systems, the identification of structural uncertainties in RO data, and the evaluation of future RO missions. Rigorous uncertainty propagation along the RO retrieval chain, based on the estimated profile uncertainties at excess phase level, also provides substantial benefit for RO climate research and monitoring, as well as for climate trend detection and weather prediction applications.).

SR 106 | 2024 Precise orbit determination and excess phase processing for radio occultation:
Integrated uncertainty estimation for climate applications
Wegener Center Verlag, University of Graz, Austria. ISBN 978-3-9505053-5-1